Strain Mechanisms in Lead-Free Ferroelectrics for Actuators

Institute of Materials Science

Technische Universität Darmstadt

Requirement to obtain the academic degree *Doctor rerum naturalium*

(Dr. rer. nat.)

of

Ing. Matias Acosta

born on the 17th of October of 1987 in Mar del Plata, Argentina

July 2015 – Darmstadt- D17

1st Advisor: Prof. Dr.-Ing. Jürgen Rödel

2nd Advisor: Prof. Dr. rer. nat. Wolfgang Donner

TECHNISCHE UNIVERSITÄT DARMSTADT

Material- und Geowissenschaften
Nichtmetallisch-Anorganische Werkstoffe

Strain Mechanisms in Lead-Free Ferroelectrics for Actuators

Dissertation approved by the Fachbereich Material- und Geowissenschaften Matias Acosta, born in Mar del Plata, Argentina

1st Advisor: Prof. Dr.-Ing. Jürgen Rödel

2nd Advisor: Prof. Dr. rer. nat. Wolfgang Donner

Date of submission: 26th of June 2015

Date of defense: 21st of July 2015

Darmstadt, 2015 – D 17

The truth is always subjected to perceptions. Analyze all imaginable perceptions and you will get a step closer to revealing it.

Matias Acosta

Darmstadt, June 15th 2015

This page intentionally left blank

Acknowledgements

I would first like to acknowledge my supervisor and mentor Prof. Rödel. He constantly showed his support to my ideas and initiatives. He allowed me to develop myself professionally and was always an example to follow; not just a boss but a professor. I learned a lot from his open mind, professionalism, organization, respectfulness, and devotion to work. He remains to me as an admirable professor to which I owe a lot of my professional development. Without his support and the economic support of the AdRIA Hesse State Center for Adaptronics and the Deutsche Forschungsgemeinschaft this work would have never been realized. I would also like to thank my co-supervisor Prof. Donner. I started having more contact with him after assisting to several of his lectures and writing some joint papers. He always supported my work and made himself time to answer my questions and discuss doubts. He was a constant mentor and was always characterized by his good predisposition and kindness.

I would also like to thank the postdocs that contributed directly to my dissertation. Wook, Kyle, (both became professors during my time in NAW), Nikola, Jurij, and Eric. I was lucky to share many discussions with them. I learned a lot during this process and I will always keep a lot of good memories. I would also like to thank the other members of the Nichtmetallisch-Anorganische Werkstoffe group to which I owe a great part of all my achievements and daily life experiences. Initially, I would like to thank the people that directly make my work possible. Gila, Roswita, and Gundel were what I would like to call my “German mothers”. I always came to them with a variety of questions from a recipe to some German tax issue, to work concerns, among many others. They always helped me and undoubtedly I could not have reached this point without their constant help. Daniel and Michael were also a great support. I always came to them in a hurry and with problems. Somehow they always manage to a get a proper solution whenever needed. I would like to thank specially some of the members of the group to which circumstances make that I spend more time with them: Eric, Jurij, Martin, Azatuhi, Raschid, and Virginia. Thank you very much for the moments shared. For all other members, my great thanks since you were always a great team that constantly helped me in the right occasions. My thoughts of the group remain totally positive and I am very happy that I had the opportunity to share moments with each of you. I will always be thankful as well to Mrs. Kunz, Mr. Jaud, and Dipl.-Ing. Fasel for being responsible for the microscopy, X-ray diffraction, and thermal studies. Transmission electron microscopy was performed by M. Sc. Scherrer and Dr. Molina-Luna and I am also very grateful for their support.

I must mention in this part other professors that forged my professional career; those that I used to call my students. I had the pleasure to supervise exceptional students throughout my work Sabrina, Heide, David, Malte, Virginia, and Sarah. I am happy to say that some of these students I can now call colleagues. I firmly believe that you all enriched my work and I learned a lot from you. Thank you very much for the shared moments and I hope I was a proper mentor for you, as you were to me. I hope I helped to build the initial steps of your professional career.

I have also maintained several active collaborations with researchers at the university and also around the globe that taught me many valuable lessons. I would like to thank Prof. Rossetti, Prof. Boccaccini, Prof. Xu, Prof. Wang, Prof. Zhang, Dr. Hinterstein (as he carried out neutron diffraction

experiments), Dr. de Luca, Dr. Glaum, Dr. Cordero, Dr. Zhukov, Dr. Genenko, Dr. Schmitt, M. Sc. Zakhozheva, and M. Sc. Liu.

Starting my dissertation, so far from my beloved country was not an easy decision. As I came here I had lived for 6 months in Darmstadt but my friends back then had left the city so the beginning of my work was also the beginning of a new cycle in my life. Pablo and Tina you were my first friends here at that time, still very close friends to me and a constant support for any problem. I am very thankful for the great help that you have always provided me. For integrating me to your activities and make me spend such good moments. Thank you very much for all!

Life continued, and living in a city like Darmstadt means seeing many people coming and leaving. I must say I have lived 3 to 4 generations of Erasmus students coming and going. Basically, after some time here, one gets used to saying goodbye. I cannot mention all since I would need another dissertation for this, but I would like to recall my Brazilian friends Renata, Rafa, Laurinha, Priscila, Estevao, my Latino friends Michael, Rodri, Tefi, Mauri, Fabian; my Spanish friends Angelito, Migue, Bea, Pao, Pau, Marta, Estersita and some more friends from other countries and cities like Nico, Luis, Toni, Bea, and Somaya. Also my thanks go to my Argentinian life colleagues, guys to you that we know each other for more than 10 years. Some that even got to know Darmstadt, even if we were separated by almost half the globe. Igna, Gas, Juan, Pablito, Furu, JP, Emi, Tomy, Mate, Orne, Luti, Lepo, Anita, Tefita, Agos, Negro, Fran, Pedrito, Mono, los varios Nicos, Guidin, Logu, Emilce. We all shared very good moments together. I hope our paths join again somewhere in the future. Thank you very much for being always there when I needed.

I must speak now of my family. I have always been afraid of being so far from them, although I never said so. I have always been scared of not being there in case anything happens. I regretted each day this situation and I sacrificed this feeling to achieve the objective of writing these words. From the very beginning I dreamed with my oral presentation and if I would be able to share it with all of you. Although I have been alone here (actually surrounded by friends), I must say you have always been here with me as well. You have always supported me and send me your kindness every Sunday which made me continue. My words can only express my deep acknowledgement to all. Without your constant help I could have never achieved this goal of being abroad and try to get the best out my education and life. I always tried to open myself and my mentality to acquire the required level of education to give something back to you and to other people of what I have received. I consider this my second written present to you and as said last time, I hope it is not my last. My great thanks to my beloved family and a reminder: I love you all deeply and you are always next to me.

To conclude this section, I would like to give my thanks to my love Ele. Honestly, you appear from nowhere, and from the very beginning that we met, we had a special connection. I have discovered the amazing person you are from the beginning of our time together and I am still wondering how I could be so lucky. My love, thank you very much for tolerating my personality, as well as my ridiculous working hours in the last months. I am very sorry that I was not there for you sometimes due to this work. Your constant support was always great and made me stronger in these lasts and difficult steps. You are my family here; you make me happy, my love. Thank you very much.

Content

This page intentionally left blank

List of Abbreviations

E_c:	Coercive field
E_{f-r}:	Electric field at which the ferroelectric state decays into a relaxor state
E_{r-f}:	Electric field required to induce a ferroelectric state
P_{max}:	Maximum polarization
P_r:	Remanent polarization
P_s^i:	Spontaneous polarization
S_{f-r}:	Strain at which the induced ferroelectric state decays into a relaxor state
S_{max}:	Maximum strain
S_{neg}:	Negative strain
S_r:	Remanent strain
S_{r-f}:	Strain output when the ferroelectric state is induced
T_0:	Curie-Weiss temperature
T_B:	Burns temperature
T_C:	Curie temperature
T_d:	Depolarization temperature
T_{f-r}:	Temperature corresponding to the ferroelectric to relaxor phase transition
T_{fr}:	Freezing temperature
T_m:	Temperature of the maximum real part of the relative permittivity
AFD:	Antiferrodistortive
BF:	Bright field
BNT:	$(Bi_{1/2}Na_{1/2})TiO_3$
BKT:	$(Bi_{1/2}K_{1/2})TiO_3$
BNT- or BKT-based:	Bismuth alkali-based materials
BNT-0.25ST:	0.75 mol fraction $(Bi_{1/2}Na_{1/2})TiO_3$-0.25 mol fraction $SrTiO_3$
BSE:	Back scattered electron
BT:	$BaTiO_3$
BT-based:	Barium titanate-based materials
BZ:	$BaZrO_3$
BZT-BCT:	$(1-x)Ba(Zr_{0.2}Ti_{0.8})O_3$-$x(Ba_{0.7}Ca_{0.3})TiO_3$

C:	Prototype cubic phase
CT:	$CaZrO_3$
DF:	Dark field
DTA:	Differential thermal analysis
DW:	Dry weight
EDS:	Energy-dispersive X-ray spectroscopy
FD:	Ferrodistortive
FT-IR:	Fourier transform infrared spectrometer
KNN:	$(K_xNa_{1-x})NbO_3$
KNN-based:	Alkali niobate-based materials
M:	Monoclinic phase
MPB:	Morphotropic phase boundary
O:	Orthorhombic phase
PNR:	Polar nanoregion
PPB:	Polymorphic phase boundary
PZT:	$Pb(Zr_xTi_{1-x})O_3$
R:	Rhombohedral phase
SAED:	Selected area diffraction
SEM:	Scanning electron microscope
SSR:	Superlattice reflections
ST:	$SrTiO_3$
STEM:	Scanning transmission electron microscopy
SWA:	Saturated weight in air
SWW:	Saturated weight in water
T:	Tetragonal phase
t:	Tolerance factor
TEM:	Transmission electron microscopy
TGA:	Thermogravimetric analysis
XRD:	X-ray diffraction

1 Introduction

Multifunctional ceramics have become increasingly important in advanced technologies because they transduce electrical, mechanical, thermal, optical, and magnetic energies.[1] These advanced ceramics are intended to meet the constantly evolving frontiers of new energy efficient products, which are desired to increase productivity and assure a better quality of life.[2] Piezoelectrics couple electrical and mechanical properties and thus are relevant in a wide variety of applications, such as actuators, motors, sensors, accelerometers, transducers, resonators, and others.[3,4] Actuators are designed to transform an electrical input into controlled displacement. They are normally implemented in fuel injectors, fabrication of semiconductor chips, optical lenses and mirrors, autofocusing of cameras, ink-jet printers, positioning video tape-recording heads, and micromachining devices, among many others.[3,4] The most important features of actuators are their physical dimensions, stroke, output force, operating frequency and temperature, weight, reliability, and cost.[5,6] Piezoelectric and electromagnetic technologies are commonly used in actuators. The former is generally more suited for miniaturization due to faster response, less moving parts, less flammable components, and higher efficiency. Moreover, piezoelectrics function with no electromagnetic noise.[7] From the viewpoint of the piezoelectric material, actuators may be classified as working in the small or large signal regime, as depicted in Figure 1.1. The small signal regime indicates that the piezoelectric responds linearly to an electric field input, on the order of 0.0005 kV/mm. Large signal indicates that higher electric field inputs on the order of 2 kV/mm lead to a non-linear electromechanical response. The high power, small signal regime entails high frequency applications with a certain degree of non-linearity due to the relatively large electric field input above 0.006 kV/mm applied during service.[8,9] This work will mostly concern the characterization of piezoceramics in the low power, small signal regime and large signal regime, as pointed out in Figure 1.1.

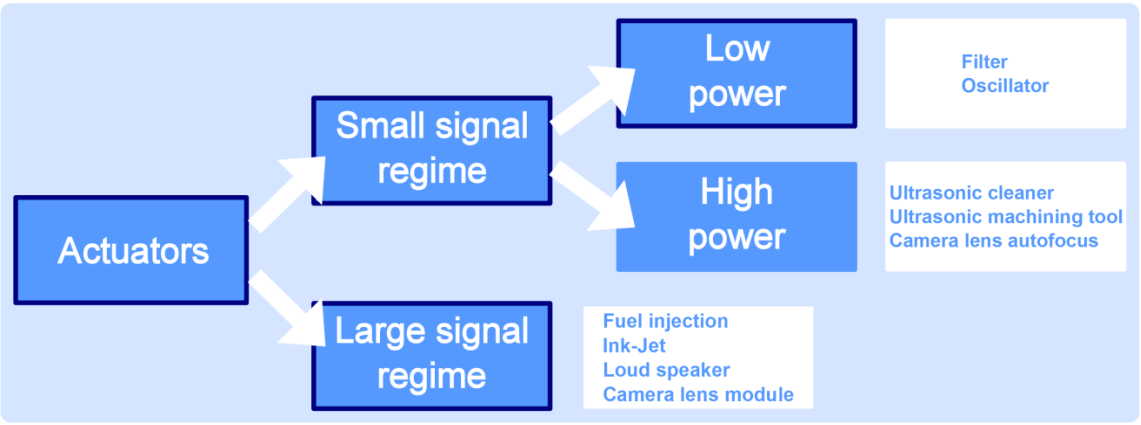

Figure 1.1: Classification of piezoelectric actuators according to the piezoelectric driving mode. Regimes investigated in this work are pointed out in dark blue.

Actuators used in fuel injectors work in the most demanding conditions.[10] Table 1.1 summarizes service requirements of piezoelectrics in fuel injectors. These physical features can be considered as a guideline for desirable piezoelectric properties required in actuators.

Table 1.1: Technologically relevant physical features for piezoelectrics in fuel injectors. Values were deduced from the current state-of-the-art materials implemented in these devices. In general variations within ± 10 % of the properties depicted are accepted. *Intensive property corresponding to blocking force.

Physical feature	Desired piezoelectric property for fuel injectors
Strain output	At least 0.20 % at 2 kV/mm.[11]
Operational temperature	Actual: - 40 °C to 150 °C. Upcoming years: - 40 °C up to 200 °C.[6,11,12]
Operational frequency	10^1 Hz to 10^2 Hz.[11]
Operation under humidity	Constant performance for humidity conditions above 85 % at 85 °C.[6]
Blocking stress*	At least - 50 MPa.[13]
Long term reliability	Strain output as constant as possible up to 10^8 cycles.[14]
Fracture toughness	At least 1 MPa $m^{1/2}$.[15]

The perovskite solid solution family of Lead Zirconate Titanate $Pb(Zr_xTi_{1-x})O_3$ (PZT) has traditionally been the focus of developmental efforts in the piezoceramics community. This is due to the possibility of engineering its electromechanical properties with dopants (≤ 3 at. %) or modifiers (≥ 5 at. %) leading to desirable and relatively easily addressable functional properties for a broad range of applications.[16] As a result of more than seven decades of continuous developmental efforts, PZT-based solid solutions are the preferred piezoelectrics in present day applications, comprising ~ 95 % of the whole piezoelectric materials implemented in the international production of actuators.[3,4]

Global awareness for well-being of the environment has increased in the past decades, culminating in various international regulations and treaties, such as the “Rio Declaration on Environment and Development” of the United Nations.[17] As encompassed by the third generation of human rights, and stated in a number of international treaties, access to a healthy environment and sustainability have become global priorities.[17,18] In particular, Pb and PbO were identified as toxic for human health and the environment.[19,20] On these grounds, directives against the use of Pb and other toxic elements in consumer products have been globally introduced.[21-28] These regulations have stimulated an increased research in lead-free piezoceramics.[10,29] Although the legal situation

worldwide is still ill-defined, the interest of certain piezoelectric device producers to fulfill these regulations and to find new markets is slowly increasing the technological implementation of lead-free piezoceramics.[3,4,10] Although efforts have been made in the quest to achieve candidates for a broad range of applications, to date there is no single material class that can replace PZT entirely.[10] Three main solid solution families have been recognized as technologically relevant: barium titanate-based (BT-based), bismuth alkali-based (BNT- or BKT-based), and alkali niobate-based (KNN-based) materials.[10,29] In this work, two systems were selected as representative candidates, one from the BT-based and the other from the BNT-based family of materials. Namely, (1-x)$Ba(Zr_{0.2}Ti_{0.8})O_3$-x$(Ba_{0.7}Ca_{0.3})TiO_3$ (BZT-BCT) and $(Bi_{1/2}Na_{1/2})TiO_3$(BNT)*-$SrTiO_3$ (ST) were selected. These model materials were chosen to expand the state-of-the-art knowledge of strain mechanisms of lead-free piezoceramics in the small and large signal regimes, and thus promote their technological implementation. Figure 1.2 displays the strategy selected to investigate them.

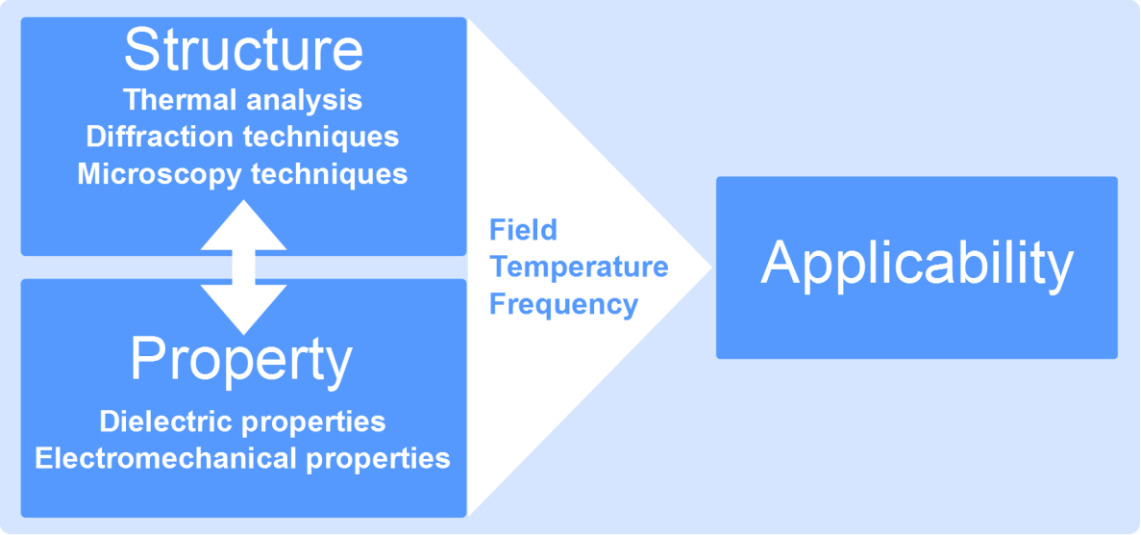

Figure 1.2: Strategy selected to investigate strain mechanisms of lead-free piezoelectrics.

Emphasis on the relationship between structural and electromechanical properties is made throughout this work. For this purpose, atomic crystal structure and microstructure were investigated by means of thermal analysis, as well as diffraction and microscopy techniques. Electric field-, temperature-, and frequency-dependent electromechanical properties in the small and large signal regimes were also examined. Apart from the correlation between structure and properties, the characterization was also performed to form a bridge between basic research and application-oriented knowledge required for technological implementation. More specifically, for the BZT-BCT system, emphasis on the relationship between phase instabilities and electromechanical properties was explored. For the BNT-ST, a thorough investigation in the 0.75

* Note that ½ is used as subscript instead of 0.5. The reader should be aware that this nomenclature is used to indicate that $Bi_{1/2}Na_{1/2}TiO_3$ is a stoichiometric compound rather than a solid solution.

mol fraction $(Bi_{1/2}Na_{1/2})TiO_3$-0.25 mol fraction $SrTiO_3$[†] was performed to give insights into the electric field induced phase transformation and the core-shell microstructure of this material. Following this introduction, this work is divided into eight subsequent main sections. Section 2 treats the physics behind dielectrics and their classification with emphasis on ferroelectrics and relaxor ferroelectrics, as well as strategies to enhance their electromechanical properties. Section 3 is a comprehensive review of the current state-of-the-art of lead-free piezoelectrics. The reasons for selecting the model materials of this study will become apparent in this section. Section 4 describes the experimental procedures chosen to synthesize the materials and the characterization techniques selected to investigate their strain mechanisms with emphasis in structure-property relationships. Section 5 presents the results and discussion of the experimental work performed. Sections 6 and 7 summarize this work and give concluding remarks, as well as possible future research opportunities.

[†] Unless stated, all compositions in this work will be given in mol fractions.

2 Theoretical Background

This chapter introduces the fundamental physics and concepts of dielectrics[30-39] and their classification[38-46], as well as of ferroelectrics[2,16,29,37-50], and relaxor ferroelectrics.[51-57] The information of many textbooks and review papers related to the physics of materials science was employed throughout these sections. Unless explicitly stated otherwise, mathematical relationships displayed throughout this work hold for linear and homogeneous materials. For more detailed mathematical treatments the reader is referred to Refs.[40,41]

2.1 Dielectrics

Dielectrics are electrically insulating materials. Gauss´s law indicates that the free charge density ρ_{fr} of a dielectric medium enclosed by a surface leads to an electric displacement D_i[‡], as given in Equation 2.1.

$$\nabla_i \cdot D_i = \rho_{fr} \qquad \textbf{Equation 2.1,}$$

where ∇_i is the nabla operator. It is convenient to define the concept of an order parameter. An order parameter is a scalar or tensor variable of state that is defined such that its thermal or compositional average is distinguishable in the different phases or states of a system. For instance, D_i can be considered as an order parameter in the case of a dielectric medium where two different phases or states develop with different thermal or compositional averages of this quantity.

Upon the application of an external electric field E_i, a dielectric medium will react by forming a density of permanent and/or induced electric dipole moments. This leads to the formation of a macroscopic polarization density P_i, as expressed in Equation 2.2.

$$P_i = D_i - \varepsilon_0 E_i \qquad \textbf{Equation 2.2,}$$

where ε_0 is the permittivity of vacuum, given by $\varepsilon_0 = \frac{1}{\mu_0 C^2} = 8.854118 \cdot 10^{-12}\ \mathrm{F/m}$ (μ_0: vacuum permeability, C: speed of light). The term $\varepsilon_0 E_i$ describes the vacuum contribution caused by the application of the external electric field E_i. According to Equation 2.1, the presence of free charges, generates a D_i that can be calculated using Equation 2.3 in the presence of E_j.

$$D_i = \varepsilon_{ij} E_j = \varepsilon_0 \varepsilon_r^{ij} E_j \qquad \textbf{Equation 2.3,}$$

where ε_{ij} is the permittivity of the medium, ε_r^{ij}[§] is the relative permittivity and is a dimensionless physical quantity defined as the ratio between ε_{ij} and ε_0.

[‡] Subscripts indicate tensor variables. In case no tensor notation is used, the variable is either a scalar or the norm of the variable considered. The Einstein convention of repeated indexes is used for all tensor relations.

All order parameters can be modified by a thermodynamic external conjugate variable. Note that for simplicity, only the relevant relationships to this work will be introduced. In the case of D_i, its conjugate variable is E_j. From Equation 2.2 and Equation 2.3 a proportionality between P_i and E_j can be deduced (Equation 2.4), and thus P_i can also be defined as an order parameter with E_j being its conjugate.

$$P_i = \varepsilon_0 \varepsilon_r^{ij} E_j - \varepsilon_0 E_j = \varepsilon_0 E_j \left(\varepsilon_r^{ij} - 1\right) = \varepsilon_0 \chi_{ij} E_j \qquad \textbf{Equation 2.4,}$$

where $\chi_{ij} = \varepsilon_r^{ij} - 1$ is the dielectric susceptibility. In the case of dielectrics where ε_r^{ij} >> 1, $P_i \approx \varepsilon_0 \varepsilon_r^{ij} E_j \approx D_i$.

Equation 2.2 to Equation 2.4 describe the mean linear properties of a dielectric medium. The order parameter P_i in dielectrics is coupled to other order parameters such as strain gradient $\frac{\partial S_{ij}}{\partial x_j}$ (where S_{ij} is the strain tensor and x_j position). Additionally, P_i is coupled to $\emptyset_i$, which represents either octahedral tilting for perovskites or rotation angle around a helical or spiral axis for structures with handedness.[58] Only perovskite dielectrics are relevant to this work, so $\emptyset_i$ will only be considered as the octahedral tilt angle. Coupling between P_i and $\frac{\partial S_{ij}}{\partial x_j}$ is termed flexoelectricity, while the coupling between P_i and $\emptyset_i$ is designated as rotoelectricity. Equation 2.5 introduces the influence of the aforementioned couplings to P_i for the case of a material subjected to E_j, $\frac{\partial S_{jk}}{\partial x_l}$, and $\emptyset_j$.

$$P_i = \varepsilon_0 \chi_{ij} E_j + \mu_{ijkl} \frac{\partial S_{jk}}{\partial x_l} + r_{ijk} \emptyset_j \emptyset_k \qquad \textbf{Equation 2.5,}$$

where μ_{ijkl} is the flexoelectric coefficient and r_{ijk} is the rotoelectricity coefficient. A converse relationship can be constructed relating strain S_{ij} to other order parameters. This establishes several strain mechanisms for dielectrics displayed in Equation 2.6.

$$S_{ij} = Q_{ijkl} P_k P_l - \mu_{ijkl} \frac{\partial P_k}{\partial x_l} + R_{ijkl} \emptyset_k \emptyset_l \qquad \textbf{Equation 2.6,}$$

where Q_{ijkl} is the electrostrictive coefficient and the non-linear term that comprises it is known as the electrostrictive effect. The R_{ijkl} is termed the rotostriction coefficient and is the converse effect of rotoelectricity. The converse effect of flexoelectricity is represented by the second term of Equation 2.6. Note that electrostriction does not possess a direct effect (*i.e.*, it is not present in Equation 2.5). This is due to the fact that the order parameter S_{ij} obtained by its conjugate thermodynamic variable stress σ_{ij} will not break the center of symmetry as it acts on mass points. However, E_i acts on charge points and thus breaks the center of symmetry of a dielectric leading to non-zero S_{ij}. Rotoelectricity, electrostriction, and rotostriction are higher-order terms that are proportional to even orders of their respective conjugate thermodynamic variables. Thus a change

[§] For proper reading, indexes of tensor variables with subscripts are displayed as upper scripts.

in polarity of their conjugate thermodynamic variable does not modify the resulting P_i or S_{ij}. Odd terms of P_i coupled to $\emptyset_i$ are not introduced in Equation 2.6 since they are rarely encountered in nature. The presence of odd electrostrictive terms indicates piezoelectricity. Odd electrostrictive terms are forbidden in several dielectrics depending on their symmetry, as will be discussed in Section 2.2.

The macroscopic approach introduced so far neglects the microscopic origin of P_i. Alternatively to the constitutive equations of state described, P_i can also be obtained by adding all the k dipole moments p^i of a dielectric material, as depicted in Equation 2.7.

$$P_i = \sum_k N_k p_k^i \qquad \textbf{Equation 2.7.}$$

The microscopic origin of p^i in materials is due to five different mechanisms:

- *Electronic polarization* exists in all dielectrics and is based on the displacement of the negatively charged electron shell against the positively charged atomic nucleus.
- *Ionic polarization* exists in ionic materials due to the displacement of positive and negative sublattices under electric field.
- *Orientational polarization* is a result of the alignment of permanent dipoles in a material under an electric field.
- *Space charge polarization* exists in dielectrics that feature spatial heterogeneities of charge carrier densities and is commonly found in materials with grain boundaries with different electrical conductivity than the bulk. This contribution is also denominated Maxwell-Wagner polarization.
- *Domain wall polarization* is relevant only for ferroelectrics. It is a result of the movement of the boundaries that separate differently oriented polarization volumes, as it will be treated in Section 2.2.1.

Electronic and ionic polarization mechanisms are lattice contributions and thus termed intrinsic. Orientational polarization, space charge, and domain wall polarization are not a result of the lattice itself and thus are termed extrinsic contributions. Each polarization contribution is characterized by a distinctive microscopic polarizability α_i giving rise to a local electric field E_{local}^i. Therefore, Equation 2.7 can be alternatively expressed as displayed in Equation 2.8.

$$P_i = \sum_k N_k \alpha_k^i E_{local}^i(k) \qquad \textbf{Equation 2.8.}$$

These microscopic polarization responses can be distinguished by characteristic response frequencies, as displayed in Figure 2.1.

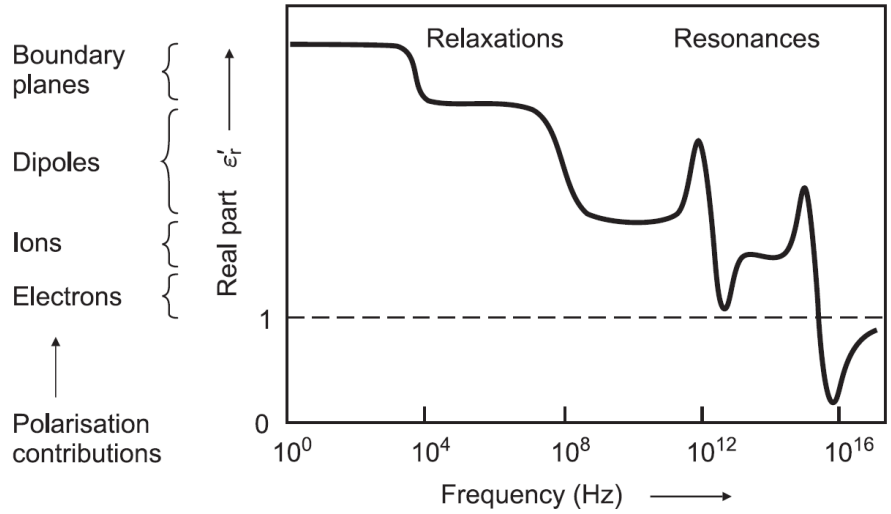

Figure 2.1: Frequency dependence of real part of the relative permittivity $\varepsilon_r^{'}$.[38]

The characteristic time response of each microscopic polarization mechanism under alternating electric field leads to dielectric losses and thus complex variables are required to represent the ε_r^{ij}. Since Equation 2.7 and Equation 2.8 relate microscopic and macroscopic variables, macroscopic variables may also depict complex values. In an ideal, loss-free dielectric there is a phase difference between current and voltage of 90° indicating that ε_r^{ij} is a real-valued tensor. However, in dielectrics with finite conductivity, ε_r^{ij} is a complex-valued tensor such as displayed in Figure 2.2. The phase angle $\theta = 90^0 - \delta$ determines the phase difference between the real part ($\varepsilon_r^{'}$) and the imaginary part ($\varepsilon_r^{''}$). Therefore, the tangent of the angle δ (*i.e.*, $tan\,\delta$) is normally designated as the loss factor of dielectrics.

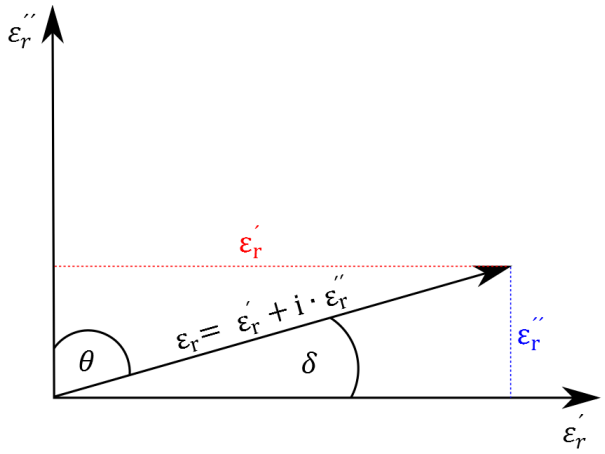

Figure 2.2: Representation of ε_r in the complex plane. The real part of the relative permittivity is indicated by $\varepsilon_r^{'}$ and the imaginary part by $\varepsilon_r^{''}$.

2.2 Classification of Dielectrics

There exist 32 crystallographic point groups in nature that describe all crystalline materials based on symmetry operations. Dielectrics can be classified based on their point groups and polarity, among other physical features as introduced in Figure 2.3.

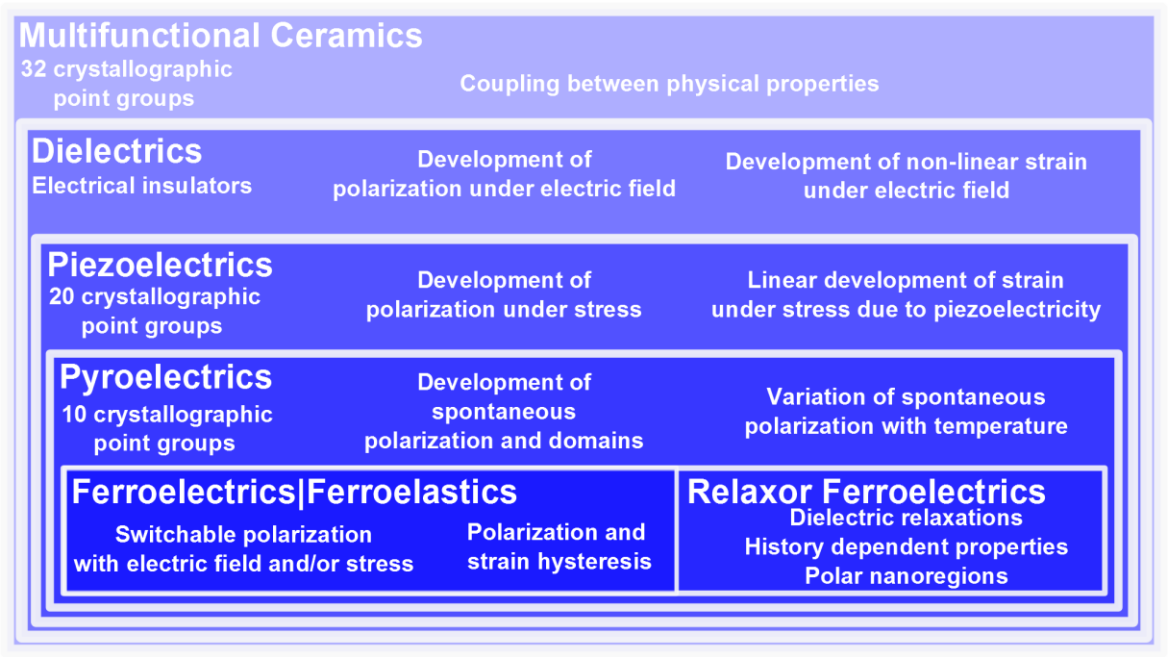

Figure 2.3: Multifunctional ceramics classification indicating the subclasses of dielectrics found in nature and their respective physical features. To allow proper visualization, some classes of dielectrics like flexoelectrics and rotostrictors are not displayed in the image.

Table 2.1 introduces the 32 crystallographic point groups and their classification according to symmetry considerations. As discussed in Section 2.1, application of an electric field to dielectrics will lead to an induced P_i and non-linear S_{ij}. From the aforementioned 32 crystallographic point groups, 11 are centrosymmetric due to the presence of a center of inversion. In these crystallographic point groups, odd couplings between S_{ij} and any other order parameter is forbidden due to symmetry reasons, according to Neumann's principle.

Table 2.1: Crystallographic point groups classification according to symmetry considerations. Notation is given according to Hermann-Mauguin notation. Modified from Uchino.[59]

Crystal system	Centrosymmetric point groups	Non-centrosymmetric point groups-	
	Non-Polar		Polar
Cubic	$m\bar{3}m$, $m\bar{3}$	432, $\bar{4}3m$, 23	-
Hexagonal	$6/mmm$, $6/m$	622, $\bar{6}m2$, $\bar{6}$	$6mmm$, 6
Trigonal	$\bar{3}m$, $\bar{3}$	32	$3m$, 3
Tetragonal	$4/mmm$, $4/m$	422, $\bar{4}2m$, $\bar{4}$	$4mm$, 4
Orthorhombic	mmm	222	$mm2$
Monoclinic	$2/m$	-	$2, m$
Triclinic	$\bar{1}$	-	1
Total	11	11	10

The 21 remaining point groups, except the point group 432[**], depict at least one non-vanishing coupling coefficient between the order parameters P_i and S_{ij}. Therefore, non-centrosymmetric materials from these 20 final point groups will develop D_i (or in analogy P_i) when subjected to σ_{ij}, which is a conjugate thermodynamic variable of S_{ij} and thus also of D_i. The reversible and linear coupling between the order parameter D_i and the conjugate variable σ_{ij} under constant E_i and temperature introduced in Equation 2.9 defines a piezoelectric material. Since the effect is linear, any change of σ_{ij} will result in a change of D_i.

$$D_i = d_{ijk}\sigma_{jk} \qquad \textbf{Equation 2.9,}$$

where d_{ijk} is the direct piezoelectric coefficient. It should be noted that the couplings described for dielectrics in Equation 2.5 will also result in D_i in a piezoelectric, for the case where the material is subjected to the described conjugate thermodynamic variables. The converse piezoelectric effect is

[**] The point group 432 is the only group with both a 4-fold and a 3-fold rotation axes. The 4-fold rotation axis leaves seven of the piezoelectric coefficients non-zero, and the 3-fold axis vanishes these coefficients leading to no coupling between D_i and σ_{ij}.

defined as the linear change of S_{ij} that develops with application of E_k under constant σ_{ij} and temperature, as depicted in Equation 2.10.

$$S_{ij} = d_{ijk}E_k \qquad \textbf{Equation 2.10,}$$

where d_{ijk} is the indirect piezoelectric coefficient that is numerically identical to the direct piezoelectric coefficient. As with the direct effect, the converse effects described for dielectrics (Equation 2.6) also contribute to S_{ij} in piezoelectrics. The efficiency of the piezoelectric effect on a given material can be determined by the electromechanical coupling factor k. This parameter indicates the electrical energy converted into mechanical energy, as given in Equation 2.11.

$$k^2 = \frac{electrical/mechanical\ energy\ converted\ into\ mechanical/electrical\ energy}{input\ electrical/mechanical\ energy} \qquad \textbf{Equation 2.11.}$$

Another subdivision of piezoelectrics can be made analyzing the 20 remaining crystallographic point groups. From them, 10 possess a polar axis (*i.e.*, a dipole moment) without being subjected to any conjugate thermodynamic variable and thus they display a non-zero P_i (or in analogy D_i) normally denominated spontaneous polarization P_s^i. Uniform changes in the conjugate thermodynamic variable temperature T will result in a change of P_s (note that upper script is avoided intentionally to indicate the norm of the tensor). These types of materials are known as pyroelectrics. Equation 2.12 introduces the definition of the direct pyroelectric coefficient pc_i.

$$pc_i = \frac{\partial P_i}{\partial T} \qquad \textbf{Equation 2.12.}$$

Note that all polarization and strain mechanisms described for dielectrics and piezoelectrics also hold for pyroelectrics. Although pyroelectrics feature a polar axis, families of crystallographically equivalent orientations are allowed by symmetry in the ten pyroelectric point groups. The crystallographically and energetically equivalent orientations, as well as the need to minimize electrostatic energy, leads to the formation of regions in the material with the same spatial orientation of the P_s^i denominated domains. These regions are separated by domain wall boundaries. The interface charge density γ accumulated at the interface between two domains is described by Equation 2.13.

$$\gamma = \left(P_i^1 - P_i^2\right) \cdot \hat{n} = \left\|P_i^1\right\| cos(\vartheta) - \left\|P_i^2\right\| cos(\vartheta) \qquad \textbf{Equation 2.13,}$$

where P_i^1 and P_i^2 indicate the polarization of both domains, $\hat{n}$ is the unit vector normal to the interface, and ϑ the angle between domain interfaces. Any domain configuration will lead to charged domain interfaces with the exception of two cases.[60] The surface charge will be zero for the case of antiparallel domains if $\left\|P_i^1\right\| \equiv \left\|P_i^2\right\|$ or for the case that the domain interfaces are orthogonal. The former case is generally denominated 180°-domain walls, while the latter non-180° domain walls (or 90° domain walls for the tetragonal phase). Domain arrangements generally have a mirror followed by a center of inversion, and thus arrange themselves as twin structures "head-to-tail" in space to avoid discontinuity of polarization at the interface.[61,62] Figure 2.4 introduces a

pyroelectric material with (a) 180°-domain walls, (b) non-180° domain walls, and (c) both domain configurations.

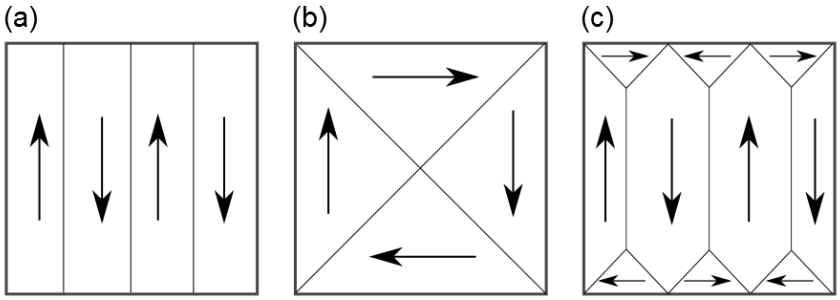

Figure 2.4: Domain patterns for pyroelectrics and ferroelectrics. (a) Ferroelectric, (b) ferroelastic, and (c) polydomain patterns.

Since the order parameters D_i and S_{ij} in pyroelectrics are coupled, the formation of non-180° ferroelastic domains builds up stresses. For this reason, the schematic representation introduced in Figure 2.4 (b) is rarely encountered. The state with 180° domain walls (Figure 2.4 (a)) typically forms in strain-free states. These domains characterize single crystals or coarse grain materials.[63] In most polycrystalline materials, however, the grains are in a clamped state due to the interactions between randomly oriented grains, and therefore the situation in Figure 2.4 (c) is generally favored. Although the energy of the polarized ground state is lost during domain formation, their presence compensates the electrical stray field energy caused by free charges and defects (Equation 2.1). The energy gained is also compensated by domain wall formation and strain fields.

By definition, it is not possible to reorient P_s^i of domains in pyroelectrics. Therefore, a pyroelectric material will only develop a macroscopic measurable pc_i if domains within the material are arranged such that a non-zero macroscopic P_s^i is developed. Ferroelectric and ferroelastic materials are a subgroup of pyroelectrics that also feature a P_s^i and domains. They are unique since their domains can be reoriented between equivalent crystallographic orientations by conjugate thermodynamic variables such as E_i or σ_{ij}. Relaxor ferroelectrics are a subclass of ferroelectrics with complex structure and properties that depend on history and observation time. Therefore, frequency-dependent relaxation effects are common in these materials. Moreover, in most cases, they feature polar nanoregions (PNRs)[64] instead of domains. Ferroelectrics and relaxor ferroelectrics will be treated in the subsequent sections separately in detail due to their relevance to this work.

2.2.1 Ferroelectrics

Since the discovery of ferroelectricity in the single crystal Rochelle salt in 1921[65] and polycrystalline ceramics during the 1940's[66-68], there has been a continuous succession of new materials and related technological developments. Appearance of a P_s^i in ferroelectrics is a consequence of a

structural change that breaks the center of symmetry of points groups. These structural changes are normally termed phase transitions and can be of first or second order. First order phase transitions are characterized by discontinuous changes in physical properties such as enthalpy corresponding to the evolution of latent heat of the transformation. This leads to thermal hysteresis in functional properties during phase transformation. Second order phase transitions are characterized by a continuous change of enthalpy and thus no latent heat is observed for these transformations. Either first or second order phase transitions can develop as order-disorder or displacive. In general, the former implies an ordering process while the latter refers to short-range displacements of atoms. Any of the phase transitions described may be responsible for lowering the symmetry of the high temperature point group in ferroelectrics. The phase transition and formation of a P_s^i occurs at the Curie temperature T_C and is accompanied by an anomaly in the temperature dependence of permittivity ε, as displayed in Figure 2.5 for a first order phase transition (black) and for a second order phase transition (red).

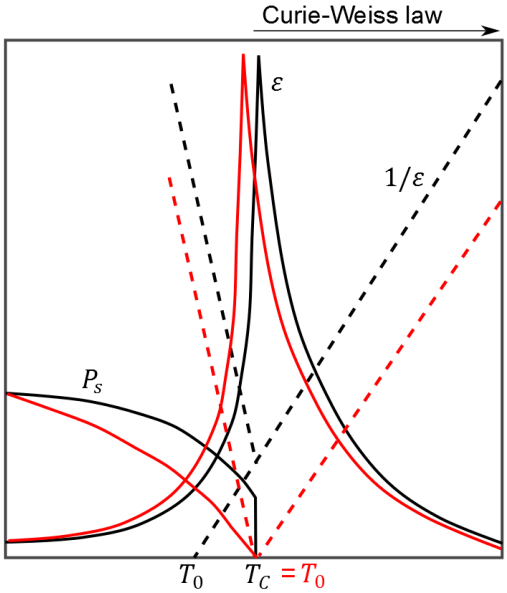

Figure 2.5: Schematic representation of ε, $1/\varepsilon$, and P_s as a function of temperature for a ferroelectric. Black lines indicate a first order phase transition from the paraelectric to the ferroelectric state. If $T_C = T_0$, the phase transition is of second order (marked in red).

The high temperature ε above T_C can be described by the Curie-Weiss law given in Equation 2.14.

$$\varepsilon = \varepsilon_0 + \frac{C}{T - T_0} \approx \frac{C}{T - T_0} \qquad \textbf{Equation 2.14,}$$

where C is the Curie constant and T_0 is the Curie-Weiss temperature, which is obtained by extrapolating the trend of the high temperature $1/\varepsilon$ data to its intersection with the abscissa axis.

Only for second order phase transitions $T_0 = T_C$. Note that P_s and P_r vanish at T_C discontinuously for a first order phase transition or continuously in the case of a second order phase transition.

Ferroelectrics can be categorized into four groups: (1) pyrochlore group ($A_2B_2X_6$ or $A_2B_2X_7$), (2) tetragonal tungsten bronze group ($A1_2A2_4C_4B1_2B2_8X_{30}$), (3) bismuth-layer structure group ($A_{n-1}B_nX_{3n+1}$), and (4) octahedral group (ABX_3). The latter group, often simply called the perovskite group (due to the mineral perovskite $CaTiO_3$), is by far the most technologically relevant category and focus of this work. Figure 2.6 introduces the sequence of phase transitions featured in perovskite ferroelectrics such as for instance in the prototypical barium titanate, $BaTiO_3$ (BT).[69] The high temperature prototype cubic structure (C) has a $Pm\bar{3}m$ space group. It is observed that the A-site cation has a 12 fold coordination, while the B-site cation has a 6 fold coordination. The generic X term is typically associated with an O^{2-} anion that is coordinated with 4 A-site cations and 2 B-site cations.

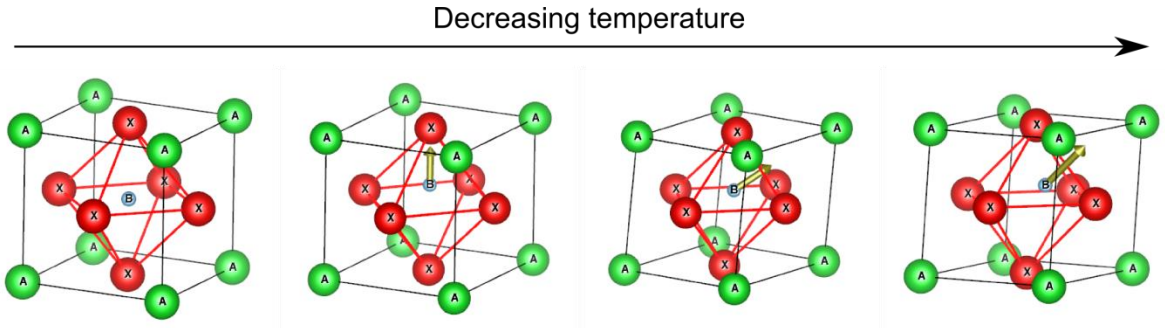

Figure 2.6: Unit cells of a perovskite structure ABX_3. Octahedra of X anions are depicted in red, while arrows indicate P_s^i. With decreasing temperature, the prototypical cubic perovskite structure distorts to tetragonal, then orthorhombic, and finally rhombohedral phase.

The distortions of perovskites are related to the structural frustration of the cubic structure. Due to structural and energetic considerations, the ferrodistortive (FD) distortions leading to ferroelectricity (Figure 2.6) compete energetically with octahedral distortions.[70] The latter involve rigid rotations or tilting of octahedra and are known as antiferrodistortive distortions (AFD) since they may lead to antiferroelectricity. Goldschmidt developed an empirical criterion of stability for perovskite ferroelectrics, as given in Equation 2.15. The tolerance factor t for ionic materials is based on a geometrical model that accounts for the filling of a unit cell by rigid spheres of radii r that represent ions.

$$t = \frac{r_A + r_x}{\sqrt{2}(r_B + r_x)} \qquad \textbf{Equation 2.15.}$$

For $t \approx 1$ cubic perovskite structures are energetically favored. For $t > 1$, the cation on the B-site is small relative to the X octahedra, indicating that the structure will develop a polar distortion through displacement of the B-site cation. Conversely, for $t < 1$ the A-site cation is small relative to

the center of the X octahedra, leading to a weakened bond between A-site cations and X-site anions. This gives rise to distortions of the X octahedra, such as rigid rotations or tilting. It should be noted that this empirical model neglects the degree of covalence of the bonds that also partially determines the preferred distortion.[70] The competing FD and AFD mechanisms responsible of ferroelectricity lead to a further classification of phase transitions. Octahedral distortions will result in formation of crystallographic structures that are modulated and give rise to incommensurate transitions. These transitions indicate that the periodicity of the forming phase is incommensurate with respect to the principal periodicity of the host lattice and leads to the presence of superlattice reflections (SSR) in diffraction patterns. In contrast, if the periodicity of the phase coincides with that of the host lattice phase, the phase transition is commensurate.

In the schematic view of Figure 2.6, decreasing temperature below T_C can lead to the formation of a non-centrosymmetric tetragonal phase (T). In general, this phase is characterized by a $P4mm$ (commensurate) or $P4bm$ (incommensurate, not shown) space group. In this case a non-zero P_s^i develops along one of the six crystallographic directions of the ⟨00l⟩ family. Further cooling leads to the formation of an orthorhombic phase (O) with the space group $Amm2$ and P_s^i along one of the 12 crystallographically equivalent ⟨hh0⟩ family of directions. Subsequently, at even lower temperatures, a rhombohedral phase (R) develops with symmetry $R3c$ and P_s^i along one of the eight equivalent ⟨hhh⟩ directions. Domain formation is common to all ferroelectrics upon development of P_s^i due to the energetic considerations treated in Section 2.2. One of the fundamental properties of ferroelectrics and ferroelastics is the ability to reorient their P_s^i by the application of E_i or σ_{ij} and thus a net macroscopic P_s^i can develop due to domain reorientation. A domain reorientation by either application of E_i or σ_{ij} is normally called a switching process and is understood as an extrinsic phenomenon, in contrast to P_s^i reorientation which is an intrinsic phenomenon. Domain switching is considered extrinsic because it is a process that takes place on a scale larger than the unit cell and requires the growing or shrinking of domains through motion of the domain walls. Two extrinsic effects have to be distinguished, since during the application of E_i, domain walls move reversibly or irreversibly in the local potential generated by the interaction between lattice, defects, and domain walls. A schematic representation of this process is displayed in Figure 2.7. Reversible domain wall movements are due to displacement of the domain wall from its local minimum, while irreversible movements can be regarded as jumps above a potential barrier into other local minima.

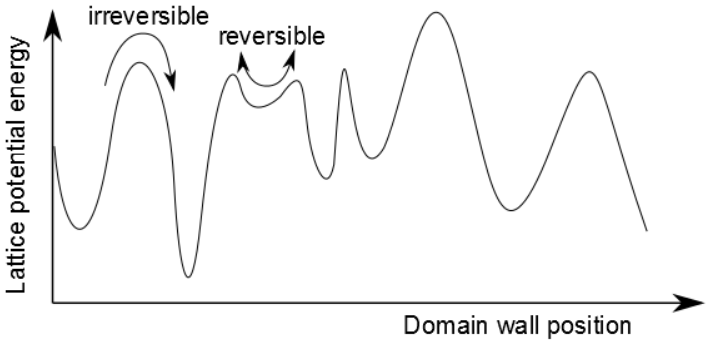

Figure 2.7: Scheme of domain wall displacements in the lattice potential.

Extrinsic contributions lead to the characteristic polarization and strain hysteresis loops in ferroelectrics. Figure 2.8 (a) and (b) introduce the prototypical bipolar polarization and strain hysteresis loops measured in the 333 mode[††], respectively. Solid lines indicate the bipolar loops, while dashed lines the unipolar loops.

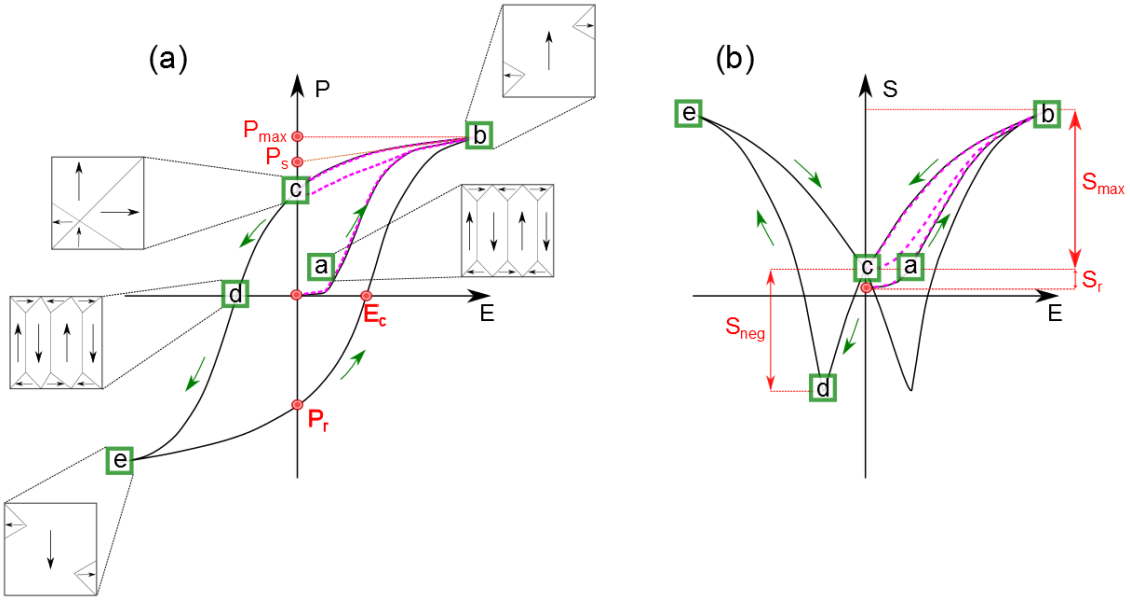

Figure 2.8: (a) Schematic bipolar polarization and (b) bipolar strain loops of a ferroelectric. Relevant parameters for the characterization of ferroelectrics are marked, together with a scheme of the domain patterns expected at each point of the loop. The unipolar strain and polarization loops are also depicted in (a) and (b) with dashed purple lines, respectively.

[††]The 333 mode describes the polarization and strain response of a sample poled in the measurement direction.

The virgin domain state is generally determined by a complex energy interaction between electrostatic and elastic energy, as described in Section 2.2. The domain patterns associated with different points of the polarization and strain hysteresis loops are displayed schematically. At point $\boxed{a}$ in Figure 2.8, a virgin state characterized by a random polydomain pattern with 180° and non-180° domains leading to negligible macroscopic P_s^i is displayed. Note that point $\boxed{a}$ is at higher electric field strength that the onset required to obtain macroscopic properties, however, the electric field strength is not high enough to promote appreciable irreversible domain wall motion. However, non-linearity may be present at low electric fields and is ascribed to reversible domain wall motion.[71] Nevertheless, at this electric field polarization and strain are approximately linear and reversible mostly due to direct and converse piezoelectricity, electrostriction, as well as plausibly due to rotostriction, and flexoelectricity. The slope of the strain curve at this point is equal to d_{333}. From now on, Voigt notation is considered and the piezoelectric coefficient will be referred to as d_{33}. As the electric field strength is increased, domains start to align in the positive direction due to reversible and irreversible switching. This gives rise to a rapid increase in both polarization due to non-180° and 180° domain switching, as well as in strain mostly due to non-180° switching. At any given electric field strength, where strain output deviates considerably from linearity, a large signal piezoelectric coefficient can be defined as in Equation 2.16.

$$d_{33}^* = \frac{S_{33}}{E_3} \qquad \textbf{Equation 2.16.}$$

The small signal d_{33} and large signal d_{33}^* are normally considered as figures of merit for actuator applications. Once domain switching saturates at point $\boxed{b}$, further increase in applied electric field activates only an intrinsic response leading to a linear increase in polarization and strain similar as at point $\boxed{a}$. The saturated domain state achievable generally does not result in a monodomain state due to the random orientations of grains inherent to polycrystalline ceramics, but even in single crystals there is stray energy, defects and/or stresses that must be taken into account. The maximum polarization P_{max} and maximum strain S_{max} could, but do not necessarily always, indicate saturation values. The latter term is generally an indication that a maximum domain orientation was achieved leading to a purely linear response. Once the electric field is removed, domains will partially switch back to the crystallographically allowed orientations at point $\boxed{c}$. The lattice intrinsic response may not be fully reversible and a number of 180° and non-180° domains will remain oriented with the previously applied electric field direction, indicating irreversible switching. Therefore, intrinsic and irreversible extrinsic switching leads to a non-zero remanent polarization P_r and remanent strain S_r. The remanent state is normally termed a poled state since it features a non-zero macroscopic P_s^i due to a preferred domain alignment direction. The P_s can be estimated by extrapolating the linear polarization region near P_{max} to zero applied electric field along the saturated polarization tangent. If an electric field with an opposite polarity to the initial poling field is applied to the material, it will promote switching along this new direction. Once the electric field reaches a magnitude equal to the coercive field E_c, the material's P_s will vanish. This is achieved by establishing a random domain state (point $\boxed{d}$) that does not necessarily coincide with the virgin state (point $\boxed{a}$). Therefore, the E_c can be regarded as the macroscopic electric field indicative of switching processes. However, as previously stated, switching can occur at electric

fields much lower than E_c.[72] The polarization decrease from point $\boxed{c}$ to point $\boxed{d}$ will be directly reflected in a compression of the material leading to a "negative strain" S_{neg}. This is a result of the compression experienced by domains opposed to the electric field direction at point $\boxed{d}$ prior to switching. Further increase of the electric field results in the development of a P_{max} and S_{max} with an opposite polarity to the first half-cycle. Decreasing the electric field back to zero results in a remanent state characterized by a P_r and S_r, also with opposite polarity compared to the first half-cycle. Further electric field cycles retrace the path described from point $\boxed{b}$ to point $\boxed{e}$ leading to a continuous hysteresis. Point $\boxed{a}$ will only be achieved again if the ferroelectric is depolarized to its virgin state by annealing it above T_C. The process described will not vary considerably at different temperatures if the ferroelectric state is conserved. In general, increasing temperature will decrease the E_c due to enhanced domain switching, which is logical considering that this process is thermally activated.[73] Above T_C, hysteresis will disappear and the dielectric will respond to the electric field, as described in Section 2.1. For unipolar electric field input, the purple unipolar polarization and strain hysteresis loops will be obtained leading to a hysteresis with the processes described from point $\boxed{a}$ to point $\boxed{c}$.

2.2.2 Relaxor Ferroelectrics

2.2.2.1 General Description

Relaxor ferroelectrics, often referred to as relaxors, exhibit complex physical features. These properties are the result of a chemically and/or structural disorder at the local scale, although they are generally represented in long-range analytical methods by a pseudocubic crystal structure. They have attracted considerable research attention due to their large responses to external stimuli.[74] Smolenskii *et al.*[75-77] reported the first relaxors during the 50s and 60s. At high temperatures, perovskite relaxors depict a paraelectric cubic phase similar to that described for perovskite ferroelectrics (Figure 2.6). However, upon cooling below the so called Burns temperature T_B[78,79] they transform to an ergodic relaxor state with the presence of nanometer scale randomly oriented dipoles normally called polar nanoregions PNRs.[64] These PNRs can be regarded as clusters on the order of 10 nm composed of thermally activated dipolar entities that originate from local deviations in crystal structure and/or chemical heterogeneities in the A- and/or B-site cation sublattices.[80-84] Several attempts have been made to rationalize relaxors within one theoretical model. However, so far no general agreement in their microscopic picture has been achieved. The most widely accepted attempts capable of describing only some of their features are known as the diffuse phase transition model[76,77], superparaelectric model[53], glassy state model[85-87], random fields model[88-91], spherical random bond-random field model[92-96], and breathing model.[97,98] These models can be categorized according to two microscopic views. Figure 2.9 (a) displays PNRs embedded in a non-polar pseudocubic matrix and is supported by all models with the exception of the random fields model that describes relaxors as a frustrated ferroelectric state with nanodomains (Figure 2.9 (b)).

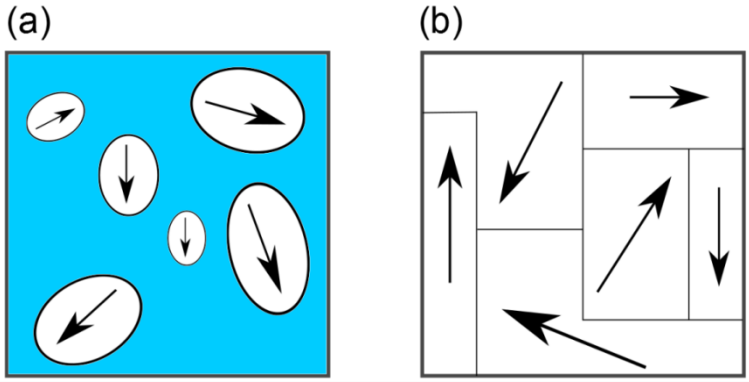

Figure 2.9: Schematic representation of PNRs according to different models. Microscopic view (a) indicates a dipolar glass with embedded PNRs in a pseudocubic matrix, whereas (b) shows a frustrated ferroelectric with nanodomains due to the presence of random fields. Arrows are used to designate dipole moments.

The high temperature state of relaxors, just below T_B, was named an ergodic state due to its similarity to the ergodicity term from statistical mechanics. An ergodic property or state is when the time average characteristic of the property is indistinguishable from the ensemble average for the distribution of all accessible points in the phase space of the system. In other words, in an ergodic system an arbitrary function can be defined in a certain mathematical space within the phase space of the whole system, in which the characteristic property´s time average becomes indistinguishable from the ensemble over all accessible points.[99,100] Expressing a higher degree of ergodicity can be understood as increasing the fraction of phase space in which its property time average characteristic becomes indistinguishable from the ensemble average for the distribution of all accessible points in the phase space of the system. Expressing a degree of non-ergodicity within a phase space is therefore not proper but a consequence of the degree of ergodicity. In this context, the ergodic state of relaxors can be understood as a state in which the polarization of uncorrelated PNRs has an equal probability of being found in any direction and at any point of the material. Therefore, ergodic relaxor can be distinguished from ferroelectrics based on their polarization. Ferroelectrics feature a non-zero value of P_s^i along crystallographically allowed orientations as indicated by $\sum_i P_s^i \neq 0, \sum_i \left\|P_s^i\right\|^2 \neq 0$. In contrast, relaxor materials have zero macroscopic P_s^i values but their quadratic contribution is non-zero due to the presence of PNRs $\sum_i P_s^i = 0, \sum_i \left\|P_s^i\right\|^2 \neq 0$. Characterization of physical features that depend on $\left\|P_s^i\right\|^2$ such as refractive index can be used to corroborate the presence of PNRs.[78,79] On further cooling, different situations arise depending if the relaxor is canonical or non-canonical, as depicted in Figure 2.10.

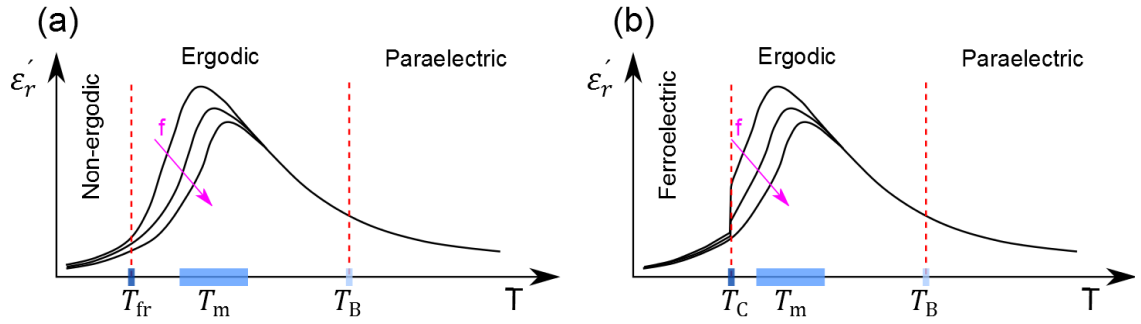

Figure 2.10: (a) Prototypical ε_r' for canonical relaxors. (b) Prototypical ε_r' for non-canonical relaxors. Increasing measurement frequency is displayed with a purple arrow.

Figure 2.10 (a) represents a canonical relaxor that features a dynamic slowing down or relaxation of the PNRs fluctuations giving rise to a frequency-dependent maximum of ε_r' (as well as ε_r'', not displayed in Figure 2.10). The temperature corresponding to the highest magnitude of ε_r' is normally defined as T_m and is a result of a dielectric relaxation. Cooling below T_m does not lead to changes of the average long-range cubic phase.[54] With further cooling, the PNRs of canonical relaxors become frozen leading to a glassy non-ergodic state at the freezing temperature T_{fr}. The concept of a T_{fr} was previously coined for spin glasses. These magnetic materials are characterized by localized interacting magnetic moments.[101] The T_{fr} represents a magnetic relaxation that can be determined from the frequency dependence of the susceptibility which approaches a constant value at lower frequencies.[85] This magnetic relaxation can be described by a relationship attributed to Vogel[102] and Fulcher[103] as defined in Equation 2.17.

$$\omega = \omega_0 e^{\frac{-E_a}{k(T_m - T_{fr})}} \qquad \textbf{Equation 2.17,}$$

where ω is the frequency of the relaxation process, E_a is the activation energy, ω_0 is the Debye frequency, and k is the Boltzmann constant. The Vogel-Fulcher relationship may be interpreted as a Debye relaxation with a temperature-dependent activation energy, which increases as the temperature decreases and becomes undefined at T_{fr}.[85] When Viehland *et al.*[85] first demonstrated that the Vogel-Fulcher relationship is applicable to relaxor ferroelectrics, this led to the categorization of these materials as dipolar glasses. Dipolar glasses differ from spin glasses in that they depict long-range dipolar interactions and non-negligible coupling of dipolar and structural degrees of freedom.[90] For the case of relaxors, the Vogel-Fulcher entails a temperature-dependent correlation length of PNRs. The divergence of the PNRs correlation length leads to divergence of their relaxation time and to a frozen state at T_{fr}.[104,105] This state is characterized by distinct history-dependent functional properties[55,86], as a result of the multiple metastable states of canonical relaxors in their non-ergodic state.[100] Non-canonical relaxors feature an analogous high temperature paraelectric and ergodic state when compared to canonical relaxors, as displayed in Figure 2.10 (b). Upon further decrease in temperature below T_m, however, they have a spontaneous transition into a ferroelectric state. The temperature corresponding to this spontaneous transformation may be termed T_C since upon crossing this temperature the value of

their macroscopic P_s^i vanishes. Only canonical relaxors will be further analyzed due to their relevance to this work.

As schematically shown in Figure 2.11, applying an electric field of sufficient magnitude in both ergodic and non-ergodic states may induce a long-range ferroelectric state.[106] It should be noted that due to the history-dependent properties in the non-ergodic state of canonical relaxors[100], isothermal (red) and isofield (blue) representations differ.[106,107] An electric field induced phase transition that originates from an ergodic state will be reversible, whereas from a non-ergodic state (below T_{fr}) will be irreversible. Increasing temperature without an external electric field destabilizes the induced ferroelectric state. The depolarization temperature T_d indicates the detexturization of ferroelectric domains and as a consequence is accompanied by the decay of macroscopic piezoelectric properties. Decay of the detextured domains into PNRs occurs at the ferroelectric to relaxor phase transition temperature T_{f-r}.[108,109]

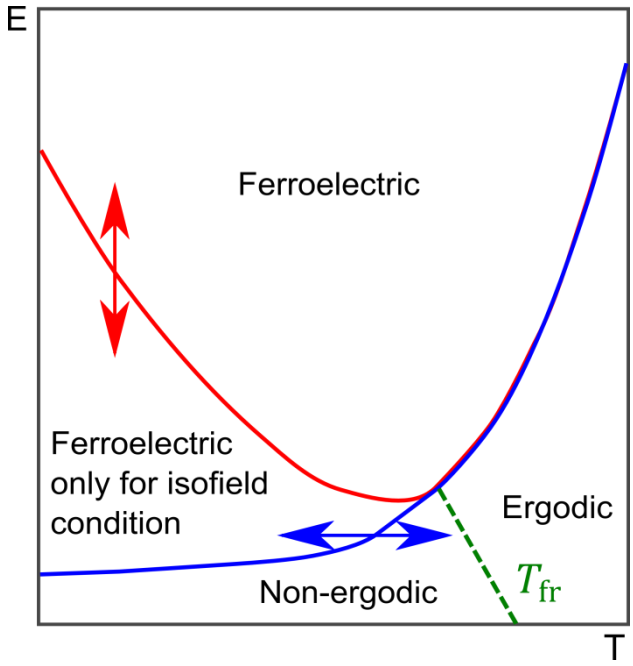

Figure 2.11: Schematic representation of temperature and electric field evolution of canonical relaxors. Red line indicates isothermal conditions, while blue line isofield conditions.

One of the most important properties of canonical relaxors is that upon application of an electric field they display a slim and/or pinched polarization hysteresis loop, as displayed in Figure 2.12. Compared to ferroelectric materials (Figure 2.8 (a)), this loop is characterized by a considerably smaller P_r. Point $\boxed{a}$ in Figure 2.12 indicates that the electric field strength is not high enough to induce a long-range ferroelectric state. Increasing further the applied electric field, however, induces a ferroelectric state along its direction (point $\boxed{b}$). Reduction of the electric field leads to the partial decay of the ferroelectric state in a material with a certain degree of ergodicity (point

[c]) or to a random ergodic relaxor state with negligible macroscopic P_s and P_r. Increasing electric field with an opposite polarity to the first half-cycle leads to the same processes previously described (points [d] and [e]). Further electric field cycles retrace the path from point [b] to point [e] leading to a continuous hysteresis. The induced ferroelectricity depicts similarities with a normal ferroelectric state in the sense that the material features a polarization loop attributed to some degree of interactions of PNRs. However, in the case of an ergodic relaxor the points [a], [c], and [d] are indistinguishable. Relaxors feature generally large electrostrictive coefficients and therefore high electric field induced strains, which makes them technologically relevant for actuator applications.[54,110,111] Since both polarization and electrostriction are induced by the electric field, increasing temperature leads to diminished outputs.[112]

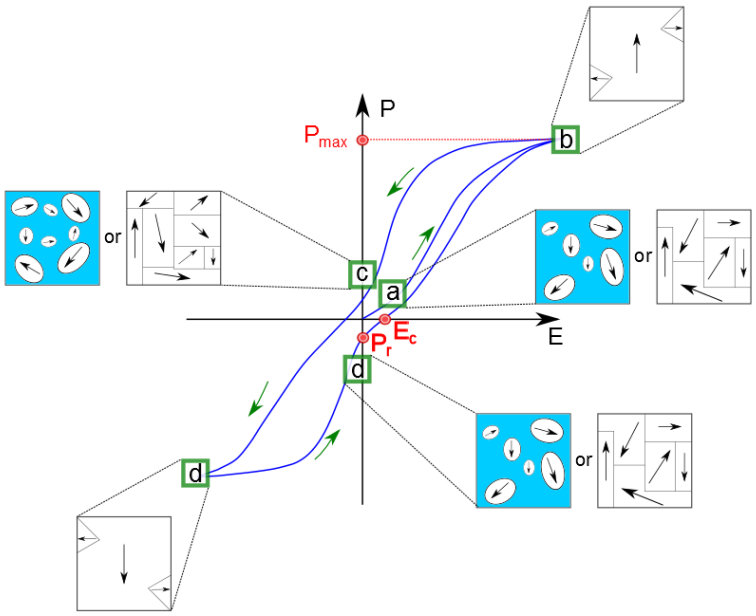

Figure 2.12: Relaxor bipolar polarization loop and prototypical microscopic relaxor views for different electric field strengths.

Figure 2.13 introduces the thermal evolution of the P_s values for a ferroelectric with a first order phase transition (black), a second order phase transition (red), and a canonical relaxor with certain degree of non-ergodicity (blue). Since polarization in relaxors is ascribed to PNRs, it persists up to T_B.[78,79] Note that for both canonical and non-canonical relaxors the Curie-Weiss law holds only for temperatures above T_B.[113]

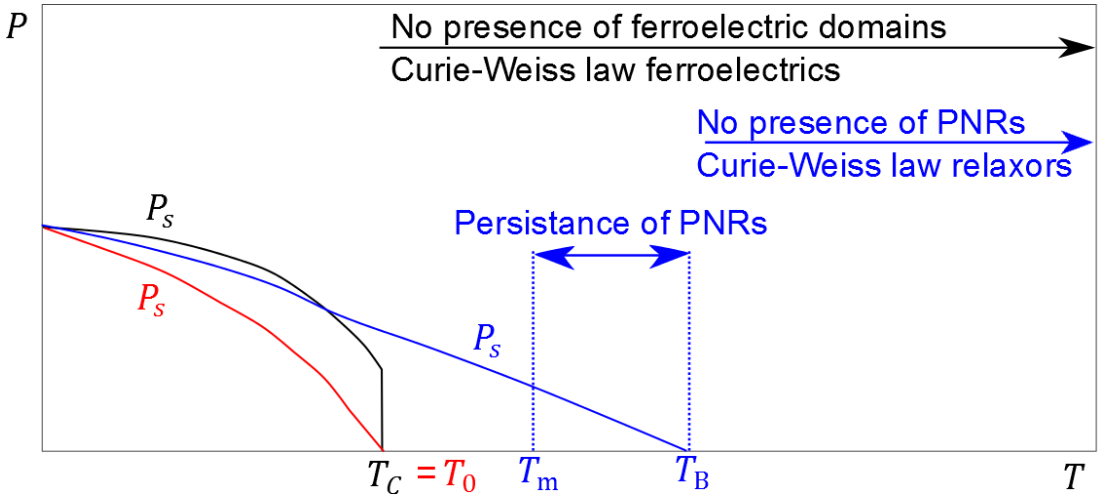

Figure 2.13: Comparison of polarization decay with increasing temperature for a ferroelectric with first order phase transition (black), second order phase transition (red), and relaxor (blue).

2.2.2.2 Lead-Free Relaxor Ferroelectrics

The exact nature of the relaxor state in lead-free perovskites remains an active matter of debate within the research community. Lead-free perovskite relaxors can be considered as materials with a quasi-continuous order parameter in 3 dimensions, which leads to 3 dimensional PNRs, similarly to those found in lead-containing perovskite relaxors. Both the Aurivillius and tetragonal tungsten bronze lead-free relaxor systems depict 2 and 1 dimensional order parameters with PNRs of the same dimensionalities, respectively. The general features of lead-containing canonical relaxors introduced previously are also observed in lead-free relaxors. However, some more complex physical phenomena have also been observed:

- In contrast to lead-containing materials, in which relaxor properties are observed for heterovalent A- or B-site modified materials (*e.g.* $Pb(Mg_{1/3}Nb_{2/3})O_3$), lead-free relaxors are found in both homovalent and heterovalent A- and B-site modified materials, such as BT with Zr^{4+}, Ca^{2+}, Na^{+}, Nb^{5+}, among many others.[114-116]
- An average long-range pseudocubic structure is not always observed in lead-free relaxors.[117]
- Local antiferroelectric PNRs were proposed.[118]
- A distribution in the degree of ergodicity may develop locally, which could be ascribed to different coexisting symmetries of PNRs.[119]
- Temperature insensitive electrostrictive strain output was discovered in some materials.[120]

One of the most thoroughly investigated class of lead-free relaxors are BNT-based incipient piezoelectrics. Incipient piezoelectrics can be defined as materials that possess a destabilized ferroelectric state achieved by the addition of chemical dopants or modifiers. The term incipient denotes “beginning to happen or develop”. This indicates that at zero bias-field these materials depict an ergodic relaxor state with negligible d_{33}, whereas under electric field they develop a

ferroelectric state and a reversible induced giant strain[121-139] and d_{33} values[121], as schematically introduced in Figure 2.14. Research on these materials has focused on understanding their strain mechanism in order to further enhance it. The origin of the large electromechanical response of incipient piezoelectrics is generally attributed to an electric field induced phase transition.[140-147]

Figure 2.14 at point $\boxed{a}$ displays an ergodic relaxor state, as previously discussed. For BNT-based lead-free incipient piezoelectrics, it was demonstrated that the electric field induced phase transition coincides with the inflection point of the strain output[148] and the transformation is followed by switching of the newly created domains.[143,144] Note that the inflection point of the strain curve also coincides with increased polarization.[148] Both processes lead to maximized d_{33} values (*i.e.*, d_{33}^{max}) and a maximized $\frac{\partial S_{33}}{\partial E_3} = S_{r-f}$.[121,149] Therefore, the inflection point of the strain curves indicate the electric field required to trigger the phase transition from the relaxor to the ferroelectric state at E_{r-f}. An electric field hysteresis ΔE_{r-f} is observed when the development and decay processes are compared.[148] Saturation of small and large signal electromechanical response is subsequently achieved, as displayed in point $\boxed{b}$. Upon removal of the electric field, the induced ferroelectric state decays into an ergodic state at E_{f-r} (point $\boxed{c}$) and is accompanied by a strain output with a value of S_{f-r}. When the electric field is removed, incipient piezoelectrics with a distribution of ergodicity may retain part of the induced ferroelectric state.[119] Prior to switching, the retained domains contract, similarly as in ferroelectrics (Figure 2.8 point $\boxed{d}$), leading to non-zero S_{neg}. Further electric field cycles retrace the response described resulting in hysteresis. Unipolar cycling will lead to the strain response displayed with dashed lines and a similar structural evolution as described for the bipolar case from points $\boxed{a}$ to $\boxed{c}$. As it will be seen in Section 3, incipient piezoelectrics depict a giant strain output surpassing the strain of lead-containing and other lead-free materials. Thus they are especially relevant for applications such as actuators.

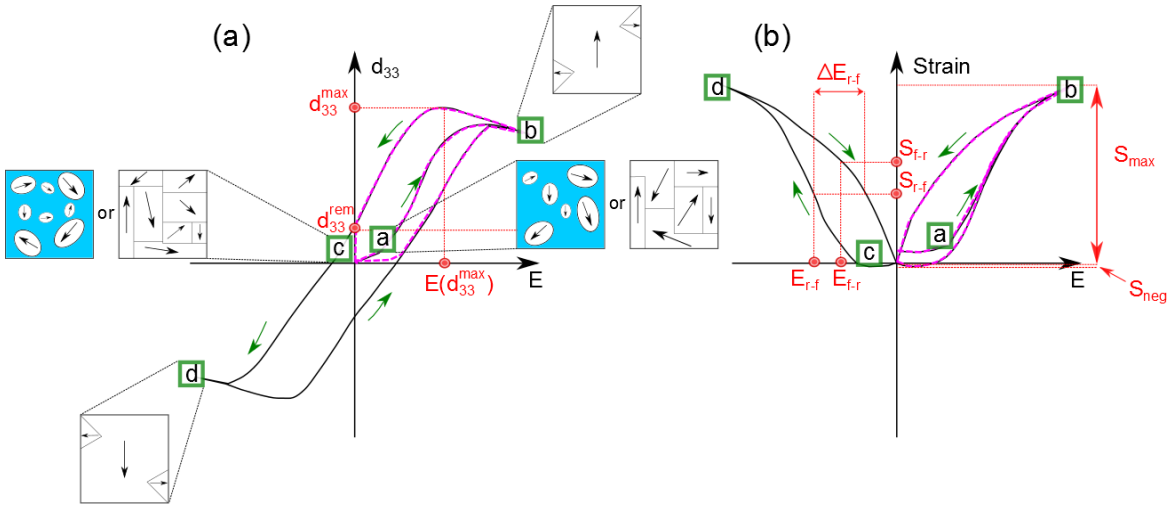

Figure 2.14: Schematic curves of (a) d_{33} and (b) bipolar (solid black line) and unipolar (dashed purple line) strain output of incipient piezoelectrics as a function of electric field. Prototypical microscopic relaxor views for different electric field strengths are also displayed.

2.3 Electromechanical Enhancements in Ferroelectrics

The last seven decades of research on ferroelectrics yielded strategies to enhance strain mechanisms[150,151], as displayed in Figure 2.15. To date, compositional engineering remains the preferred approach, although structural engineering has also led to technologically relevant achievements.[150] The strategies in white modify both intrinsic and extrinsic contributions to the piezoelectric activity, while those in light blue modify mostly the extrinsic contributions. Note that other approaches not directly related to the modification of material parameters can also be employed to enhance electromechanical properties. External stimuli such as optimization of the poling procedure through temperature or mechanical loading, as well as mechanical loading during service are also fruitful strategies. Nonetheless, they will not be treated in this work.

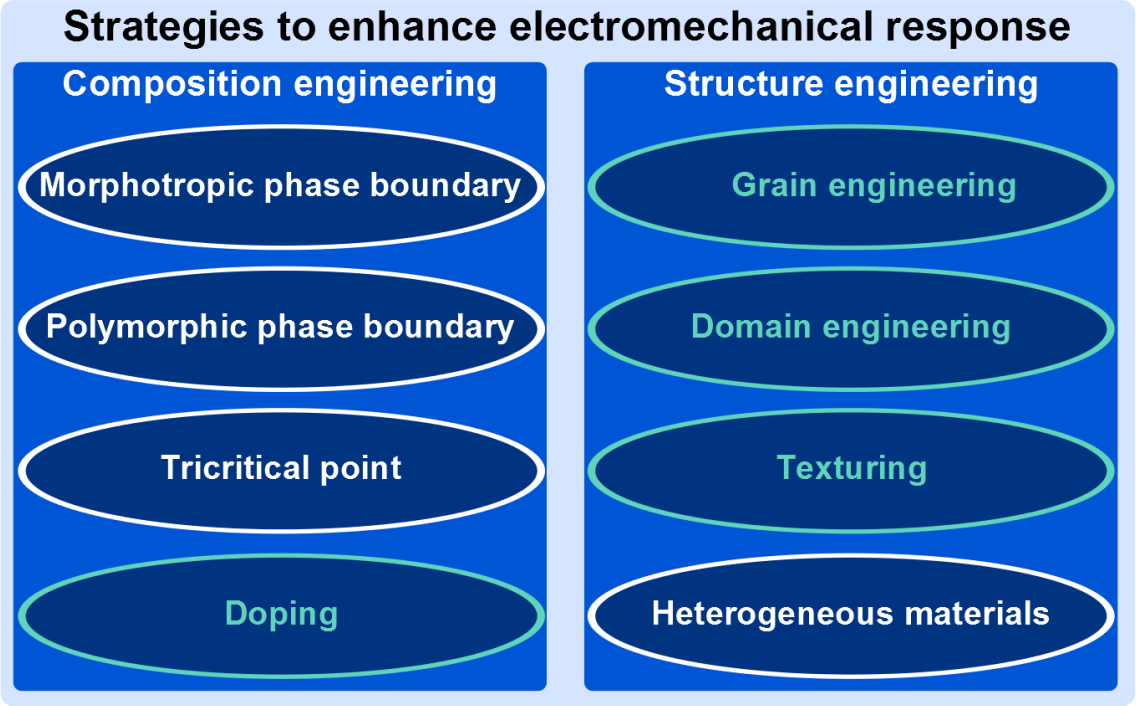

Figure 2.15: Compositional and structural engineering strategies to optimize electromechanical response of ferroelectrics. Strategies in white are used to enhance both intrinsic and extrinsic contributions to the piezoelectric activity, while those in light blue mostly modify extrinsic contributions.

2.3.1 Composition Engineering

2.3.1.1 Phase Instabilities

It is well-known that dielectric and electromechanical properties are enhanced around phase instabilities.[42] Phase instability indicates that a material possesses polymorphism; *i.e.*, it features

two or more different crystal structures depending upon changes in composition and/or thermodynamic variables. In contrast, isomorphism is defined as the case where compounds possess the same crystal structure, although they have different chemical composition.[152] Goldschmidt[152] proposed a distinction between the compositionally-driven polymorphs from those that arise as a result of changes in thermodynamic variables. The former boundary indicating a compositionally-driven change in polymorph, was designated a morphotropic phase boundary (MPB). The latter boundary, occurring as a consequence of a change in thermodynamic variables and at constant chemical composition, was denominated a polymorphic phase boundary (PPB). It must be pointed out, however, that the term MPB has also been employed in several occasions in the ferroelectrics community to indicate an increased multiplicity of polarization states contributing to enhanced electromechanical properties.[153] Figure 2.16 displays a schematic of a composition-temperature phase diagram representing MPBs and PPBs in ferroelectrics. The presence of five symmetries and three phase boundaries is depicted. Second order phase transitions are indicated by dashed lines, while the solid line represents a first order phase transition.

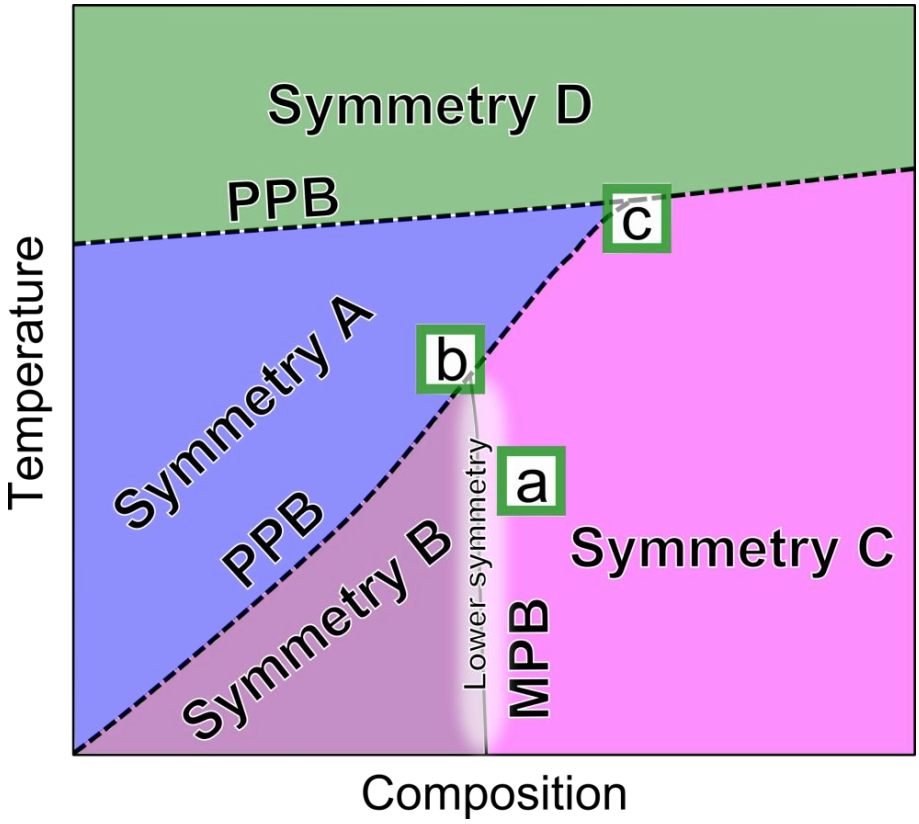

Figure 2.16: Schematic composition-temperature phase diagram depicting five symmetries, two PPBs, and one MPB. The white shaded region indicates the presence of an average lower symmetry structure than symmetries B and C. The dashed phase boundaries indicate second order phase transitions, whereas the solid line represents a first order phase transition.

Considerable research has been performed in BT-based materials or KNN-based materials characterized by presence of PPBs.[29,150,154] Alternatively, research has also focused considerably on systems with presence of a MPB-like[‡‡] transition such as in lead-based piezoelectrics or in some BNT-based materials.[10,29,150,151,154,155] The origin of maximized properties at interferroelectric phase boundaries has been commonly attributed to a FD transverse instability of P_s^i that ease its reorientation due to increased multiplicity of polarization states, reduced free energy anisotropy, and softening of the crystal lattice.[42,150,156-160] Transverse instabilities have been pointed out in several works as the key for the enhancement of dielectric and electromechanical properties.[157,159-167] Based on the soft-mode theory of ferroelectricity[168], crystal softening is a result of an optical phonon that dramatically reduces its frequency down to zero during phase transitions. The disappearance of the phonon gives rise to the new symmetry and consequently enhances dielectric and piezoelectric properties. Moreover, crystal softening can further enhance extrinsic contributions due to intergranular stress accommodation.[168] These mechanisms seem to be common to all displacive interferroelectric phase boundaries.[169] For the case of a ferroelectric to paraelectric phase transition, an analogous phenomenon has been proposed. At this phase boundary a FD longitudinal instability favors the P_s^i contraction/extension.[157,169] Figure 2.17 introduces the phase diagram of PZT and the free energy profiles calculated near phase boundaries. The dashed lines indicate easy paths for P_s^i to either rotate or extend and contract. The easy paths for P_s^i reorientation are determined by a minimization in free energy anisotropy (*i.e.*, the free energy surface is flattened giving a lower energy barrier for P_s^i to change its spatial direction). Therefore, this rationalization of strain enhancements mostly deals with intrinsic contributions to the piezoelectric activity. Approaching T_C to maximize the polarization extension contribution is not a convenient strategy due to the inherent reduced temperature stability of this enhancement. In order to develop technologically relevant materials using the longitudinal instability of P_s^i approach, the development of a temperature insensitive phase boundary between a polar phase and a non-polar phase is necessary.[169] This prospect was raised during the research of the mechanisms responsible for incipient piezoelectricity discussed in Section 2.2.2.2, as they feature this type of instability. Irrespective of the type of instability, systems with MPBs are preferred over those with PPBs. The technological advantage of an MPB over a PPB is that it enables temperature insensitive enhancement of electromechanical properties. Therefore, this phase boundary has traditionally been the focus of ferroelectrics development.[150] In general, it was pointed out that apart from the temperature insensitive electromechanical response, piezoelectric activity in materials with MPBs persists to higher temperatures than in materials with PPBs since any crossover of a phase boundary degrades piezoelectricity.[150] Retention of the P_r to higher temperatures in systems with MPBs can be attributed to a steeper free energy anisotropy reduction surrounding this phase boundary. In other words, the more tilted the PPB the more shallow the free energy profile becomes. This results in a reduced free energy anisotropy, which aids polarization mobility leading to a transverse instability of the P_s^i and thus lower retention of the P_r.[156,159,161]

[‡‡] To the best of the author´s knowledge, none of the phase boundaries known in ferroelectrics is strictly in accordance with the definition of an MPB proposed by Goldschmidt.

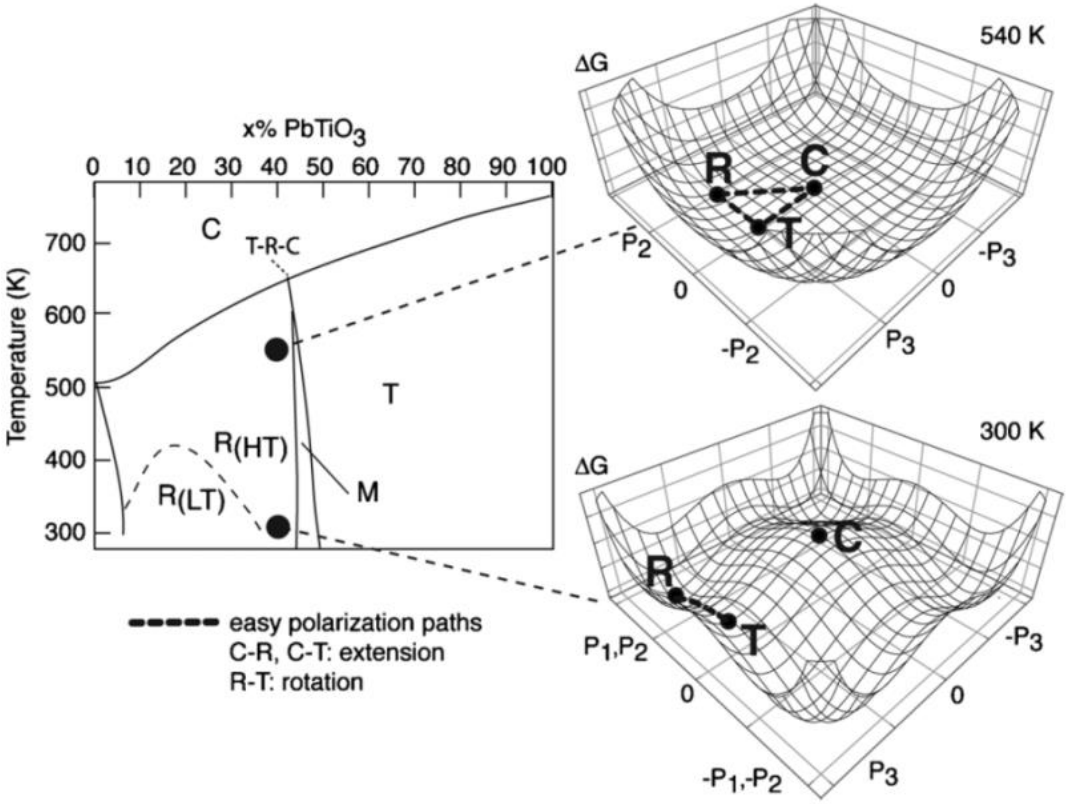

Figure 2.17: Composition-temperature phase diagram of PZT and Gibbs free energy profiles calculated at 300 K and 540 K with the phenomenological Landau-Ginsburg-Devonshire theory. Black dots in the phase diagram indicate the temperature at which energy profiles were calculated, while black dots on the energy profiles indicate the equilibrium phases. Lines between equilibrium phases indicate the easier polarization paths for phase transformation.[169] C: cubic phase, R_{HT}: high temperature rhombohedral phase, R_{LT}: low temperature rhombohedral phase, M: monoclinic phase, T: tetragonal phase.

The MPB region marked with point $\boxed{a}$ in Figure 2.16 has been generically characterized as O or Monoclinic (M) phases.[170-176] This interleaving region was proposed to be a bridge phase between the nearby phases B and C, as there is no group-subgroup relation between the commonly found $P4mm/P4bm$ and $R3c$ symmetries. It was stated that these phases aid P_s^i reorientation, indicating that this model mostly rationalizes intrinsic contributions. However, it has been pointed out that the M phase may be in fact composed of finely twinned R and T domains[178-180] or that its existance may only be metastable.[174] There have also been other mechanisms proposed in order to rationalize the extrinsic contributions to the electromechanical enhancement around MPBs. For instance, chemical ordering[181,182], formation of nanodomains[174,183,184] with facilitated switching[185], and others have been invoked. However, even in the case of domain miniaturization, it has been pointed out that the most important factor to consider is the mobility of domains rather than their size.[186]

The electromechanical enhancement around phase instabilities remains an open research area. It has been pointed out that reduced free energy anisotropy, crystal softening, nanodomain formation, local chemical/structural ordering, and local low symmetry phases may be in fact intrinsically related and the most fundamental reason behind strain enhancement a "matter of taste" as far as how it is described by a given scientist.[176] Damjanovic[157] highlighted that a structural instability is only a sufficient condition but not necessary for enhanced electromechanical properties, the crucial property for high piezoelectric activity is that the free energy instability leads to reduced free energy anisotropy. In fact, ferroelectric or ferroelastic domain switching is a result of a free energy instability achieved by an external electric field or stress, respectively. This in turn gives rise to the maximized changes of polarization and strain around E_c in ferroelectrics and around E_{r-f} in incipient piezoelectrics. In the case, where no electric field induced phase transition is observed, the drastic change of polarization and strain are due to a P_s^i instability in either the transverse (non-180° domain switching) or longitudinal (180° domain switching) sense. Nonetheless, switching remains an extrinsic effect and several factors other than lattice considerations should be examined in order to understand it.[157,187]

Some authors extended the concept of a free energy anisotropy further and evoked criticality as the fundamental reason behind enhanced properties.[188-191] A critical point is defined as a continuous transition from a first order to a second order phase transition under thermodynamic equilibrium that does not involve thermal hysteresis. Near these critical points, the energy barrier for a phase transition is considerably diminished. This indicates a more pronounced decrease of the free energy anisotropy and enhanced properties.[39,159,192,193] It was pointed out that maximizing the number of coexisting phases near multicritical points leads to increased entropy and thus higher enhancement of electromechanical properties.[192] Point $\boxed{b}$ in Figure 2.16 exemplifies both a triple point and critical point, since a first order phase transition (solid line) leads to a second order phase transition (dashed line) as the temperature is increased. In contrast, point $\boxed{c}$ in Figure 2.16 displays a triple point with no criticality. It should be noted, however, that the triple point in Figure 2.16 marked with $\boxed{b}$ is not necessarily a tricritical point. A tricritical point, refers to the point where, at a fixed composition, the lines of critical points in the temperature-electric field-pressure phase diagram converge.[39] Therefore, their experimental determination is quite difficult.[156] The coincidence of a tricritical point with a triple point such as the one marked with $\boxed{b}$ in Figure 2.16, will only occur in the hypothetical case that the critical points in the temperature-electric field and electric field-pressure phase diagrams intersect at the same temperature-composition coordinates of the triple point (at zero electric field and atmospheric pressure). The exceptionally large electromechanical properties of some BT-based materials were previously attributed to the presence of tricritical points.[194-196]

2.3.1.2 Doping

Ferroelectrics have also been traditionally engineered with isovalent or aliovalent dopants or modifiers to improve their functional properties for specific applications.[16,29] Modifiers are used to engineer a composition in proximity to phase boundaries, as treated in the last section. Although

dopant quantity may be very low, the functional properties of doped materials can vary drastically due to modification of the extrinsic contributions to the functional properties.[47,186,197] Aliovalent doping can be classified as donor or acceptor. Donor doping indicates that the oxidation state of the dopant is higher than the oxidation state of the host lattice site. In order to maintain charge neutrality, donor doping is compensated either by cation vacancy formation, decrease in oxygen vacancies, or electronic. Donor doped ferroelectrics are referred to as soft since they feature high dielectric and electromechanical properties, square ferroelectric hysteresis loops, and high dielectric loss. These properties are attributed to a high degree of switching that can contribute to more than 40 % to piezoelectric and dielectric properties.[50,186,197] Acceptor doping describes the situation where the dopant has a lower oxidation state than the host lattice site. In this case, doping is compensated by an increase in oxygen vacancies or holes. Acceptor doping can lead to the formation of defect dipole complexes between dopant ions and oxygen vacancies.[198] These materials are known as hard materials, since the interaction between defect dipole complexes and domains leads to decreased switching processes. Hard ferroelectrics generally have low dielectric and electromechanical properties, low dissipation factor, pinched ferroelectric hysteresis loops, and an internal bias-field.[151]

2.3.2 Structure Engineering

2.3.2.1 Grain and Domain Engineering

Structure engineering is a feasible way to achieve enhanced properties via a modified processing route. In general, E_c of single crystals is lower than those of ceramics with the same composition due to unclamped domain wall motion and relatively easy P_s^i reversal.[47] Therefore, by extension to polycrystalline materials, grain size has a considerable effect on the electromechanical properties of ferroelectrics.[199-202] An optimal grain size is obtained when a maximized density of domains (and domain walls) leads to a proper balance between non-180° switchable domains and minimized back switching.[201-204] Excessive grain size leads to deterioration of dielectric and electromechanical properties due to disproportionate back switching.[202] On the other hand, too small grain size leads to suppression of ferroelectricity due to diminished non-cubic distortions.[205-207] Moreover, domains also become unfavorable at small grain sizes since P_s is compensated by interface charges at grain boundaries and/or polarization gradients.[207] This leads initially to a single domain state, followed by complete suppression of the ferroelectric state as grain size is further reduced.[208] For $PbTiO_3$ the critical grain size to induce a paraelectric state is between 4 nm and 20 nm[209,210], while for BT it is between 10 nm and 100 nm.[205-207] BT has maximized properties at grain sizes between 1 µm and 2 µm.[203,204] Optimization of grain size leads in general to higher ε_r', lower T_C, decreased E_C, and increased d_{33}, and d_{33}^*.[199,200,203] Typically grain size can be altered by modifications to the raw starting powders, as well as by modifications of calcination and sintering processes.[211]

It was suggested that domain size is proportional to the square root of the grain size.[212,213] However, the relation remains valid only for grain sizes in the micrometer range[47] and in compositions far from phase instabilities.[183] Several works on BT determine that a fine domain

structure can greatly contribute to its piezoelectric activity.[214-222] Moreover, charged domains walls were also mentioned as further enhancing the piezoelectricity of materials with fine domains.[223] Figure 2.18 introduces the relation between (a) grain size and domain size and (b) domain size and d_{33}.

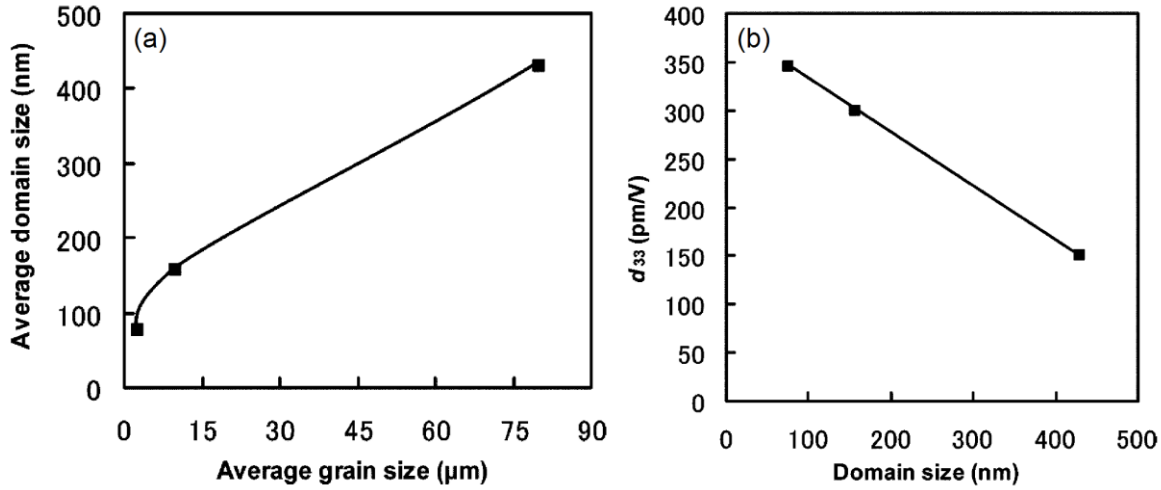

Figure 2.18: (a) Relation between grain size and domain size. (b) Relation between d_{33} and domain size for BT. Modified from Takahashi.[222]

In general, enhanced electromechanical properties observed in materials with reduced domain size are associated with an increased domain wall density and their enhanced mobility.[150,224,225] Domain engineering refers to a technique employed to induce a stable and optimized domain size in a material so that maximized functional properties can be achieved.[150,151,224] Although domain size and grain size are related in polycrystalline materials (Figure 2.18 (a)), domain engineering is also effective in single crystals.[226,227] Although coarse domain configurations generally feature diminished functional properties, they give rise to increased electric field and temperature stability.[227]

2.3.2.2 Texturing

Apart from grain and domain engineering, the electromechanical properties can be further enhanced by texturing. Wada and Pulpan[228,229] determined that the [110]-oriented BT with an average domain size of 800 nm and grain size of 75 µm features a d_{33} = 788 pC/N. Moreover, texturing was also shown to be a potential strategy to enhance the temperature stability of electromechanical properties.[132] It also has the advantage that it does not lower the operational temperature range.[29] Texturing enhances the electromechanical response of ferroelectrics because the inherent anisotropy of ferroelectrics does not allow a fully oriented domain state along the applied electric field.[29,230] Therefore, the limit of properties enhancement is given by the single crystal material variant, as displayed schematically in Figure 2.19.

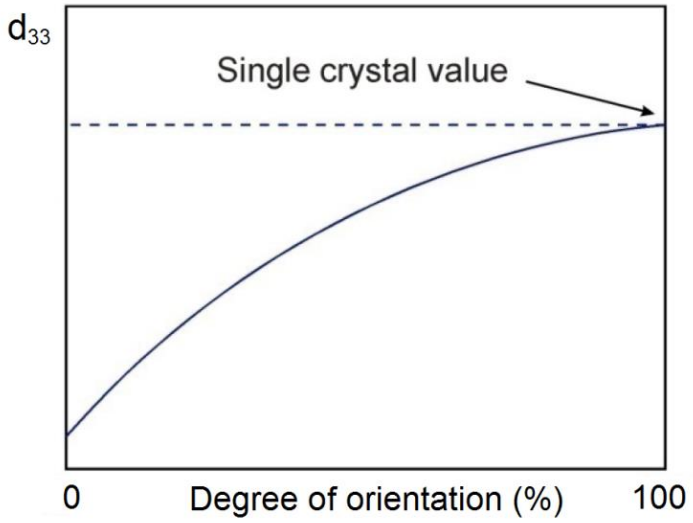

Figure 2.19: Piezoelectric response given by d_{33} as a function of degree of orientation. Modified from Leontsev and Eitel.[150]

The most commonly used texturing methods in ferroelectrics are templated grain growth and reactive templated grain growth.[230] Nevertheless, magnetic field texturing has also yielded promising results for some systems.[231] Orientation degrees between 60 % and 90 % have been achieved in lead-free ferroelectrics leading to enhancement of the electromechanical properties between 20 % and 200 %.[29]

2.3.2.3 Design of Heterogeneous Materials

Although chemical and structural modifications are the most common approaches for the production of new ceramics, further alternatives are available to improve the functional properties of ferroelectrics. Design of composite and core-shell materials affords extra variables to tailor this functionality, such as through connectivity and interface engineering. A proper design affects both intrinsic and extrinsic contributions to the piezoelectric activity. Figure 2.20 displays schematic views of the heterogeneous microstructures that have so far been attempted to tailor large signal electromechanical properties in lead-free piezoelectrics. Figure 2.20 (a) introduces a 0-3 composite (Newnham´s notation[232]) and (b) an approximate $(1_5;\ 1_\infty)_i$ core-shell microstructure. The generalized nomenclature for core-shell geometries is introduced in Appendix I.

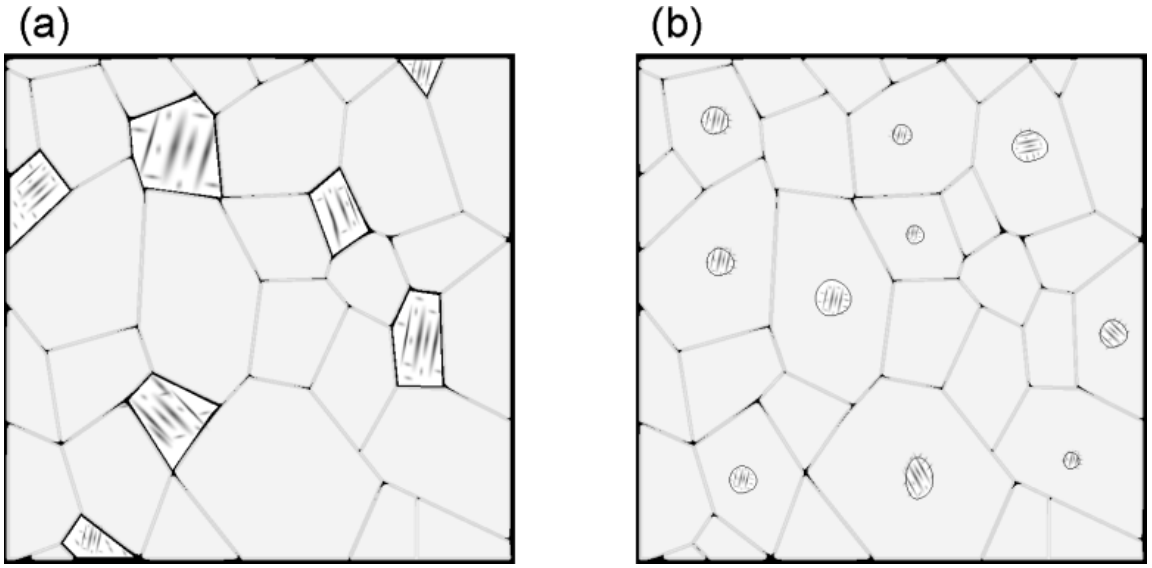

Figure 2.20: Schematic representation of heterogeneous materials (a) 0-3 composites and (b) an approximate $(\mathbf{1}_5;\ \mathbf{1}_\infty)_i$ core-shell microstructure. Macroscopically polar seeds such as a ferroelectric or non-ergodic relaxor state are displayed with presence of domain contrast, while gray regions designate a macroscopically non-polar matrix such as a paraelectric or ergodic relaxor state.

The composite approach is suited to engineer lead-free incipient piezoelectrics. For this purpose, 0-3 BNT-based composites were designed with a macroscopically polar seed such as a ferroelectric or non-ergodic relaxor state in conjunction with a macroscopically non-polar matrix such as a paraelectric or ergodic relaxor state.[233-240] This approach allowed for an enhanced strain output with reduced hysteresis, which gave between 10 % and 30 % higher electromechanical response than solid solution materials at 4 kV/mm.[233,236] The feasibility of tailoring the temperature and frequency stability with the composite approach was also demonstrated at the expense of reduced strain output.[237] The large signal strain and polarization, as well as the small signal dielectric properties, were calculated successfully in several works based on a model that regarded the microstructural constituents as two capacitors in series.[234,236,241] Since the charge of two capacitors in series is equal, the applied macroscopic electric field is distributed differently between constituents to assure a constant polarization. Generally, the macroscopically non-polar matrix depicts lower $\frac{\partial P}{\partial E}$ indicating that the electric field on the matrix will be higher. This promotes the electric field induced phase transition of incipient piezoelectrics and thus gives rise to their high electromechanical response at lower applied electric fields. Although these models considered only polarization coupling between the constituents, it was recently proposed that strain coupling should also play an important role.[242,243] Apart from the effect of changing the electric field distribution, it was suggested that the electric field induced phase transformation should be aided due to heterogeneous nucleation at the interfaces between constituents.[233,234,239] Theoretically it was demonstrated that nucleation and domain switching occur through a self-organized behavior

that is electrostatically controlled during initial stages and elastostatically controlled at later stages.[242]

The composite approach increases the complexity of the synthesis process. Difference in thermal expansion coefficients and/or the lattice mismatch between constituents should be considered as limiting factors since they can lead to defects and/or low density. Moreover, the interface between constituents can act as nucleation site of parasitic phases that can be detrimental to attaining the desired functional properties.[244,245] This reduces the attractiveness of this approach for industrial applications and hence highlights the potential of core-shell materials since they can be processed *in situ* during a conventional solid state route. Core-shell materials have experienced an increased interest due to technologically relevant dielectric[246-252], piezoelectric[253], and multiferroic[244,254] properties. Within nanotechnology developments, there has been a continuous increase in organic and inorganic core-shell nanoparticle discoveries with exceptional properties.[255] A promising lead-free core-shell piezoceramic was developed by Choi *et al.*[253] in the $CaZrO_3$-modified $(K,Na)(Nb,Ta)O_3$. This system depicted an exceptional d_{33}^* > 1000 pm/V at 3 kV/mm but only within a limited temperature range. The high strain of the system was attributed to the presence of a reversible poled state in the Ta^{5+}-rich non-polar shell indicating an analogous strain mechanism with composites. Although BNT-based core-shell microstructures have been previously reported, the functional properties associated with this microstructure were not addressed.[256,257] Moreover, an inspection of literature reveals that certain BNT-based piezoceramics may exhibit a core-shell microstructure although its effect on the functional properties was not discussed.[258]

3 Literature Review: Piezoceramics for Actuator Applications

The most widely used ferroelectric material in actuator applications is PZT due to superior electromechanical properties. This solid solution is formed by combining the $PbTiO_3$ and $PbZrO_3$ binary system. The phase diagram of the $PbTiO_3$-$PbZrO_3$ binary system is introduced in Figure 3.1.

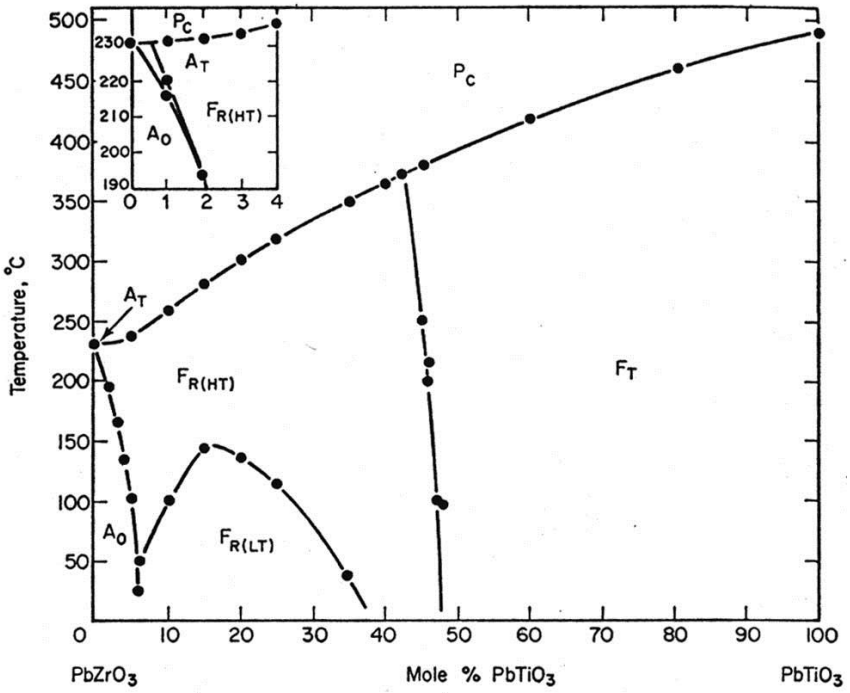

Figure 3.1: Phase diagram of the $PbTiO_3$-$PbZrO_3$ binary system obtained from Jaffe *et al.*[42] $F_{R(LT)}$: low temperature R phase. $F_{R(HT)}$: high temperature R phase. P_C: paraelectric C phase. F_T: ferroelectric T phase. A_0: antiferroelectric O phase. A_T: antiferroelectric T phase.

The $PbTiO_3$-$PbZrO_3$ binary system at ~ 48 mol % $PbTiO_3$ is characterized by an almost temperature insensitive phase boundary between R and T phases that was denominated MPB.[259] The current phase diagram of the $PbTiO_3$-$PbZrO_3$ binary system has been modified from its original version presented in Figure 3.1 and displays M phases around its MPB.[170] In the search for new lead-free piezoceramics, attempts were made in several perovskite materials. As introduced in Section 1, the BT-based, BNT-based, and KNN-based families of material are the most relevant.[10,29]

The BT was the first discovered ferroelectric compound with a perovskite structure. Ferroelectricity in BT was prove in the 1940's.[260,261] Later on, piezoelectricity and poling revealed the applicability of BT in ceramic capacitors and electromechanical devices such as phonographic pickups.[66,67,259] BT features a P_r = 0.30 C/m^2, E_c = 0.35 kV/mm, a d_{33} = 191 pC/N, and a T_C = 120 °C. Recent works demonstrated that exceptionally large electromechanical properties are achievable in pure BT obtained by an engineered synthesis route and/or microstructure.[214,216-220,222] This compound is

formed by relatively stable oxides that led to sintering temperatures around 1500 °C, which is higher than in the other lead-free counterparts. Nevertheless, usually a good sinterability is obtained in this family of materials. Nowadays, the BT-based materials are almost exclusively used in discrete and multilayer capacitors due to their high $\varepsilon_r^{'}$, good thermal shock resistance, and good dielectric reliability.[16] The research interest in this family of materials for electromechanical applications has raised recently[10] due to the discovery of the BZT-BCT.[194] Since then, other similar BT-based materials were shown to possess exceptional properties.[195,262-265] Although BT-based materials have attracted attention in the community recently, their use is limited to low temperatures. So far, chemical modifications and a controlled microstructure led to a maximum T_C $\sim$ 160 °C on this family of materials.[266-269]

In the search for new lead-free piezoceramics, an attempt was made to look for a cation comparable to Pb^{2+}. The cation Bi^{3+} was discussed as a candidate due to similar ionic radii and inert-pair $6s^2$ electrons as in Pb^{2+}.[29,151] The lead-free ferroelectric compound BNT was discovered by Smolenskii *et al.*[76] in the 1960´s. Variations of this basic perovskite compound have been thoroughly studied.[29] BNT features a P_r = 0.38 C/m^2, a E_c = 7.3 kV/mm, a d_{33} = 98 pC/N, and a high T_C = 320 °C.[42,270,271] Although the sinterability of the BNT-based materials does not seem to be a major problem for their scalability, Bi and Na volatility should be considered during synthesis.[272,273] BNT is promising for piezoelectric applications; however, its high E_c and conductivity make the poling difficult and restrict its applicability. The BNT-BT[270] and BNT-$(Bi_{1/2}K_{1/2})TiO_3$[274] binary solid solutions have attracted a considerable amount of research due to promising small signal piezoelectric properties around the MPB.[29] Zhang *et al.*[137] discovered the first incipient piezoelectric with a giant strain of 0.45 % at 8 kV/mm in the BNT-BT-KNN system. This electromechanical output surpassed that of soft PZT and thus triggered interest in a new area of research for actuators working in the quasi-static large signal regime. Since then, several binary and ternary BNT-based incipient piezoelectrics were shown to present giant strains.[121-139,258,275-278]

The KNN-based family of materials is also widely considered as a potential candidate to replace PZT.[10,29,154,279] $(K_xNa_{1-x})NbO_3$ (KNN) is a binary solid solution composed of $KNbO_3$ and $NaNbO_3$. Most of the research has traditionally focused on the 50 mol % $KNbO_3$ composition due to the proposed presence of a phase boundary. Although Egerton and Dillon[18] reported for the first time the KNN system in 1959, interest in its potential applicability was only triggered in 2004 by the discovery of Saito *et al.*[132] of a KNN-based material with d_{33} = 253 pC/N and a temperature stable d_{33}^* = 750 pm/V at 2 kV/mm. These exceptional properties were achieved through a complex texturing process. In subsequent investigations it was demonstrated that KNN-based materials depict promising small[280-283] and large[136] signal properties with conventional solid state synthesis. However, this family of materials presents major synthesis difficulties that need to be overcome for entering a reliable large scale production.[284,285] The correct choice of reagents is critical since K_2CO_3 is particularly sensitive to moisture.[279] A controlled atmosphere and humidity of the raw materials prior to calcination, during calcination, and also during sintering should be considered for obtaining the desired stoichiometry.[286-289] Additional problems arise also during sintering due to an extremely narrow sintering window in terms of temperature and dwelling time[290-292], early activation of surface diffusion that reduces the driving force for densification[273], and high volatilization of K^+ above 1000 °C.[154,288] The processing of KNN-based materials remains an open research area in

which new techniques such as pressure assisted sintering, spark plasma, and microwave sintering, and others are being investigated for developing reproducible and dense materials with high functional properties.[154,155]

A survey of d_{33} as a function of depolarization temperature (either T_C or T_d) for the most relevant lead-free material families is introduced in Figure 3.2 (a). Figure 3.2 (b) depicts d_{33}^* envelopes for each material family as a function of electric field at room temperature. This analysis is made to evaluate the suitability of lead-free material families for actuators.

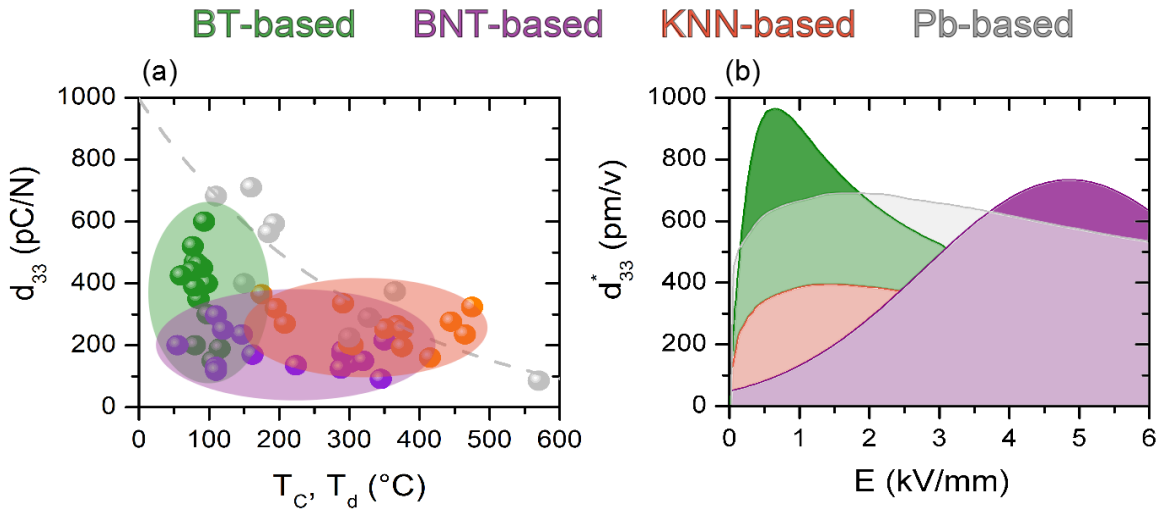

Figure 3.2: (a) Survey of d_{33} as a function of depolarization temperature (either T_C or T_d) for lead-free material families.[16,42,123,194,270,275,293-298] (b) Survey of d_{33}^* characteristic envelopes of lead-free material families at room temperature as a function of electric field.[121-139] As several publications are considered, the frequency of the strain values varies from 100 mHz to 5 Hz. For both figures representative lead-containing materials are added for comparison.

In ferroelectrics, a general trend of enhanced electromechanical response is observed with lower depolarization temperature. BT-based materials feature the highest piezoelectric coefficients of lead-free families. The d_{33}^* as a function of electric field (Figure 3.2 (b)) reveals that each material family is characterized by an electric field range in which their applicability is more suited. The working ranges of BT- and KNN-based materials are optimized for electric fields below 1 kV/mm and 2 kV/mm, respectively. Although BNT-based materials present the highest strain values, they occur at electric fields above 4 kV/mm and with high hysteresis. Therefore, reducing the electric field at which their high strain is obtained remains an open research area. For all lead-free families of materials, broader temperature and frequency operation ranges are also required to satisfy technological demands (Table 1.1).

The BZT-BCT is studied in this work as an exemplary system of BT-based piezoceramics. Therefore, the state-of-the-art knowledge of the system is presented in detail in Section 3.1. The BNT-ST

features technologically relevant properties for quasi-static large signal applications due to its high strain at reduced electric fields, reduced hysteresis, and simple stoichiometry compared to other incipient piezoelectrics.[258,275] Therefore, the BNT-ST was chosen as exemplary candidate to study the BNT-based piezoceramics and the state-of-the-art knowledge on the system is introduced in Section 3.2. Although, KNN-based materials feature promising small and large signal properties, they will not be treated in detail in this work. However, several aspects treated for the BZT-BCT system may be extrapolated to KNN-based materials.

3.1 The (1-x)$Ba(Zr_{0.2}Ti_{0.8})O_3$-x$(Ba_{0.7}Ca_{0.3})TiO_3$ System

The lead-free BZT-BCT system intended for electromechanical applications was first reported by Liu and Ren in 2009.[194] However, the synthesis and dielectric properties of the system were previously reported during the 1950's.[299] Since then, this ferroelectric material has spurred considerable research attention due to its outstanding piezoelectric properties. In the compositional range between BZT-0.40BCT and BZT-0.60BCT, a d_{33} > 500 pC/N and d_{33}^* > 1000 pm/V at 0.5 kV/mm were reported in a limited temperature range.[194] The relevance of the BZT-BCT for technological applications was already shown through prototype technological devices[300,301] and patents.[302-304] However, it must be pointed out that considerable discrepancies in the reported electromechanical properties can be found in the literature. This has been attributed to the different processing and characterization methodologies employed.[305]

3.1.1 Processing

Solid state synthesis of BZT-BCT was performed in most reports using similar conditions based on its parent compound BT.[306] Table 3.1 summarizes the different synthesis procedures found in the literature. Mishra *et al.*[307] performed a synthesis study on BZT-0.50BCT. The weight loss during heating of the uncalcined powders ended at 1000 °C, as indicated by TGA. However, the system displayed presence of second phases up to the calcination temperature of 1300 °C. More detailed studies suggested that the secondary phases remain even at higher calcination temperatures due to a limited solubility[299,308] and/or to kinetically stable intermediary phases.[309] The optimum calcination temperature for enhanced electromechanical properties was reported to be 1300 °C for 2 h under air atmosphere.[310] Increasing the sintering temperature from 1300 °C to 1400 °C improved the sharpness and intensity of X-ray diffraction (XRD) peaks, suggesting increased crystallinity and grain size.[307] It was revealed that a sintering temperature between 1480 °C to 1550 °C with dwell times between 2 h and 5 h is optimum for maximized piezoelectric properties.[310-313] Excessive sintering temperature resulted in secondary phases.[312]

Table 3.1: Synthesis parameters of BZT-BCT reported in the literature.

One step calcination	Calcination			Sintering			Ref.
	Temperature (°C)	Time (h)	Atmosphere	Temperature (°C)	Time (h)	Atmosphere	
Yes	1200	3	Air	1500	2	Air	314
Yes	1250	3	Air	1400	3	Air	315
Yes	1300	2 - 5	Air	1450 - 1500	3 - 4	Air	316-318
Yes	1350	2 - 3	Air	1450 - 1500	3	Air	194,300,319-331
Yes	1350	15	Oxygen	1400 - 1450	4	Oxygen	332,333

3.1.2 Atomic Structure

The BZT-BCT is a pseudo-binary solid solution formed by three end members $BaZrO_3$ (BZ), BT, and $CaTiO_3$ (CT).[116] A ternary phase diagram between these materials is introduced in Figure 3.3. Note that the terminology "pseudo-binary solid solution" is employed to highlight that BZT and BCT are solid solutions of two binary systems. Shaded areas I, II, and III depict pseudocubic structures with small non-cubic distortions that feature distinctive functional properties. The red blurred shaded area indicates the region of interest of the BZT-BCT for actuator applications. The region I features similar functional properties as BT, depicting the prototypical phase transitions of its parent material and ferroelectric properties. Increasing Ca^{2+} content leads to a considerably decreased R to O phase transition. Materials in the region III feature frequency-dependent dielectric anomalies indicating canonical relaxor features. Materials in region II are characterized by broader dielectric anomalies as compared to materials in region I. Although no clear frequency-dependent anomalies in dielectric properties were observed, these materials did not follow the Curie-Weiss law. The region resulting from the superposition between C and B is characterized by materials with distinctive relaxor features. In this compositional range, a ferroelectric state is induced with decreasing temperature, indicating a non-canonical relaxor state.[115,116,334] In general, it has been observed that increasing Ca^{2+} and Zr^{4+} leads to destabilization of the ferroelectric state of BT.[335,336] In similar BT-based systems detailed microscopy and *ab initio* calculations suggested that relaxor properties on these materials can be ascribed to local chemical heterogeneities.[337]

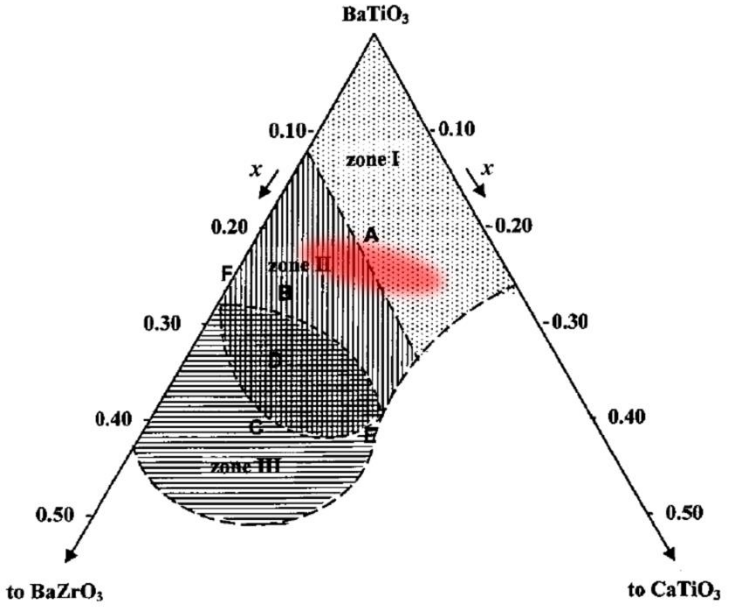

Figure 3.3: Ternary phase diagram of BZ, BT, and CT modified from Ravez *et al.*[116] Shaded areas I, II, and III are characterized by pseudocubic structures. The red blurred shaded area indicates the compositional range between BZT-0.20BCT and BZT-0.70BCT where piezoelectricity of BZT-BCT has been investigated.

The compositional range of BZT-BCT for actuator applications (red blurred shaded area) comprises pseudocubic materials with weak relaxor features.[338,339] Nevertheless, detailed XRD experiments were able to reveal the average atomic structure of the system.[331,333] It must be pointed out, however, that the short-range structure of the BZT-BCT differs from its long-range order similarly as in relaxor materials.[340] Figure 3.4 introduces the pseudo-binary phase diagram composed of digitalized data from several literature reports.[194,325,333,341]

Initially, Liu and Ren[194] proposed the presence of only one PPB from R to T phase that converge with a C phase in a triple point. The triple point was called a tricritical point, although no proof on the critically was reported.[194] Recent reports indicate unambiguously the presence of two PPBs on the system[318,322,325,331,333,341], similarly as found in other BT-based materials.[196,342] Despite the agreement of an interleaving region between R and T phases, further clearance is still required especially in the convergence region (yellow blurred shaded area), as well as the interleaving region between R and T phases. The term convergence region was coined by Keeble *et al.*[333] to indicate the area where convergence of R, T, O, and C phases seems to merge. Recent computations demonstrated that two triple points are expected in this region, although they may be difficult to access experimentally due to their close proximity.[156] Synchrotron studies determined that the R phase is characterized by a $R3c$ symmetry, while the T phase depicts a $P4mm$ symmetry.[331,333] Both symmetries originate from a prototype cubic structure with $Pm\bar{3}m$ symmetry. The atomic structure of the interleaving region, however, still remains under debate. Some authors reported an O phase with $Amm2$ symmetry[322,333,343], while others indicated that the interleaving region is a

phase mixture between R and T phases with $R3m$ and $P4mm$ symmetries, respectively.[325,331,344] A gradual symmetry change with increasing temperature was confirmed by micro-Raman studies.[345] An electric field induced phase transformation from T and R phases to an O phase has also been speculated in the literature[321], although was not proven yet.

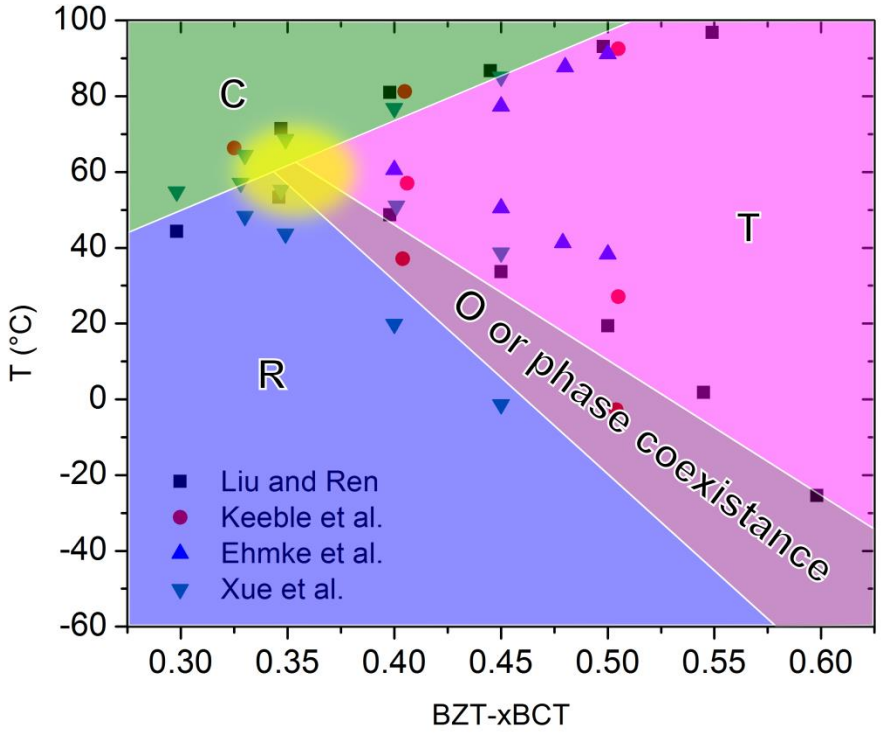

Figure 3.4: Pseudo-binary phase with data taken from Liu and Ren[194], Keeble *et al.*[333], Ehmke *et al.*[325], and Xue *et al.*[341] The shaded areas depict approximate phase stability regions. The yellow blurred shaded area indicates the phase convergence region. R: rhombohedral, O: orthorhombic, T: tetragonal, and C: cubic phases.

3.1.3 Microstructure

Functional properties of BT[202,346] and BZT-BCT[200] depend on the microstructure. Transmission electron microscopy (TEM) studies on BZT-BCT revealed a characteristic micrometer size domain morphology in each phase. The R phase is characterized by wedge-shaped domains, while the T phase depicts lamellar domains. The O phase features hierarchical domain morphology with nanometer size domains within micrometer size lamellar domains. The hierarchical domain formation was ascribed to reduced free energy anisotropy.[319] *In situ* temperature-dependent TEM indicated a considerable change in the hierarchical domain structure of the system.[347] Upon heating wedge-shaped domains in the O phase of BZT-0.50BCT disappeared progressively. Moreover, nanodomains inside wedge-shaped domains merge and transform into lamellar domains. The domain morphology transformation suggests a gradual change from R to T symmetry. Upon cooling, the domain morphology partially redeveloped indicating a considerable irreversible

switching.[347] *In situ* electric field TEM studies demonstrated that switching is also quite considerable leading to the formation of a monodomain state within grains.[321,339] The hierarchical domain morphology[319] and irreversible switching[347] were mentioned as contributors to the enhancement of electromechanical properties around the O to T PPB.

Apart from domain morphology, the grain size was also reported to have a considerable effect on the functional properties of BZT-BCT. In general, literature reports mention grain sizes between 13 µm and 50 µm.[321,324-330,348] Hao *et al.*[200] performed a grain size study and demonstrated that increasing grain size from 0.4 µm to 32.2 µm influences functional properties considerably, as displayed in Figure 3.5. All phase boundaries decreased between 10 °C and 20 °C with increasing grain size and the magnitudes of ε_r' and $\tan(\delta)$ were considerably reduced. The dielectric relaxations in ε_r' also become much more apparent for samples with grain sizes below 1 µm. It was also observed that the polarization is enhanced by 40 % and the strain output can be increased by five times with increasing grain size up to 20 µm. Further grain size increase leads to small variations of polarization and strain outputs. Small signal d_{33}, planar coupling coefficient k_p, and thickness mode coupling k_t displayed similar trends as the large signal strain output. Higher grain size also led to lower temperature stability. Maximized functional properties and temperature sensitivity in samples with higher grain size were attributed to increased domain switching and decreased residual stress.[200]

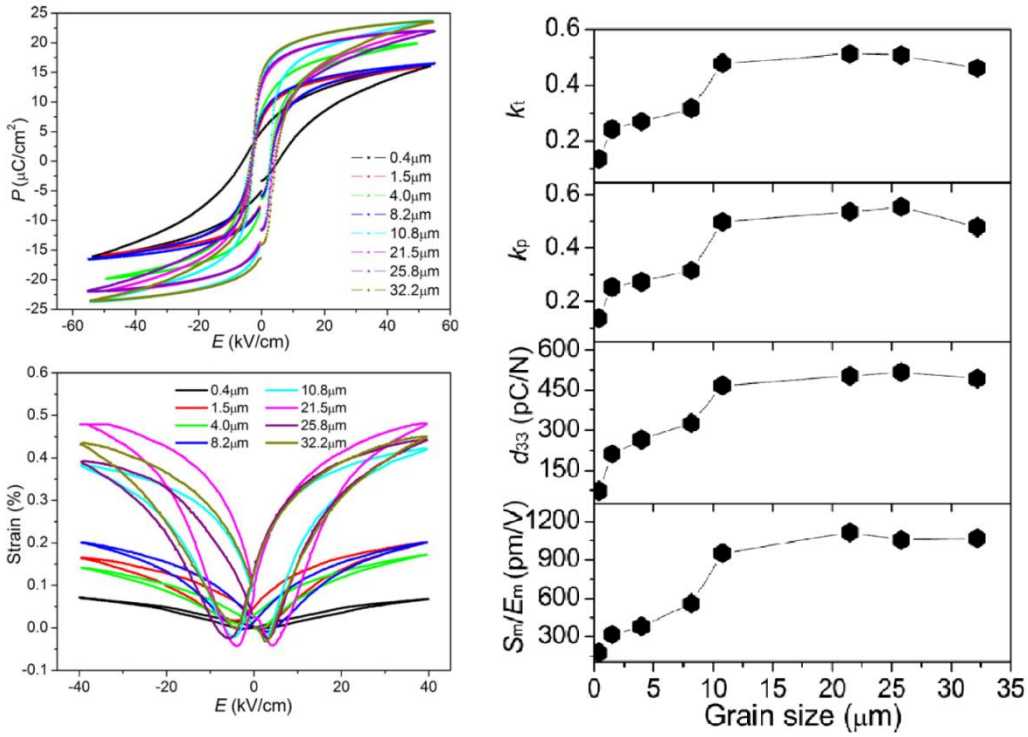

Figure 3.5: (a) Bipolar polarization and (b) bipolar strain as a function of electric field for samples with different grain size. (c) displays k_t, k_p, d_{33}, and d_{33}^* as a function of grain size. Figure was modified from Hao *et al.*[200]

3.1.4 Electromechanical Properties

A set of dynamic small signal properties of BZT-0.50BCT is contrasted with properties of BT and soft PZT (PZT5A) in Table 3.2.[320] The BZT-0.50BCT features higher electromechanical response as compared to BT and PZT5A. However, coupling coefficients for PZT5A are the highest.

Table 3.2: Small signal dynamic piezoelectric properties.[320]

Material	d_{33} (pC/N)	d_{31} (pC/N)	d_{15} (pC/N)	k_{33}	k_{31}	k_{15}	k_t	k_p
BZT-0.50BCT	546	-231	453	0.65	0.31	0.48	0.42	0.53
BT	191	-79	270	0.49	0.21	0.48	---	0.35
PZT5A	374	-171	584	0.7	0.34	0.68	0.49	0.6

The large signal strain output of BZT-BCT is 20 % higher than in soft PZT (PZT5H) at 0.5 kV/mm.[194] However, it must be considered that at high electric fields the BT-based materials depict a reduced strain output (Figure 3.2 (b)). The strain mechanism proposed by Liu and Ren[194] for BZT-BCT has been generally accepted in the literature. They suggested that any phase boundary originating from a tricritical point would result in negligible polarization anisotropy and thus these boundaries would facilitate the transverse instability of P_s^i. Nevertheless, the free energy anisotropy of the system was not provided. Recent calculations demonstrated that a broad region of the pseudo-binary phase diagram features diminished free energy anisotropy and was ascribed to tilted PPBs.[156] Recent reports also highlighted the importance of studying elastic properties of the system, as they couple with piezoelectric properties.[318,341,349] Figure 3.6 displays (a) $\varepsilon_r' P_r$ and (b) d_{33} as a function of composition.[322] It is observed that $\varepsilon_r' P_r$ and d_{33} values at the O to T PPB are higher than at the R to O PPB, similarly as reported in other BT-based materials.[342] Moreover, the O to T PPB is more elastic than the R to T PPB (Figure 3.3 (c)), and displays similar elasticity as the convergence region.[318,341,349] Li *et al.*[350] reported that the electrostrictive coefficients of BZT-BCT are $\sim$ 0.04 m^4/C^2 and remain relatively constant with composition and temperature. It was demonstrated that switching determines to a great extent small[323] and large[329] signal properties. Specifically, it was shown that reversible domain switching is maximized at the O to T phase boundary, leading to a contribution that accounts even up to 50 % of the total d_{33} response at room temperature.[323]

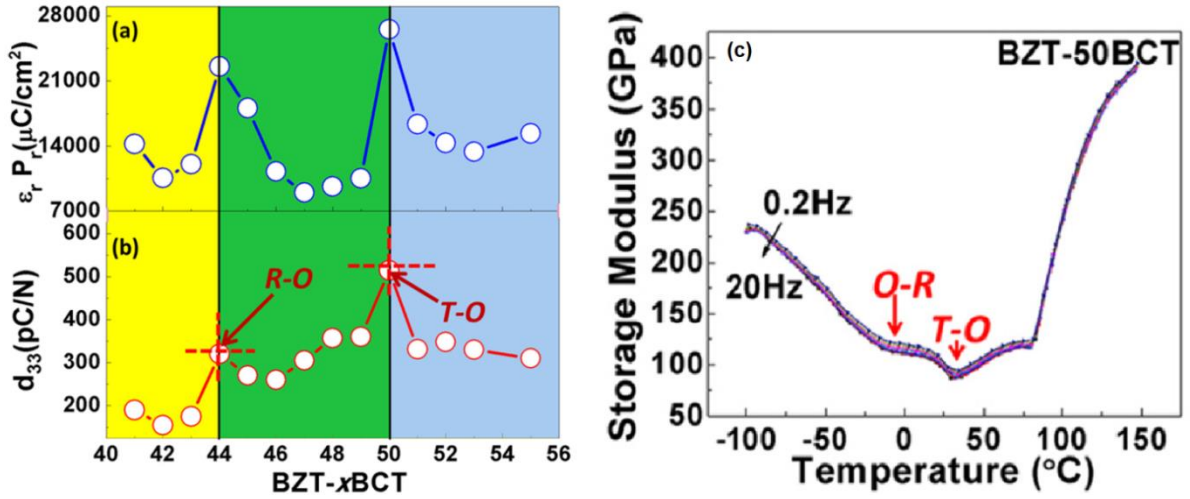

Figure 3.6: (a) $\varepsilon_r' P_r$ and (b) d_{33} as a function of composition. (c) Storage modulus as a function of temperature for BZT-0.50BCT.[322]

Small and large signal electromechanical properties of BZT-BCT are highly susceptible to poling conditions[314,324,328,351,352], stress[326,330], and temperature variations.[194,320,325] Electromechanical properties were found to have local maxima values around phase boundaries, followed by diminished properties.[194,305] Higher temperature stability was generally observed away from phase boundaries, although with diminished magnitudes.[317] At room temperature it was demonstrated that 4 kV/mm lead to saturation of the poling degree given by θ angle.[314] Considerable aging was observed after 10^4 min of the poling procedure leading to a 25 % decay of d_{33} and k_p in dry atmosphere and 30 % decay in wet conditions.[352] Ehmke *et al.*[328] realized that an electric field 20 times larger than E_C leads to 50 % increase of small signal d_{33} and asymmetry on the large signal strain. This phenomenon was ascribed to the migration of point defects. Poling effects and changes in electromechanical properties are more pronounced in the R phase than the T phase, which was considered a result of a reduced lattice distortion and a higher number of possible polarization directions.[328] The R phase was also highlighted to be more susceptible to high temperature excursions, which led to diminished piezoelectricity.[325] In general, the system susceptibility to external parameters was considered to be a result of its high elastic softness that enables an easy polarization rotation along different crystallographic orientations.[332] This was mentioned as crucial for the development of enhanced electromechanical properties. High temperature poling was proved to be quite beneficial for attaining maximized properties.[324,351] For all poling temperatures, it was observed that despite of the modification of functional properties under electric field, the remanent ferroelastic texture parallel to the electric field remained relatively constant.[324,328] This indicated that the high electromechanical response after temperature poling is a result of enhanced charge carrier migration at high temperatures.[157,188]

3.2 The (1-x)($Bi_{1/2}Na_{1/2}$)TiO_3-x$SrTiO_3$ System

The lead-free solid solution between BNT and ST was first reported by Sakata and Masuda[353] in 1974 with the aim to shift the phase transitions of pure BNT to lower temperatures, thus allowing a systematic study of the functional properties of the system. Subsequent studies, have demonstrated that increasing ST content in BNT-based materials leads to destabilization of the long-range ferroelectric state and decreased T_d as well as P_r.[258,275,276,278,354,355] These features can be ascribed to decreased unit cell distortions that culminate at a certain compositional range in a pseudocubic structure.[356] Recent studies highlighted the technological relevance of the system for actuator applications.[258,275] Additionally, the BNT-BT-ST[276,278,354,355], and BNT-($Bi_{1/2}K_{1/2}$)TiO_3-ST[277], and BNT-ST-KNN[357] were also introduced in the literature. These systems resemble BNT-ST regarding their electromechanical output, although their response at reduced electric fields is lower. Electrostrictive materials were also reported in similar systems with the presence of Sr^{2+}.[358,359] The electromechanical output of promising incipient piezoelectrics is displayed in Figure 3.7 (a). The most relevant technological feature of the BNT-ST is the large signal strain output of more than 0.25 % at 4 kV/mm and a d_{33}^* of more than 600 pm/V even at 2 kV/mm (Figure 3.7 (b)).[258,275] Moreover, the E_{r-f} (Figure 3.7 (c)) and hysteresis ΔE_{r-f} (Figure 3.7 (d)) are also considerably lower than for other BNT-based incipient piezoelectrics.

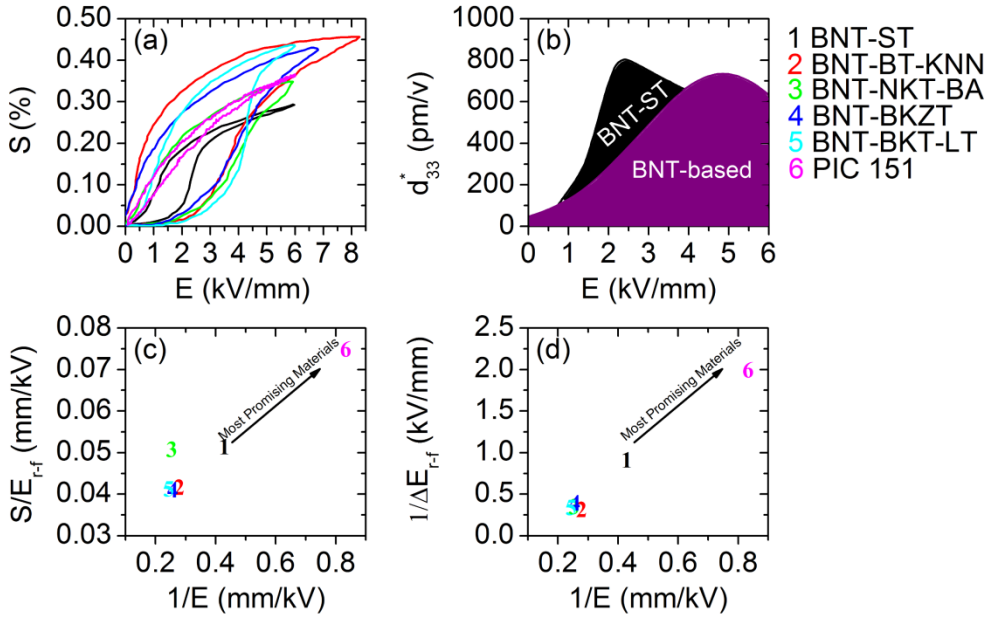

Figure 3.7: (a) Unipolar strain and (b) d_{33}^* as a function of electric field for BNT-ST in comparison to the d_{33}^* envelope of BNT-based materials previously introduced in Figure 3.2. (c) S/E_{r-f} and (d) ΔE_{r-f} as a function of the inverse of the electric field for technologically relevant lead-free materials[125,130,138,139,275] and soft PZT PIC 151. BNT-NKT-BA: (1-x)($Bi_{0.5}Na_{0.78}K_{0.22}$)$_{0.5}TiO_3$-x$BiAlO_3$[138], BNT-BKZT: $Bi_{0.5}(Na_{0.78}K_{0.22})_{0.5}(Ti_{1-x}Zr_x)O_3$[125], BNT-BKT-LT: ($Bi_{0.5}Na_{0.41-x}K_{0.09}Li_x$)($Ti_{1-y}Ta_y$)$O_3$.[130]

3.2.1 Processing

The BNT-ST system has been synthesized via the solid state route with different conditions, as introduced in Table 3.3. The different synthesis procedures reported in the literature may be attributed to complications arising due to the high temperature stability of $SrCO_3$ that inhibits the production of a homogeneous solid solution.[360,361] Three literature reports marked with * in Table 3.3 reported multi-step solid state synthesis to favor the formation of a homogeneous solid solution.

Table 3.3: Synthesis parameters of BNT-ST reported in the literature. *In a first step Bi_2O_3, Na_2CO_3, and TiO_2 were calcined to form BNT (first number given indicates parameters), secondly $SrCO_3$ and TiO_2 were calcined together to form BNT-ST (second number given indicates parameters). BNT and ST reacted during sintering to form BNT-ST. **In a first step Bi_2O_3, Na_2CO_3, and TiO_2 were calcined to form BNT (first number given indicates parameters), secondly BNT, $SrCO_3$, and TiO_2 were calcined together to form BNT-ST (second number given indicates parameters). ***In a first step Bi_2O_3, Na_2CO_3, and TiO_2 were calcined to form BNT (first number given indicates parameters), secondly $SrCO_3$ and TiO_2 were calcined together to form ST (second number given indicates parameters). The last step was to react BNT and ST to form the BNT-ST solid solution (third number given indicates parameters). #Materials with ST < 50 mol % were sintered at 1200 °C, for ST > 50 mol % were sintered at 1300 °C.

One step calcination	Calcination			Sintering			Ref.
	Temperature (°C)	Time (h)	Atmosphere	Temperature (°C)	Time (h)	Atmosphere	
Yes	800	15	Air	1050 - 1190	n/a	Air	[362]
Yes	800	4	Air	1200	4	Air	[363]
Yes	800	2	Air	1100 - 1150	2	Air	[364]
Yes	800	2	Air	1100 - 1140	2	Air	[275]
No*	750/1100	2/2	Air	1150	2	Air	[365]
No**	850/850	n/a	Air	1200 - 1300#	2	Air	[258]
No***	800/800/800	2/2/2	Air	1100 - 1150	2	Air	[366]

3.2.2 Atomic Structure

The BNT-ST is a binary solid solution between the end members BNT and ST. Jones and Thomas[367] studied the BNT with neutron diffraction from - 268 °C to 600 °C. In the temperature range from - 268 °C to 300 °C they determine that BNT features a R phase with $R3c$ symmetry and $(a^-a^-a^-)$ tilting (Glazer's notation[368]) of the oxygen octahedra about pseudocubic axes leading to an incommensurate phase. This octahedral tilting was presumed to be driven by the undersized A-site cations and the Bi^{3+} lone pair of e^-. In the temperature range from 300 °C to 400 °C, coexistence of the described R phase and a T phase with $P4bm$ symmetry characterized by $(a^0a^0c^+)$ tilting was observed. From 400 °C to 500 °C, the system depicted solely the T phase, while above 500 °C the prototype C phase with $Pm\bar{3}m$ symmetry was established.[367] The phase sequence described for the BNT indicates that both commensurate FD and incommensurate AFD transformations are found. The ST depicts a paraelectric C phase with $Pm3m$ symmetry down to - 168 °C, where it transforms to a T phase with $I4/mcm$ symmetry that features antiferroelectricity and twin domains along $\{101\}$ crystallographic planes.[369-373] No further structural changes are found in this material. Despite the strong softening of the polar mode near - 273 °C, zero-point motion suppresses ferroelectricity. This was corroborated since small doping content promotes ferroelectricity.[374] The ST is prone to display AFD distortions[375] due to the small ionic radii of Sr^{2+}.[371]

The BNT-ST displays a R structure at room temperature below 20 mol % ST.[363,365] Increasing ST content leads to a gradual increase in the lattice parameter between 3.885 Å and 3.905 Å.[366] The increase in lattice parameter is accompanied by a gradual decrease of the unit cell distortion from R to a pseudocubic below 20 mol % ST, as displayed in Figure 3.8 However, further ST content leads to a considerable change of the R distortion at room temperature and vanishing non-cubic distortions[365,366] and relaxor features.[258,362,365,366] Initially, this relaxor state was termed an antiferroelectric state[353]; however, subsequent reports discarded antiferroelectricity in the system.[366]

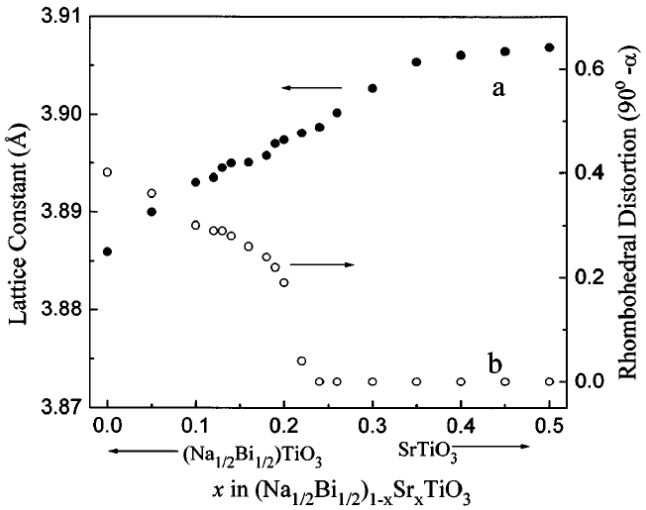

Figure 3.8: Lattice parameter and R distortion as a function of ST content in BNT-ST.[366]

Based on the results from XRD, dielectric properties, and Raman spectoscropy analysis, Rout *et al.*[363] proposed a phase diagram for the BNT-ST system (Figure 3.9). Although the phase diagram displays T_d, it should be pointed out that depolarization studies on the system were not performed and this line was considered as the low temperature frequency-dependent dielectric anomaly.

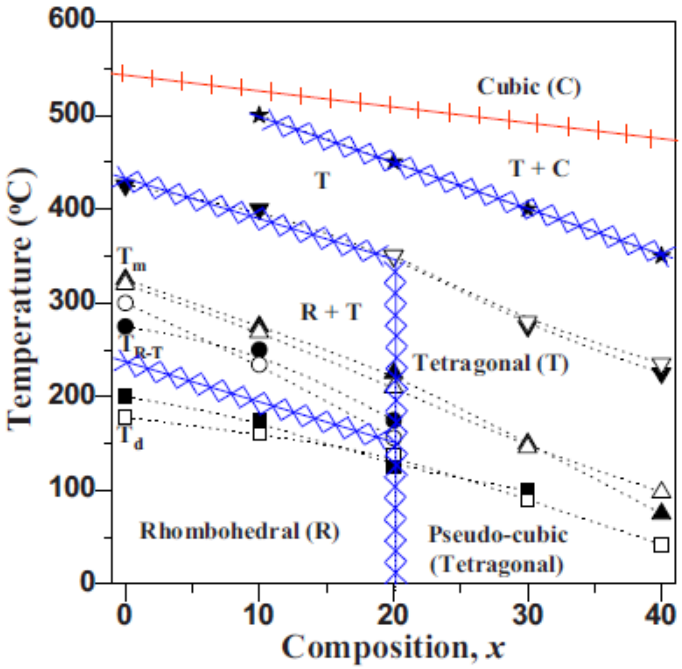

Figure 3.9: Binary phase diagram of the BNT-ST system proposed by Rout *et al.*[363] from 0 mol % ST to 40 mol % ST. Open symbols were obtained from dielectric measurements, while solid symbols from Raman spectroscopy analysis.

The only phase boundary featured in the BNT-ST at room temperature is at 20 mol % ST, indicating the transformation from a R to a pseudocubic phase, as previously indicated by changes in lattice parameter and unit cell distortion in Figure 3.8. This phase boundary was reported in other studies between 25 mol % ST and 28 mol % ST.[363,365,376] The presence of Raman modes in the whole compositional range of the BNT-ST[363] indicates that the local structure deviates from cubic, as expected in relaxor materials (Section 2.2.2).

Rout *et al.*[363] determined that the symmetry of the R phase of BNT-ST is $R3c$ and the pseudocubic phase is $Pm3m$. By means of TEM, Lee *et al.*[365] discovered the presence of $(a^-a^-a^-)$ octahedral tilting[146,377] supporting the presence of a $R3c$ symmetry for ST contents below 30 mol % ST. With increasing temperature, a gradual decrease of the unit cell distortions was found from a monotonic decrease of Raman modes. The high temperature phase was reported to be cubic for the whole compositional range investigated in Figure 3.9; however, the presence of Raman activity indicates that the local structure of the system remains distorted.[363]

3.2.3 Microstructure

Figure 3.10 displays SEM micrographs of (a) BNT-0.27ST and (b) BNT-0.40ST reported by Krauss *et al.*[258] A gradual decrease of grain size from 10 µm to 3 µm was observed with increasing ST between 10 mol % and 90 mol %.

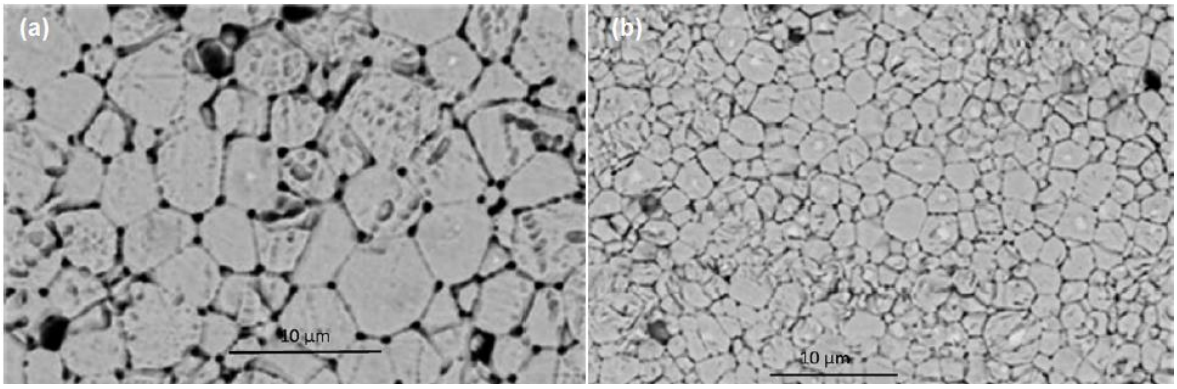

Figure 3.10: Polished and etched surfaces of (a) BNT-0.27ST and (b) BNT-0.40ST. Image modified from Krauss *et al.*[258]

Although the system was regarded as a solid solution[258], Figure 3.10 (a) and (b) display the presence of a bright second phase within certain grains, resembling a core-shell microstructure. However, the presence and nature of this phase was not discussed by the authors. Moreover, TEM analysis revealed a gradual destabilization of the ferroelectric state with increasing ST content, as indicated by a frustrated ferroelectric state with PNRs.[365]

3.2.4 Electromechanical Properties

The phase boundary between the R and the pseudocubic phases has a considerable effect on the electromechanical properties of the system. Figure 3.11 displays the bipolar polarization loops for (a) BNT-0.20ST, (b) BNT-0.28ST, (c) BNT-0.32ST, and (d) BNT-0.36ST. The P_{max} and P_r are decreased with increasing ST content, resulting in pinched loops above 28 mol % ST with P_r < 0.10 C/m^2, similarly as found in relaxor materials (Figure 2.12).[258] The variation of P_r and P_{max} with increasing ST content indicates that a decreased cooperative interaction of dipoles occurs leading to diminished ferroelectricity.[365] At this compositional range it was also found that T_d is brought near room temperature.[364]

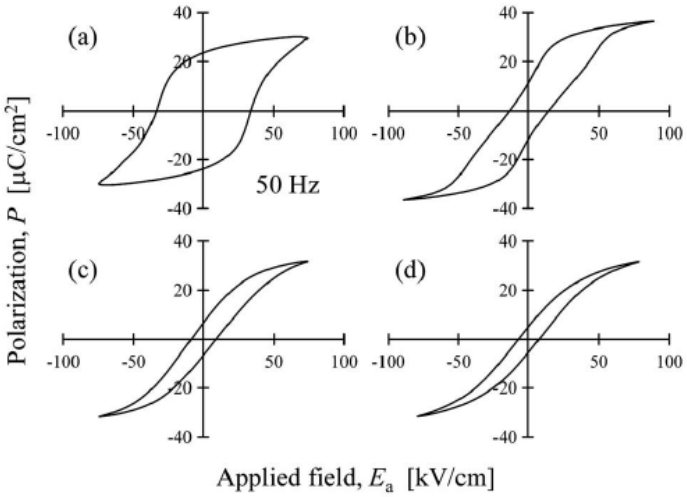

Figure 3.11: Bipolar polarization loops for (a) BNT-0.20ST, (b) BNT-0.28ST, (c) BNT-0.32ST, and (d) BNT-0.36ST measured at 0.1 Hz.[275]

Hiruma *et al.*[275] reported the dynamic d_{33} and quasi-static d_{33}^* of the BNT-ST in a broad compositional range, as depicted in Figure 3.12.

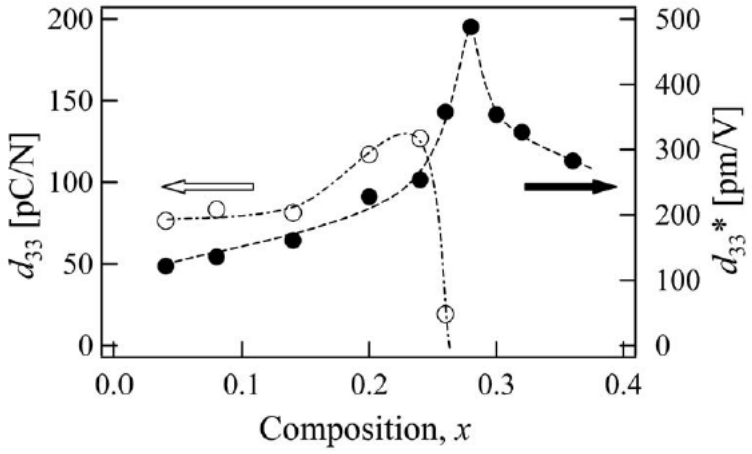

Figure 3.12: Dynamic d_{33} and quasi-static d_{33}^* as a function of ST content.[275]

The maximum quasi-static d_{33} = 130 pC/N was reported to be around 22 mol % ST, followed by an exponential decrease leading to negligible values above 28 mol % ST and maximized d_{33}^* = 500 pm/V at 6 kV/mm. Hiruma *et al.*[275] proposed that the large d_{33}^* of the BNT-ST is a result of an electric field induced phase transition from the pseudocubic phase to the R phase and the switching occurring at the induced phase. This strain mechanism is qualitatively similar as proposed for other BNT-based materials.[140,141] However, Krauss *et al.*[258] proposed that the electric field induced phase transition is from an antiferroelectric state to a ferroelectric state.

4 Experimental Procedure

All units and notations are provided in the international system following the "Guide for the Use of the International System Units".[378] Systematic or random error analysis was employed to report uncertainties. A standard distribution for the measured quantity was assumed to estimate systematic errors. The precision of the machines as provided by manufacturers was employed to evaluate random errors. Trailing zeros were used to indicate precision on measurements.

4.1 Powder and Ceramic Processing

Materials were produced via the mixed oxide route. Raw chemicals $BaCO_3$ (99.8 %), $CaCO_3$ (99.5 %), Bi_2O_3 (99.975 %), Na_2CO_3 (99.5 %), TiO_2 (99.9 %, Anatase), ZrO_2 (99.5 %), and $SrCO_3$ (99 %) (Alfa Aesar GmbH & Co. KG, Germany) were mixed according to the stoichiometric formulas $(1-x)Ba(Zr_{0.2}Ti_{0.8})O_3$-$x(Ba_{0.7}Ca_{0.3})TiO_3$ (x = 0.30, 0.32, 0.35, 0.37, 0.40, 0.45, 0.50, and 0.60) and $(1-x)(Bi_{1/2}Na_{1/2})TiO_3$-$xSrTiO_3$ (x= 0.25 and 0.28), respectively. The ternary phase diagram of BT, BZ, and CT system is introduced in Figure 4.1 in the region comprehending the BZT-BCT compositional range.

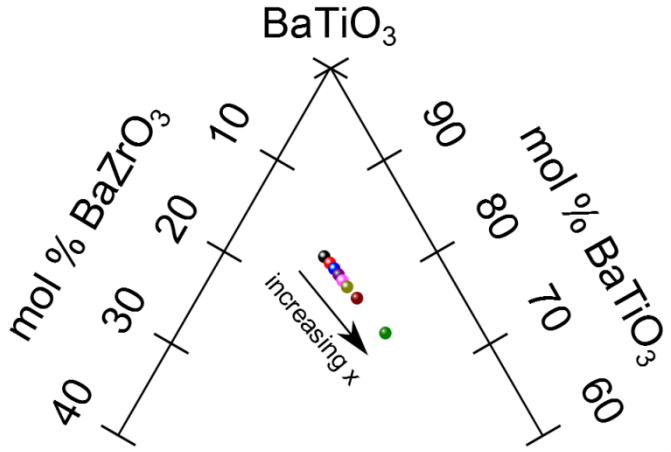

Figure 4.1: Ternary phase diagram of BZ, BT, and CT depicting the compositional range investigated. Color code for compositions is used throughout the work.

Powders were weighed using a balance with an accuracy of 0.0001 g (TE214S, Sartorius AG, Germany). Compositions of the BZT-BCT were selected taking into account representative phase diagrams proposed in the literature[194,333] with special emphasis on the phase convergence region and polymorphic phase boundaries. Compositions of the BNT-ST were selected to study the incipient piezoelectric response of the system. The optimized composition for actuator applications at moderate temperatures was found to be the BNT-0.25ST. Therefore, the research presented on this system is mostly limited to this composition. Selected batches of key compositions were

repeated 2 to 12 times. From each batch at least 16 sintered samples were produced for electromechanical characterization. From them, only samples with properties near the mean value of the batch were chosen for detailed experiments.

For the synthesis, 50 g of raw powders were filled into 400 ml home-made nylon milling containers. A total of 300 g Yttria stabilized zirconia balls (Mühlmeier GmbH & Co. KG, Germany) with diameters of 3 mm, 5 mm, and 10 mm with a ratio of 2:2:1 were added together with ethanol as solvent to promote mixing. The resulting ratio of powder:balls:ethanol was approximately 1:1:2. The suspensions were milled in a planetary ball mill (Pulverisette 5, Fritsch GmbH, Germany) for 5 h and 24 h with a rotational frequency of $^{25}/_{3}$ 1/s (250 r/min) for the BZT-BCT and BNT-ST, respectively. Afterwards, the suspensions were dried at 80 °C for 24 h (oven FT 6060, Thermo Scientific Heraeus GmbH, Germany). The resulting powders were calcined at 1300 °C and 850 °C (heating rate 5 °C/min) for 2 h for the BZT-BCT (oven HT10118, Nabertherm GmbH, Germany) and BNT-ST (oven L9/11/S27, Nabertherm GmbH, Germany), respectively. Subsequently, the powders were ball-milled again for 15 h and 24 h with a rotational frequency of $^{25}/_{3}$ 1/s (250 r/min) for the BZT-BCT and BNT-ST, respectively.

For the electrical characterization, XRD, and scanning electron microscopy (SEM) disc-shaped samples of 10 mm in diameter and 1 mm thickness (~ 0.30 g of powder) were compacted manually with uniaxial pressure (Figure 4.2 (a)). For neutron diffraction, bars of (30·3.5·3.5) mm (~ 3 g of powder) were compacted manually with uniaxial pressure (Figure 4.2 (b)). A balance with an accuracy of 0.01 g (SBC 51, Scaltec instruments GmbH, Germany) was employed to weigh the samples. For further compaction, all samples were processed using a cold isostatic press (KIP 100 E, Paul-Otto Weber GmbH, Germany) at 300 MPa for 1.5 min. The green bodies of BZT-BCT were sintered in covered crucibles with atmospheric powder of the same composition at 1500 °C (oven HT10118, Nabertherm GmbH, Germany) for 2 h (heating rate 5 °C/min). The BNT-ST samples were sintered at 1150 °C (oven L16/14, Nabertherm GmbH, Germany) with atmospheric powder of the same composition for 2 h, 5 h, 10 h, and 20 h (heating rate 5 °C/min). Unless stated, all results are presented for the samples sintered for 2 h. In order to minimize sample contamination, zirconia crucibles were used for the BZT-BCT and alumina crucibles for the BNT-ST.

For electrical characterization, disc-shape samples were ground in a semiautomatic machine (Phoenix 4000, Buehler GmbH, Germany) using grinding discs with grit sizes of 220, 600 and 1200 (MD Piano, Struers GmbH, Germany). Furthermore, they were manually ground with abrasive paper of grit size 2400 (P# 2400, Struers GmbH, Germany). Samples for neutron diffraction were ground by a semiautomatic grinding station (ZB 42T, Ziersch Fertigungstechnik GmbH & Co. KG, Germany). From the neutron diffraction samples, several 33 mode dynamic measurement bars of (2·2·5) mm (Figure 4.2 (c)) were cut by a diamond saw (4240, Well Diamond Wire Saws GmbH, Germany). Thicknesses of disc-shape samples were measured at three points by a Digimatic Indicator with an accuracy of 0.001 mm (ID-C112XB, Mitutoyo Corp., Japan). All other geometries were measured three times by a caliper with an accuracy of 0.01 mm (CD-15CPX, Mitutoyo Corp., Japan). The accuracy of all sample geometries was determined to be better than ± 0.02 %.

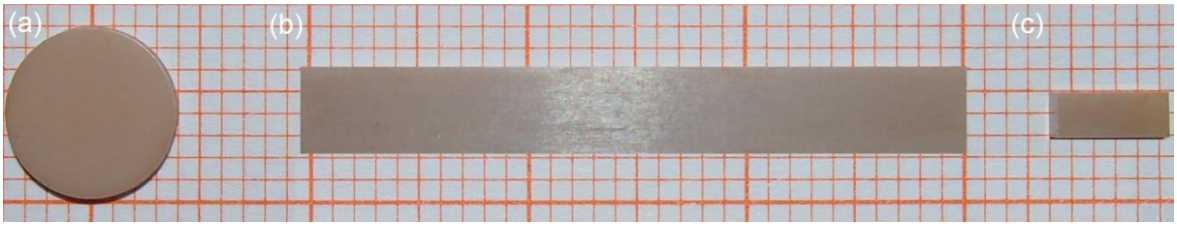

Figure 4.2: Sample geometries used in this work. (a) disc-shape sample used for electrical characterization, SEM, and XRD. (b) Neutron diffraction bars. (c) Dynamic measurement bars. Mesh size of 1 mm.

Samples for electrical characterization and electric field-dependent neutron diffraction were manually electroded with silver paste (C80415D5, Gwent Electronic Materials Ltd, United Kingdom). All samples were annealed at 400 °C for 2 h (heating rate 2 °C/min) prior to characterization (L9/11/S27, Nabertherm GmbH, Germany). The annealing procedure was employed to burn-in electrodes and minimize residual stresses, possibly introduced during machining. For comparison purposes commercial samples of soft PZT PIC 151 (PI Ceramic GmbH, Germay) were also characterized.

4.2 Structural Characterization

4.2.1 Atomic Characterization

4.2.1.1 X-Ray Diffraction

The XRD experiments were carried out on calcined powders and crushed sintered samples at room temperature. Crushed samples were annealed at 400 °C for 2 h (heating rate 2 °C/min) prior to characterization (L9/11/S27, Nabertherm GmbH, Germany). Experiments were performed in transmission geometry with a Guinier camera (G670, Huber GmbH, Germany) using Cu $K_{\alpha 1}$ radiation (λ = 1.54056 Å). The Cu $K_{\alpha 2}$ radiation was filtered using a curved Ge (111) monochromator. Powders were then placed inside a thin foil and measured in the angular range from 20° to 80° with a step size of 0.005° for both systems. Lattice parameters for both systems were obtained assuming pseudocubic unit cells by the least square intercept method.[379]

For the BNT-ST, a phase formation during calcination was also investigated. For this purpose, a homogenized stoichiometric mixture was prepared following the same experimental procedure described in Section 4.1. Subsequently, 2 g of the mixture were heated to 450 °C, 600 °C, 700 °C, and 850 °C (heating rate 5 °C/min) in a tube furnace (HTRH 100-300, Gero GmbH, Germany). Powders were subsequently quenched in air and analyzed in a Bragg-Brentano geometry D8 Advance diffractometer (Bruker Inc., Germany) with Cu K_{α} radiation (λ = 1.5406 Å) in the angular range from 20° to 80° with a step size of 0.02°. Experiments were performed by Mr. Jaud.

4.2.1.2 Neutron Diffraction

Neutron diffraction measurements were performed at the high-intensity diffractometer Wombat (Australian Nuclear Science and Technology Organization ANSTO, Sydney, Australia).[380] A schematic representation of the detector and sample disposition for the measurements are depicted in Figure 4.3 (a) and (b), respectively. Data were collected with a monochromator take-off angle of 90° using a wavelength of 2.41846(6) Å for high angular resolution. For each wavelength, a series of 12 complete diffraction patterns (detector angle from 30° to 150°) were collected with different orientations of the electric field with respect to the incident beam by moving the ω-sample table in 15° steps (-60° ≤ ω ≤ 120°). The experimental conditions allowed determining the relative orientation between the electric field vector and the scattering vectors of the individual reflections, as schematically displayed in Figure 4.3 (c). The orientation ω = 90° represents the electric field vector perpendicular to the incident beam. Experiments were performed by beam scientists and Dr. Hinterstein.

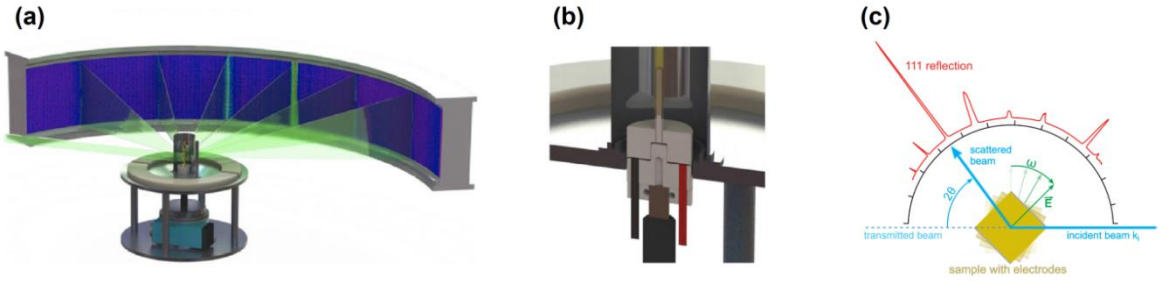

Figure 4.3: Schematic representation of the neutron diffraction experimental line. (a) Curved position-sensitive detector, (b) disposition of neutron diffraction bars, and (c) detector displaying the electric field vector E, scattered beam at an angle 2θ, and sample orientation ω. Modified from Refs.[147,381]

4.2.2 Microstructural Characterization

4.2.2.1 Scanning and Transmission Electron Microscopy

Sintered samples were polished with diamond paste (DP-Paste, Struers GmbH, Germany) of 15 µm, 6 µm, 3 µm, 1 µm, and ¼ µm (polishing discs MD Dur/Nap, Struers GmbH, Germany). SEM imaging was performed using a JSM 7600F (JEOL Ltd., Japan). Images were taken with the back scattered electron (BSE) mode at low acceleration voltages. Orientational contrast imaging was optimized at 8 kV to enhance material (Z) and grain contrasts. Experiments were performed together with Mrs. Kunz. Mean grain size was determined by considering approximately 200 grains from several micrographs. The linear interception method with a numerical multiplication factor of 1.56 was applied for the grain size calculation by assuming isometric grain shape.[382] Moreover, the core-shell microstructure of BNT-ST was quantified by a density of cores. The density of cores was defined as

the numbers of cores divided by area. Several images, taken from different positions of the sample surface, were analyzed representing a total of ~ 2500 µm^2. Energy-dispersive X-ray spectroscopy (EDS) was used to estimate the statistical composition of cores and shells. For this purpose a NCA Energy 350 EDS (Oxford Instruments plc, United Kingdom) was employed with an incident beam of 15 kV to collect spectra in the energy range between 0.50 keV and 9 keV.

TEM samples were ultrasonically cut from disc samples (Figure 4.2 (a)) into smaller discs of 3 mm in diameter by an ultrasonic cutter (Gatan 601, Gatan Inc., United States). A semiautomatic machine was used for grinding the samples between 100 µm and 200 µm with same experimental conditions as described in the previous paragraph (Allied Multiprep Polishing System, Allied High Tech Products Inc., United States). Polished samples were dimpled to a final thickness between 10 µm and 20 µm in a dimple grinder (Gatan 656, Gatan Inc., United States). Samples were annealed at 400 °C for 2 h to minimize residual stresses possibly introduced during machining. Subsequently, samples were perforated on both sides by Ar ion milling using a Dual Ion Mill unit (Gatan 600, Gatan Inc., United States). Initially milling was performed at 5 kV and 16° incidence angle, followed by 4 kV and 12° incidence angle. Prior to characterization, samples were coated with carbon in order to minimize charging under the incident electron beam. Experiments were carried out using a 2100F TEM (JEOL Ltd., Japan) operated at 200 kV and a Be double-tilt holder (EM-31640, Gatan Inc., United States). For EDS mapping in scanning transmission electron microscopy (STEM) mode, the second smallest condenser aperture C2 and an electron probe size of 1 nm with a camera length of 0.80 m were employed. The specimen was tilted by an angle of 10° to maximize the X-ray collection of the detector in the energy range from 0 keV to 20 keV. *In situ* hot-stage experiments were performed with a double-tilt heating holder (Gatan 652, Gatan Inc., United States) equipped with a SmartSet Hot-Stage Controller (Gatan 901, Gatan Inc., United States). The bright field (BF) and dark field (DF) micrographs and selected area diffraction (SAED) patterns were recorded at 165 °C, 245 °C, and 345 °C with an uncertainty of ± 20 °C. To assure isothermal conditions, temperature was held for 30 min prior to each measurement. Experiments were performed by M. Sc. Scherrer and Dr. Molina-Luna.

4.2.2.2 Density

The Archimedes method was employed for density measurements of 2 to 3 sintered samples of each composition. Initially as-sintered disc samples (Figure 4.2 (a)) were dried for 24 h at 100 °C. Thereafter, their dry weight (DW) was measured (BA110S Basic, Sartorius AG, Germany). Samples were put in distilled water and into a vacuum chamber (RD8, Vacuubrand GmbH, Germany) at a pressure of 50 mbar for 1 h. The samples were weighed in water (saturated weight in water (SWW)) and dried with a clean paper. Subsequently, they were weighed again (saturated weight in air (SWA)). The absolute density of each sample (δ_S) was calculated taking into account the Archimedes principle (Equation 4.1) and the density of the water at the measurement temperature.

$$\delta_S = \frac{\delta_{H_2O} \cdot DW}{SWA - SWW} \qquad \textbf{Equation 4.1.}$$

The theoretical density δ_t of the samples was calculated by considering the mass and volume of unit cells. Assumption of pseudocubic lattice parameters was performed, as described in Section 4.2.1.1. The relative density δ_r was calculated with Equation 4.2.

$$\delta_r = \frac{\delta_s}{\delta_t} \qquad \textbf{Equation 4.2.}$$

Results of the Archimedes method were contrasted with analysis of the surface area of micrographs. BSE micrographs of the polished surfaces described in Section 4.2.2.1 were transformed to binary colors with GIMP software (GNU Image Manipulation Software version 2.8.10, United States). Afterwards, binary images were analyzed with the ImageJ software (National Institutes of Health version 1.48v) to obtain the fraction of porosity and material. A total area of ~2500 µm^2 was analyzed in several images at different position of the sample surface to obtain representative results. The ratio between porosity and material was considered as the δ_r. Both analyses gave comparable values within measurement errors.

4.3 Thermal Analysis

In order to investigate the calcination process of BNT-ST a homogenized stoichiometric mixture of the chemical reagents was loaded into a thermogravimetric (TGA)/differential thermal analysis (DTA) STA 449C analyzer (Jupiter, Netzsch-Gerätebau GmbH, Germany). The device is coupled to a Fourier transform infrared spectrometer (FT-IR) (Tensor 27, Bruker Optik GmbH, Germany). Powder was heated in air up to 1000 °C (heating rate 5 °C/min). The spectrometer was used to analyze the outgassing species. The IR spectra were recorded during the heating process. The detected IR bands for the outgassing species were integrated and plotted versus temperature. Experiments were performed by Dipl.-Ing. Fasel.

4.4 Electrical Characterization

Poling and large signal characterization methods throughout this section were performed in silicon oil (AK 35 for room temperature and AK 200 for high temperatures, Wacker Chemie AG, Germany) to avoid electric breakdown of air, which is around 3 kV/mm.[383]

4.4.1 Temperature- and Frequency-Dependent Dielectric Properties

Temperature- and frequency-dependent real $\varepsilon_r^{'}$ and imaginary $\varepsilon_r^{''}$ relative permittivity values were obtained on poled and unpoled samples. The dielectric properties of BZT-BCT were measured in the temperature range from - 100 °C to 120 °C with a heating rate of 2 °C/min and in the frequency range from 100 Hz to 10 kHz. An Impedance analyzer Alpha-A equipped with a cryostat (Novocontrol Technologies GmbH & Co. KG, Germany) was employed for the measurements. For the BNT-ST high temperature dielectric properties were tested to evaluate the presence of dielectric relaxations prototypical of relaxors. For this purpose $\varepsilon_r^{'}$ and $\varepsilon_r^{''}$ values were measured in the temperature range from 25 °C to 500 °C with a heating rate of 2 °C/min and in the frequency range from 1 kHz up to 1 MHz. A Precision LCR Meter 4192A (Hewlett Packard Corp., United States) was used for the measurements. In order to depict dielectric relaxations, low temperature frequency-dependent real $\varepsilon_r^{'}$ and imaginary $\varepsilon_r^{''}$ relative permittivity were measured with a cooling rate of 1 °C/min and in the frequency range from 10 mHz to 1 MHz (Impedance analyzer Alpha-A equipped with a cryostat, Novocontrol Technologies GmbH & Co. KG, Germany). The temperature range selected for BZT-BCT was between - 100 °C to 120 °C, whereas for BNT-ST was from 300 °C to - 150 °C. The amplitude of the probing ac electric signal was 0.002 kV/mm peak to peak for all experiments.

4.4.2 Small Signal Properties

Prior to zero bias-field small signal measurements, all BZT-BCT samples were poled for 10 min at room temperature with an electric field of 4 kV/mm (HCN35-35000, Fug GmbH, Germany). Poling conditions were selected based on results from Wu *et al.*[314] Moreover, d_{33} was always tested in a commercial Berlincourt meter (YE2730, Sinocera Inc., China) before performing further measurements in other setups.

The incipient piezoelectric BNT-0.25ST features an almost negligible $d_{33} \sim 10$ pC/N. Therefore, most of the small signal investigations were performed solely on the BZT-BCT, with the exception of bias-field-dependent measurements that were also done in BNT-0.25ST.

4.4.2.1 Temperature-Dependent Quasi-Static Characterization

In situ d_{33} of BZT-BCT as a function of temperature was measured using a custom-designed device, which consists of a furnace controlled by two thermocouples and a laser vibrometer (sensor head OFV-505 and front-end VDD-E-600, Polytec GmbH, Germany). A pinhole was made in the middle of a thermally insulating alumina covering lid, thereby allowing the laser to pass through. Further details on the device are presented elsewhere.[384] All compositions were measured in the temperature range from 25 °C to 105 °C with a heating rate of 2 °C/min in 5 °C steps. A sinusoidal wave of 0.01 kV/mm amplitude and a frequency of 10 kHz was chosen as input voltage (function generator HM8131-2, Hameg GmbH, Germany).

4.4.2.2 Electric Field- and Temperature-Dependent Quasi-Static Characterization

Electric field-dependent characterization was performed in BZT-BCT and BNT-ST in their respective operational ranges. A sinusoidal waveform of 1 kHz and 0.02 kV/mm modulated a triangular base waveform of 3 kV/mm and 4 kV/mm with a frequency of 0.05 Hz for the BZT-BCT and BNT-ST, respectively. The waveforms used as input signals are represented in Figure 4.4.

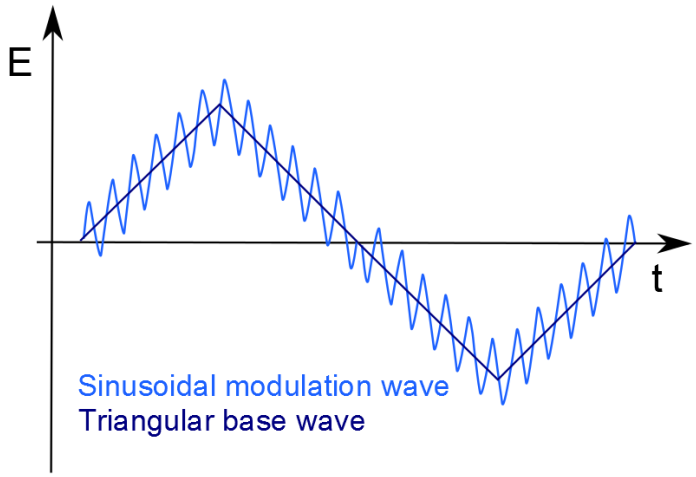

Figure 4.4: Scheme of input signal for bias-field-dependent small signal properties.

From these measurements $\varepsilon_r^{'}$, $\varepsilon_r^{''}$, and d_{33} were obtained as a function of bias-field. Measurements were performed from 25 °C to 105 °C in 10 °C steps for BZT-BCT, whereas for BNT-ST measurements were done at 25 °C, 50 °C, 80 °C, 110°C, 135 °C, and 170 °C. Prior to each measurement the temperature was stabilized within ± 0.2 °C in order to satisfy isothermal conditions. A commercial piezoelectric system TF analyzer 2000 (aixACCT Systems GmbH, Germany) was employed for the electromechanical characterization.

4.4.2.3 Dynamic Characterization

Impedance measurements were performed in the 33 mode in order to calculate dielectric, electromechanical, and elastic properties such as relative permittivity $\varepsilon_{33}^{\mathrm{T}}/\varepsilon_0$, d_{33}, k_{33}, mechanical quality factor Q_m, elastic compliances s_{33}^D and s_{33}^E, and frequency constant N_{33}. The procedure used to calculate all properties is given in Appendix II. Complex impedance measurements were carried out in all samples by the resonance-antiresonance method using an impedance analyzer (HP4294A, Hewlett Packard Corp., United States). A 0.00025 kV/mm peak to peak sinusoidal wave in the kHz range (corresponding to the resonance-antiresonance region of each sample) was used as input voltage. Data was recorded every 125 Hz to assure the proper detection of extrema. *In situ* temperature-dependent measurements were performed from 25 °C to 105 °C in 5 °C steps. Prior to each measurement the temperature was stabilized within ± 0.2 °C in order to satisfy thermal equilibrium conditions. All described properties were obtained according to the IEEE standard on

piezoelectricity.[385] The phase angle θ and free capacitance C^T at 1 kHz at each isotherm were also recorded.

4.4.3 Temperature- and Frequency-Dependent Quasi-Static Large Signal Properties

Room temperature large signal polarization measurements were performed in a Sawyer-Tower setup, as schematically represented in Figure 4.5.

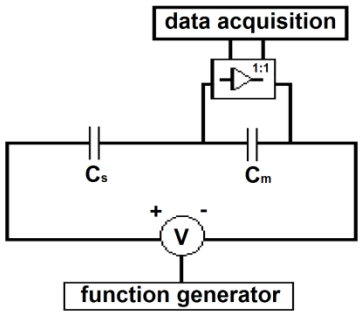

Figure 4.5: Schematic view of voltage supply, Sawyer-Tower circuit, and acquisition systems.

A sample with a capacitance C_s (on the order nF) was connected in series with a measurement capacitor C_m. To minimize the voltage drop U_m at the measurement capacitor, the condition $C_m \gg C_s$ was satisfied with difference in the capacitance values of more than 3 orders of magnitude. The measurement capacitor was C_m = 10 µF. This condition assures that U_m remains below 1 % of the voltage drop at the sample U_s.[38] The charge Q of the measurement capacitor is equivalent to the samples' charge since both capacitors are in series (Equation 4.3). A function generator (33220A, Agilent Technologies Inc., United States) was employed to provide an input signal to a high voltage supply (High Voltage Amplifier 20/20C, Trek Inc., United States). Triangular waves of 3 kV/mm and 4kV/mm with frequencies between 0.05 Hz and 50 Hz were chosen as input signals for the measurements of BZT-BCT and BNT-ST, respectively. Data acquisition was performed via an oscilloscope (MSO7014B, Agilent Technologies Inc., United States). The polarization was calculated using Equation 4.4.

$$Q = C_s \cdot U_s = C_m \cdot U_m \qquad \textbf{Equation 4.3,}$$

$$P = \frac{C_m \cdot U_m}{A} \qquad \textbf{Equation 4.4,}$$

where A is the area of the sample.

The strain was measured by an optical sensor (D63, Philtec Inc., United States) simultaneously as the polarization. Electrical contact to the sample was performed by two adjustable point contacts.

For pulse experiments, a direct voltage source DIGI 40 (Conrad Electronic SE, Germany) was used to charge a home-made fast switching device (150 ns discharge time) based on a fast high voltage transistor switch HTS-41-03-GSM (Behlke Power Electronics GmbH, Germany). The input signal chosen was a rectangular shape of 10 s duration and amplitude ranging from 1.5 kV/mm to 4 kV/mm. Large signal polarization and strain as a function of temperature and frequency were obtained using a commercial piezoelectric system TF analyzer 200 (aixACCT Systems GmbH, Germany). Triangular waves of 3 kV/mm and 4 kV/mm with frequencies ranging from 0.5 Hz to 20 Hz were chosen as input signals for the measurements of BZT-BCT and BNT-ST, respectively. The BZT-BCT samples were measured in the temperature range between 25 °C and 120 °C with 10 °C steps, whereas the BNT-ST was measured at 25 °C, 50 °C, 80 °C, 110°C, 135 °C, and 170 °C. Prior to each measurement the temperature was stabilized within ± 0.2 °C in order to satisfy thermal equilibrium conditions.

The random error in the large and small signal electromechanical measurements is on the order of 20 nm, which leads to an uncertainty on the order of 5 %. The random error in the polarization measurements is on the order of 1 %. In case that error bars are omitted, the reader should consider that data markers were selected deliberately in the same length-scale as experimental errors.

5 Results and Discussions

5.1 The (1-x)Ba($Zr_{0.2}Ti_{0.8}$)O_3-x($Ba_{0.7}Ca_{0.3}$)TiO_3 System

5.1.1 Atomic Characterization

Figure 5.1 introduces the XRD patterns of BZT-BCT calcined powders at 1300 °C. All diffractograms can be ascribed to a perovskite structure with secondary phases marked with *. Indexing throughout this work was performed based on a primitive cubic prototype, with pc denoting pseudocubic Miller indices. All XRD experiments of BZT-BCT were carried out using a monochromator to filter out Cu $K_{\alpha 2}$ radiation in order to allow a clearer distinction of reflection splitting due to non-cubic distortions. Due to the considerable amount of secondary phases present in the calcined powders, phase analysis of BZT-BCT was performed in the XRD patterns of the sintered samples.

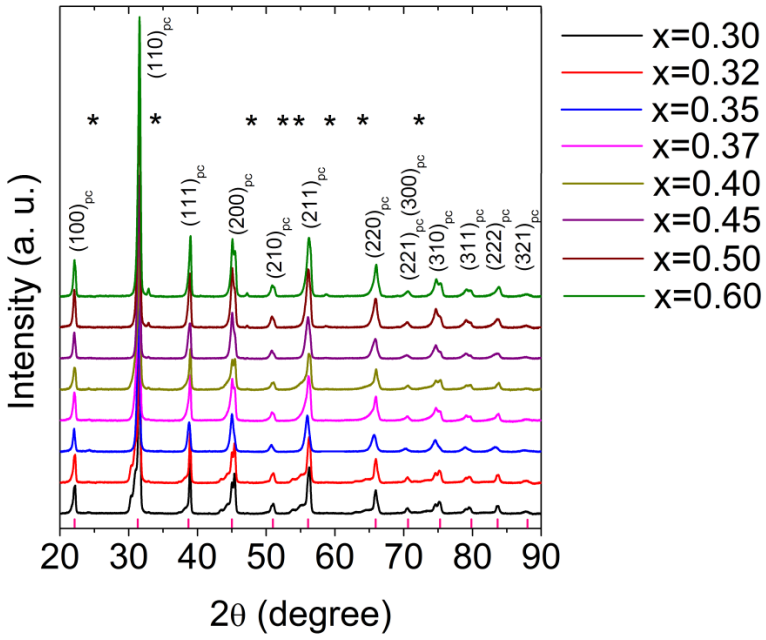

Figure 5.1: (a) XRD of BZT-BCT calcined powders. The * symbols indicate secondary phases corresponding to $Ba_6Ti_{17}O_{40}$, according to crystallographic powder diffraction card 01-077-1566. Primary phase peaks are marked with the corresponding planes of the primitive cubic prototype.

In order to identify the secondary phase/s, the XRD patterns were compared to powder diffraction cards of Ba_2TiO_4 (00-035-0813), $BaTi_2O_5$ (01-070-1188), and $Ba_6Ti_{17}O_{40}$ (01-077-1566). The main reflection of $Ba_6Ti_{17}O_{40}$ is located at 32.34°, followed in intensity by reflections located at 21.31°,

23.85°, and 42.77°. In proximity to all these angles, secondary peaks were observed in Figure 5.1. This indicates the presence of $Ba_6Ti_{17}O_{40}$ in the BZT-BCT calcined powders, as previously reported in the literature.[308,386] It was observed that formation of $Ba_6Ti_{17}O_{40}$ in BZT-BCT is correlated to the ratio of A/B stoichiometry.[386] The binary phase diagram between BaO and TiO_2 indicates that small deviations from the stoichiometry in BT (*e.g.* 0.9834 at. % Ti excess and 1.0051 at. % Ba excess at 1200 °C) results in the formation of Ba_2TiO_4, $BaTi_2O_5$, and/or $Ba_6Ti_{17}O_{40}$ above 1150 °C.[387-389] The Ba_2TiO_4 phase is commonly found in BT-based materials since it is an intermediary phase during the formation of BT. If the TiO_2 content is deficient, this phase will remain stable at room temperature after sintering.[306,389] The $BaTi_2O_5$ is generally observed in quenched materials due to a fast nucleation rate, while $Ba_6Ti_{17}O_{40}$ is characteristic of furnace-cooled (~ 5 °C/min) materials. The latter two phases are common features of BT-based materials with a deficiency in BaO content.[306,389] Therefore, it is expected that the slow cooling rate of the calcined powders below 5 °C/min limited the formation of $BaTi_2O_5$[389] and that any intermediary Ba_2TiO_4 phase reacted upon cooling, leading to BZT-BCT or other BT-based phases such as $Ba_6Ti_{17}O_{40}$ that was observed in the powders.

Figure 5.2 (a) provides the XRD patterns of BZT-BCT samples sintered at 1500 °C, subsequently crushed, and annealed at 400 °C. The material exhibits a perovskite structure without second phases within the detection limit of the employed instrument, indicating that $Ba_6Ti_{17}O_{40}$ was not stable during the sintering process.

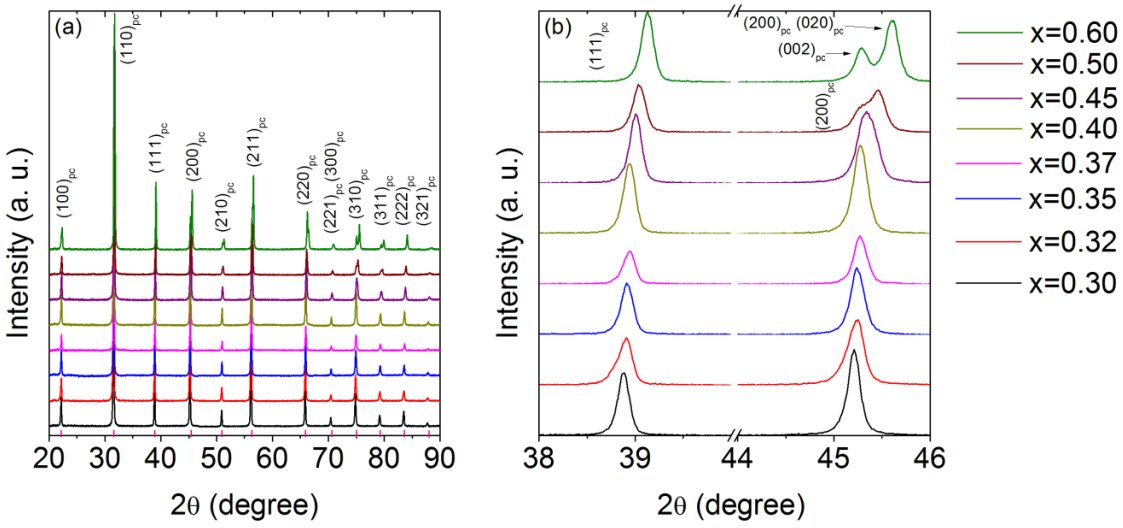

Figure 5.2: (a) XRD of BZT-BCT sintered samples and (b) close-up region from 38° to 46°. Primary phase peaks are marked with the corresponding planes of the primitive cubic prototype.

Figure 5.2 (b) displays a magnification of the region between 38° and 46° to emphasize the peak splitting in the $(111)_{pc}$ due to the presence of R and/or O phases. The $(200)_{pc}$ reflection is also highlighted in this range and allows for observation of peak splitting in the case of an O and/or T

phase. The gradual shift of the $(111)_{pc}$ and $(200)_{pc}$ reflections to higher 2θ angles indicates a decreased lattice parameter with increasing BCT content. The reduction of the lattice parameter can be attributed to a decrease of 1.53 % in the average A-site ionic radius with increasing BCT content that is not compensated by the increase of the average B-site ionic radius of 0.16 % (in the compositional range between BZT-0.30BCT and BZT-0.60BCT). For $x < 0.37$, asymmetries in the left side of the $(111)_{pc}$ reflection indicate R and/or O phase, although literature reports suggest a R phase in this compositional range.[333] However, no clear peak splitting is observed, which is ascribed to small non-cubic distortions. Note that a clear splitting of the $(222)_{pc}$ was also not observable. For BZT-0.50BCT a distortion of the $(200)_{pc}$ reflection becomes apparent, which can be either attributed to the presence of O and/or T phase. The $(200)_{pc}$ reflection for BZT-0.60BCT is even more clearly split. Since neither the $(111)_{pc}$ nor the $(222)_{pc}$ peaks display splitting, it can be suggested that BZT-0.50BCT and BZT-0.60BCT feature a T phase. The higher lattice distortion of the T phase was previously reported in the literature.[328] The intensity ratio of the $(002)_T$ (where T subscript denotes tetragonal Miller indices) reflection is 1.8:1 with respect to the $(200, 020)_T$ peaks, which is near the 2:1 intensity ratio expected for a randomly oriented T phase. Although analysis of full-width half maxima of $(200)_{pc}$ and $(222)_{pc}$ as a function of composition were performed, no tendencies were observed. The trend of a T phase for high BCT contents is in agreement with the crystal structures reported in the literature.[329,333,348]

5.1.2 Microstructure Characterization

In the subsequent sections of the BZT-BCT study, only results for BZT-0.30BCT, BZT-0.40BCT, and BZT-0.45BCT will be provided. These compositions were chosen since they display features representative of the entire range of compositions. Figures intended for data analysis will depict results of all compositions investigated. Figure 5.3 introduces the as-polished sintered surface of the BZT-0.30BCT, BZT-0.40BCT, and BZT-0.45BCT samples.

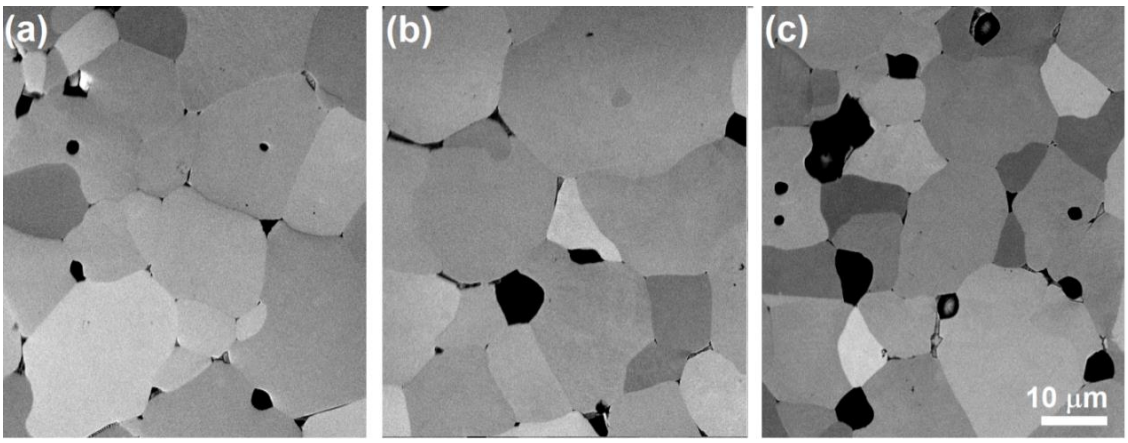

Figure 5.3: As-sintered, polished surface of (a) BZT-0.30BCT, (b) BZT-0.40BCT, and (c) BZT-0.45BCT. The image was taken with a SEM in the BSE mode.

The different contrast in Figure 5.3 is a direct consequence of the various grain orientations. The relative density and average grain size results are provided in Table 5.1 for all compositions. All materials are characterized by coarse and small round-shaped (the latter with much lower content) grains with intragranular and intergranular porosity. This morphology may be attributed to the presence of a liquid phase during sintering[390], ascribed to the eutectic point that $Ba_6Ti_{17}O_{40}$ forms with BT at ~ 1320 °C.[387-389] Liquid phase sintering could explain the presence of intragranular porosity in coarse grains, as it was reported that intragranular porosity requires fast mobility of grain boundaries above the pore shrinkage rate.[391] A detailed sintering study would be required to corroborate the aforementioned hypothesis, which is out of the scope of this work. The technological relevance of such a study is justified, however, considering that variations of $Ba_6Ti_{17}O_{40}$ content led to changes in T_C of ~ 8 °C, as well as in ε_r' and ε_r'' of ~ 15 %.[386] In contrast to previous works, secondary phases at the grain boundaries and/or triple junctions were not observed by SEM in BSE mode.[386] This result is in agreement with the XRD study of the sintered samples (Figure 5.2).

Table 5.1: Average grain size and relative density of the sintered BZT-BCT samples.

Composition	Average grain size (μm)	Relative density (%)
BZT-0.30BCT	28 ± 7	98
BZT-0.32BCT	20 ± 3	98
BZT-0.35BCT	36 ± 8	94
BZT-0.37BCT	28 ± 8	97
BZT-0.40BCT	25 ± 5	98
BZT-0.45BCT	36 ± 9	97
BZT-0.50BCT	35 ± 8	97
BZT-0.60BCT	26 ± 6	98

All compositions are characterized by relative densities above 94 %. Grain size varies non-monotonically between (20 ± 3) μm for BZT-0.32BCT and (36 ± 9) μm for BZT-0.45BCT, which is comparable to previous reports.[314] Hao *et al.*[200] reported that samples with relative densities above 94 % and grain sizes higher than 20 μm feature stable functional properties. Therefore, the deviations of the relative density and grain size are not expected to influence the functional properties considerably and will not be discussed further.

5.1.3 Electrical Characterization

5.1.3.1 Temperature- and Frequency-Dependent Dielectric Properties

The dielectric response of ferroelectrics depends on the crystal structure.[42] Therefore, measuring the dielectric properties of a system constitutes a powerful characterization method for elucidating phase instabilities. Figure 5.4 provides the $\varepsilon_r^{'}$ and $\varepsilon_r^{''}$ as a function of temperature at various frequencies for unpoled (solid line) and poled (dotted line) states. The local maxima (obtained from $\varepsilon_r^{''}$ at 1 kHz and marked with dashed lines) increase in magnitude with reducing frequency. A close inspection indicates that the high temperature local maxima slightly shift with frequency and may indicate weak relaxor properties, as was previously reported.[115,116,334] Further details on the frequency dependence of the dielectric properties are given in Appendix III.

The magnitude of $\varepsilon_r^{'}$ and $\varepsilon_r^{''}$ is determined by the polarization mechanisms treated in Section 2.1. For ferroelectrics, the most relevant mechanisms at moderate frequencies (kHz range) are the ionic polarization, orientational polarization, and reversible domain switching.[346] Nonetheless, reversible domain switching of non-180° domain walls has been generally recognized as the main contributions.[63,203,204,392] The reduction of the $\varepsilon_r^{'}$ magnitude with poling procedure may be attributed to a diminished density of domain walls.[63] The differences of $\varepsilon_r^{'}$ between poled and unpoled states above T_C can be attributed to the presence of domains, which gives further indication of weak relaxor features. *In situ* temperature-dependent TEM previously demonstrated the persistence of domains above T_C.[347]

At temperatures corresponding to phase transitions, all of the polarization contributions mentioned in the previous paragraph should reach maximized values. The intrinsic ionic and orientational polarization contributions are enhanced due to either the transverse or longitudinal instability of P_s^i, while the extrinsic domain contribution is normally maximized due to elastic softening as reported for BZT-BCT.[318,348] Therefore, the maxima observed in the temperature profiles of $\varepsilon_r^{'}$ are considered to indicate phase transitions.[42] Since the extrinsic contributions are inherently lossy[393,394], the local maxima of $\varepsilon_r^{'}$ are correlated to the local maxima of $\varepsilon_r^{''}$. Therefore, the $\varepsilon_r^{''}$ local maxima observed at 1 kHz can be used to determine phase transitions, as previously suggested.[109] As an approximation, the high temperature anomaly of the system is considered as T_C since a considerable thermal depolarization occurs at this temperature, as it will become apparent in subsequent sections.

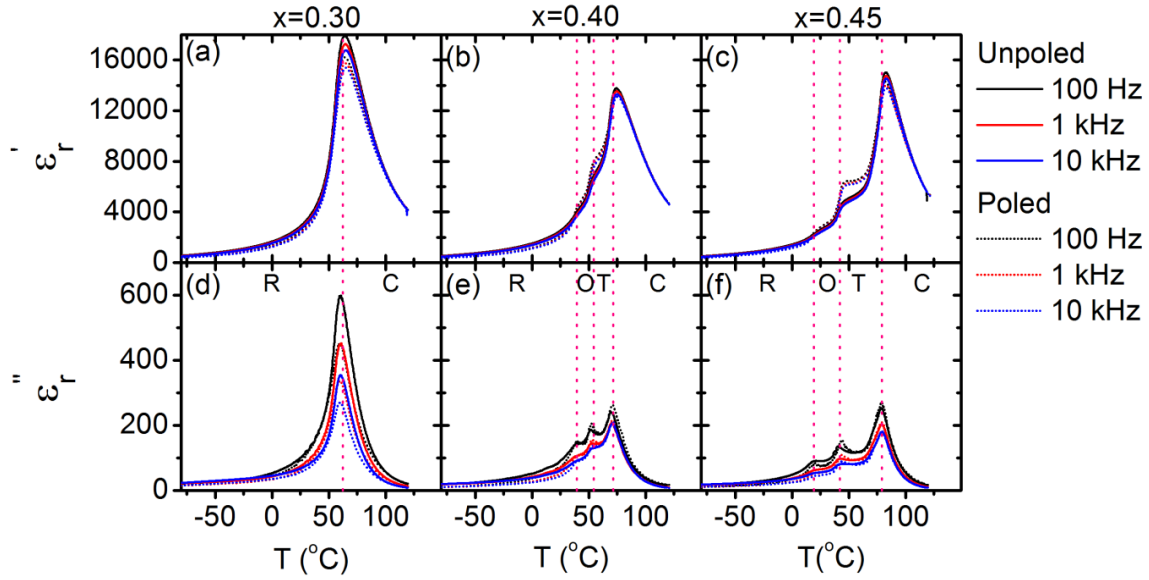

Figure 5.4: Temperature- and frequency-dependent ε_r' of representative compositions measured on heating. The unpoled state is depicted with solid lines, while the poled state is displayed with dotted lines. The local maxima of the ε_r'' curves at 1 kHz used to determine phase transition are marked with purple dotted lines.

Based on the curves from all compositions, a pseudo-binary phase diagram can be constructed (Figure 5.5). Open symbols indicate phase transitions of poled samples, while solid symbols are used to mark the phase transitions of virgin samples. Only slight modifications of the phase boundaries are depicted due to the room temperature poling procedure used. Small deviations of the phase transition temperatures between poled and virgin states may be attributed to changes in the domain configurations and the interaction of domains with point defects. The pseudo-binary phase diagram coincides, within experimental errors, with the diagram proposed by Keeble *et al.*[333], although the synthesis route and characterization techniques used to detect phase transitions differed. Therefore, phase assignment was performed following the work of Keeble at al.[333] Qualitative agreement with other diagrams found in the literature was also observed.[323,341] The O phase is separated from R and T phases by two PPBs. Note that the transition from O to T phase in BZT-0.37BCT could not be determined due to the close proximity of several phase boundaries. Therefore, the yellow shaded region displayed between BZT-0.35BCT and BZT-0.37BCT at temperatures between 55 °C and 65 °C is termed a convergence region.[333] Liu and Ren[194] proposed the existence of a tricritical point near the convergence region. Criticality was proposed due to the reduced dielectric thermal hysteresis, although non-zero hysteresis was actually reported. In agreement with previous reports a maximum $\varepsilon_r' \sim 17{,}000$ was found for BZT-0.30BCT at 60 °C[194], which is near the proposed convergence region.

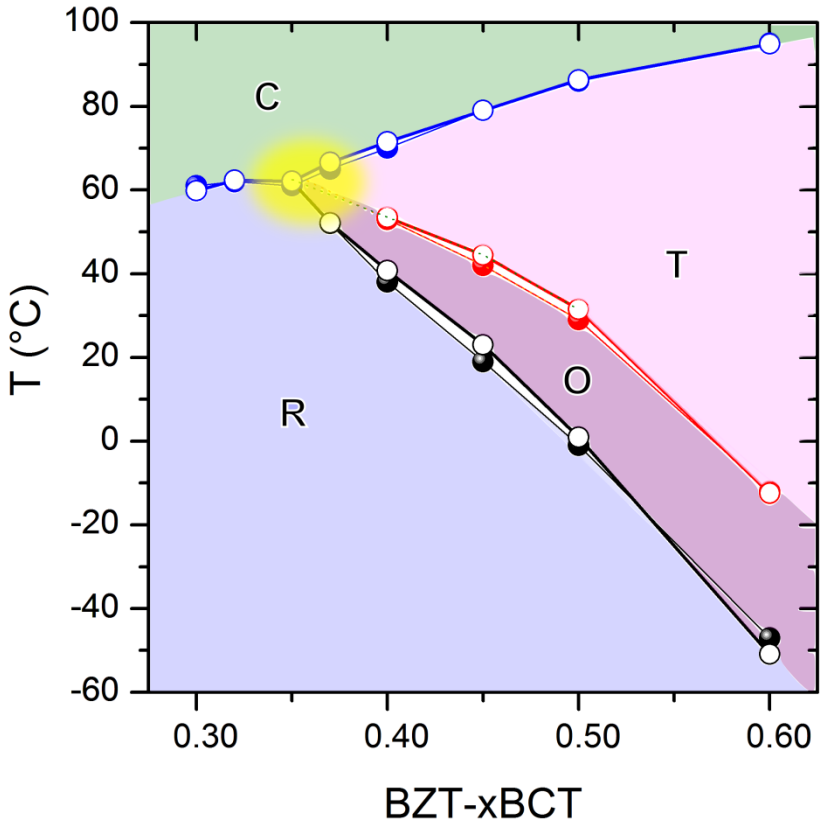

Figure 5.5: Pseudo-binary phase diagram obtained from dielectric anomalies of $\varepsilon_r^{''}$ at 1 kHz. Open symbols depict the phase boundaries after room temperature poling, while solid symbols are used to indicate phase transitions in the virgin state. The yellow shaded area indicates the phase convergence region that was hard to access and evaluate experimentally. R: rhombohedral phase, O: orthorhombic phase, T: tetragonal phase, C: cubic phase.

It should be pointed out that the statement by Keeble *et al.*[333] "…Gibbs phase rule prohibits a single four-phase invariant point in a pseudo-binary phase diagram…" casts doubts since single four-phase invariant points are not forbidden in system with a "pseudo-binary phase diagram". For systems in thermodynamic equilibrium, the Gibbs phase rule[48] states that the chemical potential of each constituent in every phase is identical. Equation 5.1 expresses the Gibbs phase rule at constant pressure.

$$Ph + Fr = Co + 1 \qquad \textbf{Equation 5.1,}$$

where Co: components, Ph: phases under equilibrium conditions, and Fr: degrees of freedom. A degree of freedom indicates an intensive thermodynamic variable of a component such as temperature or composition. For the case of a ternary system such as the BZT-BCT between the end members BZ, BT, and CT; the components $Co = 3$. In the case of a quadruple point ($Ph = 4$)

there is no degree of freedom left ($Fr = 0$). Therefore, four phases can coexist in an invariant quadruple point in BZT-BCT under thermodynamic equilibrium. Recently, Landau theory phenomenological calculations were employed to estimate the pseudo-binary phase diagram of BZT-BCT.[156] Qualitative agreement to the diagram displayed in Figure 5.5 was observed, although this approach suggested that the convergence region may consist of two triple points with close proximity to each other.

5.1.3.2 Small Signal Properties

Figure 5.6 displays the room temperature small signal quasi-static d_{33} as a function of composition. Phase transitions obtained from dielectric measurements are marked with dashed lines. This representation for phase transitions derived from dielectric measurements is used for all subsequent figures and is not further indicated.

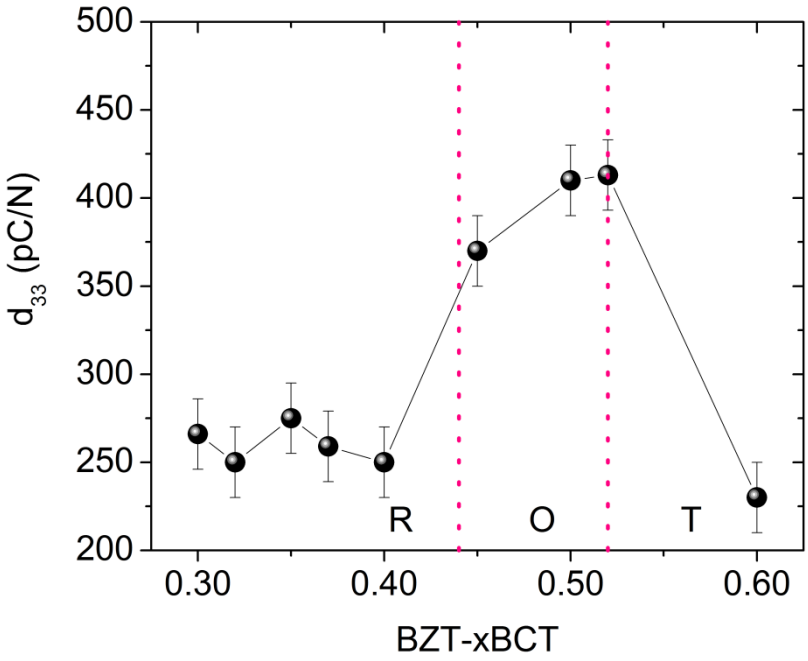

Figure 5.6: Room temperature d_{33} as a function of composition. Dotted lines indicate phase transitions obtained from dielectric properties. Note that BZT-0.52BCT was added in the d_{33} plot to visualize the PPBs effect on the electromechanical properties.

Figure 5.6 resembles the room temperature measurement of d_{33} from Zhang *et al.*[322] introduced in Figure 3.6 (b). Differences of ~ 10 % in the d_{33} values reported can be attributed to variations in processing and poling conditions. Wu *et al.*[314] reported that changes in d_{33} values of up to 500 % can be obtained if the poling field is varied between 0.5 kV/mm and 4 kV/mm at room temperature. The highest d_{33} values are observed around both PPBs. The composition close to the O to T PPB displays a d_{33} = 410 pC/N, which is 15 % higher than the d_{33} at the R to O PPB. The

compositions far from phase boundaries fall within a range of 230 pC/N < d_{33} < 260 pC/N. The R phase features on average 15 % higher d_{33} values than the T phase.

5.1.3.2.1 Temperature-Dependent Quasi-Static Small Signal Properties

In situ small signal quasi-static d_{33} was measured as a function of temperature and the resulting curves are displayed in Figure 5.7. All phase transitions in the system are again accompanied by local maxima in d_{33}. Maximized d_{33} values are not observed at T_C for all compositions but only for x < 0.40. For the range of 0.40 < x < 0.50, d_{33} is maximized at the O to T PPB, as observed in the room temperature measurement in Figure 5.6. A maximum d_{33} = 592 pC/N is found for BZT-0.45BZT at 45 °C, corresponding to the O to T phase boundary. The R and O phases display considerable temperature sensitivity in their d_{33} values. Meanwhile, the T phase BZT-0.60BCT exhibits an almost temperature insensitive d_{33} ~ 300 pC/N in the temperature range between 25 °C and 95 °C. It should be pointed out that all compositions feature residual piezoelectricity with values of d_{33} ~ 100 pC/N even up to 10 °C above their T_C.

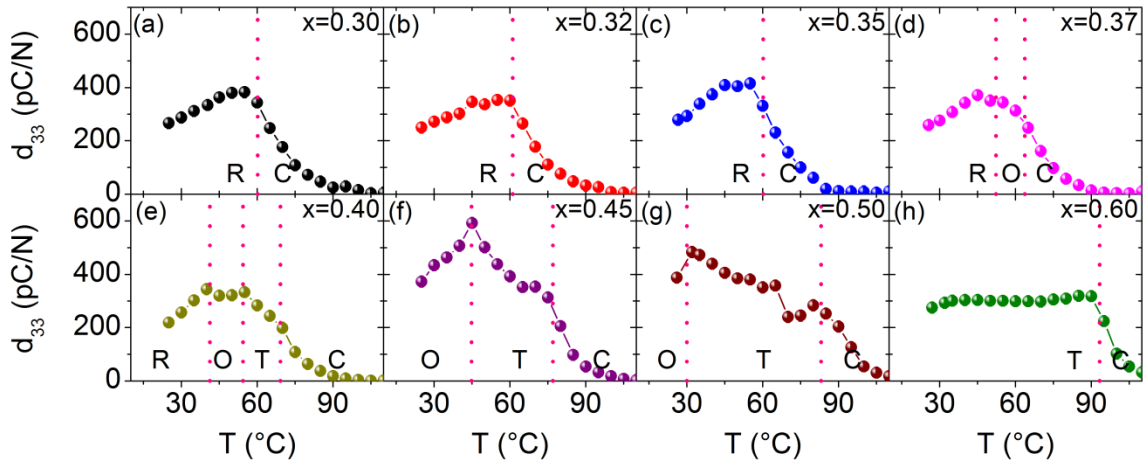

Figure 5.7: *In situ* d_{33} as a function of temperature.

In order to visualize the relationship between phase boundaries and d_{33}, the curves displayed in Figure 5.7 were combined to produce a contour plot of d_{33} as a function of temperature and composition (Figure 5.8). The phase transitions identified from the dielectric properties are superimposed in white from now on in all subsequent contour plots throughout the BZT-BCT results section and they are not further indicated. The variation of properties between the measured points in all contour plots was estimated by linear interpolation between the recorded data. Figure 5.8 reveals that the overall highest piezoelectric response of the BZT-BCT system occurs along the O to T PPB, which is consistent with literature of BZT-BCT[395,396] and literature of other BT-based materials.[342] It is also noted that the d_{33} exhibits local maxima near the O to R PPB and convergence region, but overall, these d_{33} values are not as high as at the O to T PPB. Values

of d_{33} at the R to O phase boundary and in the convergence region are found to be 30 % lower than the values at the O to T PPB.

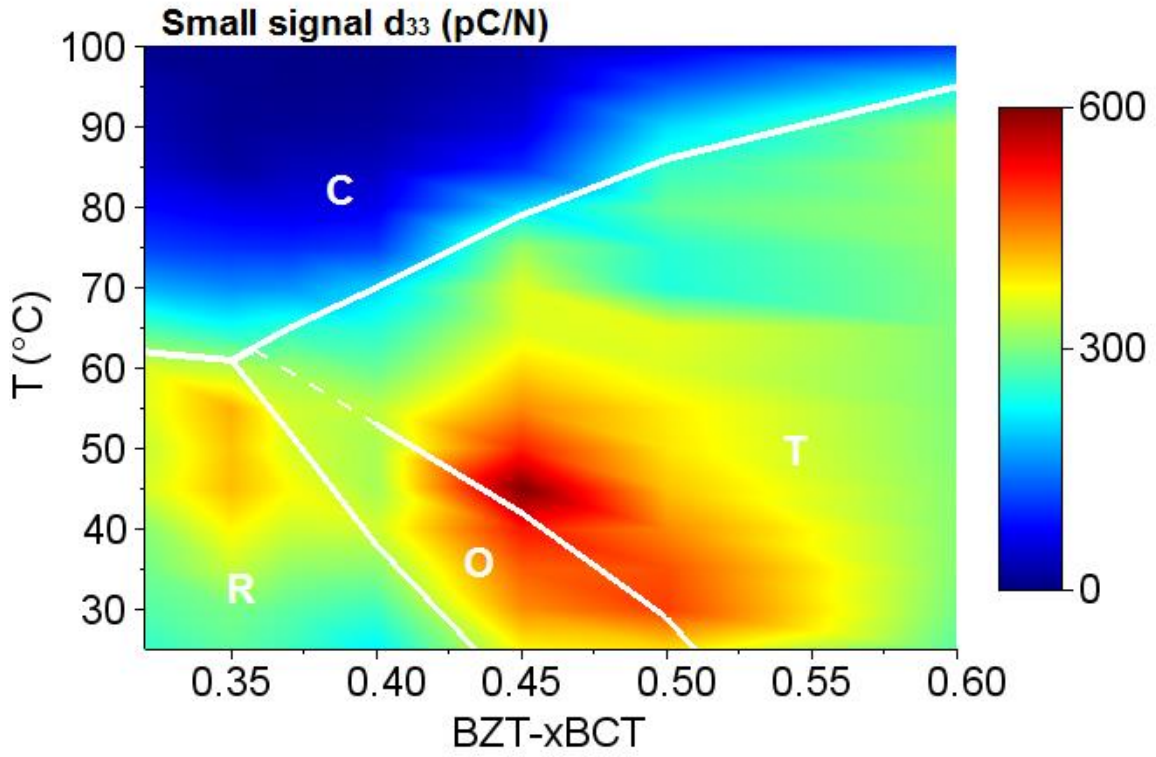

Figure 5.8: Contour plot of d_{33} as a function of temperature and composition. The resolution of the contour plot in the compositional-temperature space is indicated by 7 x 16 experimental data points.

5.1.3.2.2 Dynamic Properties

Figure 5.9 displays the small signal piezoelectric properties in the 33 mode calculated from resonance-antiresonance impedance characterization performed on the BZT-BCT system as a function of temperature. Details on the calculation procedure of all parameters are given in Appendix II. Figure 5.9 depicts the phase angle θ, dynamic relative permittivity $\varepsilon_{33}^{T}/\varepsilon_0$, piezoelectric coefficient d_{33}, coupling coefficient k_{33}, and mechanical quality factor Q_m.

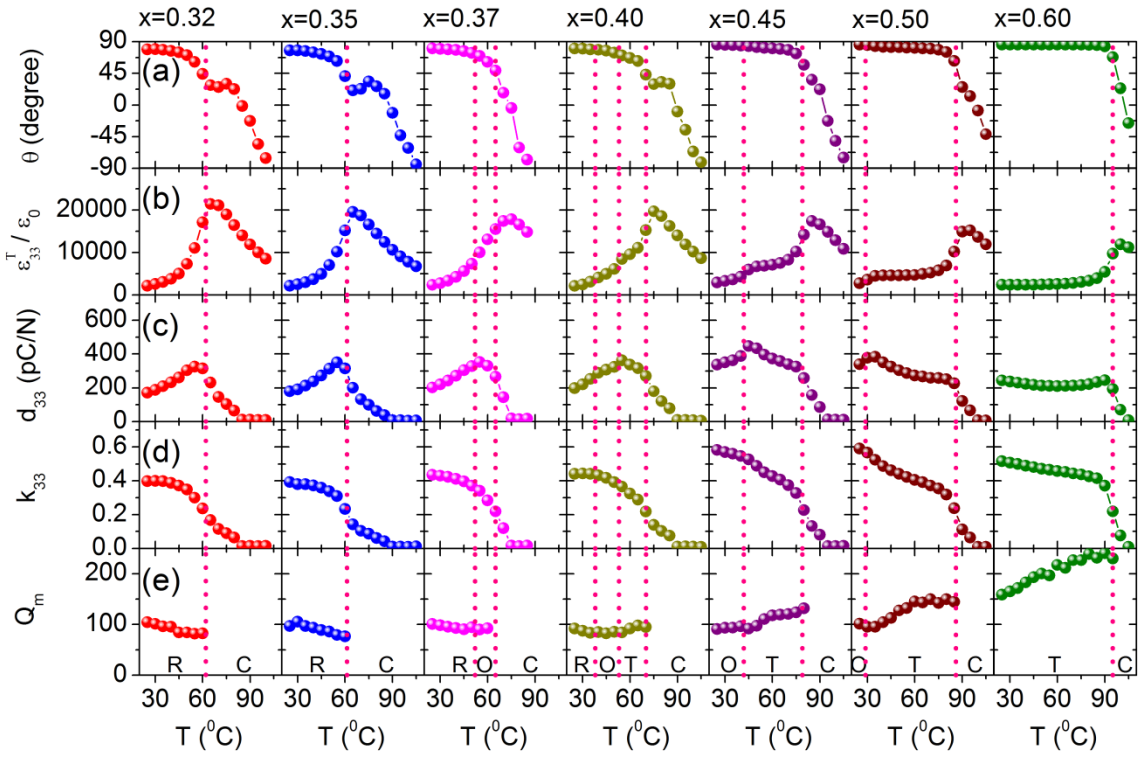

Figure 5.9: *In situ* piezoelectric and dielectric dynamic properties as a function of temperature calculated from resonance-antiresonance impedance characterization. (a) θ (b) $\varepsilon_{33}^{T}/\varepsilon_0$ (c) d_{33}, (d) k_{33}, and (e) Q_m obtained from impedance analysis.

The θ values (Figure 5.9 (a)) are normally considered as an indication of degree of poling.[314,397-399] The room temperature response of R and T phases to the poling treatment is quite different. The R phase features θ values between 78.9° and 80.1°, which are relatively far from an ideal poled condition of 90°. In contrast, the T phase is characterized by a higher value of θ = 85.9°. The O phase at room temperature features θ values comparable to the ones observed for the T phase with θ = 85.5°. All compositions are characterized by a monotonic decay of θ with increasing temperature that reflects the thermal depolarization of the system. Apart from distinct changes near phase boundaries, it should be pointed out that the T phase has a much higher poling stability than the R phase. The temperature decay of θ is enlarged after crossing the various phase boundaries, in agreement with previous works.[194,305] This is expected considering that excursions across PPBs diminish the poling state of ferroelectrics.[150] Literature reports have indicated that generally the properties of the R phase are much more susceptible to temperature and poling treatments.[317,325,328]

Although θ is commonly associated with the degree of poling[314,397-399], a word of caution is warranted near phase boundaries. As depicted in Figure 5.9 (a), the θ values above T_C discerned for x < 0.40 (with the exception of BZT-0.37BCT) are between 5° to 12° higher than the values below T_C. Naturally, the material cannot re-pole itself with increasing temperature if no electric field is applied. Moreover, the local minima in θ are accompanied by local maxima in d_{33} (Figure

5.9 (c)). This contradicts the generally known fact that a higher phase angle is associated with a higher degree of poling.[314,397-399] Therefore, near phase boundaries detailed comparisons of θ values should be avoided. The meaning of this local decrease in θ is believed to be associated either with a change in the resistivity of the sample near phase boundaries or to a solid state chemical activity between the silver electrodes and BZT-BCT.[400] Further experiments should be carried out to determine the physical origins of these observations. In order to visualize the relationship between phase boundaries and the poling state given by θ, the curves introduced in Figure 5.9 (a) were combined to produce a contour plot of θ as a function of temperature and composition, as depicted in Figure 5.10. In order to emphasize the θ contrast, thus allowing for better visualization, this contour plot is only provided up to 60 °C.

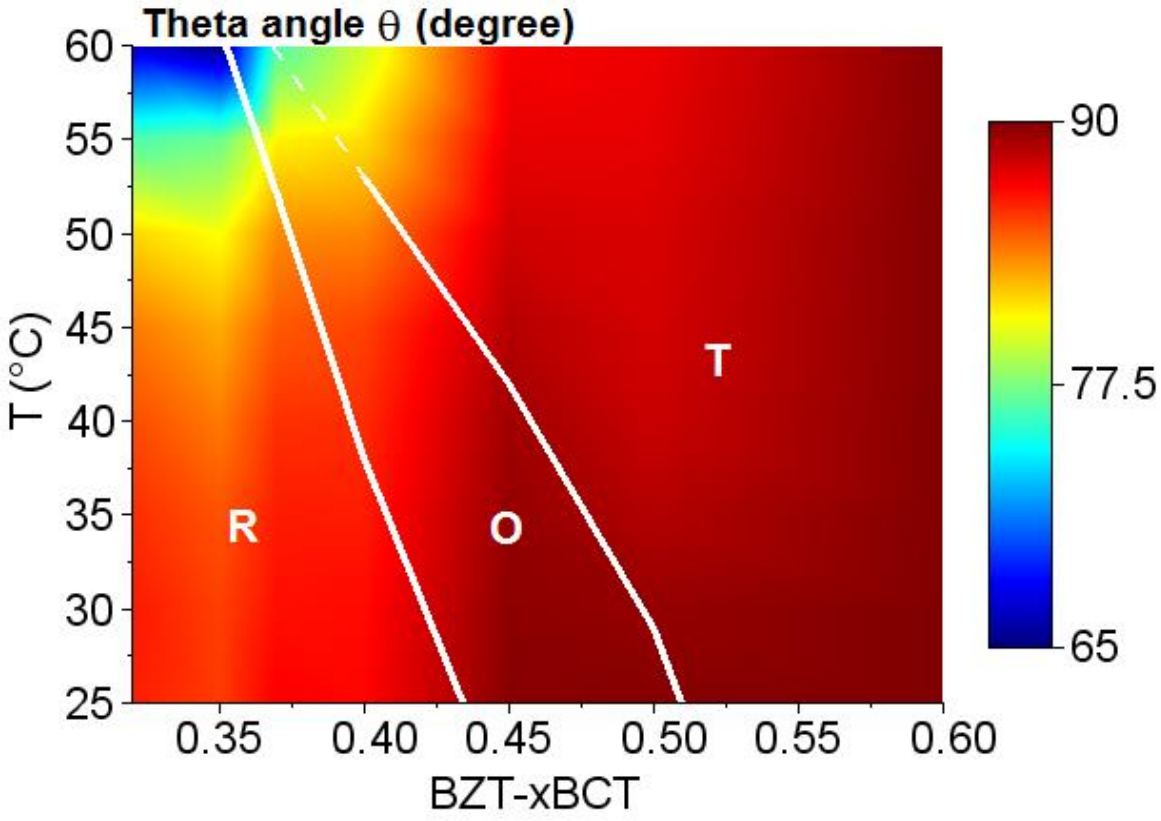

Figure 5.10: Contour plot of θ as a function of temperature and composition. The maximum temperature displayed is 60 °C in order to allow better visualization. The resolution of the contour plot in the compositional-temperature space is indicated by 7 x 8 experimental data points.

Figure 5.10 indicates that under the same poling conditions, the T phase displays higher θ values than the R phase. In the convergence region, the θ values decrease drastically indicating a much lower degree of poling and thus a lowering of P_r values, attributed to a thermally induced depolarization.

The measurements of relative permittivity $\varepsilon_{33}^{\mathrm{T}}/\varepsilon_0$ as a function of temperature are displayed in Figure 5.9 (b). The temperatures associated with the local maxima of $\varepsilon_{33}^{\mathrm{T}}/\varepsilon_0$ are in good agreement with those obtained from the non-resonant experiments in Section 5.1.3.1. The maximum values of $\varepsilon_{33}^{\mathrm{T}}/\varepsilon_0 \sim$ 20,000 in the R phase are 15 % higher than the values obtained in Section 5.1.3.1. Discrepancies in the magnitudes between quasi-static and dynamic measurements can be attributed to the different measurement conditions and input signals employed.

The dynamic d_{33} as a function of temperature is depicted in Figure 5.9 (c). As expected, all phase transitions are also accompanied by local maxima in d_{33}. The highest d_{33} values for compositions with x < 0.40 are found at T_C, whereas for 0.40 < x < 0.50, they were observed at the O to T phase boundary instead. Figure 5.11 (a) combines the d_{33} values reported in Figure 5.9 (c) in a contour plot for comparison with the quasi-static results from Section 5.1.3.2.1 (Figure 5.11 (b)).

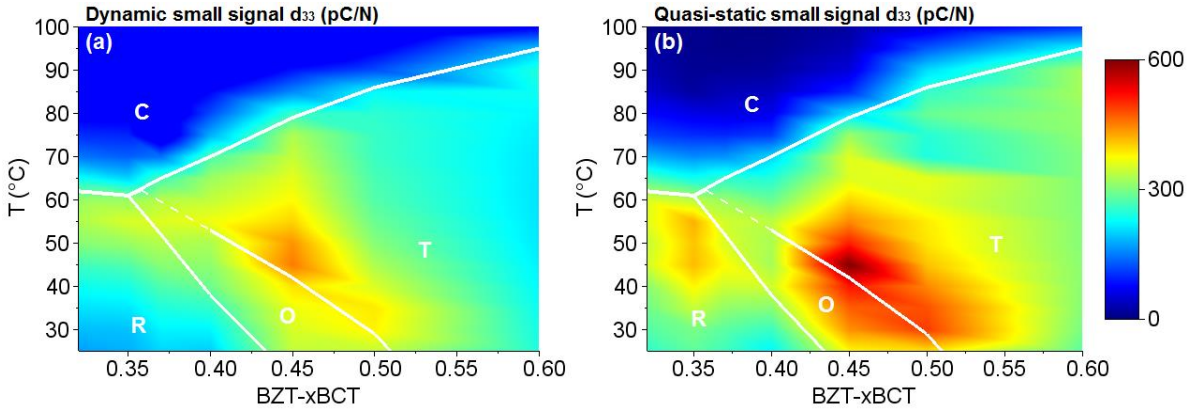

Figure 5.11: Contour plots of (a) dynamic small signal d_{33} and (b) quasi-static small signal d_{33} (measurements from Section 5.1.3.2.1) as a function of temperature and composition. The resolution of the contour plots in the compositional-temperature space is indicated by 7 x 16 experimental data points.

Figure 5.11 (a) indicates that the maximum d_{33} = 448 pC/N is found for BZT-0.45BZT at 45 °C, corresponding to the O to T phase boundary. Only local maximum values of d_{33} are found in the convergence region and at the R to O phase boundary, which are 30 % below the values at the O to T PPB. Comparison of Figure 5.11 (a) and (b) reveals similar compositional and temperature profiles obtained from dynamic and quasi-static measurements. The relative differences between d_{33} measured at PPBs and at the convergence region are in agreement in both sets of experiments. Both sets of experiments indicate that the R phase features much lower thermal stability than the T phase. The T phase depicts a relatively insensitive d_{33} = 240 pC/N in the temperature range between 25 °C and 95 °C. Moreover, in both sets of experiments all compositions feature residual piezoelectricity with values of $d_{33} \sim$ 100 pC/N, even up to 10 °C higher than the T_C. The residual piezoelectricity was also reported in other studies[200,349,352] and can be ascribed to the persistence of domains above T_C.[347]

The coupling coefficient k_{33} is displayed in Figure 5.9 (d). At room temperature, k_{33} values range between 0.40 and 0.58. These values are relatively high and comparable to PZT materials[401], indicating that BZT-BCT efficiently transforms electrical energy into mechanical energy. The highest k_{33} = 0.58 is observed for BZT-0.45BZT and BZT-0.50BZT compositions with O phase at room temperature. Meanwhile, values between 0.40 and 0.50 are found for the R and T phases. Comparably large k_{33} values in the O phase were also reported in the literature.[313,320] Although the temperature dependence of k_{33} also shows a relation to the phase boundaries, it does not exhibit variations as pronounced as those observed in $\varepsilon_{33}^{T}/\varepsilon_0$ or d_{33}. In general, it is observed that phase boundaries are accompanied by changes in the slope of k_{33}. Consistent with the d_{33} results, residual k_{33} values also persist to temperature of approximately 10 °C above T_C. The contour plot of k_{33} as a function of temperature and composition is provided in Figure 5.12.

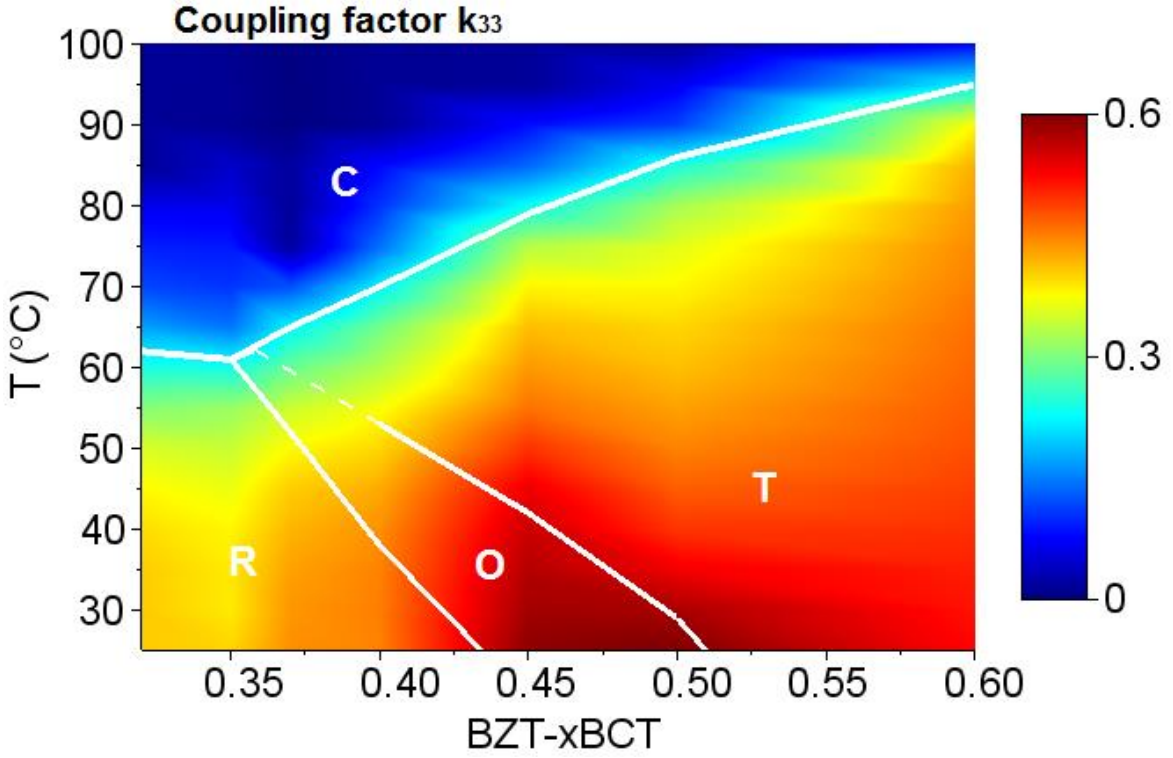

Figure 5.12: Contour plot of k_{33} as a function of temperature and composition. The resolution of the contour plot in the compositional-temperature space is indicated by 7 x 16 experimental data points.

It is clearly seen that the T phase features higher k_{33} values than the R phase. Moreover, a broad maximum in the O phase near to the O to T phase boundary and at room temperature is observed. Consistent with the data for d_{33}, the values of k_{33} do not peak in the convergence region.

The mechanical quality factor Q_m is provided in Figure 5.9 (e). At room temperature, increasing BCT content leads to a monotonic increase of Q_m values from 100 to 160. The highest Q_m values in the T phase can be attributed to the increased amount of Ca^{2+}, as it was shown that this cation

promotes hardening in BT.[402] It should be pointed out, however, that Q_m exhibits two different temperature dependencies over the compositional range studied. The compositional range with x < 0.45 provides a weak, linear decrease with increasing temperature. In contrast, for the compositional range with x > 0.45, the temperature profiles change leading to increased Q_m values with increasing temperature. This indicates a drastic change in the hardening properties when approaching the T phase. Hardening of electromechanical properties with increasing temperature was already observed in the $(Sr,Ca)_2NaNb_5O_{15}$.[403]

Impedance characterization also enables to calculate of elastic properties (Appendix II). Figure 5.13 (a) introduces the open circuit s_{33}^D and short circuit s_{33}^E elastic compliances as a function of temperature, whereas Figure 5.13 (b) depicts the frequency constant N_{33} as a function of temperature.

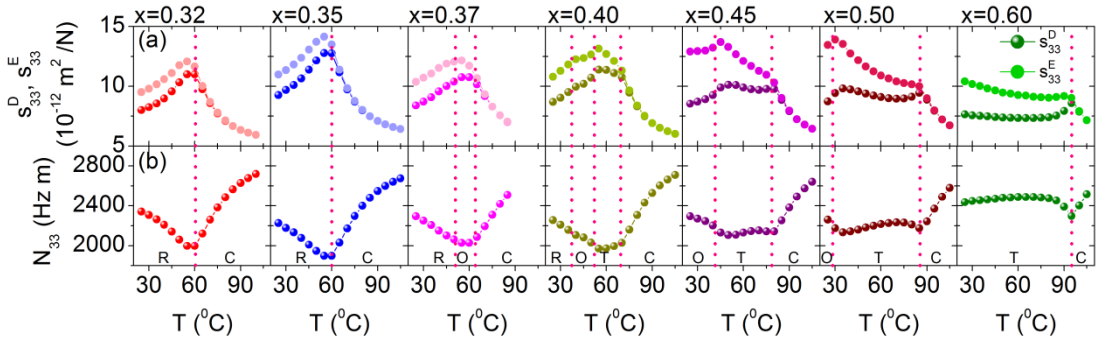

Figure 5.13: *In situ* elastic properties as a function of temperature. (a) elastic compliances s_{33}^D and s_{33}^E, (b) frequency constant N_{33}.

Equation 9.7 in Appendix II indicates that s_{33}^D and s_{33}^E are proportional to each other. Therefore, similar temperature profiles and local maxima values are expected. For all compositions the difference between s_{33}^D and s_{33}^E merges at T_C, which indicates thermal depolarization. Nevertheless, the values of s_{33}^D and s_{33}^E remain slightly unequal several degrees above T_C due to residual k_{33} values (Figure 5.12). Due to the proportionality between s_{33}^D and s_{33}^E, only s_{33}^E will be further analyzed. At room temperature, s_{33}^E has values between $9.5 \cdot 10^{-12}$ m^2/N and $13.5 \cdot 10^{-12}$ m^2/N. Maximized values are observed at room temperature for BZT-0.45BCT and BZT-0.50BCT compositions. Different temperature profiles of s_{33}^E are characteristic for each phase. For the R phase, increasing temperature leads to higher s_{33}^E, which indicates the typical elastic softening expected in ferroelectrics[42] and was previously reported by different experimental techniques in BZT-BCT.[318,349] Interestingly, compositions with x > 0.40 in the temperature range where the T phase is stable feature decreasing s_{33}^E values with temperature, which indicates elastic hardening. The BZT-0.60BCT displays a weak temperature dependence and relatively low s_{33}^E values, which are typical properties for hard ferroelectric materials.[401] The described softening and hardening behavior of R and T phases are correlated with the observed temperature profiles of Q_m. Materials that become stiffer with temperature feature the so called hard-spring effect.[403] The rationalization

of this effect in BZT-BCT will become apparent in the subsequent sections. Figure 5.14 displays the contour plot of s_{33}^E as a function of temperature and composition in order to establish a relation between the phase boundaries, piezoelectric properties, and elastic properties.

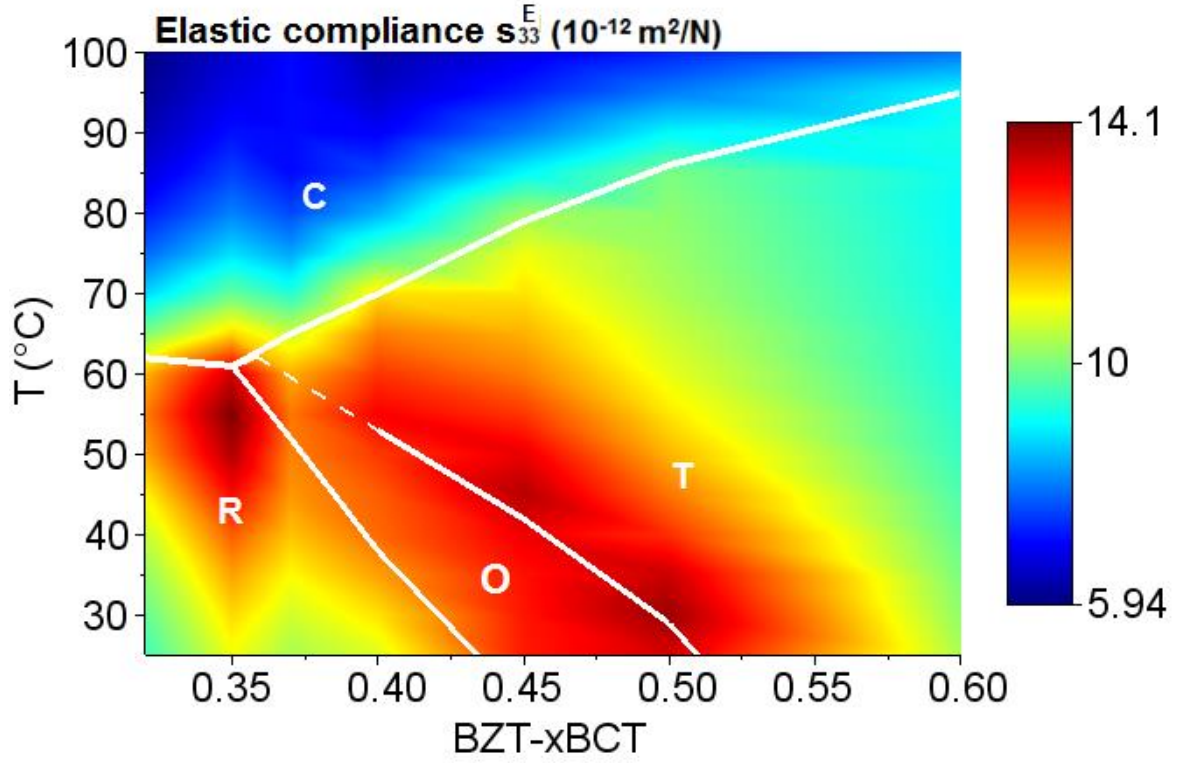

Figure 5.14: Contour plot of s_{33}^E as a function of temperature and composition. The resolution of the contour plot in the compositional-temperature space is indicated by 7 x 16 experimental data points.

As observed for $\varepsilon_{33}^T/\varepsilon_0$, the overall highest s_{33}^E = 14·10^{-12} m^2/N is found in the R phase near the convergence region. The local maximum s_{33}^E = 13.8·10^{-12} m^2/N values found at several positions along the O to T phase boundary are also quite high and comparable to those obtained in the convergence region. These values are consistent with literature reports where s_{33}^E ranges between 11·10^{-12} m^2/N and 14.5·10^{-12} m^2/N in the compositional range from BZT-0.45BCT to BZT-0.55BCT.[318,320] The results obtained here and in the literature[318,322,341,349] reveal that the O to T phase boundary is considerably softer than the R to O phase boundary.

The behavior of N_{33} is displayed in Figure 5.13 (b). At room temperature, N_{33} features values between 2200 Hz·m and 2400 Hz·m. These values are relatively high in comparison to lead-containing materials, indicating that BZT-BCT can vibrate at high resonance frequencies.[404] The temperature profiles of N_{33} indicate local minima that reflect the phase transition temperatures. The broad minimum observed for BZT-0.32BCT and BZT-0.35BCT in the vicinity of the convergence region may support the presence of two phase boundaries. It is observed that the R and O phases feature N_{33} values that decrease with increasing temperature. It is found that N_{33} is almost

temperature insensitive in the temperature range where the T phase is stable (x > 0.40), which is a result of the stable temperature profiles of elastic compliances (Figure 5.13 (a)).

5.1.3.2.3 Bias-Field- and Temperature-Dependent Quasi-Static Small Signal Properties

The analysis of small signal properties as a function of bias-field is a convenient technique to analyze the effect of extrinsic contributions to d_{33}.[405,406] It should be noted that the possibility of electric field induced phase shifts were not accounted for in the labeling of phase transition temperatures in the figures of the current and subsequent sections.

Figure 5.15 introduces the *in situ* quasi-static d_{33} measured as a function of bias-field and for representative temperatures between 25 °C and 85 °C. All curves are characterized by a maximum d_{33}^{max} at a given bias-field $E(d_{33}^{max})$. The d_{33}^{max} and $E(d_{33}^{max})$ values exhibit hysteresis with increasing and decreasing electric field. Note that d_{33}^{max} is analyzed based on values measured only on decreasing electric field for comparison purposes. All three compositions display a high remanent d_{33}^{rem} at temperatures below T_C. The magnitude and degree of hysteresis of d_{33}^{max}, $E(d_{33}^{max})$, and d_{33}^{rem} vary with composition and temperature.

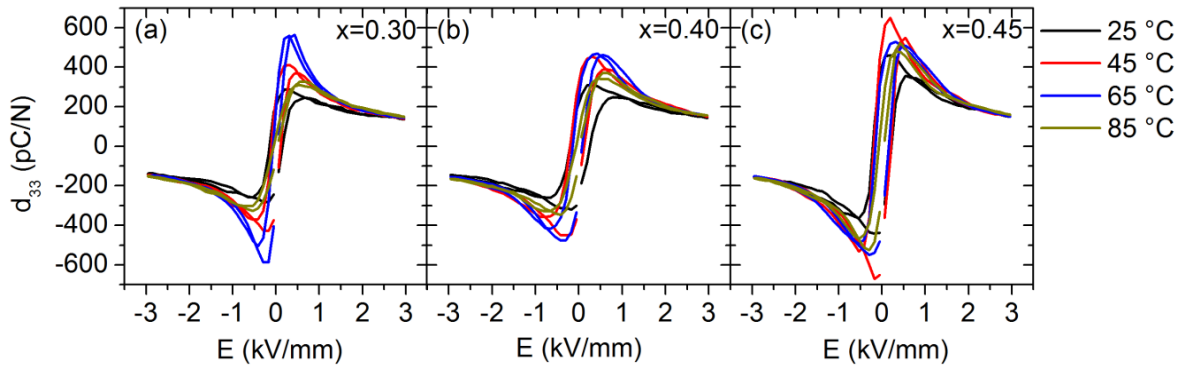

Figure 5.15: *In situ* d_{33} as a function of bias-field and temperature. Only a few representative temperatures are plotted to allow for proper visualization.

The local maxima in small signal properties observed at a given bias-field are normally attributed to switching processes in lead-containing ferroelectrics[405,406], as was also reported for BZT-BCT.[323,327,328] The piezoelectric coefficient d_{33} only features contributions of non-180° domain switching.[327] Therefore, the high d_{33}^{max} values indicate that non-180° domain switching processes are quite relevant in the electromechanical properties of these materials. It should be kept in mind that unless explicitly stated, all switching processes described throughout the subsequent sections refer to non-180° domain switching. The fact that d_{33}^{max} values exist above T_C for all compositions suggests switching processes ascribed to an electric field induced ferroelectric state in this temperature regime. Existence of a T ferroelectric/ferroelastic state at temperatures above T_C induced by either electric field or stress was also confirmed for BT.[407-409] Quantification of the

extrinsic processes in the induced T phase in BT indicated switching comparable as in the ferroelastic T phase below T_C.[408,409]

Figure 5.16 depicts the room temperature d_{33}^{max}, $E(d_{33}^{max})$, and d_{33}^{rem} as a function of composition. The R phase features intermediate d_{33}^{max} = 300 pC/N, $E(d_{33}^{max})$ = 0.31 kV/mm, and d_{33}^{rem} = 220 pC/N. The T phase has similar d_{33}^{max} values compared to the R phase, although the d_{33}^{rem} is 25 % higher. The higher d_{33}^{rem} values in the T phase correlate with its higher degree of poling (Figure 5.9 (a)). The $E(d_{33}^{max})$ = 0.67 kV/mm value of the T phase is more than twice the value found in the R phase. The lowest $E(d_{33}^{max})$ = 0.12 kV/mm is found for the O phase near PPBs. Moreover, the highest d_{33}^{max} = 468 pC/N is found in the O phase, which is 25 % higher than the d_{33}^{max} values in the R phase and 20 % higher than the d_{33}^{max} values in the T phase. The O phase near PPBs also features the highest d_{33}^{rem} = 418 pC/N, which is 50 % higher than the d_{33}^{rem} values in the R phase and 25 % higher than the d_{33}^{rem} values in the T phase. Therefore, the O phase can be said to promote enhanced switching at reduced electric fields.

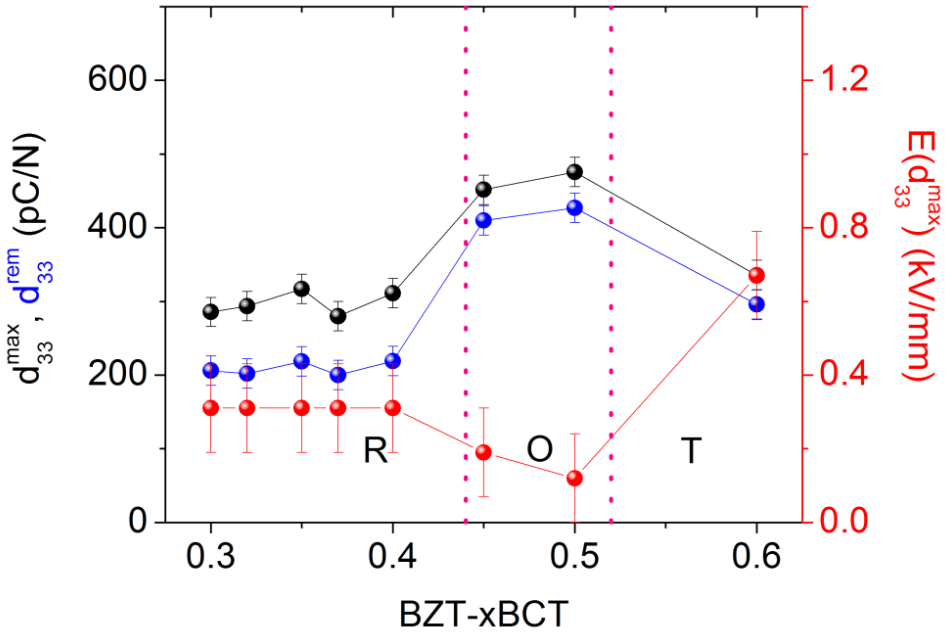

Figure 5.16: Room temperature d_{33}^{max}, $E(d_{33}^{max})$, and d_{33}^{rem} parameters as a function of composition.

The temperature dependence of d_{33} is displayed in Figure 5.17 for bias-field strengths between 0.31 kV/mm and 2.97 kV/mm.

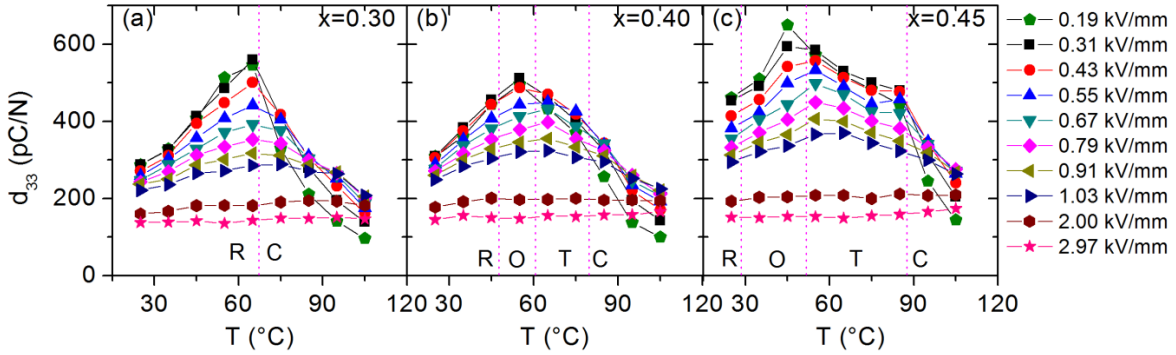

Figure 5.17: Small signal d_{33} as a function of temperature at a given bias-field. Error bars in d_{33} were omitted for clear visualization.

The d_{33}^{max} values above T_C are associated with an electric field induced phase transition that occurs at $E(d_{33}^{max})$ = (0.40 ± 0.12) kV/mm. It is revealed that the d_{33}^{max} values are recorded at temperatures slightly higher than those of the zero-field phase transitions, as expected in ferroelectrics with weak first order phase transitions.[408-410] The reduction in d_{33} for electric fields above $E(d_{33}^{max})$ is attributed to a saturation of switching processes, leading to a reduced contribution of domain wall motion. As previously shown[323], the intrinsic piezoelectric response of BZT-BCT can be estimated from the electromechanical response at high applied electric fields. Intrinsic d_{33} increase with increasing BCT content between 140 pC/N and 180 pC/N in the compositional range investigated, in good agreement with previous findings.[323]

The values of d_{33}^{rem}, d_{33}^{max}, and $E(d_{33}^{max})$ are plotted as a function of temperature in Figure 5.18. Either local extrema or changes in slope are observed in all parameters near the zero-field phase boundaries.

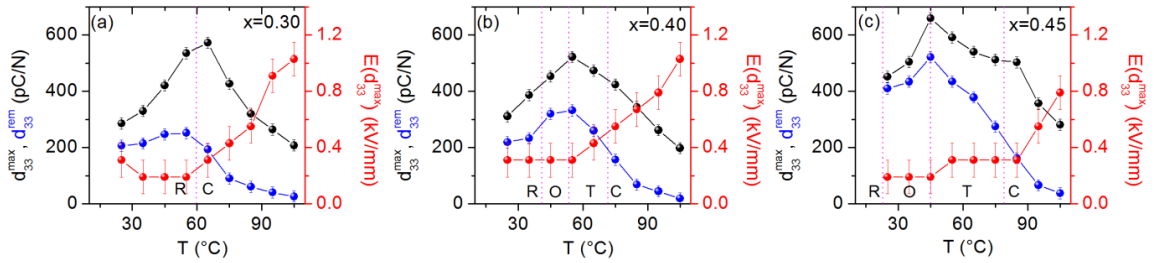

Figure 5.18: d_{33}^{max}, d_{33}^{rem}, and $E(d_{33}^{max})$ as a function of temperature.

The difference between d_{33}^{rem} and d_{33}^{max} is maximized at the paraelectric to ferroelectric phase transition due to the ferroelectric state decay upon removal of the electric field. Therefore, this process involves substantial switching, as demonstrated for BT.[408,409] The BZT-0.45BCT displays high d_{33}^{rem} and d_{33}^{max} values below 40 °C, due to a high degree of poling achieved during the application of a bias-field. Applying a bias-field leads to comparable d_{33} values in both the convergence region

and near the O to T PPB, which is in sharp contrast to the trends observed for d_{33} obtained from quasi-static and dynamic properties (Figure 5.11). Coordinates of composition, temperature, and d_{33}^{max} can be extracted from the aforementioned results to visualize the different regions of maximized properties. Figure 5.19 displays the pseudo-binary phase diagram obtained from dielectric properties (Section 5.1.3.1) in the temperature range from 25 °C to 100 °C together with the combined two regions of maximized d_{33} superimposed in white.

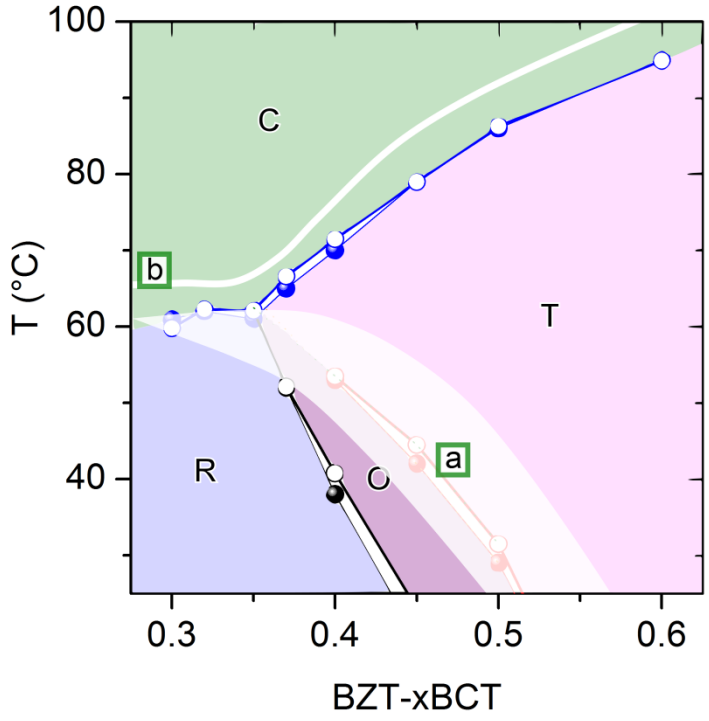

Figure 5.19: Pseudo-binary phase diagram obtained from dielectric properties between 25 °C and 100 °C. A broad region and a line are superimposed in white indicating the highest d_{33}^{max} obtained at a given non-zero bias-field.

The enhanced d_{33}^{max} region marked with $\boxed{a}$ is ascribed to enhanced switching due to the proximity to the O to T PPB. It is noted, however, that an electric field induced nucleation of an O phase at expense of the T phase[321] or a change in the relative content of R and T phases cannot be discarded. The peak in piezoelectric response observed above T_C marked with $\boxed{b}$ indicates that the electric field induced paraelectric to ferroelectric transitions in BZT-BCT are of first order[156,188,191], which is supported by the non-zero thermal hysteresis in dielectric properties.[194] The high d_{33}^{max} values above T_C that were obtained at finite bias-fields $E(d_{33}^{max})$ = (0.40 ± 0.12) kV/mm implies a line of critical points.[188-191] This observation casts doubt on the assertion that triple points of the zero-field pseudo-binary phase diagram are also tricritical points.[194,333]

In order to allow a better understanding of the strain mechanisms in BZT-BCT, quantification of the intrinsic and extrinsic contributions to d_{33} is required. The extrinsic contributions can be separated

into irreversible and reversible domain switching processes such that the total piezoelectric response is given by Equation 5.2.[405,406]

$$d_{33} = d_{33}^{intrinsic} + d_{33}^{irreversible\ extrinsic} + d_{33}^{reversible\ extrinsic} \qquad \textbf{Equation 5.2.}$$

The d_{33}^{rem} is comprised of intrinsic contributions and irreversible switching processes[406], as given by Equation 5.3.

$$d_{33}^{rem} = d_{33}^{intrinsic} + d_{33}^{irreversible\ extrinsic} \qquad \textbf{Equation 5.3.}$$

Equation 5.3 is valid with the assumption that reversible switching is considerably reduced at zero bias-field. It should be noted that the probing sinusoidal wave chosen was below the Rayleigh threshold field of BZT-BCT. For BZT-0.44BCT, it was reported that the Rayleigh threshold field is 0.04 kV/mm at 2 Hz.[323] Since $d_{33}^{intrinsic}$ can be estimated[323] and d_{33}^{rem} was explicitly measured, all contributions to the piezoelectric response of BZT-BCT measured under applied electric field can be quantified. Upon these considerations, it is also apparent for all compositions that the reduced d_{33} values for electrics fields higher than $E(d_{33}^{max})$ (Figure 5.15) is a consequence of the reduction of reversible switching due to a saturated domain state. Figure 5.20 displays percentage of intrinsic and extrinsic contributions to d_{33} as a function of composition. It is seen that the maximized d_{33}^{rem} and d_{33}^{max} correlate directly with a high irreversible switching contribution. These contributions become quite dominant and greatly surpass the intrinsic contribution near both PPBs. Intrinsic contributions seem especially enhanced in the T phase, where the lattice distortion is maximized and switching processes are relatively diminished.[348]

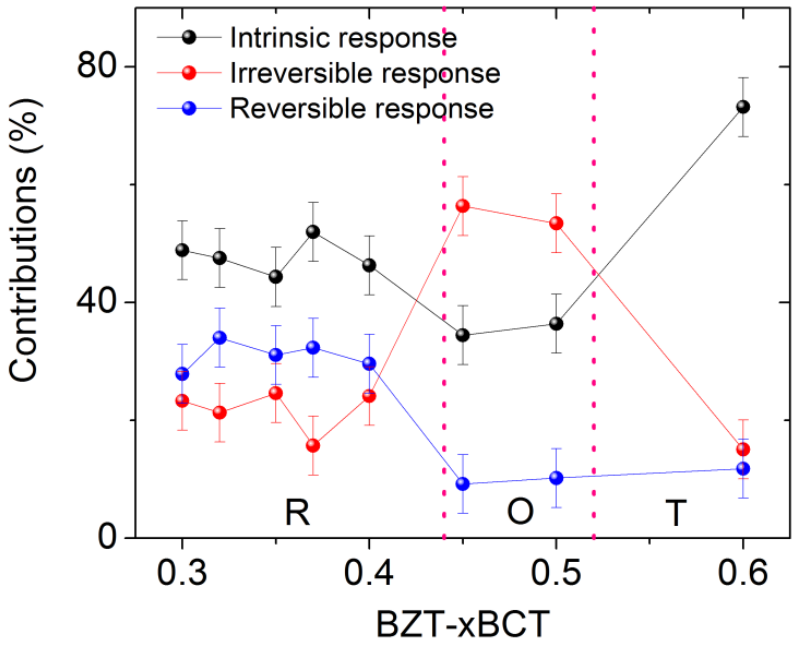

Figure 5.20: Intrinsic, irreversible extrinsic, and reversible extrinsic contributions to d_{33} as a function of composition.

In order to investigate the effect of temperature on strain contributions, Figure 5.21 (a) to (c) depicts the percentage of intrinsic and extrinsic contributions to d_{33} as a function of temperature. Irreversible and reversible extrinsic contributions comprise more than 50 % of the electromechanical response of BZT-BCT (with exception of BZT-0.60BCT).[323,326,327] However, Figure 5.21 reveals that differing distribution of contributions are characteristic of each ferroelectric phase at a given temperature.

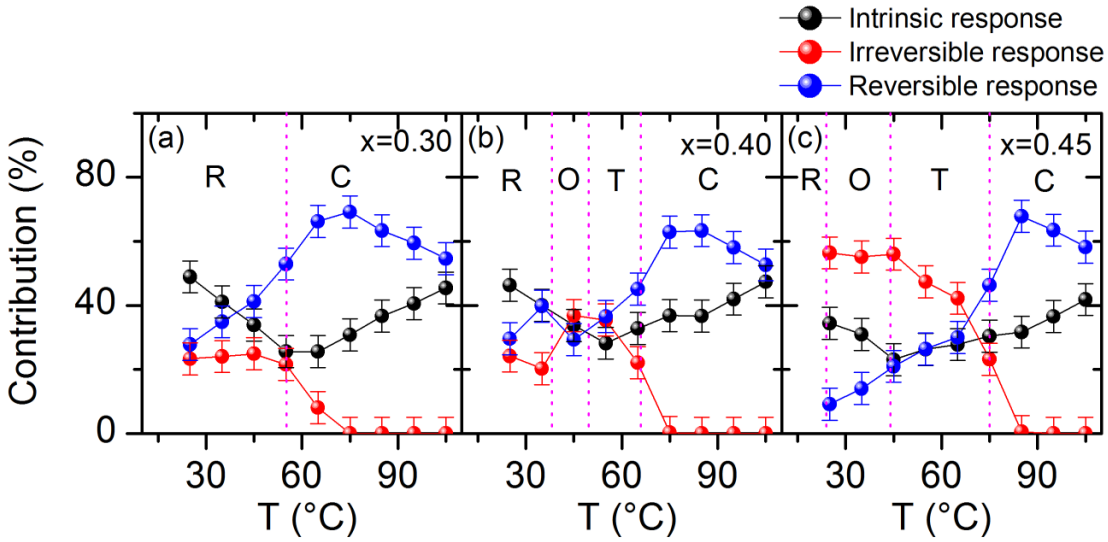

Figure 5.21: Intrinsic, irreversible, and reversible contributions to d_{33} as a function of temperature.

Increasing temperature diminishes the intrinsic contributions and increases the reversible switching in the R phase, leading to reversible switching values between 30 % and 40 % below T_C. This means that the R phase features the highest reversible switching contribution at temperatures far from phase boundaries. The response in the O phase is characterized by high irreversible switching, ranging between 35 % and 55 % of the total piezoelectric response, as previously reported.[321,339,348] When both irreversible and reversible switching processes are considered, 65 % of the total response arises from extrinsic contributions. If both irreversible and reversible contributions are summed, the fraction of extrinsic response in the R and O phases shows a linear increase with temperature (0.69 ± 0.03) %/°C. Based on these findings, the maximized d_{33}^{max} and d_{33}^{rem} in the O phase (Figure 5.16) can be assigned mostly to irreversible switching at room temperature that reduces with temperature and is compensated by increased thermally activated reversible switching. Moreover, high irreversible switching is also found at the O to T phase boundary, in agreement with literature.[347] For the T phase close to the O to T PPB, 68 % of the total piezoelectric response is due to extrinsic contributions. When both irreversible and reversible switching processes are summed, the fraction of extrinsic response displays a linear decrease with temperature (– 0.24 ± 0.02) %/°C. This decay of switching with temperature is a result of a substantial decrease in irreversible switching upon approaching T_C, which is not fully counterbalanced by the thermally activated reversible switching. For a complete overview of the

strain mechanisms in the pseudo-binary phase diagram of BZT-BCT, Figure 5.22 displays contour plots of (a) intrinsic, (b) irreversible extrinsic, and (c) reversible extrinsic strain contributions as a function of composition and temperature. The R phase far from phase boundaries features a considerable contribution from reversible switching, which can be expected considering its high poling susceptibility[328] and relatively small lattice distortions (Section 5.1.1). Intrinsic contributions are observed to be quite high in the T phase far from phase boundaries, as corroborated in the literature.[348] This reconciles the high poling and thermal stability of this phase. It is observed that the O phase and the O to T PPB feature the overall highest irreversible switching contribution. Reversible switching is maximized above T_C for all compositions due to the electric field induced ferroelectric phase transition that involves domain formation and switching. It is noted, however, that a source of error in calculating the reversible contribution at high temperatures could be generated due to the volume change associated with the electric field induced ferroelectric transition.

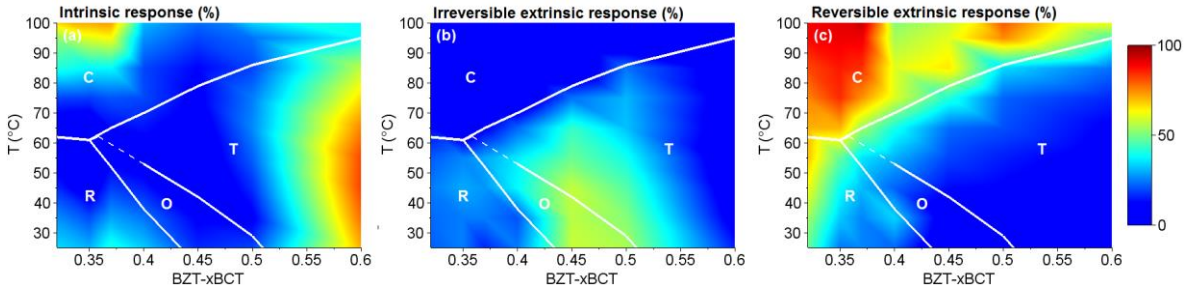

Figure 5.22: (a) Intrinsic, (b) irreversible extrinsic, and (c) reversible extrinsic strain contributions to d_{33} as a function of composition and temperature. The resolution of the contour plot in the compositional-temperature space is indicated by 7 x 9 experimental data points.

Based on the aforementioned quantification, maximized properties of the region marked with $\boxed{a}$ in Figure 5.19 can be attributed to the considerably high degree of irreversible switching, as depicted in Figure 5.22 (b). Note that in case an electric field induced phase transition occurs near region $\boxed{a}$ in Figure 5.19, it must be accompanied by considerable switching. At room temperature, irreversible switching plays the largest role, while contributions from reversible switching increase significantly with temperature. This can be attributed to the low T_C of the system in this compositional range. The line of the enhanced d_{33} above T_C marked with $\boxed{b}$ in Figure 5.19 features maximized properties due to reversible extrinsic switching, since this contribution accounts for more than 65 % of the total response at this temperature (Figure 5.22 (c)). Irreversible switching is negligible above T_C due to the decay of the induced ferroelectric state with the removal of the electric field. Above the line of critical points, the reversible switching processes diminish and the relative intrinsic response increases monotonically due to a continuous decrease of extrinsic contributions. Reduced switching in the supercritical regime of BT was also previously demonstrated.[408,409]

5.1.3.3 Quasi-Static Large Signal Properties

Figure 5.23 displays the (a) bipolar polarization, (b) bipolar strain, and (c) unipolar strain measured at 3 kV/mm and 5 Hz. Although neither long term reliability studies nor defect chemistry are treated in the present work, it should be noted that after the poling cycle BZT-BCT materials featured an internal bias-field leading to shifts of the bipolar polarization loops ranging between 40 % for the R phase down to 10 % for the T phase relative to the E_c values.

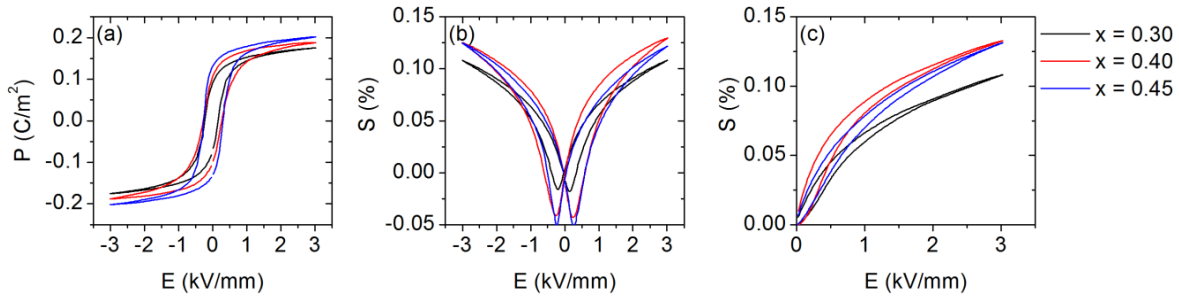

Figure 5.23: (a) Bipolar polarization, (b) bipolar strain, and (c) unipolar strain for BZT-BCT measured at 5 Hz.

Saturation of the electromechanical properties is attained at lower electric field for the R phase, indicated by BZT-0.30BCT. Moreover, this material features the lowest P_{max} and S_{max}. Figure 5.24 introduces the (a) E_C, (b) P_r and P_{max}, and (c) d_{33}^* as a function of composition.

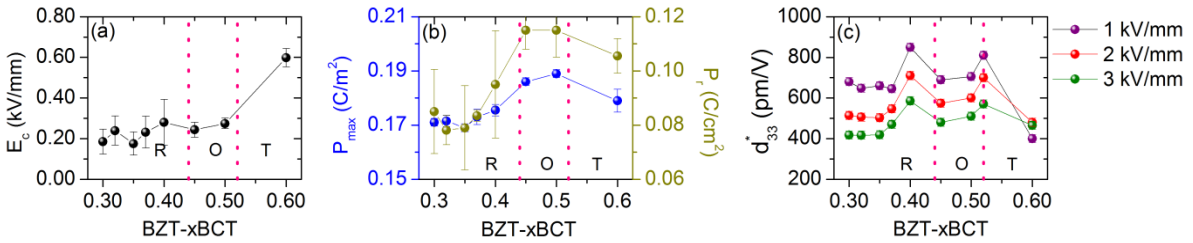

Figure 5.24: Room temperature (a) E_c, (b) P_{max} and P_r, and (c) d_{33}^* at 1 kV/mm, 2 kV/mm, and 3 kV/mm as a function of composition obtained at 5 Hz. Note that BZT-0.52BCT was added in the d_{33}^* plot to visualize the PPBs effect on the electromechanical properties.

A gradual increase of E_C is observed with increasing BCT content ranging from E_C = 0.18 kV/mm for the R phase up to E_C = 0.60 kV/mm for the T phase (Figure 5.24 (a)). The E_C of the O phase is 10 % lower than the E_C of the R phase that immediately precedes it. It should be pointed out that $E(d_{33}^{max})$ (Figure 5.16) and E_C display almost equal magnitudes (within experimental errors) for all compositions. This indicates that most of the switching processes occur at this electric field. The P_r

has maximized values in the O phase, which are 20 % higher than in the R phase and 10 % higher than in the T phase (Figure 5.24 (b)). The P_{max} profile depicts the same compositional trend but the O phase features 6 % higher values than the R and T phases. Far from phase boundaries, the O phase features the highest d_{33}^* = 630 pm/V at 1 kV/mm. The R phase displays the second highest values with d_{33}^* = 600 pm/V at 1 kV/mm, whereas the T phase displays the lowest d_{33}^* = 465 pm/V at 1 kV/mm (Figure 5.24 (c)). The overall highest d_{33}^* value above 800 pm/V at 1 kV/mm is found for compositions near both PPBs. The fact that the highest d_{33}^* is observed in BZT-0.40BCT rather than in BZT-0.45BCT suggests small shifts of the phase boundaries under electric field, which is expected for ferroelectrics with weak first order phase transitions.[408-410] Therefore, it should be pointed out that the lowest $E(d_{33}^{max})$ and E_C are found for the O phase and correlate with the highest d_{33}^{max}, d_{33}^{rem}, P_r, and P_{max}, as well as a high d_{33}^*.

Figure 5.25 introduces d_{33}^* as a function of electric field, while the inset displays the electric field corresponding to the highest d_{33}^* value of each composition. The maximized d_{33}^* value at a given electric field is correlated to the E_c of each composition and thus to the degree of extrinsic contributions. For all materials, with the exception of BZT-0.60BCT, increasing electric field above ~ 1 kV/mm decreases the d_{33}^* values. This indicates that at higher electric field the switching processes gradually saturate leading to a lower $\frac{\partial S}{\partial E}$. It is noted that linearity in d_{33}^* values is not achieved below ~ 1.2 kV/mm. Note that this electric field is at least 50 % higher than the $E(d_{33}^{max})$ (Figure 5.16) and E_C (Figure 5.24 (b)) of all compositions, indicating that switching processes remain active in a broad electric field range. For the T phase, d_{33}^* is maximized only at 2 kV/mm due to the high E_C of this phase. The different electric field profile of d_{33}^* featured in this phase seems to suggest an even broader electric range where switching processes remain active.

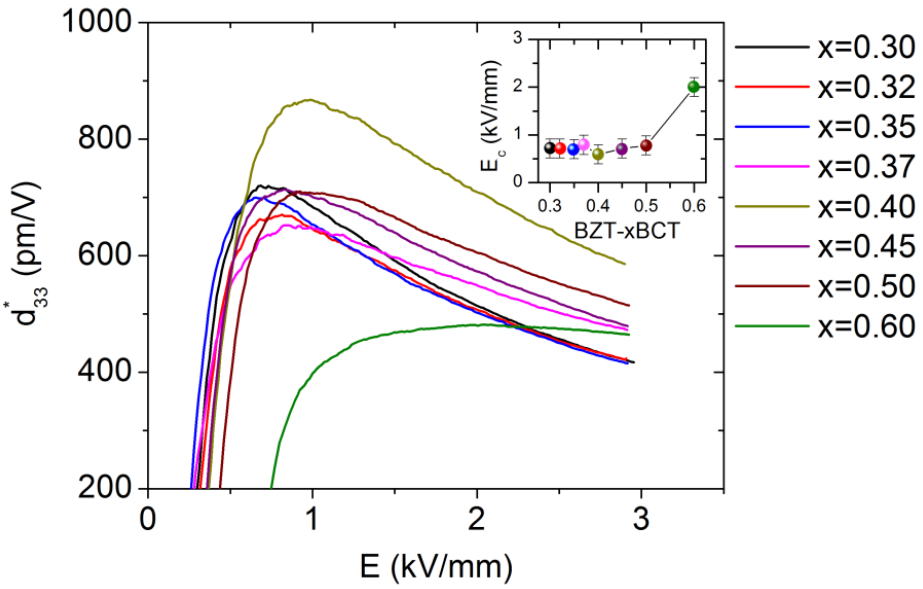

Figure 5.25: d_{33}^* as a function of electric field. Inset displays the electric field corresponding to the maximum d_{33}^* as a function of composition.

In order to explore the applicability of this system on the large signal regime, the effect of temperature on the electromechanical properties was investigated with unipolar polarization and strain curves. The contour plot of P_{max} at 3 kV/mm as a function of temperature and composition is introduced in Figure 5.26.

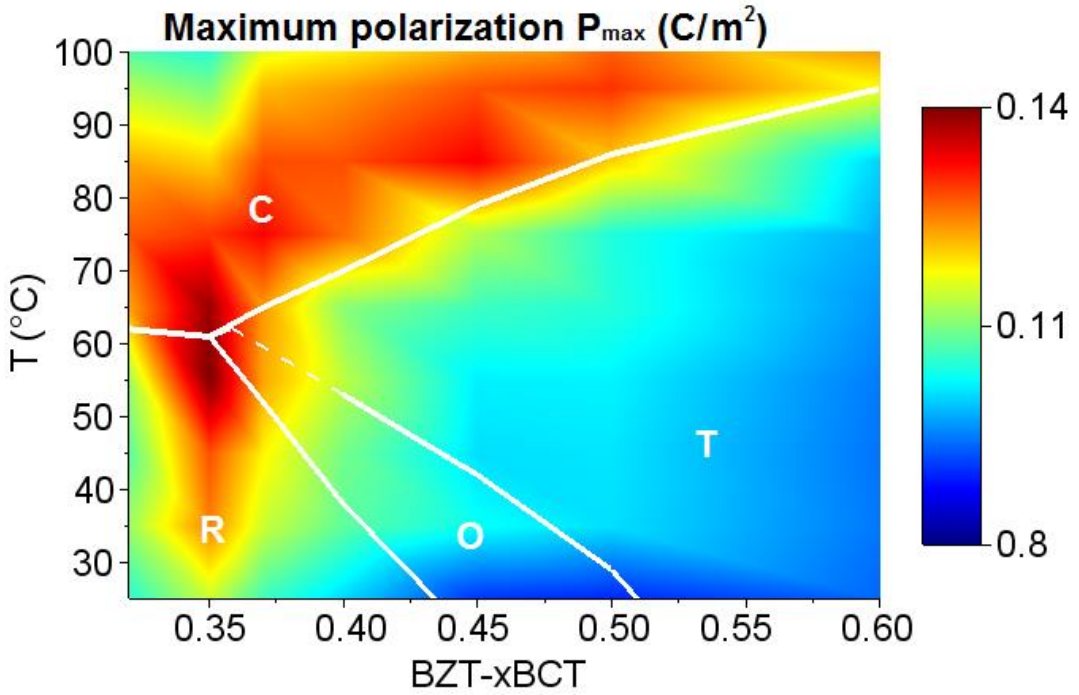

Figure 5.26: Contour plot of P_{max} as a function of temperature and composition obtained at 3 kV/mm. The resolution of the contour plot in the compositional-temperature space is indicated by 7 x 11 experimental data points.

In contrast to the quasi-static (Section 5.1.3.2.1) and dynamic (Section 5.1.3.2.2) small signal properties measured, P_{max} features maximized values of 0.14 C/m^2 in the convergence region. These values are 45 % higher than the polarization values observed at room temperature. This can be ascribed to the high degree of reversible switching that was quantified near the convergence region (Section 5.1.3.2.3). The O to T phase boundary, characterized by the highest irreversible switching, does not feature maximized P_{max} values. This indicates that reversible switching is the most preponderant mechanism responsible of polarization enhancements under an applied electric field. Figure 5.27 provides unipolar strain curves up to 3 kV/mm measured at 5 Hz at different temperatures.

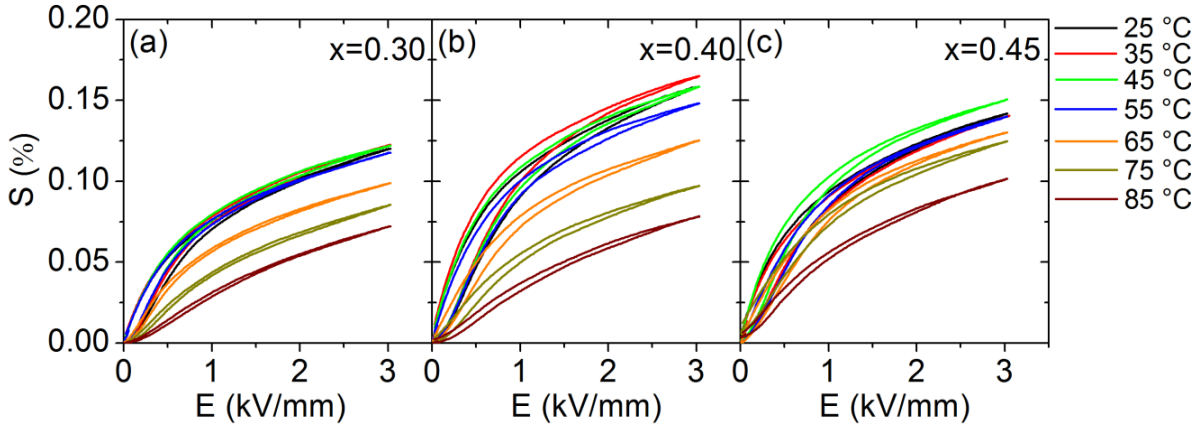

Figure 5.27: Temperature-dependent large signal unipolar strain of representative compositions measured at 5 Hz.

It is apparent that enhanced strain output is found at different temperatures for each composition. Therefore, d_{33}^* was calculated as a function of temperature, as depicted in Figure 5.28. In order to facilitate a comparison in a fully saturated state, all d_{33}^* values were calculated at 3 kV/mm.

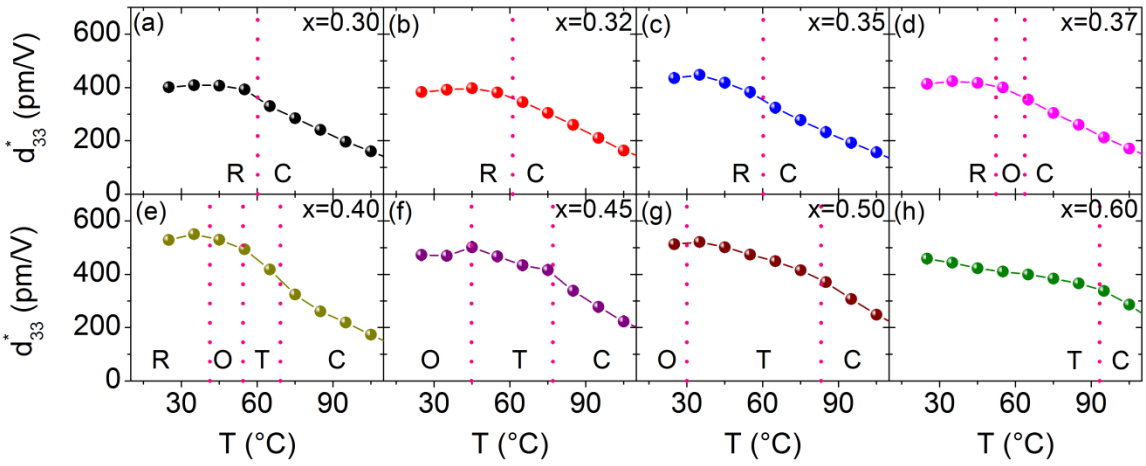

Figure 5.28: Large signal d_{33}^* as a function of temperature at 3 kV/mm.

The correlation between d_{33}^* and phase transitions is rather weak with only smooth changes around the transition temperatures. In all cases, a d_{33}^* = 200 pm/V persists even at 10 °C above T_C, which can be ascribed to the electric field induced phase transition described in this temperature regime (Section 5.1.3.2.3). The R and O phases display considerable temperature stability below T_C. Nonetheless, the BZT-0.60BCT features higher stability over a broader temperature range due to its higher T_C. It should be pointed out that the thermal stability of d_{33}^* in the R phase is considerably higher than the thermal stability of d_{33} (Section 5.1.3.2.1 and 5.1.3.2.2). However, for the T phase

the temperature stability of d_{33}^* is reduced as compared to d_{33}. More specifically for BZT-0.60BCT, a decay of 30 % in d_{33}^* is observed from room temperature up to 95 °C, while d_{33} features a relatively insensitive temperature profile. The d_{33}^* values from Figure 5.28 are used to construct the contour plot provided in Figure 5.29.

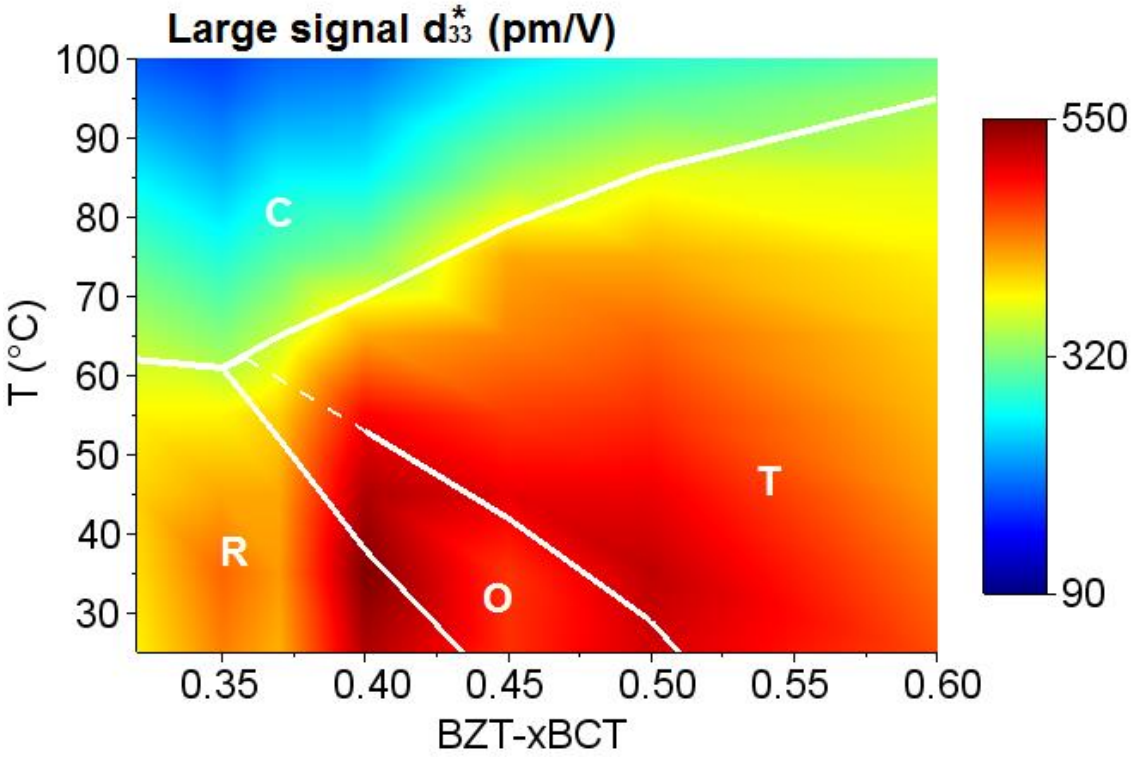

Figure 5.29: Contour plot of large signal d_{33}^* as a function of temperature and composition obtained at 3 kV/mm. The resolution of the contour plot in the compositional-temperature space is indicated by 7 x 11 experimental data points.

A broad region of high d_{33}^* values is apparent around the O phase and at both PPBs. Nevertheless, maximized d_{33}^* values still follow the phase boundaries to a significant degree. In contrast to the trends observed in the quasi-static and dynamic small signal d_{33} measurements (Figure 5.11), where maximized properties were only observed along the O to T phase boundary, maximized d_{33}^* is featured at both R to O and O to T PPBs. The region where maximized dynamic k_{33} values are found (Figure 5.12) resembles the region of maximized d_{33}^* values.

5.1.4 Strain Mechanisms of the (1-x)Ba($Zr_{0.2}Ti_{0.8}$)O_3-x($Ba_{0.7}Ca_{0.3}$)TiO_3 System

Based on the thorough characterization performed on the BZT-BCT system, it is possible to construct a model that rationalizes the origin of the small and large signal electromechanical properties of BZT-BCT. In order to achieve this goal, the existing model proposed by Liu and Ren[194] is analyzed, followed by the reconciliation of small and large signal trends. It should be pointed out

that both regimes are treated separately since their strain contributions differ significantly. Figure 5.30 uses a schematic phase diagram to summarize the experimental observations for the different regions of BZT-BCT analyzed in this work.

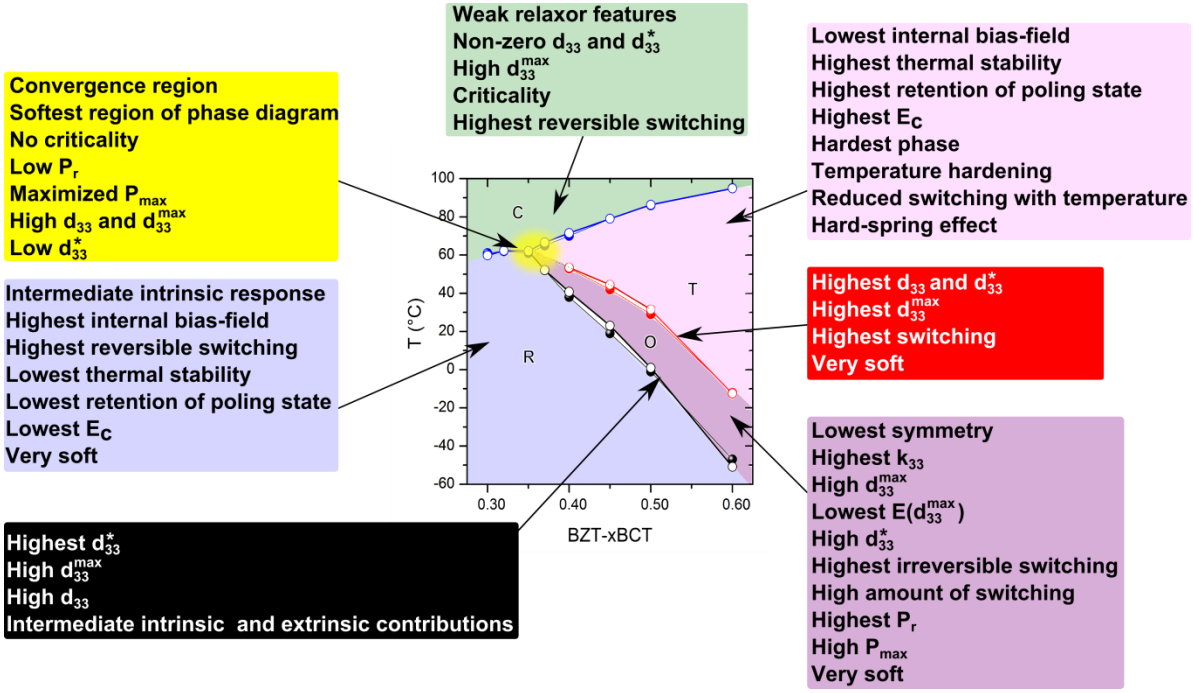

Figure 5.30: Summary of properties featured in the BZT-BCT system.

Comments on the state-of-the-art knowledge of the (1-x)Ba($Zr_{0.2}Ti_{0.8}$)O_3-x($Ba_{0.7}Ca_{0.3}$)TiO_3 system: One of the preferred strategies to enhance electromechanical properties in ferroelectrics is to design materials near phase boundaries (Section 2.3). The BZT-BCT constitutes a rich system to study the influence of longitudinal and transverse instabilities of P_s^i due to the presence of a phase convergence region and two PPBs, which should theoretically promote each of these type of instabilities.[169] From a simple inspection of Figure 5.30, it can be discerned that the existing model proposed by Liu and Ren (described in Section 3.1.4)[194] to rationalize the electromechanical response of BZT-BCT lacks a fundamental basis and is not able to describe properly all of the diverse features of the system. The so called tricritical point in BZT-BCT was labeled as such due to a reduced thermal hysteresis, which was actually non-zero.[194] The maximized d_{33}^{max} values under electric field provided in Section 5.1.3.2.3, however, suggest the presence of a line of critical points at non-zero electric field and at temperatures higher than T_C, implying that no critical points are featured in the temperature-composition pseudo-binary phase diagram of BZT-BCT at zero electric field.

The model proposed by Liu and Ren[194] indicated that phase boundaries originating from a tricritical point feature negligible free energy anisotropy. However, the existence of such a phase boundary is not a necessary condition for vanishing of the free energy anisotropy.[156,157,159-165] In fact, a reduction of the free energy anisotropy is an inherent feature of all phase boundaries, as demonstrated by

phenomenological approaches.[156-162] Heitmann and Rossetti[156] estimated the free energy along the isopleth corresponding to BZT-BCT with Landau coefficients obtained from BZT and BCT. A nearly degenerate free energy surface was obtained in the O phase region with respect to the R and T phases indicating negligible free energy anisotropy. This broad region of reduced free energy anisotropy is a direct consequence of the tilted PPBs of BZT-BCT.[156,159,161] If only the free energy profiles are considered, BZT-BCT should depict maximized properties at both PPBs, in the O phase, and at T_C (including the convergence region). It has been shown, however, that the convergence region and PPBs feature different electromechanical properties. Hence, the electromechanical properties of BZT-BCT cannot be fully reconciled solely by a reduction in the free energy anisotropy near the phase boundaries, although this concept is key for a complete physical understanding. It should also be considered that phenomenological models, such as the one proposed by Liu and Ren[194], were developed to rationalize the intrinsic properties of a monodomain single crystal.[159,193] In polycrystalline materials, however, extrinsic contributions and intergranular constraints can play a considerable role on the electromechanical properties, as shown for BZT-BCT in Section 5.1.3.2.3 and in the literature.[302,305,306] Further features of the BZT-BCT recall for a reconsideration even of its ferroelectricity due to the presence of features common to relaxor materials. Based on considerations from literature and the results from the current work, a complete model that accounts for intrinsic and extrinsic contributions to the electromechanical response of BZT-BCT was developed to reconcile all the experimental observations.

The cubic phase: Residual piezoelectricity[347,349,352], differences in the magnitude of $\varepsilon_r^{'}$ and $\varepsilon_r^{''}$ above T_C (Figure 5.4), weak dielectric relaxations (Appendix III), and persistence of domains[347] above T_C all together point towards the existence of weak relaxor features, as previously proposed.[115,116,334] The weak relaxor features depicted in BZT-BCT can be ascribed to the relative content of Zr^{4+} and Ca^{2+}.[115,116,334] The non-zero d_{33}^* above T_C is a result of a considerable amount of reversible switching (Figure 5.21), which is attributed to an electric field induced phase transition leading to criticality.[408,409] Criticality is apparent in the C phase above T_C under electric fields of (0.40 ± 0.12) kV/mm and was also observed for other relaxors and BT.[107,188,191] The d_{33} at the line of critical points is maximized and comparable to the values observed at the O to T PPB due to high reversible switching and intrinsic contributions.

The rhombohedral and tetragonal phase regions far from phase boundaries: The reduced free energy anisotropy[156], higher amount of crystallographically allowed polarization directions, reduced lattice distortion (Figure 5.2 (b))[328], and soft elastic character (Figure 5.14)[318,322,349] of the R phase implies that the transverse instability of P_s^i is enhanced leading to a favorable orientation of P_s^i along the applied electric field. This determines the low T_C (Figure 5.5), intermediate intrinsic response (Section 5.1.3.2.3), low $E(d_{33}^{max})$ (Figure 5.16) and E_c (Figure 5.24 (b)), high poling susceptibility[328], as well as the low thermal stability of d_{33} (Sections 5.1.3.2.1 and 5.1.3.2.2). Although the free energy anisotropy of the R phase should promote a high degree of poling, this was not observed (Figure 5.10). The low poling state of the R phase is a direct consequence of the high degree of reversible switching (Figure 5.21). This indicates that although switching and spatial orientation of polarization is promoted, it is not stable upon removal of the electric field due to back switching. This was corroborated by the findings of a relatively constant ferroelastic texture after high temperature poling treatment.[303,307] An opposite trend is expected for the T phase for all

of the aforementioned features due to free energy and elasticity considerations, as well as a larger lattice distortion (Section 5.1.1).[328] This means that the applied electric field to promote switching in the T phase is the highest among all phases, as indicated by the high $E(d_{33}^{max})$ (Figure 5.16) and E_c (Figure 5.24 (b)).[328] The enhanced thermal stability of the T phase is a result of the intrinsic contribution. In order to understand why the T phase has the highest intrinsic contribution, it should be noted that generally an intermediate lattice distortion is optimal for promoting switching and therefore maximum d_{33} or d_{33}^*. A high distortion provides a high strain per switching event but only few domains switch, whereas a lower distortion provides many switching events albeit with smaller individual contributions.[411] Although these are general concepts known from lead-containing ferroelectrics, Tutuncu *et al.*[348] corroborated that the BZT-BCT exhibits higher switching with reduced lattice distortion, indicating that small extrinsic contributions in the T phase are a result of its higher lattice distortion (Section 5.1.1).[328] It was also noted that the T phase features the so called hard-spring effect.[403] This terminology was employed since it was recognized that increasing temperature did not lead to increased s_{33}^E values (Figure 5.13 (a)), while properties such as Q_m (Figure 5.9 (e)) and N_{33} (Figure 5.13 (b)) increased with temperature or remain relatively constant. In general, Q_m, N_{33}, and other features such as the high power vibration velocity, are determined to a great extent by switching processes.[402,403,412] Quantification of extrinsic contributions (Section 5.1.3.2.3) indicated that the hard-spring effect featured by the T phase is a result of an overall decreased switching with increasing temperature. The overall decreased switching with temperature is ascribed to a considerable decrease of irreversible switching upon approaching T_C, which is not fully counterbalanced by the thermally activated reversible switching. The temperature profile of these extrinsic processes should also aid the thermal stability of the T phase. Although not treated here, defect chemistry of R and T phases may play an additional, distinct role on the properties of each phase and switching activity, since the internal bias-field developed is higher in the R phase as compared to the T phase. Moreover, highly asymmetric loops were reported after prolonged and/or high temperature poling treatments.[324,328]

The orthorhombic phase: Even with the consideration of the currently disputed symmetry of the interleaving region between R and T phases[318,322,325,331,333,341], it can be stated that it consists of a phase/s with the lowest average symmetry in all the pseudo-binary phase diagram of BZT-BCT. The role of low symmetry phases such as O or M has been pointed out in several works as a fundamental aspect to realize a high electromechanical response due to facilitated reorientation of P_s^i.[170-176] The results of this work indicate that the low symmetry interleaving region promotes non-180° domain switching (Figure 5.22) at reduced electric fields, indicated by the lowest $E(d_{33}^{max})$ (Figure 5.16) and E_C (Figure 5.24 (b)). The high degree of non-reversible switching enables a maximized d_{33}^{rem} and P_r, while the high overall switching contribution leads to considerably enhanced d_{33}^{max}, P_{max}, and d_{33}^*. It is also apparent that the retained P_r and reversible switching contributes significantly to achieving the highest k_{33} in the same region. The relative difference between d_{33}^{rem} and P_r of the O phase and the other phases is twice as much as the relative difference between d_{33}^{max} and P_{max}. This indicates that the predominant enhancement of electromechanical properties of the O phase is due to irreversible extrinsic switching contribution rather than reversible (Section 5.1.3.2.3). The high switching degree is ascribed to the high multiplicity of polarization states and considerably lower free energy anisotropy[156], which in turn

leads to a low barrier to reorient P_S^i and hierarchical domain morphology.[319,347] A reduced domain size was previously shown to affect mostly irreversible switching, leading to a pronounced enhancement of this strain contribution.[227] Moreover, the soft character (Figure 5.13 (a)) of the O phase and low thermal energy at room temperature are expected to favor irreversible switching due to the stress relief inherent to ferroelastic switching.[413,414] It should be pointed out that the low symmetry interleaving region does not depict the highest d_{33} (without bias-field input). Therefore, it is suggested that this region and its inherent domain morphology is more relevant to promote extrinsic contributions rather than intrinsic contributions to strain.

Polymorphic phase boundaries: The electromechanical response of the compositions close to the two PPBs is considerably distinct and warrants a separate analysis. The R to O PPB displays the highest d_{33}^*. In contrast, the O to T PPB features the highest d_{33} values, highest d_{33}^{max}, and nearly as high d_{33}^* as at the R to O PPB. Therefore, the strain contributions of both PPBs differ, as demonstrated in Figure 5.22. The main contribution at room temperature at the R to O phase boundary electromechanical response is intrinsic. This is considerably diminished with temperature, leading to thermally activated reversible switching becoming dominant. Irreversible switching is pronounced at the O to T phase boundary and additionally this boundary has a considerable reversible switching contribution, leading to the highest overall switching of BZT-BCT. The high irreversible switching of the O to T PPB near room temperature is ascribed to the same fundamental reasons as in the case of the O phase previously treated. However, multiplicity of polarization states should further increase the amount of crystallographically allowed switching possibilities due to phase coexistence. Moreover, softening along this phase boundary seems to be more dominant than at the O phase (Figure 5.13 (a)). The low thermal energy at room temperature promotes the irreversible nature of the switching processes. This makes sense, considering that high reversible switching would be indicated by lower P_r. The high reversible switching at the O to R PPB and irreversible switching at the O to T PPB are in agreement with the poling state found around the phase boundaries indicated by θ (Figure 5.9 (a)) and P_r (Figure 5.24 (b)) values. Similar to the O phase, the O to T PPB features a high d_{33}^{max} due to high overall switching contributions. Overall, enhanced extrinsic contributions also lead to large and almost equivalent d_{33}^* values at both PPBs, with reversible switching at the R to O PPB compensating for the lower amount of irreversible switching. Further analysis is required to elucidate the 30 % higher d_{33} at the O to T PPB, as compared to the R to O PPB. In fact, the relative difference of d_{33} reported in this work is quite similar to the 40 % difference reported in the literature.[322] It is noted that reversible switching contributes to the small signal properties. When the higher reversible switching observed at the R to O PPB is taken into consideration, the lower d_{33} of this phase boundary does not seem justified. Therefore, further reasoning will neglect extrinsic contributions and will be formulated for a monodomain single crystal. For ferroelectrics that have a centrosymmetric paraelectric phase, phenomenological piezoelectric and elastic equations are given in Table 5.2.[415]

Table 5.2: Electromechanical equations for ferroelectrics with different phases. Note that equations are valid for distorted materials arising from a centrosymmetric high temperature phase.[415]

Piezoelectric Coefficient	
R phase: $d_{33} \propto P_s(Q_{11}\varepsilon_{11} + Q_{12}\varepsilon_{12})$	**Equation 5.4.**
O phase: $d_{33} \propto P_s(Q_{11}\varepsilon_{33} + Q_{12}\varepsilon_{23})$	**Equation 5.5**
T phase: $d_{33} \propto Q_{11}P_s\varepsilon_{33}$	**Equation 5.6.**
Elastic Compliance	
R phase: $s_{33}^E \propto s_{11}^D + \{(Q_{11}^2 + Q_{12}^2)\varepsilon_{11} + (Q_{11}Q_{12} + Q_{12}^2)\varepsilon_{12}\}P_s^2$ $s_{33}^E \propto s_{11}^D + d_{33} + Q_{11}P_s + (\varepsilon_{12} + \varepsilon_{11})Q_{12}^2P_s^2$	**Equation 5.7**
O phase: $s_{33}^E \propto s_{11}^D + \{Q_{11}Q_{12}\varepsilon_{23} + (Q_{11}^2 + Q_{12}^2)\varepsilon_{33}\}P_s^2$ $s_{33}^E \propto s_{11}^D + d_{33} + Q_{11}P_s + Q_{12}^2\varepsilon_{33}P_s^2$	**Equation 5.8.**
T phase: $s_{33}^E \propto s_{11}^D + Q_{11}^2P_s^2\varepsilon_{33}$ $s_{33}^E \propto s_{11}^D + d_{33}Q_{11}P_s$	**Equation 5.9**

Equations in Table 5.2 indicate that d in all phases is proportional to Q, P_s, ε, and s (note that indexes are omitted to refer to norm of the coefficients). The values of $Q_{33} = 0.04$ m^4/C^2 for BZT-BCT were reported and are relatively insensitive to variations of composition and temperature.[350] This suggests that Q is not the parameter determining differences in electromechanical properties. Therefore, as a first approximation, variations in the Q values are neglected. For all symmetries the proportionality of d with P_s and ε is given as $P_s\varepsilon$, thus the multiplication of these parameters is analyzed. Considering that $\varepsilon \propto \varepsilon_r'$, either parameter could be chosen for the analysis. According to Zhang *et al.*[322] the O to T PPB features 15 % higher $P_r\varepsilon_r'$ than the R to O PPB at room temperature (Figure 3.6). For further discussion the difference between P_s and P_r should be noted. The former is an intrinsic property; however, the latter is determined by back switching processes (Section 2.2.1). Therefore, all ferroelectrics are characterized by $P_s \propto P_r$ and $P_s \geq P_r$. This indicates that the treatment from Zhang *et al.*[322] may underestimate the intrinsic contribution $P_s\varepsilon$. Apart from this polarization contribution, it is also seen from the equations in Table 5.2 that $d \propto s$. Several reports from literature found that the O to T PPB is elastically softer than the R to O PPB[318,322,349], in agreement with the results of Section 5.1.3.2.2. In order to evaluate the relative importance of both $P_s\varepsilon_r'$ and s_{33}^E, Table 5.3 introduces the compositional and temperature coordinates for both PPBs and the ratios of each intrinsic contribution (*i.e.*, $\frac{(P_s\varepsilon_r')_{R-O}}{(P_s\varepsilon_r')_{O-T}}$ and $\frac{(s_{33}^E)_{R-O}}{(s_{33}^E)_{O-T}}$). Note that due to the

limited compositional range investigated, approximation of the actual compositional coordinates of the PPBs was done. Comparisons were made at the same temperature to minimize thermal effects.

Table 5.3: Relative contribution of $P_s\varepsilon_r'$ and s_{33} to the intrinsic contribution of each PPB. Note that ε_r' values were taken at 1 kHz and P_s was estimated as the value at zero-field derived from the tangent line drawn from the saturated polarization of bipolar loops measured at 5 Hz. Coordinates of PPBs and compositions considered for the analysis are provided.

Temperature coordinate (°C)	R to O PPB		O to T PPB		$\frac{(P_s\varepsilon_r')_{R-O}}{(P_s\varepsilon_r')_{O-T}}$	$\frac{(s_{33}^E)_{R-O}}{(s_{33}^E)_{O-T}}$
	Composition coordinate (mol BCT)	Composition considered for analysis (mol BCT)	Composition coordinate (mol BCT)	Composition considered for analysis (mol BCT)		
25	0.43	0.45	0.51	0.50	0.92	0.96
30	0.42	0.40	0.5	0.50	0.72	0.81
35	0.41	0.40	0.48	0.50	0.91	0.87
40	0.4	0.40	0.46	0.45	1.02	0.93
45	0.38	0.37	0.44	0.45	0.81	0.87
50	0.37	0.37	0.41	0.40	0.86	0.95

All of the $P_s\varepsilon_r'$ and s_{33}^E relative ratios are below 1 (with exception of $P_s\varepsilon_r'$ at 40 °C, which is close to 1) indicating that intrinsic contributions are higher at the O to T phase boundary rather than at the R to O phase boundary. In a similar BT-based system, Wang *et al.*[342] also demonstrated that enhanced properties occurred along the O to T phase boundary. In fact, this general feature of BT-based piezoceramics was first predicted by the Devonshire phenomenological theory for monodomain single crystals.[415] From equations in Table 5.2 it is noted that both R and O phases possess shear components of Q, ε, and s. In contrast, the elastic and piezoelectric response of T phase can be described solely with hydrostatic components. This implies that the divergence of shear components of the elastic compliance $s_{44}^E = s_{55}^E$ at the O to T phase boundary is much steeper than the divergence of $s_{55}^E = s_{66}^E$ at the O to R phase boundary.[415,416] This result can be qualitatively explained by enhanced elastic shear occurring in the *yz* or *xz* planes due to the transition from the T to the O phase rather than in the transition from the O to the R phase. In other words, as P_s^i reorients between [100] and [110] directions, higher shear components are encountered than

when P_s^i reorients between [110] and [111] directions. Although enhanced elastic shear softening was predicted for monodomain single crystals, this effect was also shown experimentally in polycrystalline materials. Xue *et al.*[341] demonstrated for BZT-0.50BCT, that at the O to T phase boundary s_{44}^E = 37.6·10^{-12} m^2/N, which is comparable to soft PZT, and almost double that the s_{44}^E of BT. This result is to be expected considering that the monodomain properties will be reflected in polycrystalline averages as obtained, for example, using the Voigt-Reuss-Hill method.[41] Therefore, the fundamental reason behind higher values of s_{33}^E and s_{33}^D along the O to T phase boundary in BT-based ceramics is due to enhanced shear components of electrostrictive coefficients and elastic compliances.[160,163,415] Note that coupling between elastic and dielectric properties implies that the enhancement mechanism can be assigned to a dielectric transverse instability of P_s^i. Previous works highlighted the role of the O phase in BZT-BCT or the M phase in PZT leading to enhancement of piezoelectric properties.[318] This work reveals, however, that the interleaving region is not the fundamental reason for enhancement of transverse components but rather the phase boundaries are. Among several interferroelectric phase boundaries, maximization of intrinsic properties would be attained at those boundaries that maximize transverse instabilities more strongly. However, low symmetry phases will remain technologically relevant since they favor switching, as previously discussed. Therefore, maximized piezoelectric activity at phase boundaries is ascribed to an optimized combination of enhancement of both small and large signal properties, although different phase boundaries feature different strain contributions.

Convergence region: The term "convergence region" was implemented to highlight the experimental difficulty to assess phase boundaries in this temperature and compositional range. Either two triple points or an invariant quadruple point are thermodynamically feasible (Section 5.1.3.1). The high d_{33} featured in the convergence region may be partially ascribed to intrinsic contributions (Figure 5.22) due to maximized elastic softening (Figure 5.13 (a)) and to negligible free energy anisotropy, regardless of criticality.[156] Nonetheless, the convergence region features d_{33} values that are 30 % lower than the values at the O to T PPB. This cannot be reconciled with the aforementioned reasoning, since s_{33}^E and $\varepsilon_r^{'}$ values are maximized in the convergence region (Figure 5.22). Therefore, the parameter leading to reduced intrinsic contributions is the reduced poling state, which also results in a lower P_s (Figure 5.10). In contrast to previous assumptions[194], reduced free energy anisotropy is necessary[160] for enhanced properties but not sufficient for achieving a maximized d_{33}. In other words, considering that the elastic properties are comparable in the convergence region and at the O to T phase boundary, maximized d_{33} occurred along the O to T phase boundary due to a higher retained poling state (Figure 5.10) and P_s. The ability of the system to retain its poling state is, therefore, crucial in attaining a high d_{33}. Although d_{33} values were reduced due to the thermal depolarization, the bias-field input effectively poles the material at each isotherm (Section 5.1.3.2.3) leading to comparable d_{33}^{max} values between convergence region, PPBs, and O phase. Moreover, a high reversible switching contribution is depicted in the convergence region (Figure 5.22). Domain size, morphology, mobility, and activation barrier play a major role in determining the switching processes.[73,165] All these variables are especially relevant for the convergence region due to free energy degeneracy leading to hierarchical domain morphology[183] and the higher temperatures leading to increased mobility and lower activation barrier for switching. The high reversible switching enables a maximized P_{max} (Figure 5.26).

Nonetheless, d_{33}^{*} values are considerably lower than at either of the PPBs. These last two observations can be reconciled either by the assumption that reversible switching at convergence region has a considerable 180° domain contribution (not measurable with the technique of d_{33} under bias-field) or by having relatively small contribution to the strain from non-180° reversible switching events. The latter can be explained by considering that a reduced lattice strain will promote switching although only small strain output (as previously discussed). Keeble *et al.*[333] revealed that local distortions from a C phase are very small at temperatures near the convergence region supporting the latter assumption. This means that the expected longitudinal instability of P_s^i at the convergence region is not as effective for strain enhancement as the transverse instability of P_s^i treated for PPBs.

Implications: Although the findings of this section are mostly relevant for BT-based ceramics, an analogy to PZT can be made. Singh *et al.*[417] found that the highest d_{33} does not occur in the M phase bridging the R and T phases in PZT. Rather the piezoelectric activity is highest in the T phase upon approaching the T to M phase boundary. This behavior was attributed to an anomalous softening reflected by an increased s_{11}^E.[417] Therefore, it can be suggested that an analogy may exist when the P_s^i shifts through shear from the [100] direction to another direction corresponding to the M phase. In fact, Sabat *et al.*[401] showed that the s_{55}^E is more than two times higher than all of the other elastic compliance components near the T to M phase boundary. This reasoning leads to a possible generalization: the different responses of the shear components of elastic compliance across differing types of phase boundaries involving a transverse instability of P_s^i are important considerations in attaining a maximized electromechanical response.[187,416] If a change in composition and/or temperature leads to a transition from a T phase to a lower symmetry phase (such as O or M), an increase of shear constants is expected that is much more pronounced that it would be at a transition from a R phase to one of these lower symmetry phases. Maximization of intrinsic piezoelectric properties will be attained at phase boundaries that feature reduced free energy anisotropy, high softening, and high P_s (P_r). Neither the reduced free energy anisotropy, nor elasticity, nor high P_s (P_r) alone can be considered as sufficient conditions to attain maximized piezoelectric properties.[318] Therefore, in a system with several interferroelectric phase transitions (such as BT, BZT-BCT, or PZT) it is expected that maximized properties occur at the phase boundary that gives the greatest shear softening, provided that similar levels of reduced free energy anisotropy and P_s (P_r) are maintained.

This intrinsic strain mechanism rationalization mostly remains valid for commensurate materials that feature a FD transverse instability of P_s^i. For the case of $PbTiO_3$, for instance, which exhibits only a T ferroelectric phase below T_C, the shear effect described is absent.[416] In this case, other competing instabilities such as the FD longitudinal instability of P_s^i or an AFD rotational instability of octahedra may be the source of strain mechanism enhancement. Although these implications are mostly relevant for intrinsic contributions, extrinsic contributions are in close relation to these instabilities since switching can in fact be considered as a collective instability of P_s^i, although it also depends on extrinsic factors.[157] It is apparent that the maximization of extrinsic properties will be preferentially achieved in low symmetry phases and at phase boundaries.[227] The dominance of reversible or irreversible switching processes in general will be controlled by several other factors such as domain size, morphology, mobility, activation barrier, among others.[73,165]

5.2 The (1-x)($Bi_{1/2}Na_{1/2}$)TiO_3-x$SrTiO_3$ System

5.2.1 Synthesis Study

Figure 5.31 (a) provides the TGA and DTA results obtained during heating of a homogeneous stoichiometric mixture of raw oxides and carbonates employed for the synthesis of BNT-0.25ST. The simultaneous FT-IR analysis of outgassing species is depicted in Figure 5.31 (b). The DTA curve indicates a process with three steps characterized by two exothermic peaks at 270 °C marked with $\boxed{a}$, and two endothermic peaks at 600 °C and 790 °C marked with $\boxed{b}$ and $\boxed{c}$, respectively.

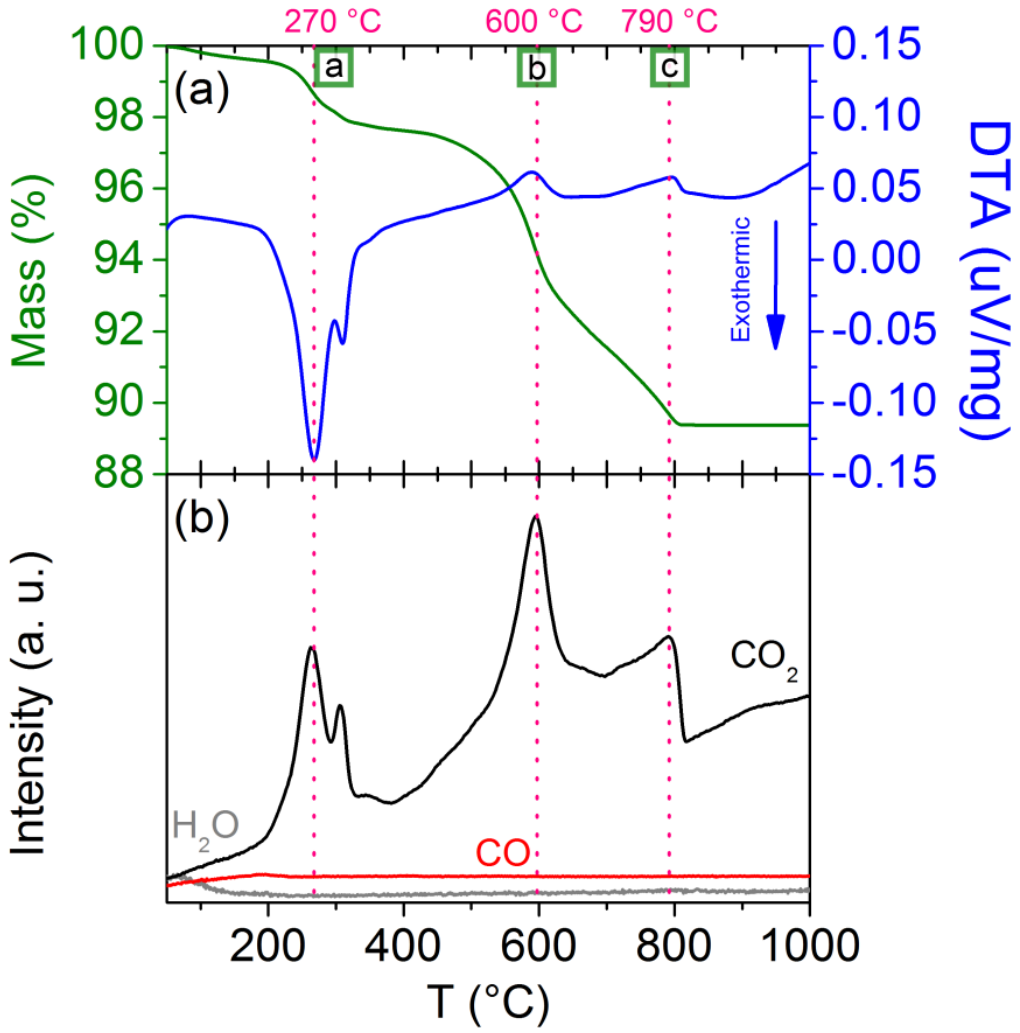

Figure 5.31: Thermal analysis of a homogeneous stoichiometric mixture of raw oxides and carbonates employed for the synthesis of BNT-0.25ST. (a) TGA and DTA and (b) FT-IR gas analysis. The gas evolution curves were drawn from the integration of selected FT-IR band ranges along the temperature axis (H_2O: 3753-3731 cm^{-1}, CO: 2116-2094 cm^{-1}, and CO_2: 2378-2302 cm^{-1}).

The initial mass loss of 2.2 % marked with $\boxed{a}$ is concluded at 330 °C and can be attributed to the evaporation of the adsorbed atmospheric water and CO_2, as well as burn-out of minor amounts of organic contaminants. The main mass loss of 8.4 % detected in the temperature range between 400 °C and 800 °C consists of two endothermic processes marked with $\boxed{b}$ and $\boxed{c}$. The CO_2 peaks in the FT-IR spectra indicate that these endothermic reactions are due to chemical decomposition of the raw carbonates. The 8.4 % mass loss of both processes is in good agreement with the theoretical mass loss of 8.6 %, calculated for the investigated stoichiometric mixture due to decomposition of the carbonates and CO_2 evaporation. According to Kainz *et al.*[418], the reaction between Bi_2O_3, Na_2CO_3, and TiO_2 begins at 450 °C (for powders with an average particle size of 0.5 µm) and leads to the first formation of the perovskite BNT phase at 530 °C. This result suggests that the mass loss below 600 °C can be mostly attributed to the decomposition of Bi_2O_3, Na_2CO_3, and TiO_2. The endothermic peak marked with $\boxed{b}$ can be thus assigned to the formation of BNT. It should also be noted that the irreversible transformation of anatase to rutile is generally reported to be at $\sim$ 600 °C and may also contribute to a certain extent to this endothermic peak.[419] The initial reaction between $SrCO_3$ and TiO_2 (anatase) was found to begin at 560 °C (for an average particle size of 0.2 µm). It was reported that the decomposition of $SrCO_3$ begins at 840 °C and leads subsequently to the formation of a pure ST perovskite phase at 1000 °C.[360,361] Therefore, the mass loss above 600 °C can be mostly attributed to the decomposition of $SrCO_3$. The endothermic peak marked with $\boxed{c}$ is thus a result of the chemical reaction between $SrCO_3$ and TiO_2 leading to the formation of ST, as well as the reaction between ST and the BNT formed at lower temperatures.

In order to corroborate the sequence of reactions proposed from thermal analysis, Figure 5.32 (a) introduces the XRD patterns obtained from homogeneous stoichiometric mixtures of raw oxides and carbonates employed for the synthesis of BNT-0.25ST, heated to a given temperature, and subsequently quenched in air. Up to 450 °C, XRD patterns remain unaltered, confirming the evaporation of the adsorbed atmospheric water and CO_2, as well as burn-out of minor amounts of organic contaminants previously suggested by thermal analysis. The XRD pattern corresponding to the powder quenched from 600 °C revealed decreased intensities of the main reflections of the raw powders Bi_2O_3, TiO_2, $SrCO_3$, and Na_2CO_3. Furthermore, the first indication of a perovskite phase is given by the reflection at 32.5° attributed to the $(110)_{pc}$ perovskite reflection. The XRD patterns obtained from the powder quenched from 700 °C and 850 °C already resemble the diffractograms of a perovskite phase, although the presence of unreacted $SrCO_3$ powders is still observed. A close-up of the angular range between 24° and 32° is displayed in Figure 5.32 (b). Normalized tick marks for Bi_2O_3 (crystallographic card: 03-065-2366), TiO_2 (crystallographic card: 00-021-1272), $SrCO_3$ (crystallographic card: 00-005-0418), Na_2CO_3 (crystallographic card: 00-037-0451), BNT (crystallographic card: 01-089-3109), and ST (crystallographic card: 00-035-0734) are also provided for comparison. The peaks at 26.9°, 27.37°, and 28° can be attributed to Bi_2O_3 without any overlap (actually overlap of a peak corresponding to Na_2CO_3 occurs, but can be neglected due to its low intensity). The XRD pattern obtained from quenched powders from 700 °C indicates the complete reaction of Bi_2O_3. This suggests an almost complete formation of BNT, in agreement with the process marked with $\boxed{b}$ in Figure 5.31.

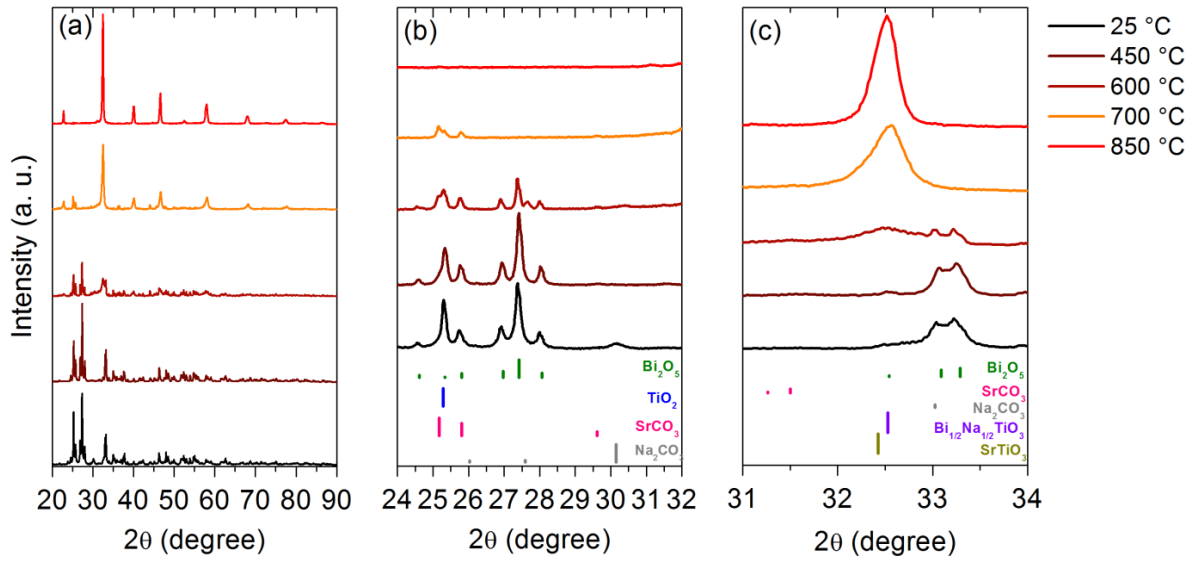

Figure 5.32: XRD patterns obtained from homogeneous stoichiometric mixtures of raw oxides and carbonates employed for the synthesis of BNT-0.25ST, heated to a given temperature, and subsequently quenched in air. (a) Complete angular range investigated. (b) and (c) close-up regions where the diffraction peaks with maximum intensity appeared. The sets of tick marks represent the reflections associated with relevant phases obtained from crystallographic databases. Tick lengths are proportional to diffraction peak intensities.

A close-up of the angular range between 31° and 34° is displayed in Figure 5.32 (c), which corroborates the presence of BNT at 600 °C with appearance of a reflection at 32.48°. It is also found that the reflection corresponding to Na_2CO_3 at 30.15° features negligible intensity at 700 °C. Although the BNT perovskite phase is formed already at 700 °C, the reflection at 25.28° indicates the presence of TiO_2 anatase phase at this temperature. Moreover, the reflections at 25.17° and 25.81° also indicate the presence of $SrCO_3$. Therefore, the decomposition and reaction between TiO_2 and $SrCO_3$ remains active above 700 °C in agreement with the process marked with $\boxed{C}$ in Figure 5.31. Note that for all temperatures the reflection corresponding to rutile at 36.5° (which is not overlapped) remained quite low (crystallographic card: 01-089-4920). This indicates that anatase reacted to form BNT rather than forming rutile as intermediary phase. The $(110)_{pc}$ perovskite reflection at 32.5° remains slightly asymmetric even at 850 °C, which suggests the presence of two perovskites phases with slightly different lattice parameters. Differences in lattice parameters can be ascribed to different ST contents throughout the powder considering that the formation of BNT and ST are diffusion controlled processes.[360,361,418] Therefore, the different temperature formation characteristic for BNT and ST, as well as a diffusion controlled reaction, are suggested to be the origin of the formation of a heterogeneous microstructure for BNT-ST, as will become apparent in Section 5.2.3 and was previously observed in the literature.[258]

5.2.2 Atomic Characterization

Figure 5.33 provides the XRD patterns for the calcined powder and sintered samples. Note that crushed and annealed sintered samples were used for the experiment. The diffractograms can be ascribed to a perovskite structure, although the presence of secondary phases in calcined powders is observed and marked with *. Indexing was performed for a pseudocubic structure, and pc denotes pseudocubic Miller indices.

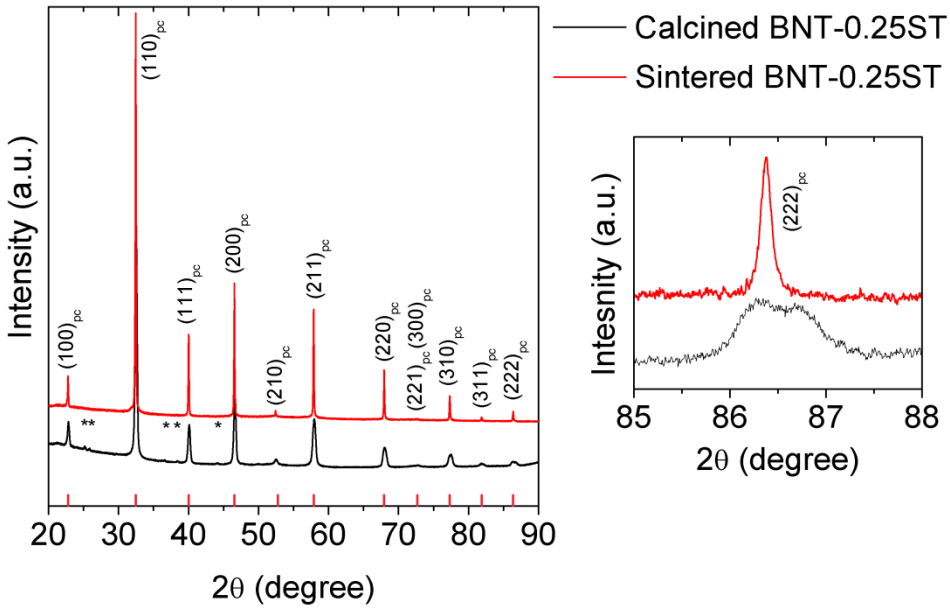

Figure 5.33: XRD pattern of calcined and sintered BNT-0.25ST. Second phases are marked with *. Magnification of the $(222)_{pc}$ peak is also displayed. Primary phase peaks are marked with the corresponding planes of the cubic perovskite structure.

In contrast to XRD patterns displayed in Figure 5.32, a monochromator was employed to filter Cu $K_{\alpha 2}$ radiation in order to allow a better distinction of reflection splitting due to lattice distortions. The high angle reflections of the calcined powder indicates peak splitting, as visible in the magnified view of Figure 5.33 in the $(222)_{pc}$ reflection. The high angle peak splitting can be attributed to the diffraction of a heterogeneous material with the presence of two perovskite phases with different lattice parameters based on the results from the previous section, as well as the negligible non-cubic distortions of BNT-0.25ST reported in the literature.[248,356] Moreover, in agreement with literature[248,356], the sintered sample features sharp and narrow peaks ascribed to a pseudocubic perovskite structure with no obvious splitting in either the $(111)_{pc}$, $(222)_{pc}$, $(100)_{pc}$, or $(200)_{pc}$ reflections. It should be noted that small FD distortions are a common feature of several BNT-based lead-free materials.[141] In general, this is due to competing FD and AFD instabilities.[367] In order to corroborate the existence of AFD instabilities leading to octahedral tilting, neutron

diffraction was performed because this technique is sensitive to the position of all O^{2-} isotopes due to their relatively large neutron scattering length.[420] *In situ* electric field and orientation-dependent neutron diffraction patterns are displayed in Figure 5.34 in the most relevant 2θ angular range to investigate the presence and the changes under electric field of $½(311)_{pc}$, $(111)_{pc}$, and $(200)_{pc}$ reflections. It is noted that no presence of $½(310)_{pc}$ corresponding to a $P4bm$ symmetry was observed, thus the angle corresponding to this reflection is omitted. Figure 5.34 (a) provides the pattern under electric field and in the remanent state for the sample with an orientation angle ω = 33°, whereas (b) introduces the pattern under electric field and in the remanent state for the sample with ω = -57°. The virgin state almost perfectly mimics the remanent state and is not displayed. Since a diffraction pattern in polycrystalline materials is composed of intensities of randomly oriented diffracting grains in space that fulfill the Bragg condition[379], grains leading to $½(311)_{pc}$, $(111)_{pc}$, and $(200)_{pc}$ reflections do not necessarily coincide. The diffraction patterns presented in Figure 5.34 indicate the two extreme cases where the scattering vectors k_{hkl} are parallel (ω = 33°) or orthogonal (ω = -57°) to the applied electric field, respectively. From now the scattering vectors are referred to as k, since the spatial grain orientation for the analyzed cases compensates the spatial orientation of k.

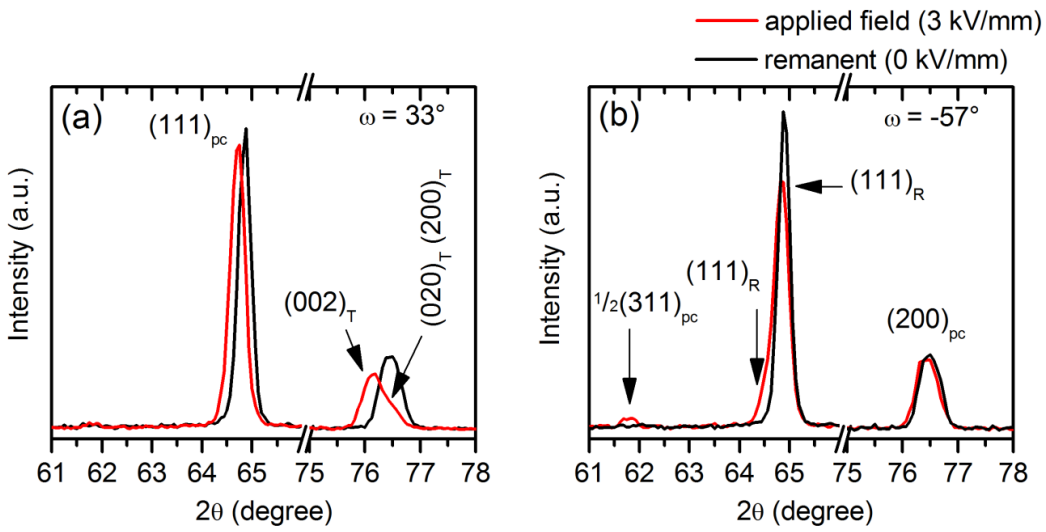

Figure 5.34: Selected angular range of *in situ* neutron diffraction pattern depicting the most relevant reflections for (a) ω = 33° and (b) ω = -57°.

In the remanent state, the $(111)_{pc}$ and $(200)_{pc}$ display features corresponding to a material with small non-cubic distortions. This result is in agreement with the high resolution XRD results from sintered samples (Figure 5.33). Even though patterns of Figure 5.34 are plotted in a logarithmic scale, the $½(311)_{pc}$ SSR cannot be distinguished from the background indicating a commensurate phase. Upon the application of an electric field of 3 kV/mm, the $½(311)_{pc}$, $(111)_{pc}$, and $(200)_{pc}$ reflection positions and intensities vary significantly from the remanent state and with sample orientation. For the case of $E \| k$ (Figure 5.34 (a)), the maximized shift in position of the main reflections indicates a strong electric field induced lattice strain. Apart from lattice strain, the considerable shift of the $(200)_{pc}$ and the apparent asymmetry of the reflection indicates peak

splitting ascribed to texturing as indicated by the indexing performed for a T material with reflections corresponding to the $(002)_T$ and $(020)_T/(200)_T$ lattice planes. The pronounced splitting of the $(200)_{pc}$ indicates the presence of a T phase. It is noted that the absence of $½(311)_{pc}$ SSR indicates that the $R3c$ symmetry previously observed in the BNT-ST with low ST content[366] is not favored for this orientation and the electric field induced phase is commensurate. Moreover, since the $½(310)_{pc}$ was not visible neither with nor without applied electric field, the most probable symmetry for the T phase is $P4mm$ with polarization along [001]. Although a certain small amount of asymmetry becomes apparent in the $(111)_{pc}$ is not as clear as in $(200)_{pc}$. For the case of $E \perp k$ (Figure 5.34 (b)), main reflections are only slightly shifted from their positions. A considerable change of the $(111)_{pc}$ reflection is discerned for this sample orientation suggesting texturing. The two $(111)_R$ peaks resulting from the texturing effect under electric field are marked. The presence of the $½(311)_{pc}$ SSR with a non-zero intensity indicates that an incommensurate phase was nucleated with electric field. The $½(311)_{pc}$ SSR are a result of either an increase in the correlation length of the octahedral tilting with respect to the virgin/remanent state that was formerly below the detection limit of the measurement or to a non-zero $(a^-a^-a^-)$ octahedral tilt angle.[366] In either case, the results suggest the presence of a R phase with $R3c$ symmetry and polarization along [111]. Therefore, the results indicate a selective orientation-dependent electric field induced phase transformation to either R or T phase. Moreover, the features of the $½(311)_{pc}$, $(111)_{pc}$, and $(200)_{pc}$ reflections indicating a pseudocubic structure in the remanent state suggest that the electric field induced processes described are almost entirely reversible. In order to give further insight into the orientation-dependent phase transition, Figure 5.35 provides a contour plot of the $½(311)_{pc}$, $(111)_{pc}$, and $(200)_{pc}$ reflection intensities as a function of sample orientation ω and 2θ angular range. The cases previously analyzed for $E \| k$ and $E \perp k$ are marked by a white line. Note that the lines indicating each orientation with respect to the applied electric field have a non-zero slope since ω = 90° represents the electric field vector parallel to the incident beam. The contour plot in the remanent state (Figure 5.35 (a)) displays orientation independent intensities and positions corroborating the reversibility of the phase transition. In contrast, application of an electric field leads to a maximized shift in the peak position observed for $E \| k$, although considerable peak shift is featured in a relatively broad ω range of 60° around the 33° sample orientation (Figure 5.35 (b)). This angular range indicates negligible intensity of the $½(311)_{pc}$ SSR, similar to the virgin and remanent states. Note that the negligible intensity of the $½(311)_{pc}$ SSR cannot be assigned to texturing, since this reflection does not admit splitting. Vanishing of the $½(311)_{pc}$ SSR intensity may be explained by considering that this reflection is closer to $\langle 00l \rangle$ family of directions, than to the $\langle hhh \rangle$ ones. Therefore, the pseudocubic phase seems to transform preferentially under electric field to the T phase for the grains satisfying the Bragg condition oriented along the $½(311)_{pc}$. For the ω range near $E \perp k$, the main reflections are slightly shifted to higher diffraction angles indicating macroscopic shrinking perpendicular to the electric field direction. Meanwhile, the $½(311)_{pc}$ SSR display a non-zero intensity in a considerably broad ω range. Therefore, it can be concluded that an orientation-dependent reversible phase transformation from a commensurate virgin state to an incommensurate state under electric field is observed, with the exception of grains satisfying the diffraction condition of the $½(311)_{pc}$ for $E \| k$ where the intensity of the SSR remains negligible.

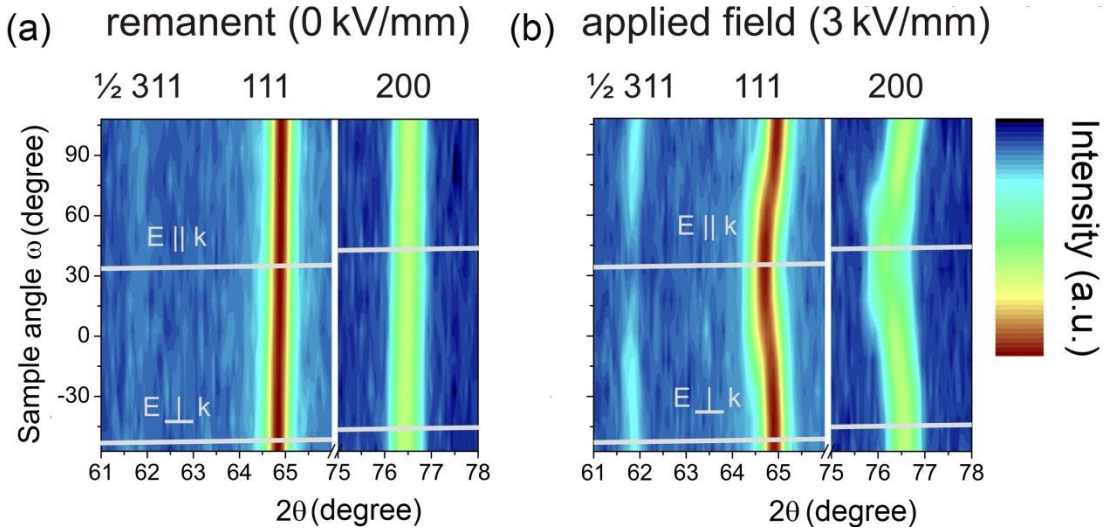

Figure 5.35: *In situ* neutron diffraction patterns of the remanent state at 0 kV/mm and applied electric field at 3 kV/mm for different sample orientation angles. The cases corresponding to $E \| k$ (ω = 33°) and $E \perp k$ (ω = -57°) are marked. The resolution of the contour plot in the ω-θ space is indicated by 274 x 12 experimental data points.

5.2.3 Microstructure Characterization

The heterogeneity of BNT-0.25ST discussed in Sections 5.2.1 and 5.2.2 is revealed by BF TEM of calcined powders in Figure 5.36 (a), which was taken along <112>$_{pc}$ zone axis. Figure 5.36 (b) introduces a DF micrograph obtained using the R ½{ooo} SSR. The difference in contrast in both images is ascribed to different crystallographic orientations of the core and shell suggesting the presence of an incoherent interface. This result is in agreement with the XRD results of calcined powders (Figure 5.33).

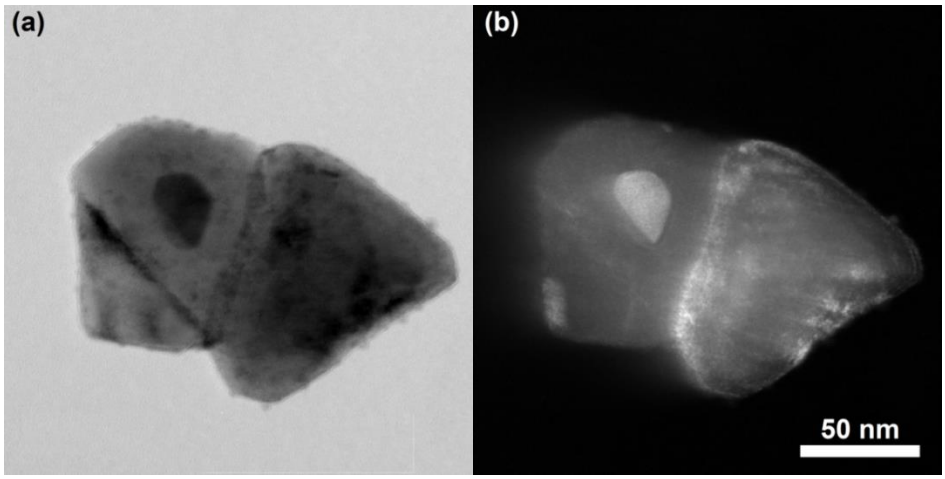

Figure 5.36: (a) BF micrograph of calcined powder particles taken along <112>$_{pc}$ zone axis. (b) DF image using ½{ooo} SSR.

Figure 5.37 (a) displays the polished surface of BNT-0.25ST obtained using the BSE mode of the SEM. An average grain size of (2.2 ± 0.4) µm and a relatively dense microstructure with relative density above 95 % were obtained in the sintered samples. The heterogeneous structure of the calcined powder persists in the sintered samples. The secondary phase inside several grains has an average size between 180 nm and 360 nm. From here on, this chemically heterogeneous morphology will be termed a core-shell structure, as pointed out in Figure 5.37 (a). The core-shell microstructure is characterized mostly by $(1_4; 1_\infty)_s$ and $(1_5; 1_\infty)_s$ geometries (Appendix I introduces the nomenclature proposed), although several shells with further mirror planes are also found. In order to obtain a statistical representative qualitative view of the compositional difference between core and shell, EDS experiments were performed in several core and shell constituents. Figure 5.37 (b) provides an average EDS spectra in the energy range of interest. The peak marked with * corresponds to the signal of Al obtained from the sample holder. No differences in the amount of Ti^{4+} were observed between core and shell. However, the core features a higher Bi^{3+} and Na^{+} content, while shell features a higher Sr^{2+} content. Since Bi^{3+} is the element with highest atomic number in BNT-ST, it determines the bright contrast of cores in Figure 5.37 (a). It should be noted, however, that quantification of the chemical composition of core and shell with EDS is avoided since it would give incorrect results because the volume of interaction of secondary electrons is expected to be higher than the core size. It should also be noted that the different absorption rates of the species involved would lead to artifacts without a proper calibration step.[421]

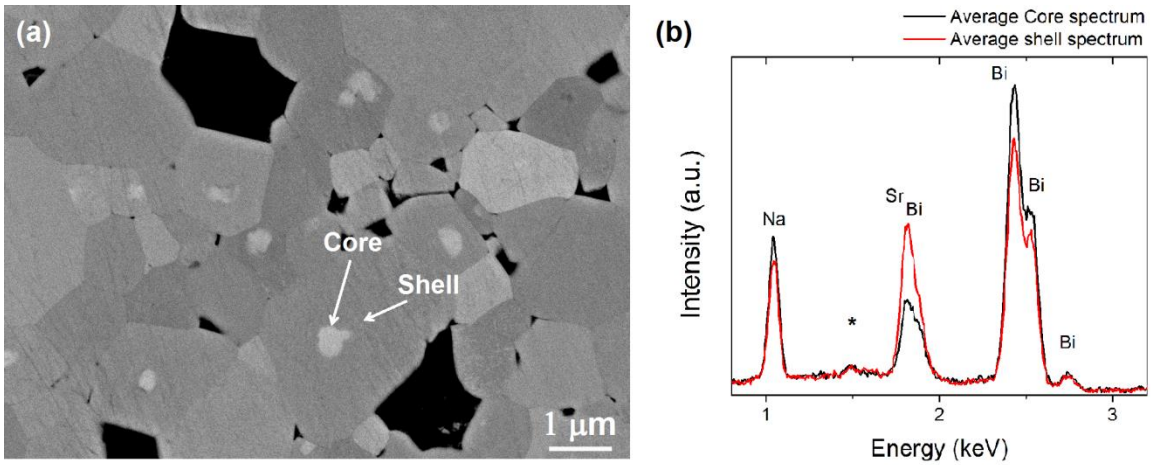

Figure 5.37: (a) As-sintered, polished surface of BNT-0.25ST sintered for 2 h at 1150 °C. The image was taken with a SEM in the BSE mode. (b) Average EDS spectrum obtained from several cores and shells. *Indicates that the peak at 1.48 keV corresponding to Al is observed due to the signal obtained from the sample holder.

Figure 5.38 (a) provides a BF TEM image of the core-shell microstructure of the sintered sample. A strong diffraction contrast indicates local deviations from cubic symmetry in terms of R and T octahedral tilting. The core contains a set of complex and irregular aligned domains with the size of several hundred nanometers. The shell exhibits a finely dispersed grainy contrast. No dislocation contrast could be observed suggesting a semicoherent interface between the core and shell.[253,257,285,422-425] It was demonstrated that dislocations, which lead to a gradual increase of incoherency, are a result of local strains.[426] This supports the findings of the XRD studies in the sintered samples (Figure 5.33) considering that the beam coherence length (~ 80 nm) should allow partial detection of core and shell. Domains tend to smear out at the outer edges of the core, indicating that there is no sharp boundary between core and shell.[427] Towards the core-shell interface, the tips of the domain walls feature a wedge-shaped. This morphology reduces the electrostatic energy in comparison to that of charged fine domain walls, since the charges involved can be distributed over a larger area.[428] Formation of these types of domain morphology indicates the presence of charge carriers and/or local stresses.[37,428] Note that the latter should not be considerably high since no dislocation contrast was observed. However, both effects may play a role in BNT-0.25ST, since local strain gradients are a common feature in core-shell materials[427] and the difference in polarization states of the constituents leads to a Maxwell-Wagner effect.[429]

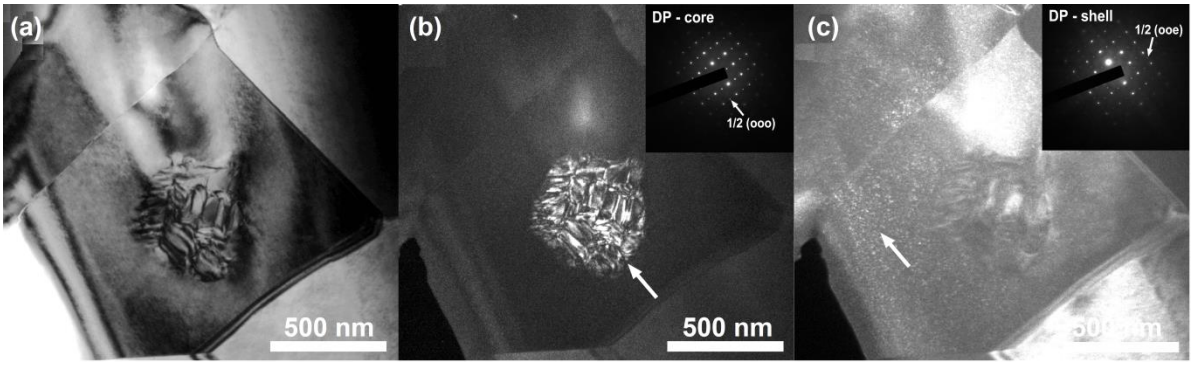

Figure 5.38: (a) BF micrograph of one representative grain with a core and a shell. SAED patterns of core and shell were obtained along <112>$_{pc}$ zone axis and depict the presence of two particular types of SSR. (b) DF micrograph using ½{ooo} SSR. (c) DF micrograph using a weak ½{ooe} SSR.

Figure 5.38 (b) depicts a DF micrograph obtained using the R ½{ooo} SSR revealing an excited contrast in the core region marked with an arrow. The discussed wedge-shaped nanodomain morphology becomes clearer in this image. Encompassing the weaker T ½{ooe} SSR for image formation, however, results in a faint stimulation of the nano-sized platelets marked with an arrow in the shell region of Figure 5.38 (c). The contrast of these platelets is attributed to the existence of a fine nanodomain-like pattern of much smaller size than in the core. The associated SAED patterns of core and shell along the <112>$_{pc}$ zone axis are introduced as insets in Figure 5.38 (b) and (c), respectively. Bright fundamental perovskite reflections without indication of spot splitting are visible. By overexposure of the SAED patterns two types of SSR can be discerned. As previously

reported in other BNT-based lead-free systems, T ½{ooe} and R ½{ooo} SSR are observed.[430,431] Similar to the XRD patterns, indexing was performed for a pseudocubic structure. The SSR are induced either by $(a^0a^0c^+)$ octahedral tilting corresponding to a $P4bm$ symmetry or $(a^-a^-a^-)$ octahedral tilting corresponding to a $R3c$ symmetry.[432,433] It was noted that in the virgin state the average structure of BNT-0.25ST is pseudocubic (Section 5.2.2). From TEM studies, however, it becomes apparent that even the virgin state displays tilt systems corresponding to the $R3c$ and $P4bm$ space group. Similar discrepancies were reported in a comparative study between TEM and neutron diffraction in other BNT-based materials.[434] Discrepancies between both experimental techniques can be understood by recognizing the relatively short length-scale that TEM analyses in comparison to the larger volume averaged probed by neutron diffraction. In other words, the short correlation length of $(a^0a^0c^+)$ and $(a^-a^-a^-)$ octahedral tilting systems in BNT-0.25ST leads to an overall negligible contribution to the diffraction patterns depicted in Section 5.2.2. The differences in crystallographic structure between core and shell are ascribed to difference in the chemical composition between these constituents, as statistically treated in Figure 5.37 (b). In order to corroborate the chemical difference between core and shell locally, EDS in STEM mode was performed on a representative core-shell (Figure 5.39).

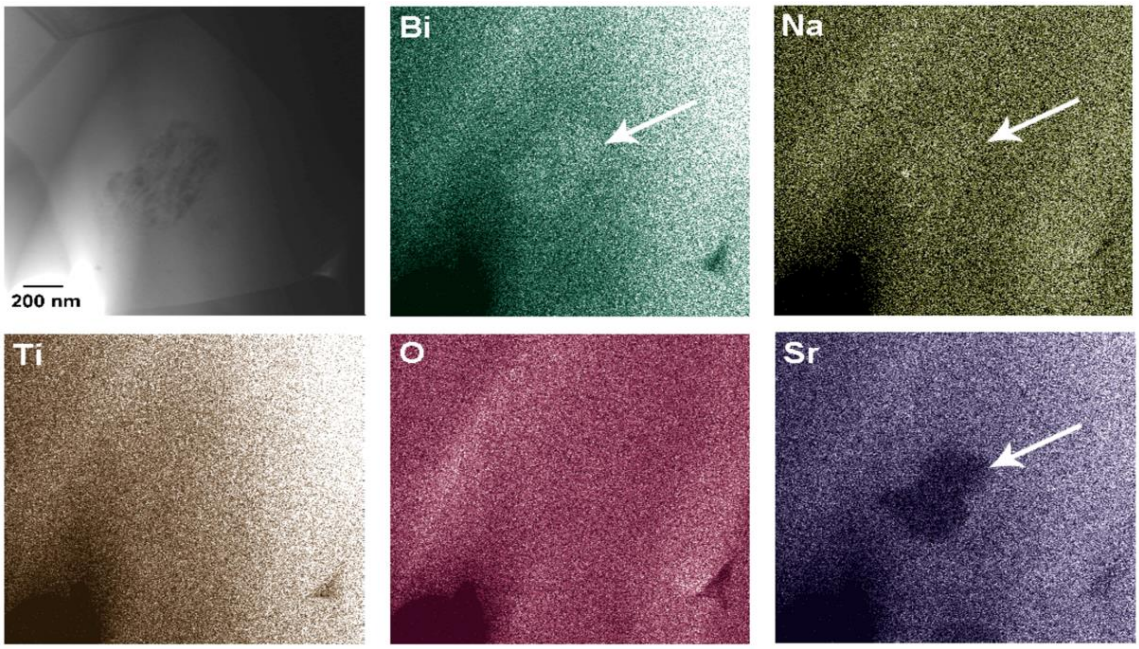

Figure 5.39: BF STEM micrograph of a representative grain with chemical element maps recorded for Bi^{3+}, Na^{+}, Ti^{4+}, O^{2-}, and Sr^{2+}.

The results are consistent with the statistical analysis depicted in Figure 5.37 (b). This indicates that the diffraction contrast of the core is a result of a lower $Sr^{2+}/(Bi^{3+},Na^{+})$ ratio, as compared to the shell. Therefore, two different physical features distinguish the core and shell: chemical contrast and diffraction contrast. It was corroborated that increasing the content of Sr^{2+} substitution leads to the weakening of dipoles and disturbance of the long-range coupling between Na^{+} and Bi^{3+}.[365]

Therefore, similar to the investigation of Lee *et al.*[365], shells characterized by a higher $Sr^{2+}/(Bi^{3+},Na^{+})$ ratio feature only nano-sized platelets indicating an area devoid of domains. This entails that the non-ergodic relaxor state of BNT-0.25ST can be mostly correlated with a $Sr^{2+}/(Bi^{3+},Na^{+})$-depleted core embodying domain-like contrast (Figure 5.38 (b)). On the other hand, the ergodic relaxor state is attributed mostly to the shell since it displays nano-sized platelets (Figure 5.38 (c)). The non-ergodic cores and ergodic shells lead to a distribution of ergodicity on the macroscopic scale that determines the functional properties of the system, as it will become apparent in the subsequent sections. The *in situ* evolution of the core-shell as a function of temperature is introduced in Figure 5.40.

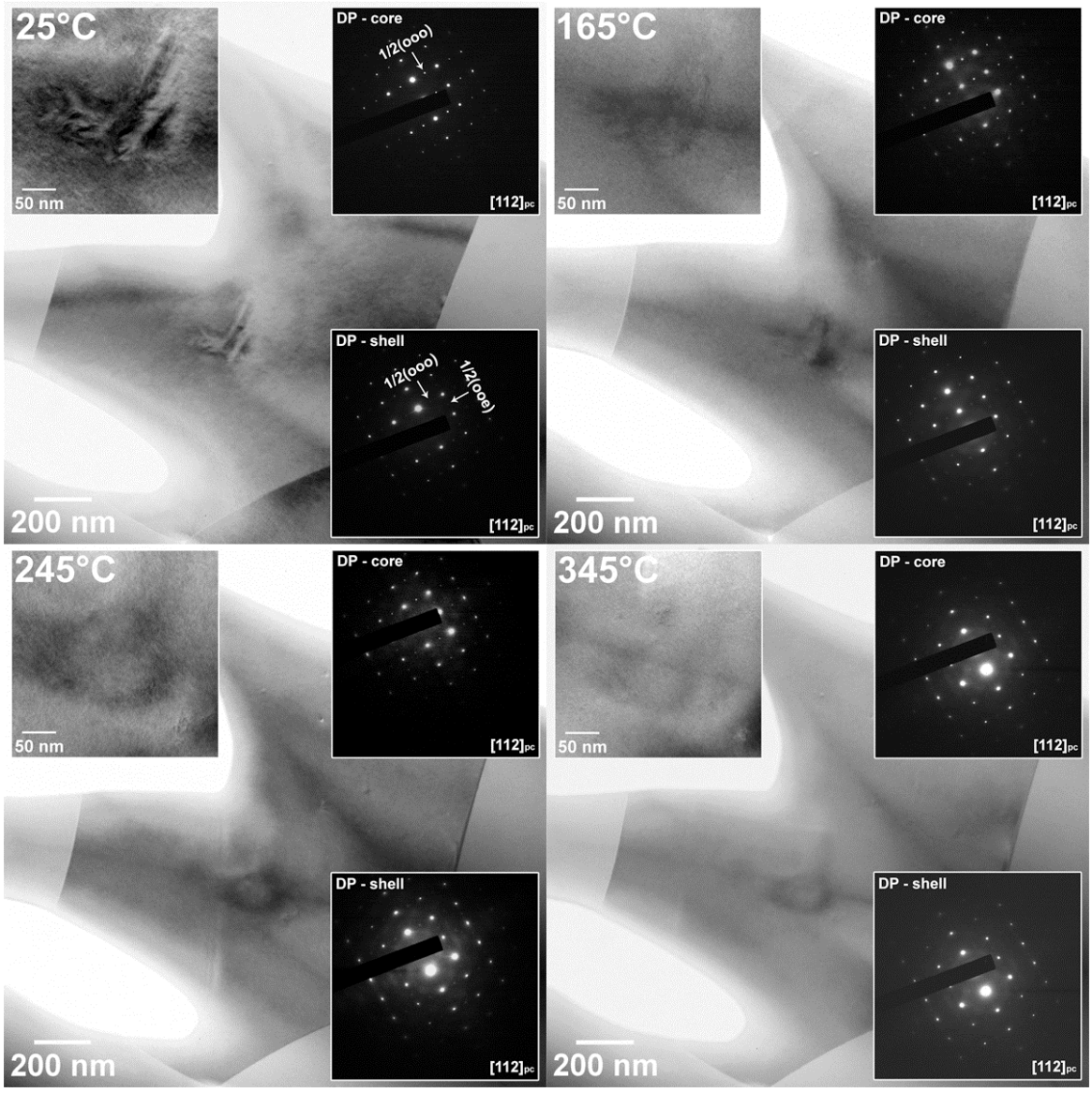

Figure 5.40: *In situ* BF hot-stage TEM imaging series. Corresponding SAED patterns of the core and shell obtained along <112>$_{pc}$ zone axis are displayed in the right top and bottom corner, respectively. Left top image displays a magnified view of the core.

Increasing temperature up to 165 °C leads to a gradual disappearance of the irregular nanodomain configuration in the core, as well as disappearance of the nano-sized platelets in the shell. The SAED patterns reveal that T ½{ooe} SSR become detectable within the core and persist up to 345 °C. At 245 °C, the original appearance of a domain-like contrast within the core is replaced by a blurred contrast that is slightly softened upon approaching 345 °C, indicating a gradual phase transformation into a state of homogenized absence of domain morphology.[435] At 345 °C, only minor contrast is visible in both the core and the shell. Moreover, the SSR fade, indicating that the tilting has either vanished or is at least reduced to a level below the detection limit of the TEM. During cooling a similar domain configuration and contrast redeveloped, indicating that the thermally induced changes to the tilting systems are reversible (not shown). It is deduced from these experiments that all temperature anomalies detected by TEM can be attributed to changes in the octahedral tilts, as previously found in other BNT-based ceramics.[367,436] The persistence of the chemical heterogeneity between core and shell leads to the reversibility of the process.

5.2.4 Electrical Characterization

5.2.4.1 Temperature- and Frequency-Dependent Dielectric Properties

Figure 5.41 provides the ε_r' and ε_r'' as a function of temperature and frequency for the unpoled and poled states of BNT-0.25ST. Solid arrows indicate the shift of the ε_r' and ε_r'' curves with increasing frequency. Two frequency-dependent local maxima are found in the ε_r' and ε_r'' curves. The ε_r'' signal at 1 kHz was used to define the temperatures corresponding to the relaxation processes. The first local maxima are found at T_{fm} = 110 °C and the second local maxima at T_{sm} = 320 °C. The relaxation process found at T_{fm} occurs in a broad temperature range of 30 °C for the frequency range between 1 kHz and 1 MHz, while in the case of T_{sm} the temperature range is over 80 °C. The ε_r'' values indicating both anomalies are shifted to higher temperatures with increasing frequency. The magnitude of the ε_r'' peak at T_{fm} increases with frequency, while the magnitude of the peak at T_{sm} decreases. The poling process increases the magnitude of the overall ε_r' response but the increase at T_{sm} is more preponderant, whereas the ε_r'' values at T_{fm} are increased and at T_{sm} reduced. Dielectric relaxations with the features described above are generally considered as the fingerprints of relaxors (Section 2.2.2). This behavior is also common to other lead-free materials[119,121-123,127,135,437] and was associated with the relaxation of PNRs; *i.e.*, a dynamic slowing down of the PNRs thermally activated fluctuations.[437] Therefore, as the temperature decreases, either a spontaneous transformation into a long-range ferroelectric order (non-canonical relaxor) or freezing of the PNRs fluctuations (canonical relaxor) can be expected (Section 2.2.2).[51] There is no indication of a transformation into a long-range order ferroelectric state and thus the BNT-0.25ST is hereafter classified as a canonical relaxor. The poled sample depicts a diffuse shoulder in ε_r'' at $\sim$ 50 °C, which is related to the decay of the induced ferroelectric state. The thermally stimulated loss of the electric field induced ferroelectric state of BNT-based materials has been generally recognized as a two-stage process.[108,109] Upon heating, the ferroelastic texture of the induced ferroelectric state of BNT-based materials is generally lost at the depolarization

temperature T_d.[108] Further temperature increase leads to domain fragmentation and PNRs formation at T_{f-r}.[108] Due to the experimental difficulties of the poling process, it was not possible to measure T_d. Since transition from the ferroelectric state to the relaxor state at T_{f-r} is generally found a few degrees above T_d, T_{f-r} is assumed to be associated with the diffuse peak in ε_r'' at ~ 50 °C and can be attributed mostly to the retained ferroelectric state in the cores. It is noted that even above T_{f-r}, the values of ε_r' and ε_r'' are slightly different before and after the poling treatment. This implies the discussed distribution of ergodicity.

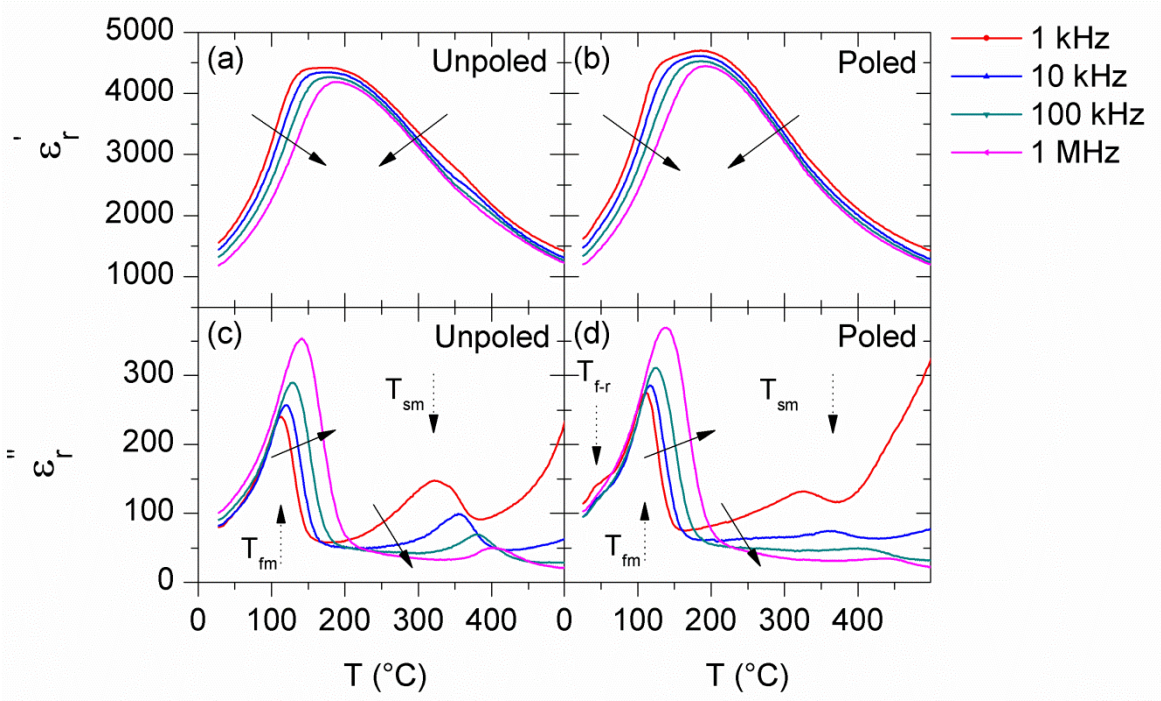

Figure 5.41: Temperature- and frequency-dependent ε_r' and ε_r'' of poled and unpoled BNT-0.25ST. Trends in frequency and dielectric anomalies are marked with solid and dashed arrows, respectively.

Canonical relaxors generally feature a freezing temperature T_{fr} associated with the divergence of their correlation length and thus relaxation time.[85,86,104,105] In lead-containing relaxors, T_d coincides with T_{fr}, and were proposed to determine a considerable thermally stimulated decrease of the P_r values.[85] Figure 5.42 displays the ε_r'' measured on cooling in a broad frequency range (from 1 Hz to 100 kHz). The inset displays the Vogel-Fulcher[102,103] fitting that indicates a T_{fr} = (17 ± 18) °C. Therefore, it becomes apparent that the T_{fr} and T_{f-r} are in proximity but, considering experimental errors, do not seem to coincide. It is noted that T_{fr} should be mostly related to the shell of the materials since they represent the ergodic state of the system. Therefore, it is suggested that PNRs in poled BNT-0.25ST diminished considerably their correlation length at T_{fr} ~ 20 °C leading to detexturing of domains within the core. Upon further heating the detexturized domains decay into PNRs at T_{f-r} ~ 50 °C.

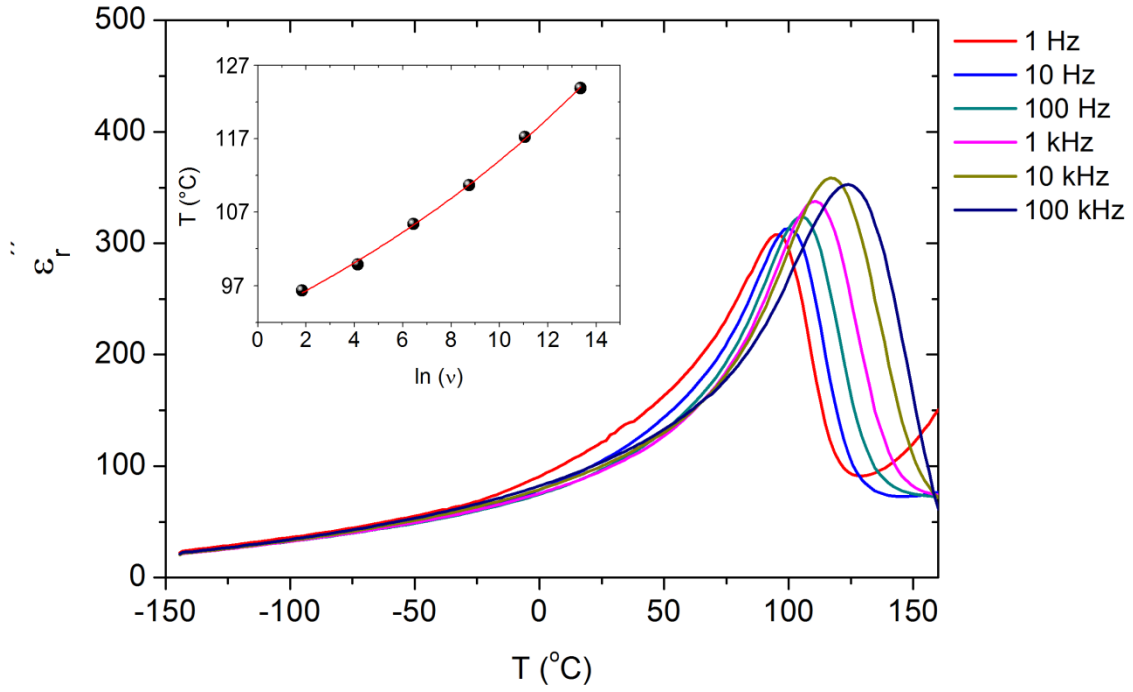

Figure 5.42: Low temperature frequency dispersion of ε_r'' for unpoled BNT-0.25ST measured upon cooling. Inset displays the local maxima fitted by the Vogel-Fulcher[102,103] relationship.

5.2.4.2 Bias-Field- and Temperature-Dependent Quasi-Static Small Signal Properties

Figure 5.43 introduces the quasi-static (a) d_{33} and (b) $\tan(\delta)$ measured as a function of bias-field and temperature. The d_{33} curve at room temperature is prototypical for incipient piezoelectrics (Section 2.2.2.2). BNT-0.25ST at room temperature features a d_{33}^{max} = 238 pC/N and $E(d_{33}^{max})$ = 1.37 kV/mm, while the d_{33}^{rem} = 80 pC/N corresponds to only 30 % of the d_{33}^{max} value and can be attributed to the retention of the poled state in the cores. Moreover, it is also in agreement with the proximity of the T_{fr} and T_{f-r} to room temperature found in the previous section. The $\tan(\delta)$ curves (Figure 5.43 (b)) display four local maxima. The electric field induced ferroelectric state is obtained at E_{r-f} = 2.42 kV/mm, as indicated by the first local maxima of $\tan(\delta)$. Upon removal of the electric field, the local maximum at E_{f-r} = 0.40 kV/mm suggests the decay of the induced ferroelectric state of shells. It is noted that the d_{33}^{max} values does not coincide either with E_{r-f} or with E_{f-r}. Since d_{33}^{max} values were recorded on decreasing electric field, it is apparent that the system has maximized reversible switching processes prior to its decay into a largely ergodic relaxor state below E_{f-r}. Reversing the polarity of the applied electric field leads to an analogous process resulting in two further, mirrored anomalies. The electric field induced phase transition and its decay are accompanied by a large degree of domain switching, as demonstrated by the aforementioned local maxima values of $\tan(\delta)_{r-f}$ = 0.19 % and $\tan(\delta)_{f-r}$ = 0.22 %.[438] It is relevant to note that $\tan(\delta)_{f-r}$ is 15 % higher than $\tan(\delta)_{r-f}$, indicating that the initial coherent switching following the electric field induced phase features a gradual increase in domain switching with

further electric field. Thus, upon electric field removal a higher degree of back switching leads to higher losses. The negligible E_{r-f} and E_{f-r} at 110 °C suggest that the applied electric field is not high enough to induced a long-range ferroelectric order at this temperature, indicating that the thermal energy is too high. The electric field induced phase transition and its reversibility depicted in the bias-field-dependent small signal properties are consistent with results in other BNT-based materials[121,149] and the diffraction studies from this work (Section 5.2.2).

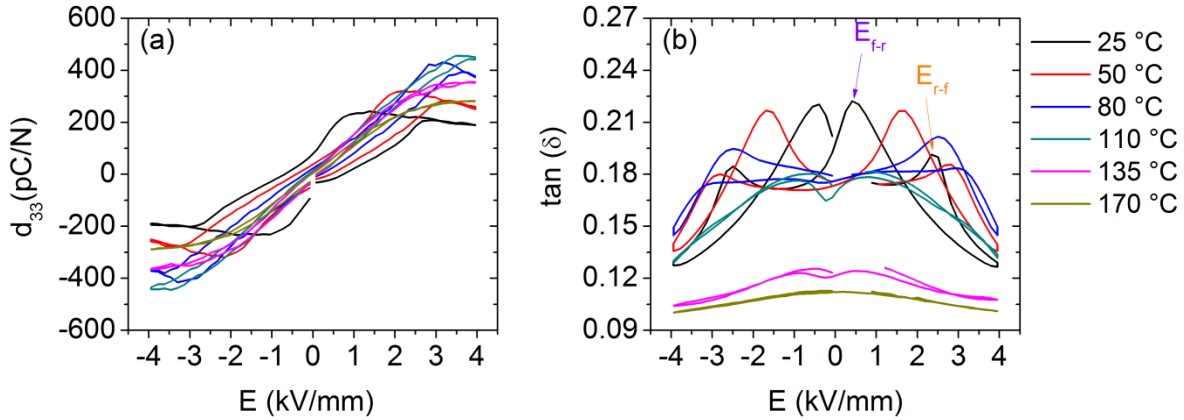

Figure 5.43: *In situ* small signal d_{33} and $tan(\delta)$ as a function of bias-field and temperature for BNT-0.25ST.

The magnitude of d_{33}^{max}, $E(d_{33}^{max})$, and d_{33}^{rem} vary with temperature, as displayed in Figure 5.44 (a). A monotonic increase of $E(d_{33}^{max})$ values and a monotonic decrease of d_{33}^{rem} values with temperature are observed. In contrast, the overall highest d_{33}^{max} value was obtained between 80 °C and 110 °C. This is the maximum temperature up to which a ferroelectric state is induced using 4 kV/mm. Figure 5.44 (b) provides the $\tan(\delta)_{r-f}$, $\tan(\delta)_{f-r}$, E_{r-f}, and E_{f-r} as a function of temperature. Increasing temperature leads to a monotonic decrease of $\tan(\delta)_{r-f}$ and $\tan(\delta)_{f-r}$, which indicates decreased switching with increasing temperature. In contrast, E_{r-f} and E_{f-r} increase monotonically with temperature indicating that a higher electric field is required at high temperatures to induce the ferroelectric state accompanied by switching. The relative difference between E_{r-f} and E_{f-r} is diminished with increasing temperature leading to almost negligible hysteresis at 80 °C, which is considered the maximum temperature up to which the ferroelectric state is induced. It should be pointed out that the electric field hysteresis between E_{r-f} and E_{f-r} suggests that the electric field induced phase transition is of first order. The gradual disappearance of this electric field hysteresis indicates that the first order phase transition evolves gradually into a second order.[439] This indicates that at temperatures between 80 °C and 110 °C, the BNT-0.25ST features criticality and the overall highest d_{33}^{max} = (436 ± 19) pC/N.

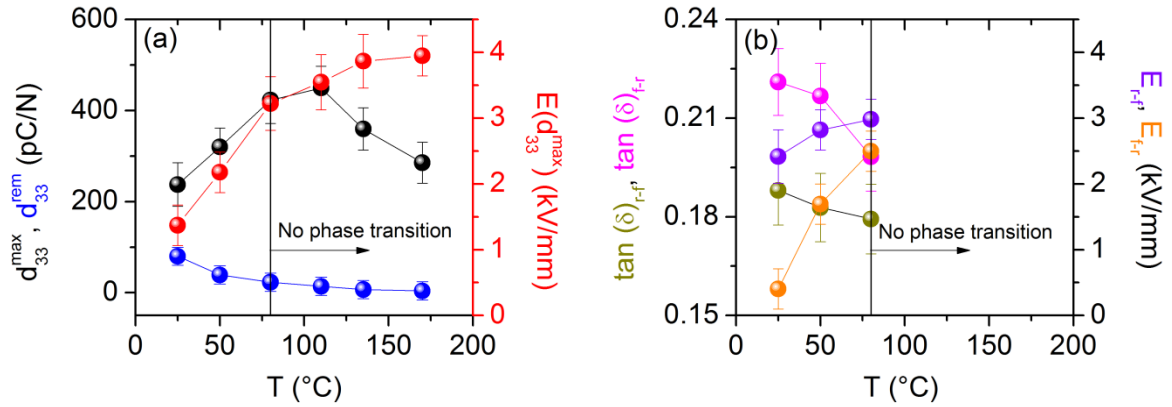

Figure 5.44: (a) d_{33}^{max}, d_{33}^{rem}, and $E(d_{33}^{max})$ as a function of temperature for BNT-0.25ST. (b) $tan(\delta)_{r-f}$, $tan(\delta)_{f-r}$, $E(\tan(\delta)_{r-f})$, and $E(\tan(\delta)_{f-r})$ for BNT-0.25ST.

The BNT-based materials may feature a considerable volume change associated with their electric field induced phase transition.[440] This volume change is a source of strain output that can lead to an inaccurate quantification of the strain mechanisms in these types of materials when using the procedure described in Section 5.1.3.2.3. Therefore, quantification of strain contributions in BNT-0.25ST was not performed.

5.2.4.3 Quasi-Static Large Signal Properties

In order to give insight into the compositional range corresponding to the FD longitudinal instability of P_s^i in the BNT-ST[258,275], electromechanical properties of BNT-0.25ST and BNT-0.28ST were measured. Figure 5.45 provides the (a) bipolar polarization, (b) bipolar strain, and (c) unipolar strain measured at 4 kV/mm and 1 Hz for BNT-0.25ST and BNT-0.28ST. For both materials, a pinched bipolar polarization and bipolar strain hysteresis loop with almost zero negative strain are depicted. These features are typical for incipient piezoelectrics.[121] The P_r = 0.13 C/m^2 and P_{max} = 0.33 C/m^2 values in BNT-0.25ST are 30 % higher than the values of BNT-0.28ST. However, the strain output of BNT-0.25ST, S_{max} = 0.28 %, is 35 % higher than the strain output in BNT-0.28ST. It is apparent that the electric field induced phase transformation of the BNT-0.25ST entails considerable increase in polarization and strain values for an electric field input higher than 2 kV/mm. The inflection point of the unipolar strain curve was used to estimate the E_{r-f} = 2.85 kV/mm in BNT-0.25ST, which is in relatively good agreement with E_{r-f} = 2.42 kV/mm obtained from small signal $\tan(\delta)$ as a function of bias-field in the previous section. The decay of the ferroelectric state obtained from large signal measurements at E_{f-r} = 0.60 kV/mm is also in good agreement with the results from the previous section. Discrepancies are inherent to the change in probing frequencies of the different characterization techniques employed.[143,144] It is noted that the removal of the electric field leads to a decay of 65 % in the polarization of BNT-0.25ST, indicating that although P_r in BNT-0.25ST is higher than in BNT-0.28ST, it still has considerably lower values than its P_{max}. For BNT-0.25ST a d_{33}^* value of 650 pm/V is obtained from the unipolar strain curve at 4 kV/mm and 1 Hz, while the value

for BNT-0.28ST is 430 pm/V. From the room temperature electromechanical characterization, it becomes apparent that the BNT-0.25ST is an appropriate selection for investigation of the FD longitudinal instability of the P_s^i.

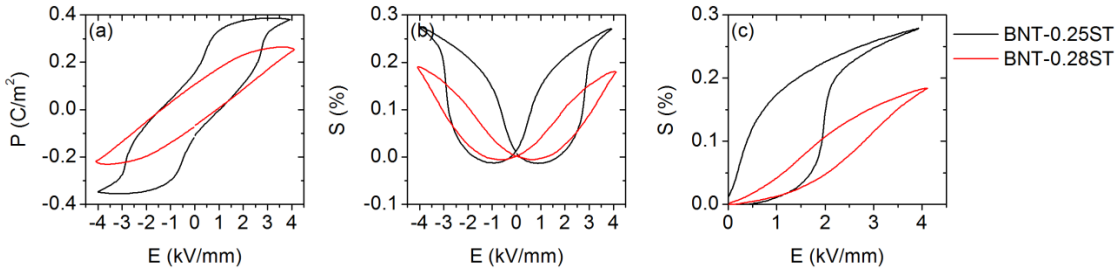

Figure 5.45: (a) Bipolar polarization, (b) bipolar strain, and (c) unipolar strain for BNT-0.25ST and BNT-0.28ST samples measured at 1 Hz.

Domain switching is a time-dependent kinetic process[73,441-443], while a first order phase transition is an infinitely fast discontinuous process occurring in the terahertz range.[39,48,444] Therefore, a feasible way to give insight into the nature of the phase transition and the origin of the volume change is to perform polarization and strain measurements at a rate faster than the time domain where the switching processes should occur. It should be noted, however, that time-dependent phase transitions in relaxors with weak first order transitions were also reported.[445-447] Figure 5.46 introduces (a) polarization and (c) strain pulse experiments as a function of time for electric fields between 1.5 kV/mm and 4 kV/mm. An increase of 45 % in the polarization and 65 % in the strain values is observed when the electric field is increased from 1.5 kV/mm to 2 kV/mm. Further increases in the electric field only lead to smaller relative changes (below 15 %) in polarization and strain. This indicates that the E_{r-f} for pulse experiments is between 1.5 kV/mm and 2 kV/mm. The reason for the lower electric field required to induce the phase transition with pulse experiments is currently not understood. At a given electric field, polarization and strain increase with time, however, they nearly reach a flat saturation level by the end of the 10 second pulse, indicating negligible leakage current. Insets of Figure 5.46 (a) and (c) depict a close-up of the decay in polarization and strain upon removal of the electric field, respectively. Increasing electric field leads to a gradual increase in the P_r values. However, the S_r for all electric fields decays to the same value (within experimental errors), except for the pulse of 1.5 kV/mm where the S_r value is lower. The P_r and S_r values 20 s after removal of the electric field are below 10 % of the maximum values under electric field. This indicates relatively high, although incomplete, reversibility of the electric field induced transition and switching processes. Figure 5.46 (b) and (d) depict the normalized polarization and strain, respectively, plotted in logarithmic scale. A close inspection for the electric field of 1.5 kV/mm indicates that the curve is non-linear up to $\sim$ 1 s and subsequently follows a linear relation in the logarithmic scale. This seems to suggest a distinction between the electric field induced phase transformation of core regions from a non-ergodic relaxor state to a ferroelectric state (t < 1 s) and their subsequent switching to align with the electric field (t > 1 s). The lower S_r

value obtained at 1.5 kV/mm indicates that the phase transition of shells is not triggered at this electric field. For the case of an electric field of 2 kV/mm, two linear regimes for t < 1 s and for t > 2.5 s are depicted. Note that the pulse of 2 kV/mm was applied after the 1.5 kV/mm, thus cores have an induced ferroelectric state prior to the 2 kV/mm pulse. Therefore, the initial linear regime could be attributed to switching of the core regions (t < 1 s), while the latter (t > 2.5) to the coherent switching of shell regions. The intermediate non-linear regime (1 s < t < 2.5 s) suggests an electric field induced phase transformation from the ergodic state to the ferroelectric state in the shell regions. Coherent switching following the electric field induced phase was previously demonstrated in BNT-based materials.[143,144] The non-zero, but considerably lower S_r and P_r values observed after 20 s of the removal of the electric field, can be attributed to certain irreversibility in the transformation of the core and presumably also in the shells adjacent to cores. Since negligible changes in S_r are observed for the applied electric fields higher than 2 kV/mm, the P_r values displayed in the inset of Figure 5.46 (a) seem to be related to a gradual increase of the electric field induced ferroelectric state at expense of the non-ergodic relaxor states near cores and/or to polarization induced due to enhanced intrinsic and extrinsic switching contributions. It is noted that even higher electric fields lead to slower reductions of S_r and P_r values, which can be attributed to switching kinetics.

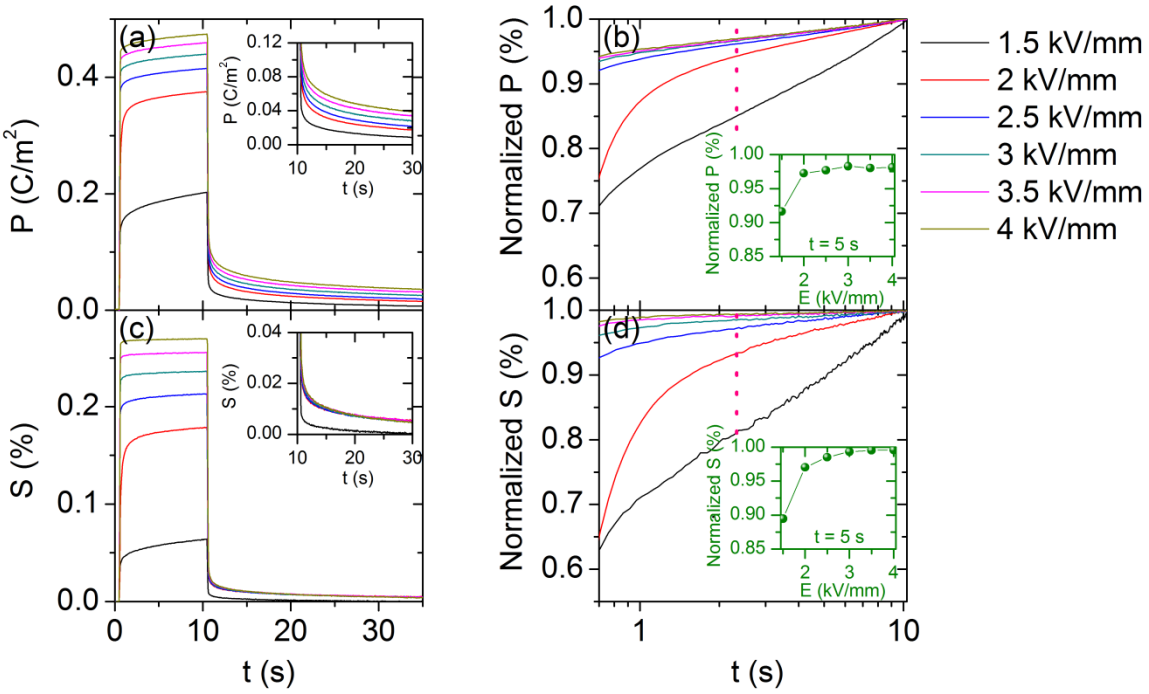

Figure 5.46: Pulse measurement of 10 s duration with electric fields ranging from 1.5 kV/mm to 4 kV/mm for BNT-0.25ST. (a) Polarization, (b) polarization fraction, (c) strain, and (d) strain fraction as a function of time are displayed. Insets in (a) and (c) present a magnification of the polarization and strain decay upon electric field removal, respectively. Insets of (b) and (d) depict the polarization and strain fraction increase as a function of electric field for a constant time of 5 s.

The polarization and strain for a constant time t = 5 s (marked with dotted lines) is introduced in the insets of Figure 5.46 (c) and (d). A discontinuous change in polarization and strain upon crossing E_{r-f} at a constant time indicates that the reversible electric field induced transformation, mostly attributed to shells, is of a first order nature. This result is in agreement with the results from the previous section.

In order to give further insight into the electric field induced phase transformation, Figure 5.47 (a) introduces an experiment performed using a continuous unipolar triangular wave with increasing amplitude from 1 kV/mm to 8 kV/mm (inset of Figure 5.47 (a)). A discontinuous change in strain is discerned at about 3 kV/mm suggesting the triggering of the electric field induced phase transition, in agreement with the E_{r-f} = 2.85 kV/mm obtained from previous large signal measurements (Figure 5.45). Saturation of unipolar strain is achieved at 4 kV/mm. For further increase in the applied electric field, a linear strain response is obtained, which was consistent with the observed saturation of the switching processes (Figure 5.43). The cycles were applied consecutively, thus the reproducible path of the loops indicates a certain reversibility of the phase transition at room temperature. The initial strain value after each cycle tends to increase, indicative of the presence of a slight but continuous increase of the P_r values (not shown). Note that if this shift would be a result of leakage current and/or temperature, the loops should be linearly shifted upwards, considering the input signal employed.

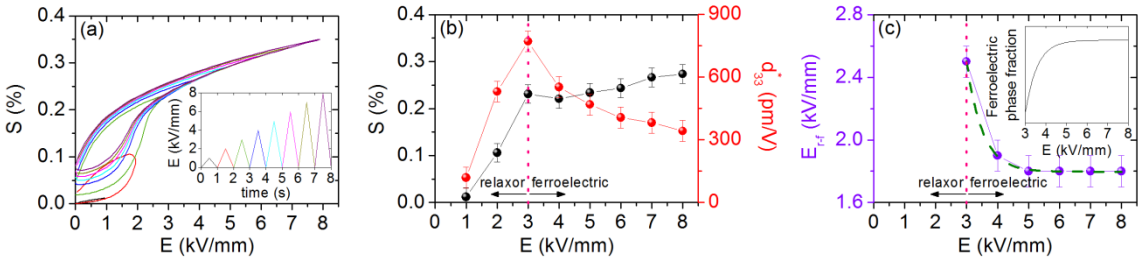

Figure 5.47: (a) Unipolar strain measured from a virgin state with successively increasing electric field amplitude for BNT-0.25ST. The inset displays the input waveform used for the measurement, which is characterized by voltage steps of 1 second and increasing electric field from 1 kV/mm to 8 KV/mm. (b) Unipolar strain and calculated d^*_{33} at each triangular step. (c) E_{r-f} obtained at each cycle. Green dotted line indicates a fitting performed with an Arrhenius function. Inset displays the induced ferroelectric state fraction upon successive cycles. For (b) and (c) the electric field regions with predominantly relaxor and ferroelectric states are marked, respectively.

The S_{max} and d^*_{33} values obtained after each sub-cycle are introduced in Figure 5.47 (b). The electric field required to trigger the phase transition is discerned by a drastic change in S_{max} and d^*_{33} values. Therefore, at electric fields below 3 kV/mm the BNT-0.25ST features a predominantly relaxor state, while above 3 kV/mm a ferroelectric state is stable under electric field. Although S_{max} for electric fields higher than 4 kV/mm is increasing monotonically, the d^*_{33} decreases in the

same region. This is consistent with the observed saturation of switching processes (Figure 5.43). Determination of E_{r-f} was performed above 3 kV/mm for each triangular sub-cycle, as displayed in Figure 5.47 (c). A gradual decrease of E_{r-f} with increasing electric field amplitude of the successive sub-cycles is depicted giving rise to a saturation value of ~ 1.8 kV/mm. This is a conclusive proof that although reversibility of the phase transition is evident (Figure 5.47 (a)), the P_r values are not equal after each sub-cycle which can be attributed to a gradually increasing retained ferroelectric state fraction. This presumably occurs in grain regions directly adjacent to the cores because their non-ergodicity facilitated heterogeneous nucleation.[242] Although, the induced phase transition is of first order, the subsequent switching of the domains formed is a kinetic process that requires time.[73,441-443] Therefore, it is expected that each sub-cycle allows a gradual increase in the amount of switching. The gradual increase of the P_r values after each sub-cycle is analogous to the increase of the P_r values observed with increasing field strength in pulse experiments (Figure 5.46). In order to assess this phenomenon, a qualitative approach was performed by fitting the resultant E_{r-f} experimental points of each sub-cycle with an Arrhenius function. Considering that the shift of the E_{r-f} was ascribed to a gradual increase of switching and thus of induced ferroelectric state fraction, the inverse mathematical function should represent their increase. A scheme of this phenomenon is provided in the inset of Figure 5.47 (c). From this reasoning, it follows that to obtain a saturated ferroelectric state, several cycles or longer times with sufficiently large electric field strengths are required. In order to depict this progression, Figure 5.48 (a) and (b) display the bipolar strain output obtained after several cycles (starting from a virgin state) at 3 and 4 kV/mm, respectively. The electric field strengths were selected taking into account the initial E_{r-f} = 2.85 kV/mm required to trigger the phase transition in the Hz frequency range.

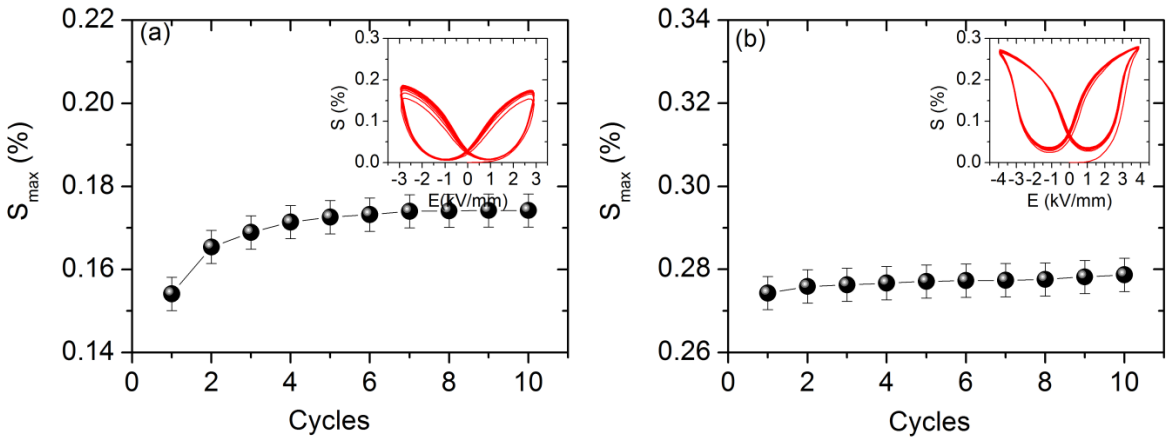

Figure 5.48: S_{max} values obtained as a function of bipolar electric field cycles at (a) 3 kV/mm and (b) 4 kV/mm. Values were calculated considering the zero of the poling cycle as the reference point. Insets display strain hysteresis loops. Measurements were performed on virgin samples at 1 Hz.

For comparison, the S_{max} values were calculated at each cycle by taking the zero of the poling cycle as the reference point. This means that the gradual phase transition of the material should be reflected in the strain output. Figure 5.48 (a) indicates that BNT-0.25ST requires 7 cycles at 3 kV/mm to reach a stable strain of 0.17 %, whereas at 4 kV/mm a stable strain of 0.28 % (within experimental errors) is reached already after the second cycle. The gradual increase in strain at 3 kV/mm after several cycles, in contrast to the already saturated strain value at 4 kV/mm achieved after the poling cycle, is an indication of the increase in the long-range ferroelectric state after each cycle. The almost constant strain obtained at the electric field strength of 4kV/mm confirms that the reversibility of the phase transition is fast enough for a 1 Hz input wave of this amplitude. Pulse experiments indicate that at 4 kV/mm, the S_r is reduced to 30 % of S_{max} 0.15 s after electric field removal. This indicates that the reversibility of the electric field induced processes at 4 kV/mm are considerably below the Hz range. A brief corroboration of the long term reliability of the strain output is introduced in Appendix IV.

Figure 5.49 displays the temperature-dependent (a) bipolar polarization and (b) bipolar strain loops from 25 °C to 170 °C. Increasing temperature leads to a gradual decrease of P_r, P_{max}, S_{neg}, and S_{max} values. A considerable reduction of all the aforementioned parameters is observed for temperatures above 80 °C. This indicates that the applied electric field was not sufficient to induce the long-range ferroelectric order above this temperature, in agreement with the results from the previous section.

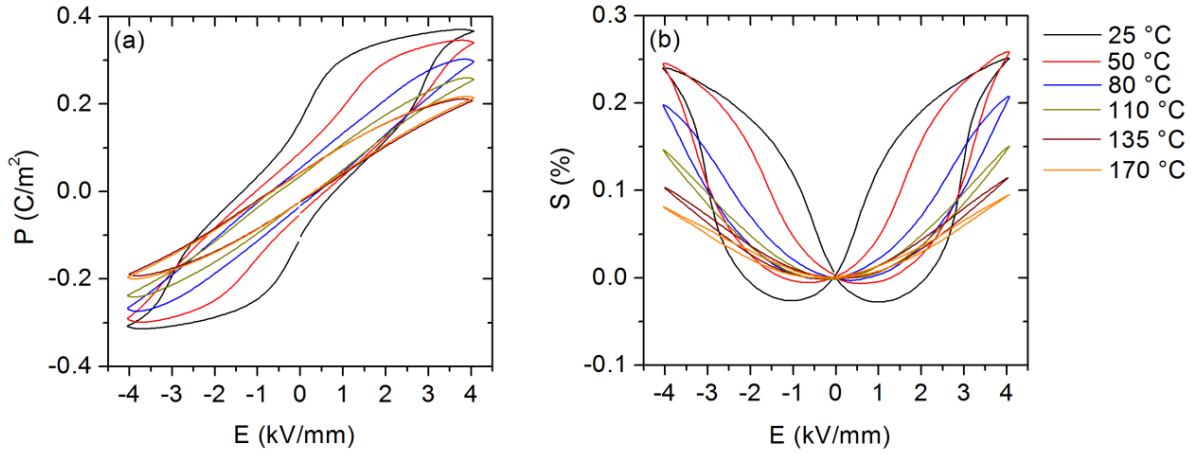

Figure 5.49: (a) Bipolar polarization and (b) bipolar strain as a function of temperature for BNT-0.25ST measured at 1 Hz.

In order to investigate the effect of temperature on the electric field induced phase transition, Figure 5.50 (a) introduces E_{r-f} and E_{f-r} as a function of temperature derived from the large signal measurements of Figure 5.49. The E_{r-f} and E_{f-r} obtained from large signal measurements depict very similar temperature profiles to those found from small signal measurements (Figure 5.44 (b)). In other words, both parameters increase monotonically with temperature and their relative

difference is diminished. This indicates that a higher electric field is required at higher temperatures to induce the ferroelectric state and that the phase transformation gradually shifts from first to second order, supporting the presence of a critical point in the temperature range between 80 °C and 110 °C (Section 5.2.4.2).

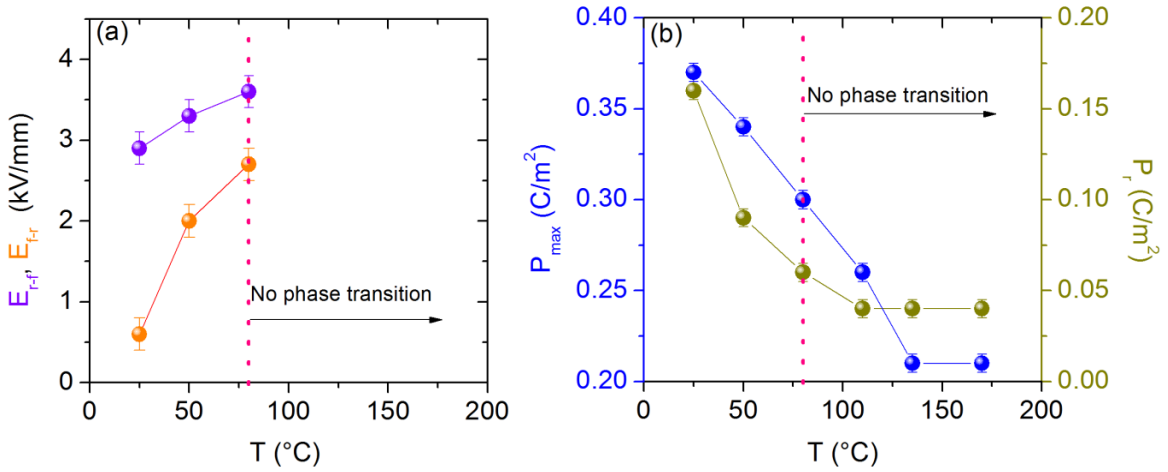

Figure 5.50: (a) E_{r-f} and E_{f-r}; (b) P_{max} and P_r parameters derived from large signal measurements as a function of temperature for BNT-0.25ST obtained from bipolar measurements up to 4 kV/mm.

Temperature dependence of P_r and P_{max} is given in Figure 5.50 (b). Both parameters feature a monotonic decrease with increasing temperature, which is a consequence of the gradual suppression of the electric field induced ferroelectric state.[112] The P_r above 110 °C is 25 % of the room temperature value. This indicates that although a certain electric field induced ferroelectric state ascribed to the non-ergodic cores remains, its fraction is considerably reduced due to the high thermal energy. In order to give further insight into the strain mechanism of BNT-0.25ST, as well as its applicability, Figure 5.51 displays the unipolar strain as a function of frequency and temperature.

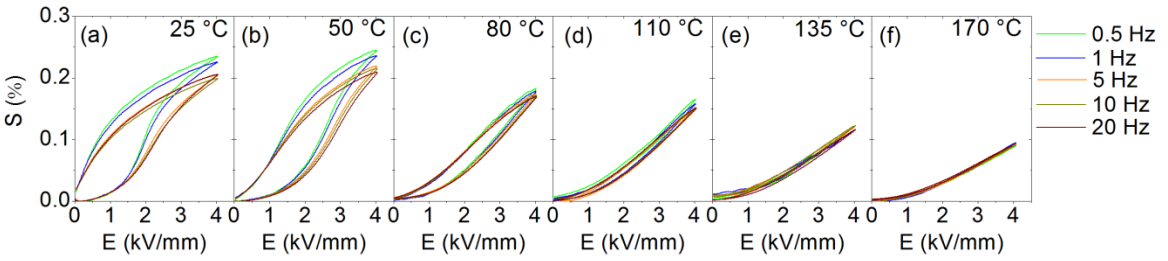

Figure 5.51: Temperature- and frequency-dependent unipolar strain for BNT-0.25ST.

The strain obtained from switching arising due to the induced ferroelectric state is accompanied by high hysteresis and frequency dependence. The amount of induced ferroelectric state is negligible above 110 °C leading to a continuously reduced strain output and hysteresis, as expected in lead-containing[112] and lead-free[120] relaxors. The observations made for unipolar measurements are consistent with bipolar measurements (Figure 5.49). Figure 5.52 (a) introduces the d_{33}^* values calculated at 4 kV/mm for frequencies of 0.5 Hz, 5 Hz, and 20 Hz. In the temperature range between 25 °C and 80 °C, the values of d_{33}^* are much higher than at higher temperatures. At 170 °C d_{33}^* reaches values that correspond only to 40 % of the room temperature values. Although the critical point found between 80 °C and 110 °C in BNT-0.25ST features maximized d_{33} values under bias-field (Figure 5.44), it does not depict the highest d_{33}^* value. This observation is consistent with the critical points elucidated for the BZT-BCT system (Sections 5.1.3.2.3 and 5.1.3.3). Figure 5.52 (b) introduces the d_{33}^* values normalized with respect to the room temperature d_{33}^* value calculated at 1 Hz. For temperatures below 80 °C, a decrease in d_{33}^* values is observed with increasing frequency. In contrast, for temperatures above 80 °C the frequency dependence was not detected, although the d_{33}^* values are lower.

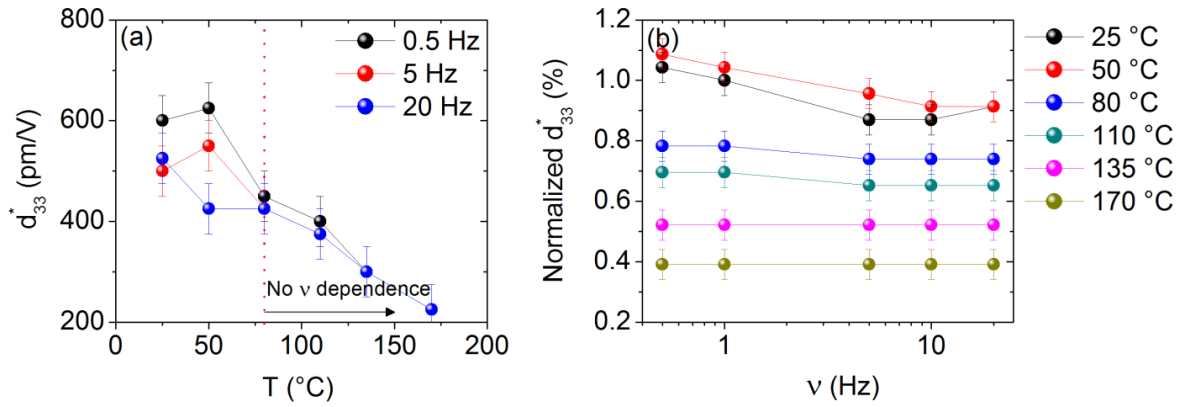

Figure 5.52: (a) d_{33}^* at 0.5 Hz, 5 Hz, and 20 Hz as a function of temperature for BNT-0.25ST. (b) Normalized d_{33}^* as a function of frequency at temperatures from 25 °C to 170 °C for BNT-0.25ST.

In the temperature range where a ferroelectric state is induced (below 80 °C), d_{33}^* has maximized values and maximized frequency dependence due to the switching of the newly formed domains. As previously discussed, switching is the time-dependent component of the strain output and reconciles the high frequency dependence and hysteresis of d_{33}^* below 80 °C. The strain at temperatures above 110 °C is attributed predominantly to electrostriction and consequently features negligible frequency dependence in the range investigated.

5.2.5 Effect of Microstructure on the Quasi-Static Large Signal Properties

Considering that the core-shell microstructure is a result of a diffusion limited process (Section 5.2.1), sintering time was modified to promote enhanced diffusion. Note that the sintering temperature was not modified to avoid changes in the sintering mechanism.[390] Figure 5.53 displays the microstructure of the polished surfaces of BNT-0.25ST samples obtained by SEM in BSE mode after sintering for (a) 2 h, (b) 5 h, (c) 10 h, and (d) 20 h. All samples feature a relatively dense microstructure. An increase in grain size and a diminished core-shell density is observed in the images as a function of increasing sintering time.

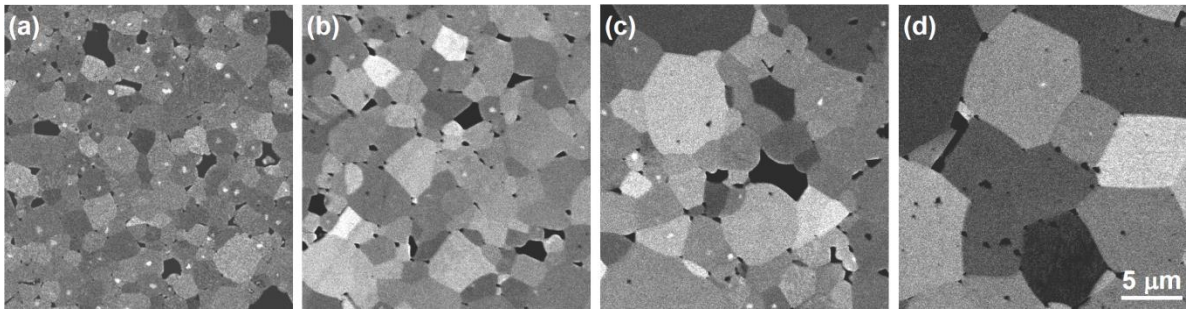

Figure 5.53: As-sintered, polished surfaces of BNT-0.25ST sintered for (a) 2 h, (b) 5 h, (c) 10 h, and (d) 20 h at 1150 °C. Images were taken with a SEM in the BSE mode.

Figure 5.54 displays the relative density, grain size, and core density as a function of sintering time. Increasing the sintering times leads to an almost linear increase of relative density from 96 % to more than 98 %. Grain size also increases nearly linearly from (2.6 ± 0.5) µm to (7 ± 1.2) µm. Generally, grain growth at a constant temperature follows approximately a parabolic dependence with time.[390] However, this was not observed during this study, which could be related to the initial chemical heterogeneity of the calcined powders. The linear densification and grain coarsening of BNT-0.25ST warrant further studies and cannot be fully rationalized within the limited synthesis study of this work. The exponential decrease of cores indicates a considerable homogenization due to a thermally activated diffusion process. Increasing the sintering time from 2 h to 5 h leads to a 75 % decrease of cores. Further increase of sintering time leads to a continuous homogenization that culminates with samples with nearly no cores after 20 h.

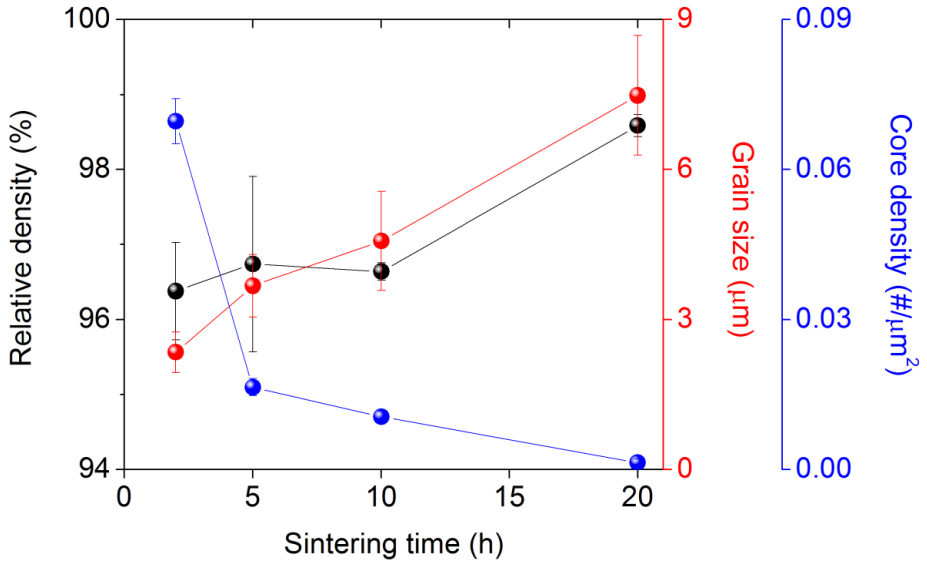

Figure 5.54: Relative density, grain size, and core density for BNT-0.25ST as a function of sintering time.

Figure 5.55 provides the (a) bipolar polarization, (b) bipolar strain, and (c) unipolar strain loops measured at 4 kV/mm and 1 Hz for BNT-0.25ST samples sintered for different times. The modification of the microstructure performed by increasing time only has a minor effect on the electromechanical properties of BNT-0.25ST. Moreover, a certain degree of asymmetry can also be observed in the strain loops, in agreement with a minor internal bias-field detected in the polarization hysteresis. In general, increasing the sintering time leads to a gradual increase of P_r, P_{max}, and S_{max}. In contrast, E_{r-f} is increasingly reduced. It is expected that the influence of the sintering time on the electromechanical properties is a result of the change in the interdependent parameters relative density, grain size, and core density.

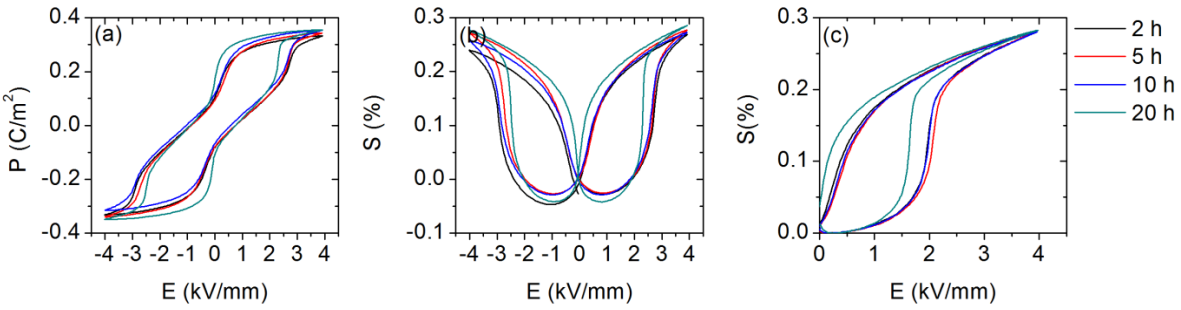

Figure 5.55: (a) Bipolar polarization, (b) bipolar strain, and (c) unipolar strain for BNT-0.25ST samples sintered for 2 h, 5 h, 10 h, and 20 h at 1150 °C.

Figure 5.56 provides S_{max} and E_{r-f} as a function of the core density obtained from Figure 5.55. The values of S_{max} indicate almost no variation as a function of core density, whereas E_{r-f} is

increased with increasing core density. In general a lower relative density and grain size result in diminished electromechanical properties.[42,150] It is noted that since increase in the relative density and grain size are found for samples with lower core density, the effect of the most relevant microstructural parameter could not be reconciled. More detailed synthesis studies are required to give further insights on the role of the core-shell in the electromechanical properties.

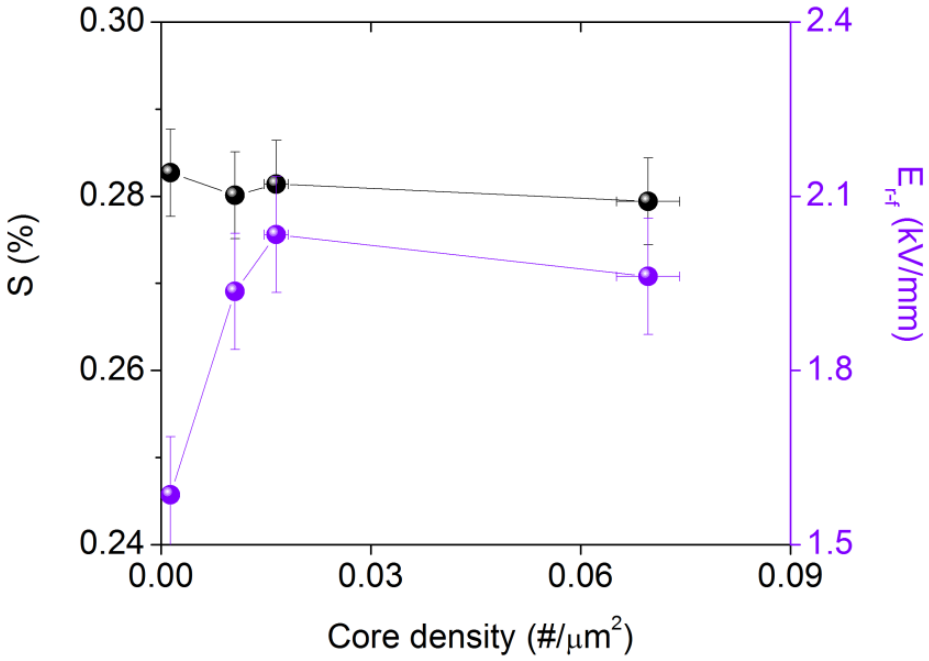

Figure 5.56: S_{max} and E_{r-f} as a function of core density obtained from unipolar hysteresis loops measured at 4 kV/mm for the BNT-0.25ST samples sintered for 2 h, 5 h, 10 h, and 20 h at 1150 °C.

5.2.6 Strain Mechanisms of the (1-x)($Bi_{1/2}Na_{1/2}$)TiO_3-x$SrTiO_3$ System

The properties of relaxor materials are dictated by the correlations of features at different length scales. At the microscopic scale, atomic disorder as well as electrostatic and local strain fields determine to a great extent functional properties.[51,53,57] In the mesoscopic scale, intergranular interactions are also relevant and must be considered.[448] Investigations on the BNT-0.25ST were performed for both the long and mesoscopic length scales, as will be treated in the next paragraphs.

Macroscopic long-range treatment: Figure 5.57 (a) from points 1 to 4 introduces the bipolar polarization, bipolar strain, small signal d_{33}, and small signal $tan(\delta)$ as a function of bias-field. Consistent with incipient piezoelectrics[121], BNT-0.25ST features large P_{max} = 0.35 C/m^2 and S_{max} = 0.28 % at 4 kV/mm, with a reduced P_r = 0.12 C/m^2, and low d_{33} = 10 pC/N at 0 kV/mm that increases dramatically at 2 kV/mm leading to d_{33} = 200 pC/N. The induced long-range ferroelectric

order occurring for an electric field of E_{r-f} between 2.42 kV/mm and 2.85 kV/mm is indicated by a change in slope in polarization, inflection point in strain, a local maximum of $tan(\delta)_{r-f}$ = 0.19, and diminished hysteresis in d_{33}. The decay of this long-range order into a relaxor state at E_{f-r} between 0.40 kV/mm and 0.60 kV/mm upon electric field removal leads to a P_r value that is 65 % lower than P_{max} and an overall maximized value of $\tan(\delta)_{f-r}$ = 0.22. Note that upon electric field removal, the highest d_{33}^{max} = 238 pC/N values are obtained for an electric field of $E(d_{33}^{max})$ = 1.37 kV/mm. This result contradicts the d_{33}^{max} values previously obtained at the transformation electric field E_{r-f} in other BNT-based materials[121,149] and may be ascribed to a maximization of the reversible switching processes prior to the destabilization of the ferroelectric state, similar to what was found near the line of critical points of BZT-BCT (Figure 5.22 (c)). The non-negligible P_r indicates a varying distribution of ergodicity, as previously reported in other materials.[119,449] It should be pointed out that the described features do not characterize the electric field induced phase transition directly, but only indicate that this phase transformation is accompanied by a considerable degree of switching. Therefore, increasing electric field above E_{r-f} leads to saturation. Since switching is a thermally activated kinetic process[73,441-443], the macroscopic observation of the anomalies ascribed to the development of the ferroelectric long-range order in the small and large signal properties depends on frequency. Since the small signal properties under bias-field were measured with a 0.05 Hz large signal base waveform (Section 4.4.2.2), inherent differences are expected with the large signal results performed at 1 Hz. This proves that the frequency dependence of the switching originates from the domains developed by the induced ferroelectric long-range order. A lower frequency allows a higher degree of switching, and thus at a given bias-field the polarization and strain outputs should be higher, as observed in Figure 5.51. The interdependent relation between switching and phase transition in relaxors may, in some cases, lead to considerably sluggish time-dependent phase transitions.[445-447] Nonetheless, in general P_s^i rearrangements leading to weak first order phase transitions occur at extremely short time-scales in ferroelectrics on the order of terahertz.[444] Pulse experiments indicate that for very fast electric field input, implying negligible time for switching processes, the phase transition of the BNT-0.25ST apparently occurs at electric fields between 20 % and 40 % lower than conventional measurements in the Hz range (Figure 5.46). This is justified considering that the small and large signal measurements indicate time-dependent switching processes that follow the phase transition rather than the phase transition that seems to be probed during the pulse experiments.[143,144] This entails the cycle- and electric field-dependent P_{max}, P_r, S_{max}, and S_r values observed in Section 5.2.4.3. Note that pulse experiments lead to a much lower switching as indicated by a decay of P_r values that are 10 % of P_{max}, in contrast to the studies performed on the Hz range that indicated a decay of P_r values that are 35 % of P_{max}. Further studies are required to shed light into the complex dynamics of the system. However, it should be pointed out that the reversibility of the polarization and strain outputs in the Hz range was proved (Appendix IV).[140] Several BNT-based materials feature a similar electric field induced phase transition.[125,130,138-140,275,434] Further details that point towards certain unique features of the BNT-ST system, will be discussed in the subsequent paragraphs.

Figure 5.57 (b) provides an overview of the macroscopic average phenomena featured in BNT-0.25ST as a function of temperature and electric field. Note that the terminology “temperature-

electric field phase diagram" is avoided to highlight that the evolution of the material is not under thermodynamically stable conditions but rather depends on kinetics and history. It should be pointed out that the microstructural evolution under electric field was always examined under isothermal conditions. Isofield conditions will result in different transitions from the ones displayed (Section 2.2.2).[106,107]

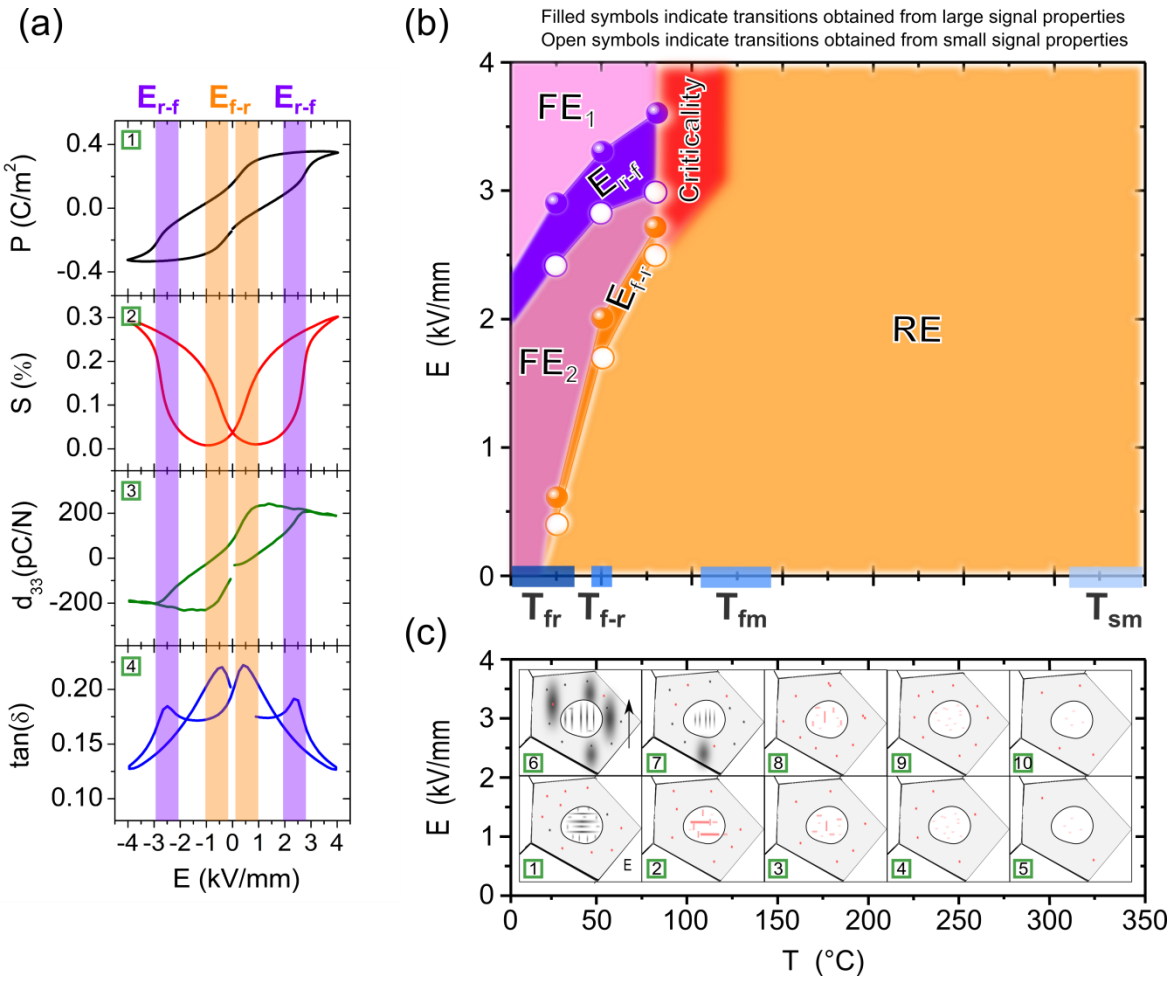

Figure 5.57: (a) Room temperature macroscopic polarization, strain, d_{33}, and $tan(\delta)$ as a function of electric field. (b) Average phenomena in BNT-0.25ST as a function of temperature and electric field. FE_1: stability region of the induced ferroelectric state, FE_2: stability region of the induced ferroelectric state when the applied electric field surpassed E_{r-f}. RE: ergodic relaxor state, and *criticality*: approximate temperature-electric field region where transformation from a first order phase transition evolves to a second order leading to criticality. (c) Mesoscopic schematic representation of the core-shell evolution under electric field and temperature. The Sr^{2+}/(Bi^{3+}, Na^{+})-depleted cores are depicted as a circular region within grains that is not modified by electric field or temperature. Domain-like contrast can be visualized by black (non-ergodic relaxor or ferroelectric state) or by red dots/dashes (ergodic relaxor state).

Due to an ergodicity distribution ascribed to the presence of a non-ergodic core and ergodic shell, the BNT-0.25ST features a non-zero P_r that leads to variation of $\varepsilon_r^{'}$ and $\varepsilon_r^{''}$ values in the poled state as compared to the unpoled state. The decay of the induced ferroelectric state to the relaxor state occurs at $T_{f-r} \sim 50$ °C (Figure 5.41) and is attributed mostly to core regions and regions of the shells adjacent to them. It is noted that this transition is dependent on poling conditions[106,107] and thus a direct comparison between different studies should be made carefully. The freezing of PNRs into a non-ergodic state occurred at $T_{fr} \sim 20$ °C and is mostly attributed to shells. It is expected, that upon crossing T_{fr} on heating in any relaxor with an induced ferroelectric state, this state should become unstable due to thermal energy promoting frustration. Therefore, further increase of temperature leads to the decay of the ferroelectric state to an ergodic relaxor state at T_{f-r} and reconciles that $T_{f-r} > T_{fr}$. Two typical dielectric relaxations found in lead-free ferroelectrics, termed in this work T_{fm} (~ 110 °C) and T_{sm} (~ 320 °C) are also observed at higher temperatures. The rationalization of these anomalies will become apparent in the mesoscopic treatment.

The E_{r-f} and E_{f-r} at room temperature depicted in Figure 5.57 (a) display a temperature dependence, because they entail switching processes (Figure 5.57 (b)). Open symbols of E_{r-f} and E_{f-r} were obtained from small signal properties, whereas solid symbols indicate values obtained from large signal properties. As described for room temperature, the E_{r-f} and E_{f-r} obtained from small signal properties are consistently depicted at lower electric field values due to the lower probing frequency. Increasing temperature leads to higher electric field values for the development and decay of the long-range ferroelectric order. The lower E_{r-f} and E_{f-r} values at room temperature can be ascribed to the near room temperature frustration of the ferroelectric state of BNT-0.25ST caused by the presence of Sr^{2+}.[365,366] Since BNT-0.25ST is the boundary between a ferroelectric and a frustrated ferroelectric state, a FD longitudinal instability of P_s^i is expected in this compositional range. This entails that the free energy anisotropy should be minimized in this compositional range.[169] Therefore, increasing temperature leads to a gradual increase in the energy barrier required to develop a long-range ferroelectric order out of a relaxor state. The energy barrier arises from the energy required to promote the percolation of PNRs.[104] Consequently, as in antiferroelectrics, increasing temperature leads to higher transformation electric fields because more energy is required to induce and keep the metastable ferroelectric state.[450] This means that above 80 °C the electric field induced phase transition can no longer be triggered, and thus the low strain output can be ascribed to electrostriction predominantly (Figure 5.51). Increasing temperature also leads to a minimized hysteresis between the development and decay of the long-range order, as indicated by diminished difference between E_{r-f} and E_{f-r}. This is directly related to a gradual transformation of the phase transition from first to second order. The culmination of this process occurs around electric fields of (3.7 ± 0.3) kV/mm and temperatures of (90 ± 20) °C and indicates criticality since $E_{r-f} \approx E_{f-r}$. This region features the highest $d_{33}^{max} \sim 436$ pC/N (Figure 5.44) and relatively low $d_{33}^{*} \sim 440$ pm/V (Figure 5.52). Note that a supercritical region is not depicted in Figure 5.57 (b), since with 4 kV/mm it was not possible to induce a ferroelectric state at temperatures higher than the critical region. It is interesting to note, however, that the relative difference between the E_{r-f} and E_{f-r} obtained from small and large signal properties becomes gradually broader with increasing temperature. Moreover, extrapolation of small and large signal E_{r-f} and E_{f-r} seems to indicate that the critical points obtained at the two different frequencies

do not coincide. The latter two phenomena can be attributed to the complex switching dynamics described. The region between E_{r-f} and E_{f-r} denominated FE_2 could either depict a relaxor state or a ferroelectric state. If the applied electric field did previously not exceed E_{r-f}, FE_2 will depict relaxor features in the regular experimental time scale. It is noted, however, that for considerably long times of applied electric field or with electric field cycling within FE_2 a long-range ferroelectric order may plausibly be induced.[445] In the case where an electric field above E_{r-f} is applied, a ferroelectric state will be induced in the region marked as FE_1. If this is followed by a reduction of the electric field down to within the FE_2 region, a ferroelectric state will remain stable. Therefore, the phase corresponding to FE_2 depends on history and time. The region marked with RE is an ergodic relaxor state and in general no long-range ferroelectric order is expected with the application of electric field.

Mesoscopic treatment: The BNT-0.25ST displays a relatively high strain and low hysteresis at lower electric field than most other incipient piezoelectrics (Figure 3.7). This is the result of the low electric field required to trigger its phase transition. The macroscopic analysis performed cannot reconcile these differences. For this purpose, the core-shell microstructural evolution was investigated by *in situ* TEM in Section 5.2.3. The mesoscopic view of BNT-0.25ST indicates the presence of an approximate $(1_5;\ 1_\infty)_s$ core-shell microstructure. Figure 5.57 (c) marked from 1 to 10 schematically represents the expected temperature and electric field evolution of the core-shell structure. The black color represents either non-ergodic relaxor or ferroelectric state depending on temperature and electric field, according to Figure 5.57 (b). The red color denotes the ergodic relaxor state, which is predominantly observed in the shell regions and at high temperature throughout all of the grains.

Figure 5.57 (c) 1 depicts the core-shell structure of BNT-0.25ST below 75 °C and for electric fields below 2 kV/mm that features domain and chemical contrast. At temperatures considerably above $T_{fr} \sim$ 20 °C the core and shell should undergo a transformation to an ergodic state (Figure 5.57 (c) 2). Increasing temperature up to 165 °C, leads to the gradual disappearance of the irregular wedge-shaped nanodomain configuration within the core and to the disappearance of the nano-sized platelets in the shell (Figure 5.40). Moreover, T ½{ooe} SSR become detectable within the core at 165 °C (Figure 5.40). This means that the crystal structure of the core and the shell in Figure 5.57 (c) 3 cannot be further discerned from the octahedral tilt system point of view. Note, however, that the chemical heterogeneity remains for temperatures where diffusion processes are not considerable and is what leads to the formation of reversible nanodomains within the core. The disappearance of $(a^-a^-a^-)$ octahedral tilting and appearance of $(a^0a^0c^+)$ tilting within the core at $\sim$ 165 °C may be correlated to the first dielectric relaxation observed at $T_{fm} \sim$ 110 °C, considering its broad frequency dispersion and the inherent experimental errors of the *in situ* TEM measurements of ± 20 °C. Further temperature increase up to $\sim$ 345 °C indicates a gradual phase transformation into a state of homogenized absence of domain morphology (Figure 5.57 (c) 4 and 5).[435] The vanishing of SSR also indicates that the tilting becomes either negligible or is below the detection limit of the TEM. The disappearance of the SSR coincides, within experimental errors, with the second dielectric relaxation occurring at $T_{sm} \sim$ 320 °C. It is inferred from these experiments that all anomalies detected by the *in situ* TEM experiments can be attributed to

changes in the octahedral tilt angles, which are related to the observed dielectric relaxations, as previously found for other BNT-based ceramics.[367,436] This result is expected since changes in domain morphology indicate local changes of the polarization and thus of dielectric properties ($\varepsilon_{ij} = \frac{\partial P_i}{\partial E_i}$). Note that the poling process increases the $\varepsilon_r^{''}$ values preferentially at T_{fm}, indicating that on the macroscopic scale the poling procedure favors the $(a^-a^-a^-)$ octahedral tilting. This is suggested since this dielectric relaxation of $\varepsilon_r^{''}$ at T_{fm} seems to be mostly related to the disappearance of the $(a^-a^-a^-)$ octahedral tilting (Figure 5.40). Moreover, neutron diffraction patterns confirmed that the $(a^-a^-a^-)$ tilting is favored with the application of an electric field (Figure 5.35). Increase in the $\varepsilon_r^{'}$ values in the poled state seems to indicate an increased presence of PNRs with domain-like dynamics, as previously proposed for prototypical lead-containing relaxor.[451] The latter two phenomena warrant further investigations.

The electric field induced phase transformation of the core-shell at 4 kV/mm and 25 °C is schematically suggested in Figure 5.57 (c) 6. The core and shell react differently to the electric field considering their different starting relaxor states, as was analyzed with pulse experiments (Figure 5.46). Initially the cores are expected to transform irreversibly to an induced ferroelectric state and experience switching along the electric field vector. Subsequently, the shell should feature an increased blurred contrast. Upon electric field removal, the ergodic shell should feature a reversible transformation to its initial contrast state (Figure 5.57 (c) 1), as proposed for other core-shell materials.[253] It is noted, however, that certain irreversibility of the transformed shell regions adjacent to cores may also exist due to heterogeneous nucleation.[242] Differences in polarization gradients between core and shell should lead to a higher electric field in the shell, thereby enabling the electric field induced phase transition at reduced electric fields.[234,236] The ferroelectric state can still be induced at 80 °C and 4 kV/mm (Figure 5.57 (c) 7). Although, considering the lower values in the peak of $tan(\delta)$ at 80 °C compared to room temperature (Figure 5.43), a lower ferroelectric state fraction and switching processes are expected. Further temperature increases above 110 °C with an applied electric field of 4 kV/mm (Figure 5.57 (c) 8 to 10) should not modify considerably the microstructural evolution described with no application of electric applied. Although electric field increases the correlation length of the $(a^-a^-a^-)$ tilting system (Figure 5.34), the thermal energy is considerably high and restricts development of a long-range ferroelectric order.

Bridging the macroscopic and mesoscopic treatments: Although the core-shell microstructure of the BNT-0.25ST is instrumental to the high strain and seems to be responsible for the dielectric relaxations of the system, the reconciliation of the strain mechanism of this material solely by this approach neglects the fact that for compositions between 25 mol % and 28 mol % ST BNT-ST features a phase boundary.[258,275,363] The presence of the core-shell contributed to the large electromechanical response of BNT-0.25ST only to a certain limited extent (Section 5.2.5), as compared to changes of 3 mol % ST (Figure 5.45). Therefore, it is apparent that the dominating reason behind the high strain output of BNT-0.25ST is the destabilization of the ferroelectric state ascribed to the high Sr^{2+} content. *In situ* electric field neutron diffraction was used to bridge mesoscopic scale treatment with the averaged long-range scale because the orientation-dependent study revealed information about the differently oriented grains (Section 5.2.2). More specifically,

this study revealed that the virgin and remanent states of BNT-0.25ST feature an average pseudocubic structure, although the mesoscopic TEM investigation indicated tilted structures. This can be ascribed to the short correlation length of the tilting system observed by TEM, indicating a contribution below the detection limit of the neutron diffraction.[434]

In non-textured polycrystalline materials, grain orientations are random and fixed. Therefore, the interdependent relationship between grain orientation and constraints, switching events, and intergranular stresses should determine the relative content of electric field induced phases.[144,452,453] BNT-based ceramics have been shown to feature either an electric field induced transformation into a single phase[142] or a phase mixture[141,143,145,146,434,454] depending on chemical composition.[430] Moreover, the electric field required to induce a phase transition and its completeness depends on crystallographic direction.[454,455] Despite the specifics described for the phase transition of BNT-based materials with a crystallographic dependence, it has been generally recognized that the electric field induced phase transformation in BNT-based materials occurs due to an average non-polar to polar phase or phases, indicating a FD longitudinal instability of P_s^i.[140] Nonetheless, these materials may also feature AFD distortions considering that this is a feature of pure BNT.[367] Generally covalency[70] and anionic radii[152] determine the prevailing type of instability. The Sr^{2+} was shown to promote AFD instabilities in perovskite ferroelectrics due to its relatively small cation radii.[456] Together with considerations of the covalency of the bonds, it was determined that ST features prominent AFD distortions.[70,371] The competing nature of both instabilities[70] and the presence of Sr^{2+}, implies that the electric field induced transformation and the predominant coupling between order parameters resulting in large strains in BNT-0.25ST must depend on grain orientation with respect to the applied electric field (Section 5.2.2). Figure 5.58 (a) provides a schematic representation of two grains, one with $\langle hhh \rangle$ and the other with $\langle 00l \rangle$ oriented along the direction where the electric field will be applied. Figure 5.58 (b) displays a strain output (marked with S) that results from a selective transformation to either T (red) or R (blue) phases. Note that the two grains are meant as a representation of the core and shell microstructure but shown separately to allow for easier visualization. The representation considers reversibility of the phase transition from both constituents, as was seen from neutron diffraction (Figure 5.35).

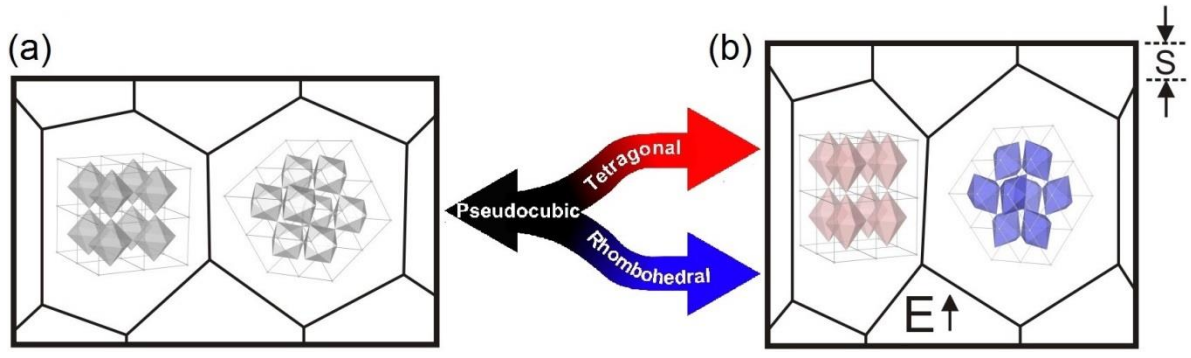

Figure 5.58: Schematic representation of the two ideal cases of grains with $\langle hhh \rangle$ and $\langle 00l \rangle$ orientation along an applied electric field direction that respond with a strain indicated by S. Grains in the (a) virgin state (gray) transform preferentially and reversibly to either (b) tetragonal (red) or rhombohedral (blue) phases.

Both of the grain orientations provided in Figure 5.58 correspond to $k \| E$, and the electric field directly affects the P_S^i since both first order tensors lie on the same spatial direction for T and R phases due to the grains' different orientations in space. Note that the grains oriented along ½$(311)_{pc}$ are not displayed since it was observed that they transform to a T phase due to the proximity of the ½$(311)_{pc}$ to ⟨00l⟩, rather than to ⟨hhh⟩. Since strain and polarization are coupled order parameters (as described in Section 2), a considerable lattice strain is promoted due to a longitudinal instability of P_S^i, which leads to a maximized converse piezoelectric effect and electrostriction. Consequently, the case of $k \perp E$ displays minimized lattice strain along [100] and [111] directions due to maximized shrinkage and thus compressive stresses. Nonetheless, intensity of ½$(311)_{pc}$ SSR is not maximized for a given direction in space. This indicates that the electric field induced phase transformation is active. In contrast, other BNT-based materials feature passive phase transformations as a consequence of compressive stresses.[141,142] Since stresses seem to play a secondary role, the non-zero intensity of the ½$(311)_{pc}$ SSR indicates that the electric field is a conjugate thermodynamic variable of the octahedral tilt angle ∅. This entails that the correlation length of $(a^-a^-a^-)$ tilting increases considerably upon application of electric field. Coupling between the electric field and ∅ in the T phase can be discarded since the ½$(310)_{pc}$ SSR corresponding to a $P4bm$ symmetry remained below the detection limit of the neutron diffraction experiment. Therefore, the strain of grains with $R3c$ symmetry is a result of converse piezoelectric effect and/or electrostriction, as well as rotostriction. The latter is, to the author's knowledge, the first experimental proof of the coupling between strain and ∅ in a bulk perovskite ferroelectric. The average pseudocubic phase of BNT-0.25ST can thus be indicated as a bridging phase between the FD longitudinal instability of P_S^i as well as of the AFD instability. This leads to an analogy between M and O phases that are generally considered to be bridging phases for FD transverse instabilities of P_S^i.[173] Moreover, an orientation-dependent coupling between different order parameters implies a considerable degree of texturing since the development of polar phases is preferential in space (Figure 5.34). Therefore, the intrinsic nature of the orientation-dependent coupling promotes texturing, which is an extrinsic contribution. The switching associated with this texturing process was normally considered as indicative of the phase transition (Sections 5.2.4.2 and 5.2.4.3). Since the virgin state remains untextured, the reversible texturing of the bridging pseudocubic phase attributed mostly to the ergodic shells allows the FD longitudinal and AFD instabilities to be exploited at each cycle of applied electric field. The correlation between the development of the phase transition and subsequent switching was previously demonstrated in similar BNT-based materials.[143,144] It seems feasible that the orientation-dependent phase transformation in BNT-0.25ST is favored due to the core-shell microstructure, since it promotes competition between order parameters due different tilt systems and polarization gradients (Section 5.2.3). Therefore, the considerably high switching (and thus texturing) leading to the high electromechanical response of BNT-0.25ST is due to an orientation-dependent transformation facilitated by competing FD and AFD instabilities and the core-shell microstructure. This reconciles the low electric field required to attain the phase transformation into a long-range order in BNT-0.25ST as compared to the higher electrics fields needed for other BNT-based materials. The competing instabilities leading to a frustrated ferroelectric state should be also responsible for the reversible character of the phase transition that allows assessing a maximized strain output.

Implications: As treated throughout this entire work and specifically in Section 2.3, design of ferroelectrics around phase instabilities is one of the preferred choices to attain enhanced functional properties. So far AFD instabilities and their ability to generate strain have been largely ignored experimentally, although they have been treated theoretically in several phenomenological studies.[58,457-459] It is interesting to note that even PZT, which is probably the most technologically relevant perovskite, features the presence of competing order parameters leading to FD and AFD instabilities depending on composition, temperature, and pressure.[460-463] A literature survey indicated that this is a common feature of perovskite ferroelectrics that determines the stability of their ferroelectricity.[456] A recent framework for frustrated ferroelectricity in tetragonal tungsten bronzes was developed based on competing instabilities.[464] This suggests that a proper understanding of structural instabilities and associated order parameters, as well as their couplings, is mandatory in order to engineer the functionality of several classes of advanced ceramics. Ferroelectrics have been traditionally designed around FD phase instabilities[169] to maximize strain output such as was treated for BZT-BCT (Section 5.1). However, the results of this section imply that AFD instabilities also contribute to the maximum achievable strain.

6 Conclusions

In this work, the strain mechanisms of two different lead-free ferroelectrics, the (1-x)$Ba(Zr_{0.2}Ti_{0.8})O_3$-x$(Ba_{0.7}Ca_{0.3})TiO_3$ and the (1-x)$(Bi_{1/2}Na_{1/2})TiO_3$-x$SrTiO_3$, have been thoroughly investigated and analyzed in order to identify the different contributions to the electromechanical output. With the purpose of describing the relations between functional properties, crystal structure, and microstructure various different techniques were employed on different length scales. Special emphasis was done to elucidate different types of phase instabilities and their influence on the electromechanical properties. Moreover, the broad range of experiments performed also enabled an application-oriented characterization, as given in Appendix V for interested readers.

From the results obtained for the (1-x)$Ba(Zr_{0.2}Ti_{0.8})O_3$-x$(Ba_{0.7}Ca_{0.3})TiO_3$ system, it can be concluded that although both intrinsic and extrinsic contributions to the piezoelectric activity are relevant, extrinsic contributions are generally larger. It was observed that the rhombohedral phase is less distorted and much softer than the tetragonal phase, which means that the rhombohedral phase had higher extrinsic contributions and less temperature stability. In contrast, the tetragonal phase was observed to be much harder from a piezoelectric and elastic properties point of view. In this phase small signal, large signal, and elastic properties were shown to be quite insensitive to temperature up to the Curie temperature of 95 °C. This was attributed to a high intrinsic contribution and an overall decrease of switching processes with increasing temperature. The interleaving region between rhombohedral and tetragonal phases, termed in this work as an orthorhombic phase, displayed a large piezoelectric activity in the small and large signal regimes. It was observed that this phase features the highest irreversible switching in the compositional range investigated and high coupling coefficient values. These properties are a result of the high elastic softening of this phase as well as the high multiplicity of polarization directions. Three regions of the phase diagram near phase boundaries were investigated in detail. The convergence region, found between 0.65 mol fraction $Ba(Zr_{0.2}Ti_{0.8})O_3$-0.35 mol fraction $(Ba_{0.7}Ca_{0.3})TiO_3$ and 0.63 mol fraction $Ba(Zr_{0.2}Ti_{0.8})O_3$-0.37 mol fraction $(Ba_{0.7}Ca_{0.3})TiO_3$ at temperatures between 55 °C and 65 °C, was predicted to consist either of a quadruple point or two triple points. Without the presence of a bias-field, the convergence region displays relatively low d_{33} due to a reduction of the poling state at these temperatures. The low value of d_{33}^* in this region is, however, the consequence of small non-cubic distortions. A line of critical points at a finite bias-field higher than the coercive field values was observed above the Curie temperatures of all the compositions investigated, revealing that the convergence region does not feature criticality. It was found that the line of critical points depicts maximized d_{33} and intermediate d_{33}^* values. Maximized d_{33} at the critical line resulted from a high reversible extrinsic contribution, as well as intrinsic contributions although to a minor extent. Similarly, as the convergence region little non-cubic distortions led to non-maximized d_{33}^* values. Two polymorphic phase boundaries characterized by different electromechanical response were also found in the (1-x)$Ba(Zr_{0.2}Ti_{0.8})O_3$-x$(Ba_{0.7}Ca_{0.3})TiO_3$. The rhombohedral to orthorhombic polymorphic phase boundary displays maximized d_{33}^* ascribed to relatively high intrinsic and extrinsic contributions, the latter being mostly reversible switching. In contrast, the highest d_{33} and nearly equally large d_{33}^* was observed in the orthorhombic to tetragonal phase boundary. This

enhancement of both measures of piezoelectric coefficient is a consequence of the maximized intrinsic properties and a high degree of irreversible extrinsic switching. The most relevant contribution to the intrinsic properties on the system near polymorphic phase boundaries was found to be the ferrodistortive transverse instability of the spontaneous polarization.

From all the research performed for the (1-x)($Bi_{1/2}Na_{1/2}$)TiO_3-x$SrTiO_3$ system, it can be concluded that the large signal strain output is a result of switching processes arising from a first order, orientation-dependent phase transformation from a macroscopically pseudocubic to a combination of tetragonal and rhombohedral phases. The orientation-dependent phase transformation evolves as a consequence of the competing ferrodistortive longitudinal and antiferrodistortive instabilities near room temperature ascribed to a pseudocubic bridging phase. In the mesoscopic scale, each grain will either transform to tetragonal or rhombohedral symmetry depending on grain orientation with respect to the electric field vector. This entails that grains oriented unfavorable to the electric field vector can still transform and contribute to the strain output. The intrinsic contributions resulting from the competing instabilities were found to be piezoelectricity, electrostriction, and rotostriction. Piezoelectricity and electrostriction were found for grains transforming to the tetragonal phase. Grains transforming to the rhombohedral phase display the latter strain mechanisms, as well as rotostriction. The competing instabilities mean that a relatively low electric field between 2.42 kV/mm and 2.85 kV/mm is required to develop the long-range ferroelectric state in the hertz frequency range. Moreover, the orientation-dependent transformation also results in a considerable degree of reversible texturing since each phase can nucleate preferentially in space with respect to the electric field vector. The 0.75($Bi_{1/2}Na_{1/2}$)TiO_3-0.25$SrTiO_3$ ceramics consist of a core-shell microstructure, which is a product of the limited diffusion between ($Bi_{1/2}Na_{1/2}$)TiO_3 and $SrTiO_3$ during processing. The core features a lower Sr^{2+}/(Bi^{3+},Na^{+}) ratio compared to the shell, which implies a non-ergodic relaxor state in the core in contrast to the ergodic relaxor state of the shell. Therefore, the electric field induced phase transformation described is mostly attributed to the shells. Differences in polarization gradient and tilting systems between core and shell are a consequence of their chemical difference and favor the coexistence of the discussed competing ferrodistortive and antiferrodistortive instabilities. Moreover, this microstructure imparts a higher local electric field distribution in the shells. This in turn promotes the reduction of the average electric field needed in order to induce the phase transformation. Criticality was found between 80 ° and 110 °C with electric fields between 3 and 4 kV/mm. Similarly as found for (1-x)Ba($Zr_{0.2}Ti_{0.8}$)O_3-x($Ba_{0.7}Ca_{0.3}$)TiO_3, maximized d_{33} and intermediate d_{33}^{*} values were observed in the critical region and were ascribed to the same fundamental reasons previously discussed.

Analysis of the results presented in this work and the work performed within various collaborations led to several conclusions that, in the author´s opinion, may be considered as guidelines for the future design of ferroelectrics:

- Maximization of the intrinsic contribution to d_{33} will be attained at phase boundaries that present a reduced free energy anisotropy, high softening, and high spontaneous/remanent polarization. Neither the reduced free energy anisotropy, nor elasticity, nor high spontaneous/remanent polarization can be considered as sufficient conditions on their own in order to attain maximized piezoelectric properties, but rather each part is necessary.

- The intrinsic contribution to d_{33} in a system with several interferroelectric transitions is expected to be maximized at the phase boundary that provides the greatest shear softening. This holds true only in cases where similar levels of reduced free anisotropy energy and spontaneous/remanent polarization are maintained.
- Critical points entail maximized small signal d_{33} rather than d_{33}^*. This statement is valid for ferroelectrics with first order (or weak first order) phase transitions that evolve to second order at relatively high temperature. The maximized small signal d_{33} is a consequence of the balance between a considerably high thermally activated reversible extrinsic switching with a minor proportion of intrinsic response. Since the non-cubic distortions are small at high temperatures maximized d_{33}^* values should not be expected due to little strain per switching event.
- Bridging phases are of fundamental importance since they facilitate instabilities of order parameters which is another key to achieving enhanced properties. These phases will promote switching processes and thus texturing due to the high multiplicity of polarization directions that they enable.
- Maximizing the number of instabilities related to different order parameters may maximize outputs in several multifunctional ceramics.

From an application point of view, the systems investigated can be considered as potential candidates for actuator applications mostly in low operational temperatures (up to $\sim$ 100 °C). It was observed that the (1-x)$Ba(Zr_{0.2}Ti_{0.8})O_3$-x$(Ba_{0.7}Ca_{0.3})TiO_3$ system is a promising lead-free candidate for applications working in the quasi-static, dynamic, and potentially high power small signal applications. Large signal actuator applications requiring high strain output, but at reduced electric fields of 1 kV/mm, can also be considered as a potential field of application for this system. Large signal applications, requiring a considerably high strain output above 0.25 %, may implement the 0.75$(Bi_{1/2}Na_{1/2})TiO_3$-0.25$SrTiO_3$ as a possible candidate. However, it should be taken into consideration that the optimal driving electric field for this material was found to be 4 kV/mm. The lack of the need for a dc bias poling process and reliable reversibility of the phase transition even after several cycles are beneficial for its implementation.

7 Remarks and Future Work

Ferroelectric materials have been traditionally designed around phase boundaries to enhance electromechanical properties. The enhancement has been attributed to several fundamental reasons and remains an open research area. Namely, reduction of the free energy anisotropy, crystal softening, nanodomain formation, local chemical/structural ordering, and local low symmetry phases, among others have been evoked to reconcile the superior properties found around phase boundaries. Nevertheless, in the desperate search of finding the key fundamental reason behind exceptional electromechanical properties, the interdependent relation between them has been largerly ignored due to a limited view of the physical problem in question. This resembles the parable of the elephant:

“Four blind men encounter an elephant. One grabs the leg and concludes it is a tree trunk. One holds the tail thinking it is a whip. Another touches the elephant’s trunk and decides it’s a hose and the fourth man pats the side concluding it’s a wall”.[176]

Although the four blind men got a correct answer of what they hold, a more enriching view would have been made if they would have talked to each other and as a group discussed their findings trying to integrate their limited knowledge into a complete view. In general scientists have realized this concept, as the amount of peer reviewed papers with increasing scientific cooperation have increased in last years.[465] Nonetheless, new multidisciplinary approaches should contemplate existing concepts and their interrelationships to construct a complete view of the “elephant”. Although a broad investigation from several perspectives was achieved during this work, the limited time duration of a doctoral degree entails restricted research and thus remaining open questions. In the case of the (1-x)$Ba(Zr_{0.2}Ti_{0.8})O_3$-x$(Ba_{0.7}Ca_{0.3})TiO_3$, a synthesis study is required to elucidate consistently the effect of the variations of the secondary phase $Ba_6Ti_{17}O_{40}$ content in the structural and functional properties, as actually modifications of $Ba_6Ti_{17}O_{40}$ were shown to determine to a certain extent the functionality of the system.[386] Variation of the synthesis conditions and secondary phases entails an effect in the defect chemistry. A non-negligible internal bias-field that varied with composition was observed in this work and indicates that defect chemistry should be analyzed since defects affect domain switching processes. In this work only processes related to non-180° switching and without variation of synthesis conditions were investigated. Future works relating point defects and all domain switching processes could be of great technological impact.[328,466] Specifically, stabilization of an engineered domain structure through proper poling or defects could be seen as a promising approach to enhance electromechanical properties. Considering the almost degenerate free energy between rhombohedral and orthorhombic phases, *in situ* neutron diffraction studies are encouraged to explore the possible presence of an electric field induced phase transition on the system. This structural study, together with Rayleigh measurements, could lead to a much more fundamental understanding of the strain mechanisms of the system. Further insights into the relaxor-like nature of (1-x)$Ba(Zr_{0.2}Ti_{0.8})O_3$-x$(Ba_{0.7}Ca_{0.3})TiO_3$ are also required and warrant further studies. The relaxor properties of the (1-x)$(Bi_{1/2}Na_{1/2})TiO_3$-x$SrTiO_3$ system were found to be quite relevant in the determination of its functional properties. Therefore, a study of switching dynamics should be performed to expand the current knowledge on the relaxor physical features and the electric field

induced ferroelectric state. This approach could also provide relevant insights for its applicability. Engineering the core-shell microstructure of the $0.75(Bi_{1/2}Na_{1/2})TiO_3$-$0.25SrTiO_3$ remains an open research area and should be further investigated to evaluate the role of this microstructure on the system. Moreover, the core-shell microstructure of $0.75(Bi_{1/2}Na_{1/2})TiO_3$-$0.25SrTiO_3$ is a unique research platform for fundamental interface studies in two materials with different local structures and polarization states.

Further studies are also required in case that technological implementation is desired. Reliability studies such as influence of humidity, aging, and fatigue were not treated in this work and constitute indispensable studies for the technological implementation of ferroelectrics. Scalability of synthesis processes is also a considerable technological challenge that was out of the scope of this work. Selection of proper electrodes is of crucial importance considering that most of the cost of an actuator is due to the metal electrodes.[467] Biocompatibility studies also offer a great opportunity to implement lead-free piezoelectrics in medical applications. It was noted that for specific niche markets lead-free piezoceramic have superior properties than lead-containing counterparts.[10] The perspective on the technological implementation of lead-free piezoelectrics, considering solely the foreseen niche markets applicability, indicates that device designers should produce by their own the materials with the specific requirements for each application in order to assure economic viability. This indicates that, unless a lead-free piezoceramic with a broad range of tunable properties becomes available, the market of lead-free piezoceramics will remain relatively small as compared to lead-containing materials. Nevertheless, considering the relatively “young” field of research of lead-free piezoelectrics further improvements are to be expected.[10] It is interesting to note that in 1946 von Hippel, one of the most well-known scientists in the history of ferroelectricity, stated: “Barium titanate, on the other hand, cannot be recommended as a capacitor dielectric except in special cases”.[260] Today barium titanate is the preferred material for ceramic capacitors worldwide.[16] Therefore, one question that remains is: how will the implementation of lead-free piezoceramics evolve in the upcoming years? To the author´s opinion, further insight into the strain mechanisms of these materials should aid to achieve more attractive properties leading to their implementation.

8 Appendix I: Nomenclature for Core-Shell Microstructures

Bulk core-shell dielectrics have shown to be technologically relevant for high temperature applications.[285,468] With the advent of nanotechnology, there has also been a continuous increase in organic and inorganic core-shell nanoparticle discoveries with exceptional properties.[8] This gave rise to the discovery of several types of core-shell microstructures, such as spherical[256,284,285,468], hexagonal[469,470], multiple cores within a single shell[471,472], onion-like[473,474], movable core within shell[475,476], and 2-D structures such as rods[477-479], among others. A general notation is described here in an attempt to standardize the nomenclature used to define core-shell microstructures. The complete nomenclature can be described as:

$$\left(Sh_n(sh), Co_k(co)\right)_{i(co)},$$

where Sh is the number of shells that can vary from 1 to ∞ and Co is the number of cores that can vary from 1 to (∞-1). The subscripts n and k define the number of mirror planes of each shell and core, respectively, where sh and co define the corresponding shell or core under consideration. In the specific case of a 2-D structure n and k can take values up to Sh + 1 and/or Co + 1, since a mirror plane exists along the longitudinal axis and normal to it. Core-shell structures with a 2-D dimensionality should be indicated with a bar; *i.e.*, $\bar{n}$ and $\bar{k}$. The final subscript i defines the coherency of each interface between core and shell. The nomenclature should be only utilized under certain considerations:

- Only a repeatable core-shell structure should be considered for the analysis. This is exclusively relevant for bulk core-shell materials in order to avoid the consideration of certain undesired inherent microstructural defects such as porosity as a core.
- A core is defined as a region with chemical and structural properties differing from the material that surrounds it. The region that surrounds the core is defined as the shell. It is possible, for example in "onion/matryoshka-like" structures[473,474], that several constituents can be simultaneously considered as both a core and a shell.
- The order for counting different constituents should always be performed from the outermost to the innermost constituent. An intentional engineered "void" or "hollow", such as in Refs.[475,476] is considered an extra constituent that can be either core and/or shell.
- The view of the core-shell structure during analysis should be such that the longest rotational axis of the core is parallel to the normal of the investigated surface. In the case of so called 2-D nanostructures, such as wires, rods, or tubes the extra dimension will result in an extra mirror plane perpendicular to the normal of the surface.
- Core-shell bulk materials may present a shell distribution rather than a defined shell geometry. The reason for this is that grain geometries (*i.e.*, shells) in bulk materials are expected to present a geometry distribution.
- In the case of a change in the geometry of an internal core, the outer cores need to be mentioned to avoid misinterpretations of the structure. There is no need to repeat n and k indexes in case all inner constituents present the same number of mirror planes such as for instance in conventional "onion/matryoshka-like" structures.[473,474]

Based on these considerations, the generalized nomenclature for core-shell geometries proposed is exemplified in Figure 8.1. Examples of the core-shell geometries found in literature are also given.

Core-shell geometries	Nomenclature in literature	Number of shells S	Mirror planes of each shell n(S)	Number of cores C	Mirror planes of each core k(C)	Interface between each core and shell i(C)	Generalized nomenclature	References of core-shell geometries
A 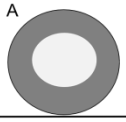	spherical core-shell	1	∞	1	∞	coherent	$(1_{\infty}; 1_{\infty})_c$	256, 284, 285, 468
B 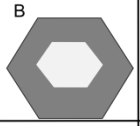	hexagonal core-shell	1	6	1	6	semicoherent	$(1_6; 1_6)_s$	469, 470
C 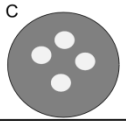	multiple cores coated by single shell	1	∞	4	∞;∞;∞;∞	coherent, coherent, coherent, coherent	$(1_{\infty}; 4_{\infty})_c$	471, 472
D 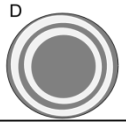	onion-like/ matryoshka core-shell	4	∞;∞;∞;∞	4	∞;∞;∞;∞	coherent, coherent, coherent, incoherent	$(4_{\infty}; 4_{\infty})_{c,c,c,i}$	473, 474
E 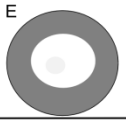	movable core within hollow shell	2	∞;∞	2	∞;∞	coherent, incoherent	$(2_{\infty}; 2_{\infty})_{c,i}$	475, 476
F 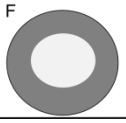	rod/cable/wire core-shell	1	∞	1	∞	coherent	$(1_{\overline{\infty}}; 1_{\overline{\infty}})_c$	477-479

Figure 8.1: Representative core-shell geometries with their respective nomenclatures.

9 Appendix II: Electromechanical Equations

Relevant electromechanical equations for this work are given in this section. Impedance and capacitance measurements enable the dynamic piezoelectric characterization from which a set of piezoelectric, dielectric, and elastic properties can be obtained for a specified geometry excited in a given vibration mode. Figure 9.1 (a) and (b) introduce reactance and impedance curves with relevant parameters to be considered, respectively. Figure 9.1 (c) displays the 33 mode employed for the measurements in this work.

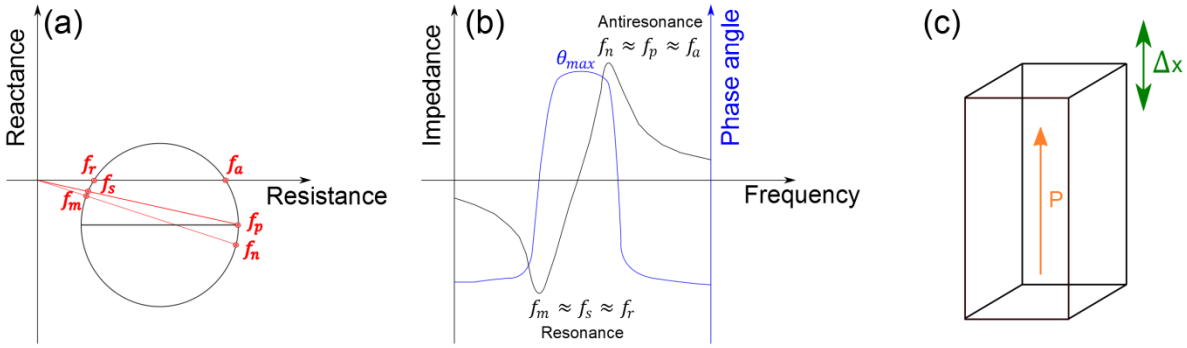

Figure 9.1: (a) Vector impedance diagram and (b) typical impedance and phase angle measurement curves. (c) scheme of 33 mode employed in this work indicating that the polarization P and measured displacement Δx are parallel.

The resonance-antiresonance frequencies f_r and f_a correspond to a material with pure real resistance. The frequencies f_s and f_p represent the resonance-antiresonance values that would be measured in a material with no losses. The frequencies f_m and f_n depict the smallest and largest magnitudes of impedance, respectively. The frequencies $f_m \approx f_s \approx f_r$ and $f_n \approx f_p \approx f_a$ coincide approximately for a low loss piezoelectric resonator. Based on this assumption, it is possible to calculate $\varepsilon_{33}^{\mathrm{T}}$, k_{eff}, k_{33}, d_{33}, Q_m, s_{33}^{D}, s_{33}^{E}, and N_{33} as displayed in Table 9.1.[385,468,480]

Table 9.1: Dynamic piezoelectric and elastic coefficients that can be calculated from a 33 mode resonance measurement.[385,480] t: thickness, l: longitude, Z: impedance.

Denomination	Equation	Equation number
Permittivity of the medium	$\varepsilon_{33}^{T} = C^{T}\frac{t}{A}$	**Equation 9.1**
Effective coupling coefficient	${k_{eff}}^{2} = \frac{{f_p}^2 - {f_s}^2}{{f_p}^2}$	**Equation 9.2**
Coupling coefficient	${k_{33}}^{2} = \frac{\pi}{2}\frac{f_r}{f_a}\cot(\frac{\pi}{2}\frac{f_r}{f_a})$	**Equation 9.3**
Dynamic piezoelectric coefficient	$d_{33} = k_{33}(\varepsilon_{33}^{T}s_{33}^{E})^{1/2}$	**Equation 9.4**
Mechanical quality factor	$Q_m = \frac{1}{2\pi f_m \lvert Z\rvert C^{T}{k_{eff}}^{2}}$	**Equation 9.5**
Open circuit elastic compliance	$s_{33}^{D} = \frac{1}{4\delta_s {f_p}^2 l^2}$	**Equation 9.6**
Short circuit elastic compliance	$s_{33}^{E} = \frac{s_{33}^{D}}{1-{k_{33}}^{2}}$	**Equation 9.7**
Frequency constant	$N_{33} = f_p l$	**Equation 9.8**

10 Appendix III: Dielectric Relaxation in the (1-x)Ba($Zr_{0.2}Ti_{0.8}$)O_3-x($Ba_{0.7}Ca_{0.3}$)TiO_3 System

Ravez *et al.*[115,116,334] reported that the ternary system between BT, BZ, and CT depicts relaxor features. Depending on the compositional range the relaxor features of the ternary system may be weak. An input signal in the frequency range between 1 Hz and 1 MHz was employed to characterize the dielectric properties as a function of temperature to elucidate the frequency dispersion of dielectric properties on the system, as introduced in Figure 10.1. Insets display the position of the ε_r' maximum as a function of frequency. A non-zero frequency shift of the maxima is featured in all BZT-BCT compositions. The non-zero frequency shift does not follow for any composition the Vogel-Fulcher relationship indicating that the relaxation process does not seem to be a conventional relaxor-like type. It seems to shift from a thermally activated Arrhenius increase in temperature with increasing frequency for BZT-0.30BCT to an almost linear increase of the maxima for the BZT-0.45BCT. A detailed treatment of the non-conventional relaxor features of the BZT-BCT is out of the scope of this work. It should be noted that the dielectric relaxation depicted may also be related to a Maxwell-Wagner effect[429] due to the presumably existent secondary phases at grain boundaries.[386]

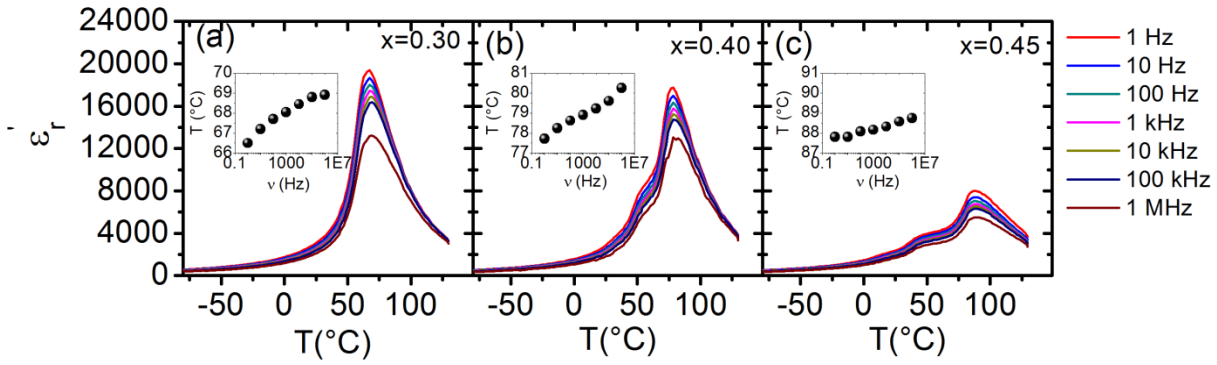

Figure 10.1: Temperature- and frequency-dependent ε_r' measured over a broad frequency range between 1 Hz and 1 MHz for BZT-BCT measured upon cooling. Insets depict the maximum of ε_r' as a function of frequency.

11 Appendix IV: Cycling Reliability of the (1-x)($Bi_{1/2}Na_{1/2}$)TiO_3-x$SrTiO_3$ System

In order to study the cycling stability of BNT-0.25ST, Figure 11.1 introduces (a) bipolar polarization and (b) bipolar strain for the 2nd cycle, after 10^5 cycles, and after 10^6 cycles. It is depicted that the material features reliable cycle stability. It is actually found that polarization and strain output increases with increasing number of cycles. Fatigue-free BNT-based materials were also reported in the literature.[481,482] The creation of fresh domains after each cycle due to the reversible character of the electric field induced phase transition in incipient piezoelectrics was proposed to be responsible for fatigue-free materials. Similarly as in BNT-BT-ST[354], defects and charges accumulated at the core-shell interface may play a role in the fatigue effect. Further detailed studies are required to reconcile the fatigue behavior of BNT-0.25ST.

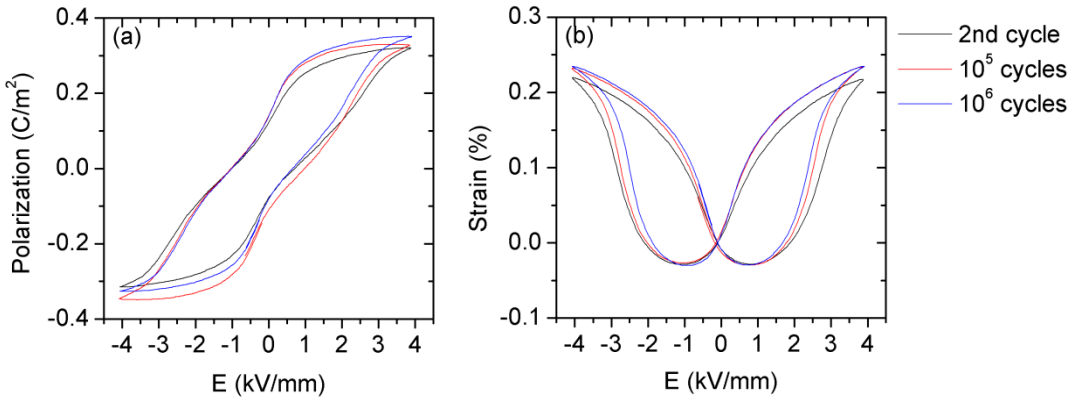

Figure 11.1: Bipolar (a) polarization and (b) strain as a function of electric field for BNT-0.25ST. Polarization and strain are displayed after virgin cycle, 10^5, and 10^6 cycles.

12 Appendix V: Application-Oriented Characterization

A thorough research was performed on the BZT-BCT and BNT-ST systems in order to elucidate their strain mechanisms. However, the applicability of these materials for small and large signal applications was also investigated by these experiments. In this section a brief comparison between soft PZT (PIC 151), BZT-0.40BCT, and BNT-0.25ST is made to elucidate the applicability of the lead-free materials analyzed in the small and large signal regimes. Note that the BZT-0.40BCT was selected for comparison purposes since this composition features a compromise between enhanced properties and temperature stability. In case maximization of small signal properties is required at room temperature the optimum composition is BZT-0.50BCT, although for large signal applications either BZT-0.40BCT or BZT-0.50BCT can be considered. In the case that temperature stability is required, the BZT-0.60BCT could be selected due to the highest temperature stability, although with a lower electromechanical output.

12.1 Small Signal Regime

Apart from the electromechanical output, two of the most relevant parameters to elucidate the applicability of a ferroelectric material in small and large signal applications are the temperature and frequency operational ranges (Table 1.1). Figure 12.1 provides the normalized quasi-static d_{33} of PIC 151 and BZT-0.60BCT as a function of temperature. Normalization was performed with respect to the room temperature d_{33} of each material. Note that the small signal d_{33} of BNT-0.25ST is not shown because it is considerably low due to the discussed incipient piezoelectricity of this material.

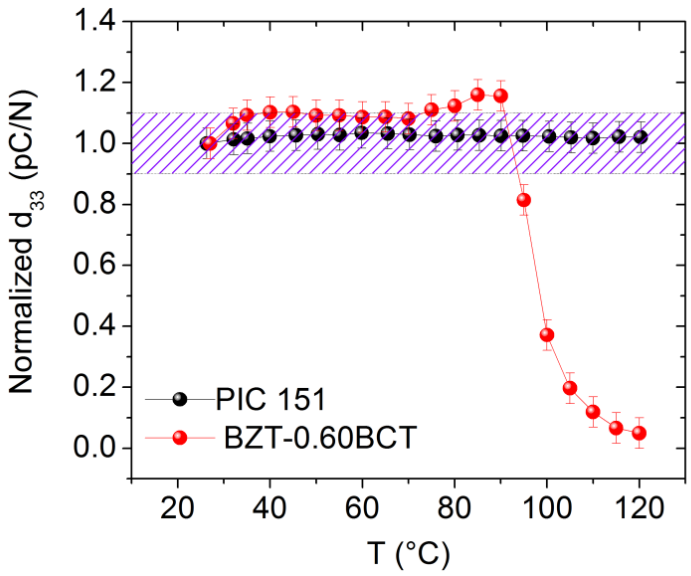

Figure 12.1: Comparison of normalized d_{33} as a function of temperature for PIC 151 and BZT-0.60BCT.

Figure 12.1 specifies that PIC 151 features variation of d_{33} below ± 10 % in the temperature range between 25 °C and 120 °C. If ± 10 % variation of properties is set as an acceptable variation in service, the operational range of BZT-0.60BCT is between 25 °C and ~ 80 °C. Note that the small signal temperature range of applicability of BZT-BCT can be greatly enhanced by superimposing a bias-field with a proper temperature profile. Figure 12.2 displays the d_{33} as a function of bias-field obtained for BZT-0.30BCT at different temperatures. This composition was chosen to explain this concept since it displays a low T_C = 61 °C. It is observed that it is possible to apply a bias-field at a given temperature even up to 105 °C such that d_{33} remains ~ 200 pC/N for a superimposed sinus wave function of 0.02 kV/mm. The bias-field required to obtain these intersections is displayed in the inset. It is observed that it displays a parabola profile (green dotted line indicates fitting performed with a parabola function). Note that with this approach temperature operability almost twice as high as without bias-field can be obtained for this composition with considerably low bias-field voltages below 0.70 kV/mm. In the hypothetical case of a multilayer actuator with layers of ~ 20 µm thickness[483], a maximum bias-field input voltage of 14 V would be needed based on this analysis. This strategy seems feasible for BZT-BCT considering its low E_c (Figure 5.24). A conventional proportional-integral-derivative controller would be required to regulate the bias-field input.

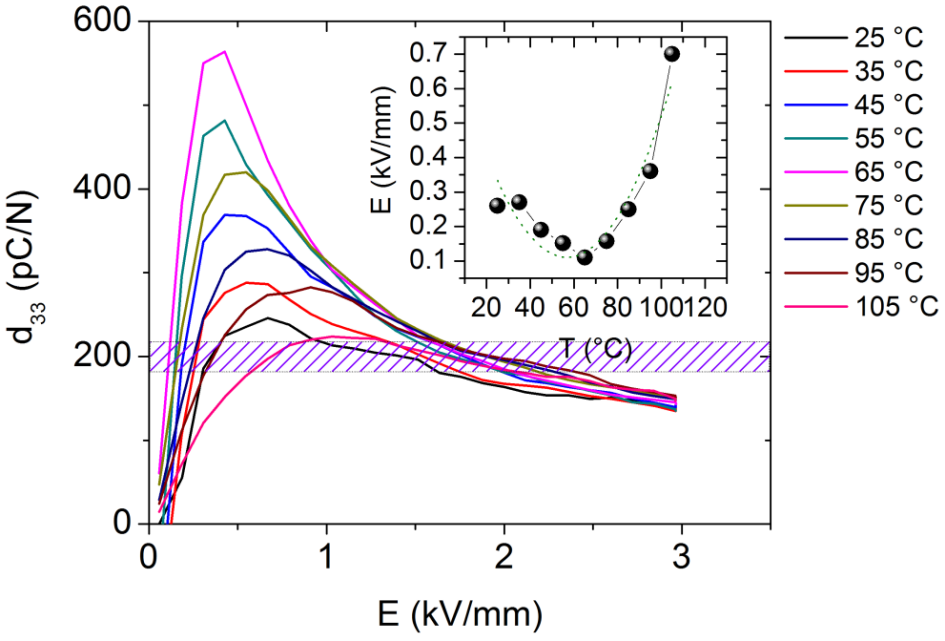

Figure 12.2: Small signal d_{33} as a function of bias-field for different temperatures. Inset displays the bias-field input electric field required to obtain a $d_{33} \approx$ 200 pC/N. Dotted lines indicate fitting performed with a parabola.

During the dynamic characterization of BZT-BCT (Section 5.1.3.2.2), it was noted that the T phase of BZT-BCT features promising piezoelectric properties for high power applications. The positive temperature profile of Q_m with increasing temperature ascribed to the hard-spring effect can be

beneficial for high power applications due to an "auto regulation" of the temperature indicating that as the material temperature increases during service, the increase in Q_m should lead to a gradual stagnation of the self-heating process. Moreover, the relatively high and temperature stable N_{33} also indicates that the BZT-BCT can vibrate consistently at high frequencies.

12.2 Large Signal Regime

Figure 12.3 provides the (a) normalized d_{33}^* as a function of temperature, (b) normalized d_{33}^* as a function of frequency, and (c) heat dissipated per cycle. The shaded regions indicate the accepted stability of properties considering the stability of PIC 151. Normalization of d_{33}^* was performed with respect to the room temperature d_{33}^* of each material at the optimized operational electric field corresponding to 2 kV/mm for PIC 151, 1 kV/mm for BZT-0.40BCT, and 4 kV/mm for BNT-0.25ST at 5 Hz. The heat dissipation was calculated by integration of the unipolar polarization loops $\oint PdE$.

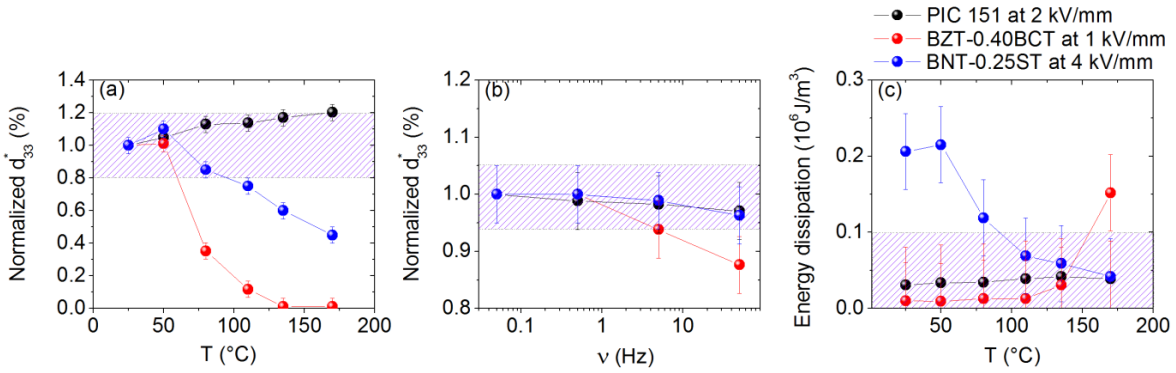

Figure 12.3: Comparison of normalized d_{33}^* as a function of (a) temperature and (b) frequency for PIC 151 at 2 kV/mm, BZT-0.40BCT at 1 kV/mm, BNT-0.25ST at 4 kV/mm. (c) Introduces the energy dissipation per cycle on each material. All values are given at 5 Hz.

PIC 151 features a ± 20 % variation of d_{33}^* in the temperature range between 25 °C and 170 °C. Therefore, ± 20 % was set as the acceptable temperature variation in service. This indicates that the temperature working range of BZT-0.40BCT is between 25 °C and ~ 60 °C, whereas of the BNT-0.25ST is between 25 °C and ~ 95 °C. Note that the lower limit of 25 °C is actually given due to the characterization performed and not due to d_{33}^* variations. Encapsulation and/or coatings, apart from further properties optimization, are a viable strategy to reduce the impact of high temperature on these materials and to improve reliability.[12,484] PIC 151 depicts ± 5 % variation of d_{33}^* in the frequency range between 0.05 Hz and 50 Hz (Figure 12.3 (b)). This is a similar frequency response than observed in BNT-0.25ST, whereas the BZT-0.40BCT has the lowest frequency stability. It is noted, however, that at higher frequencies PIC 151 should depict higher stability than BNT-0.25ST. Figure 12.3 (c) indicates that BZT-0.40BCT has the lowest heat dissipation, which can be attributed to the characteristic slim hysteresis loops of this system (Figure 5.23). In the

temperature region where the BNT-0.25ST features the highest strain outputs associated with the induced ferroelectric state, it also depicts higher losses, which are five times larger than in PIC 151. Nonetheless, it should be considered that other incipient piezoelectrics depict losses an order of magnitude higher than BNT-0.25ST, indicating the benefits of this system compared to other BNT-based materials.[485] It is noted that the heat dissipation is highly correlated to switching processes, which also entail non-linearity in the strain output that can be detrimental for certain applications. Nonetheless, there have been developments to compensate for non-linearity of ferroelectrics by driving electronics.[486,487]

13 Bibliography

[1] A. Testino, International Journal of Applied Ceramic Technology **10**, 723 (2013).

[2] J. Rödel, A. B. N. Kounga, M. Weissenberger-Eibl, D. Koch, A. Bierwisch, W. Rossner, M. J. Hoffmann, R. Danzer, and G. Schneider, Journal of the European Ceramic Society **29**, 1549 (2009).

[3] *Piezoelectric Actuators and Motors - Global Markets and Market Trends* (Innovative Research and Products Inc. Stamford, USA, www.innoresearch.net, 2010).

[4] *Piezoelectric Ceramic, Polymer and Ceramic/Polymer Composite Devices - Types, Materials, Applications, New Developments, Industry Structure and Global Markets* (Innovative Research and Products Inc. Stamford, USA, www.innoresearch.net, 2014).

[5] M. Zupan, M. F. Ashby, and N. A. Fleck, Advanced Engineering Materials **4**, 933 (2002).

[6] R. Müller-Fiedler and V. Knoblauch, Microelectronics Reliability **43**, 1085 (2003).

[7] K. Uchino, Journal of Electroceramics **20**, 301 (2008).

[8] *European Standard: Part 3-Methods of measurement-High power, EN 50324-3* (2002).

[9] K. Uchino, J. Zheng, A. Joshi, Y. H. Chen, S. Yoshikawa, S. Hirose, S. Takahashi, and J. W. C. de Vries, Journal of Electroceramics **2**, 33 (1998).

[10] J. Rödel, K. G. Webber, R. Dittmer, W. Jo, M. Kimura, and D. Damjanovic, Journal of the European Ceramic Society **35**, 1659 (2015).

[11] M. S. Senousy, R. K. N. D. Rajapakse, D. Mumford, and M. S. Gadala, Smart Materials and Structures **18**, 045008 (2009).

[12] R. W. Johnson, J. L. Evans, P. Jacobsen, J. R. Thompson, and M. Christopher, IEEE Transactions on Electronics Packaging Manufacturing **27**, 164 (2004).

[13] K. G. Webber, D. J. Franzbach, and J. Koruza, Journal of the American Ceramic Society **97**, 2842 (2014).

[14] D. C. Lupascu and J. Rödel, Advanced Engineering Materials **7**, 882 (2005).

[15] Y. H. Seo, M. Vögler, D. Isaia, E. Aulbach, J. Rödel, and K. G. Webber, Acta Materialia **61**, 6418 (2013).

[16] G. H. Haertling, Journal of the American Ceramic Society **82**, 797 (1999).

[17] *Rio Declaration on Environment and Development. United Nations Conference 151/25, 1 ILM 874* (1992).

[18] R. L. Ottinger, N. Robinson, and V. Tafur, *Stockholm Declaration of the United Nations Conference on the Human Environment Compendium of Sustainable Energy Laws* (Cambridge University Press, U.K., 2005).

[19] P. Lyn, Alternative Medicine Review **11**, 1 (2006).

[20] W. J. Foster, J. K. Meen, and D. A. Fox, Cutaneous and ocular toxicology **32**, 18 (2013).

[21] *Law for the Promotion of Effective Utilization of Resources. Ministery of Economy, Trade and Industry, Japan* (2001).

[22] *EU-Directive 2002/96/EC: Waste Electrical and Electronic Equipment (WEEE). Official Journal of the European Union L 37, 24* (2003).

[23] *California's Restriction on the Use of Certain Hazardous Substances in Some Electronic Devices (RoHS). Section 25214.10 of the State Health and Safety Code* (2003).

[24] *Prohibition on Certain Hazardous Substances in Consumer Products. Product Regulations Norway* (2004).

[25] *Measures for the Administration on Pollution Control of Electronic Information Products. Ministry of Information Industry China 39* (2006).

[26] *Act for Resource Recycling of Electrical and Electronic Equipment and Vehicles. Environment and Labor Committee of the National Assembly of Korea 6319* (2007).

[27] *Restriction of the Use of Certain Hazardous Substances in Electrical and Electronic Equipment. Ministry of Environment and Forestry Turkey Regulation 26891* (2008).

[28] *EU-Directive 2011/65/EU: Restriction of the Use of Certain Hazardous Substances in Electrical and Electronic Equipment (RoHS). Official Journal of the European Union L 174, 88* (2011).

[29] J. Rödel, W. Jo, K. T. P. Seifert, E. M. Anton, T. Granzow, and D. Damjanovic, Journal of the American Ceramic Society **92**, 1153 (2009).

[30] P. Zubko, G. Catalan, and A. K. Tagantsev, Annual Review of Materials Research **43**, 387 (2013).

[31] D. E. Aspnes, American Journal of Physics **50**, 704 (1982).

[32] F. Cardarelli, *Materials Handbook: A Concise Desktop Reference. Chapter 8: Insulators and Dielectrics* (Springer, 2008).

[33] C. Kittel, *Introduction to Solid State Physics. Chapter 13: Dielectrics and Ferroelectrics* (John Wiley & Sons, 1996).

[34] K. C. Kao, *Dielectric Phenomena in Solids* (Elsevier Academic Press, 2004).

[35] M. Lallart, *Ferroelectrics: Characterization and Modeling* (InTech, 2011).

[36] H. F. Kay, Reports on Progress in Physics **18**, 230 (1955).

[37] M. E. Lines and A. M. Glass, *Principles and Applications of Ferroelectrics and Related Material* (Oxford University Press, 1977).

[38] R. Waser, U. Böttger, and S. Tiedke, *Polar Oxides* (Wiley-VCH, 2005).

[39] B. A. Strukov and A. P. Levanyuk, *Ferroelectric Phenomena in Crystals: Physical Foundations* (Springer, 1998).

[40] J. F. Nye, *Physical Properties of Crystals* (Oxford University Press, 1967).

[41] R. E. Newnham, *Properties of Materials Anisotropy: Anisotropy, Symmetry, Structure* (Oxford University Press, 2005).

[42] B. Jaffe, W. R. Cook, and H. Jaffe, *Piezoelectric Ceramics* (Academic Press London, 1971).

[43] F. Jona and G. Shirane, *Ferroelectric Crystals* (Dover Publications, 1993).

[44] K. Rabe, C. H. Ahn, and J. M. Triscone, *Physics of Ferroelectrics: A Modern Perspective* (Springer, 2007).

[45] A. Safari and E. K. Akdogan, *Piezoelectric and Acoustic Materials for Transducer Applications* (Springer, 2008).

[46] D. Damjanovic, Reports on Progress in Physics **61**, 1267 (1998).

[47] L. Jin, F. Li, and S. Zhang, Journal of the American Ceramic Society **97**, 1 (2014).

[48] D. A. Porter, *Phase Transformations in Metals and Alloys* (Chapman & Hall, 1996).

[49] E. K. H. Salje, ChemPhysChem **11**, 940 (2010).

[50] D. Damjanovic, Journal of the American Ceramic Society **88**, 2663 (2005).

[51] A. A. Bokov and Z. G. Ye, Journal of Materials Science **41**, 31 (2006).

[52] Z. G. Ye, Key Engineering Materials **155-156**, 81 (1998).

[53] L. E. Cross, Ferroelectrics **76**, 241 (1987).

[54] G. A. Samara and E. L. Venturini, Phase Transitions **79**, 21 (2006).

[55] P. N. Timonin, Ferroelectrics **400**, 427 (2010).

[56] W. Kleemann, Journal of Materials Science **41**, 129 (2006).

[57] V. V. Shvartsman and D. C. Lupascu, Journal of the American Ceramic Society **95**, 1 (2012).

[58] V. Gopalan and D. B. Litvin, Nature materials **10**, 376 (2011).

[59] K. Uchino, *Ferroelectric Devices* in *Materials Science and Technology: A Comprehensive Treatment*, *Vol. 11* (1994).

[60] M. Y. Gureev, A. K. Tagantsev, and N. Setter, Physical Review B **83**, 184104 (2011).

[61] W. Cao and L. E. Cross, Physical Review B **44**, 5 (1991).

[62] H. L. Hu and L. Q. Chen, Journal of the American Ceramic Society **81**, 492 (1998).

[63] G. Arlt, D. Hennings, and G. de With, Journal of Applied Physics **58**, 1619 (1985).

[64] T. Egami, Ferroelectrics **267**, 101 (2002).

[65] J. Valasek, Physical Review **17**, 475 (1921).

[66] W. L. Cherry and R. Adler, Physical Review **72**, 981 (1947).

[67] S. Roberts, Physical Review **71**, 890 (1947).

[68] B. T. Matthias, Physical Review **75**, 1771 (1949).

[69] G. H. Kwei, A. C. Lawson, S. J. L. Billinge, and S. W. Cheong, The Journal of Physical Chemistry **97**, 2368 (1993).

[70] W. Zhong and D. Vanderbilt, Physical Review Letters **74**, 2587 (1995).

[71] Q. M. Zhang, W. Y. Pan, S. J. Jang, and L. E. Cross, Journal of Applied Physics **64**, 6445 (1988).

[72] D. A. Hall, Ferroelectrics **223**, 319 (1999).

[73] M. Vopsaroiu, J. Blackburn, M. G. Cain, and P. M. Weaver, Physical Review B **82**, 024109 (2010).

[74] S. E. Park and T. R. Shrout, Journal of Applied Physics **82**, 1804 (1997).

[75] G. A. Smolenskii and V. A. Isupov, Soviet Physics Solid State **24**, 1375 (1954).

[76] G. A. Smolenskii, V. A. Isupov, A. I. Agranovskaya, and N. N. Krainik, Soviet Physics Solid State **2**, 2651 (1961).

[77] G. A. Smolenskii, V. A. Isupov, A. I. Agranovskaya, and S. N. Popov, Soviet Physics Solid State **2**, 2584 (1961).

[78] G. Burns and F. H. Dacol, Solid State Communications **48**, 853 (1983).

[79] G. Burns and F. H. Dacol, Ferroelectrics **104**, 25 (1990).

[80] P. Bonneau, P. Garnier, G. Calvarin, E. Husson, J. R. Gavarri, A. W. Hewat, and A. Morell, Journal of Solid State Chemistry **91**, 350 (1991).

[81] C. Malibert, B. Dkhil, J. M. Kiat, D. Durand, J. F. Berar, and A. Spasojevic-de Bire, Journal of Physics: Condensed Matter **9**, 7485 (1997).

[82] N. Takesue, Y. Fujii, M. Ichihara, and H. Chen, Physics Letters A **257** 195 (1999).

[83] P. Ganesh, E. Cockayne, M. Ahart, R. E. Cohen, B. Burton, R. J. Hemley, Y. Ren, W. Yang, and Z. G. Ye, Physical Review B **81**, 144102 (2010).

[84] D. La-Orauttapong, J. Toulouse, J. Robertson, and Z. G. Ye, Physical Review B **64**, 212101 (2001).

[85] D. Viehland, S. J. Jang, L. E. Cross, and M. Wuttig, Journal of Applied Physics **68** (1990).

[86] D. Viehland, M. Wuttig, and L. E. Cross, Ferroelectrics **120**, 71 (1991).

[87] A. J. Bell, Journal of Physics: Condensed Matter **5**, 8773 (1993).

[88] W. Kleemann, International Journal of Modern Physics B **7**, 2469 (1993).

[89] W. Kleemann, Phase Transitions **65**, 141 (1998).

[90] W. Kleemann and A. Klossner, Ferroelectrics **150**, 35 (1993).

[91] V. Westphal, W. Kleemann, and M. Glinchuk, Physical Review Letters **68**, 847 (1992).

[92] R. Blinc, J. Dolinsek, B. Gregorovic, B. Zalar, C. Filipic, Z. Kutnjak, A. Levstik, and R. Pirc, Journal of Physics and Chemistry of Solids **61**, 177 (2000).

[93] R. Blinc, B. Gregorovic, B. Zalar, R. Pirc, and S. G. Lushnikov, Physical Review B **61**, 253 (2000).

[94] R. Pirc and R. Blinc, Physical Review B **60**, 13470 (1999).

[95] R. Pirc, R. Blinc, and V. Bobnar, Ferroelectrics **259**, 169 (2001).

[96] R. Pirc, R. Blinc, and V. Bobnar, Physical Review B **63**, 054203 (2001).

[97] A. E. Glazounov and A. K. Tagantsev, Ferroelectrics **221**, 57 (1999).

[98] A. K. Tagantsev and A. E. Glazounov, Physical Review B **57**, 18 (1998).

[99] T. Komatsuzaki, A. Baba, S. Kawai, M. Toda, J. E. Straub, and R. S. Berry, *Advancing Theory for Kinetics and Dynamics of Complex, Many-Dimensional Systems: Clusters and Proteins* (John Wiley & Sons, p. 171, 2011).

[100] C. R. Oliveira and T. Werlang, Revista Brasileira de Ensino de Fisica **29**, 189 (2007).

[101] D. L. Stein, AIP Conference Proceedings **1389**, 965 (2011).

[102] H. Vogel, Physikalische Zeitschrift **22**, 645 (1921).

[103] G. Fulcher, Journal of the American Ceramic Society **8**, 339 (1925).

[104] R. Pirc and R. Blinc, Physical Review B **76**, 020101 (2007).

[105] A. Levstik, Z. Kutnjak, C. Filipič, and R. Pirc, Physical Review B **57**, 11204 (1998).

[106] V. Bobnar, Z. Kutnjak, R. Pirc, and A. Levstik, Physical Review B **60**, 6420 (1999).

[107] N. Novak, R. Pirc, M. Wencka, and Z. Kutnjak, Physical Review Letters **109**, 037601 (2012).

[108] W. Jo, J. E. Daniels, D. Damjanovic, W. Kleemann, and J. Rödel, Applied Physics Letters **102**, 192903 (2013).

[109] E. M. Anton, W. Jo, D. Damjanovic, and J. Rödel, Journal of Applied Physics **110**, 094108 (2011).

[110] K. Uchino, Ferroelectrics **151**, 321 (1994).

[111] L. E. Cross, S. J. Jang, R. E. Newnham, S. Nomura, and K. Uchino, Ferroelectrics **23**, 187 (2011).

[112] M. B. Rauls, W. Dong, J. E. Huber, and C. S. Lynch, Acta Materialia **59**, 2713 (2011).

[113] Z. G. Ye and A. A. Bokov, Ferroelectrics **302**, 227 (2004).

[114] H. Khemakhem, A. Simon, R. V. D. Mühll, and J. Ravez, Journal of Physics: Condensed Matter **12**, 5951 (2000).

[115] J. Ravez, R. Von der Mühll, A. Simon, and P. Sciau, Journal of Materials Chemistry **9**, 2829 (1999).

[116] J. Ravez, C. Broustera, and A. Simon, Journal of Materials Chemistry **9**, 1609 (1999).

[117] A. Aydi, H. Khemakhem, C. Boudaya, A. Simon, and R. Von der Mühll, Solid State Sciences **7**, 249 (2005).

[118] C. Ma and X. Tan, Journal of the American Ceramic Society **94**, 4040 (2011).

[119] H. S. Han, W. Jo, J. Rödel, I. K. Hong, W. P. Tai, and J. S. Lee, Journal of Physics: Condensed Matter **24**, 365901 (2012).

[120] V. D. N. Tran, H. S. Han, C. H. Yoon, J. S. Lee, W. Jo, and J. Rödel, Materials Letters **65**, 2607 (2011).

[121] R. Dittmer, W. Jo, J. E. Daniels, S. Schaab, and J. Rödel, Journal of the American Ceramic Society **94**, 4283 (2011).

[122] Y. Hiruma, H. Nagata, and T. Takenaka, Journal of Applied Physics **104**, 124106 (2008).

[123] Y. Hiruma, H. Nagata, and T. Takenaka, Applied Physics Letters **95**, 052903 (2009).

[124] Y. Hiruma, H. Nagata, and T. Takenaka, Japanese Journal of Applied Physics **48**, 09KC08 (2009).

[125] A. Hussain, C. W. Ahn, J. S. Lee, A. Ullah, and I. W. Kim, Sensors and Actuators A: Physical **158**, 84 (2010).

[126] A. Hussain, C. W. Ahn, A. Ullah, J. S. Lee, and I. W. Kim, Japanese Journal of Applied Physics **49**, 041504 (2010).

[127] A. Hussain, J. U. Rahman, A. Zaman, R. A. Malik, J. S. Kim, T. K. Song, W. J. Kim, and M. H. Kim, Materials Chemistry and Physics **143**, 1282 (2014).

[128] W. Jo, E. Erdem, R. A. Eichel, J. Glaum, T. Granzow, D. Damjanovic, and J. Rödel, Journal of Applied Physics **108**, 014110 (2010).

[129] A. Maqbool, A. Hussain, J. U. Rahman, T. Kwon Song, W. J. Kim, J. Lee, and M. H. Kim, Ceramics International **40**, 11905 (2014).

[130] V. Q. Nguyen, H. S. Han, K. J. Kim, D. D. Dang, K. K. Ahn, and J. S. Lee, Journal of Alloys and Compounds **511**, 237 (2012).

[131] K. N. Pham, A. Hussain, C. W. Ahn, W. Kim Ill, S. J. Jeong, and J. S. Lee, Materials Letters **64**, 2219 (2010).

[132] Y. Saito, H. Takao, T. Tani, T. Nonoyama, K. Takatori, T. Homma, T. Nagaya, and M. Nakamura, Nature **432**, 84 (2004).

[133] K. T. P. Seifert, W. Jo, and J. Rödel, Journal of the American Ceramic Society **93**, 1392 (2010).

[134] A. Ullah, C. W. Ahn, A. Hussain, I. W. Kim, H. I. Hwang, and N. K. Cho, Solid State Communications **150**, 1145 (2010).

[135] K. Wang, A. Hussain, W. Jo, and J. Rödel, Journal of the American Ceramic Society **95**, 2241 (2012).

[136] K. Wang, F. Z. Yao, W. Jo, D. Gobeljic, V. V. Shvartsman, D. C. Lupascu, J. F. Li, and J. Rödel, Advanced Functional Materials **23**, 4079 (2013).

[137] S. T. Zhang, A. B. Kounga, E. Aulbach, H. Ehrenberg, and J. Rödel, Applied Physics Letters **91**, 112906 (2007).

[138] A. Ullah, C. W. Ahn, A. Hussain, S. Y. Lee, H. J. Lee, and I. W. Kim, Current Applied Physics **10**, 1174 (2010).

[139] S. T. Zhang, A. B. Kounga, E. Aulbach, T. Granzow, W. Jo, H. J. Kleebe, and J. Rödel, Journal of Applied Physics **103**, 034107 (2008).

[140] W. Jo, T. Granzow, E. Aulbach, J. Rödel, and D. Damjanovic, Journal of Applied Physics **105**, 094102 (2009).

[141] M. Hinterstein, M. Knapp, M. Hölzel, W. Jo, A. Cervellino, H. Ehrenberg, and H. Fuess, Journal of Applied Crystallography **43**, 1314 (2010).

[142] J. E. Daniels, W. Jo, J. Rödel, and J. L. Jones, Applied Physics Letters **95**, 032904 (2009).

[143] A. J. Royles, A. J. Bell, A. P. Jephcoat, A. K. Kleppe, S. J. Milne, and T. P. Comyn, Applied Physics Letters **97**, 132909 (2010).

[144] A. J. Royles, A. J. Bell, J. E. Daniels, S. J. Milne, and T. P. Comyn, Applied Physics Letters **98**, 182904 (2011).

[145] H. Simons, J. E. Daniels, W. Jo, R. Dittmer, A. Studer, M. Avdeev, J. Rödel, and M. Hoffman, Applied Physics Letters **98**, 082901 (2011).

[146] H. Simons, J. E. Daniels, J. Glaum, A. J. Studer, J. L. Jones, and M. Hoffman, Applied Physics Letters **102**, 062902 (2013).

[147] H. Simons, J. E. Daniels, A. J. Studer, J. L. Jones, and M. Hoffman, Journal of Electroceramics **32**, 283 (2014).

[148] J. Kling, X. Tan, W. Jo, H. J. Kleebe, H. Fuess, and J. Rödel, Journal of the American Ceramic Society **93**, 2452 (2010).

[149] E. Sapper, N. Novak, W. Jo, T. Granzow, and J. Rödel, Journal of Applied Physics **115**, 194104 (2014).

[150] S. O. Leontsev and R. E. Eitel, Science and Technology of Advanced Materials **11**, 044302 (2010).

[151] F. Li, L. Wang, L. Jin, D. Lin, J. Li, Z. Li, Z. Xu, and S. Zhang, IEEE Transactions on Ultrasonics, Ferroelectrics, and Frequency Control **62**, 18 (2015).

[152] V. M. Goldschmidt, Naturwissenschaften **14**, 477 (1926).

[153] W. Jo, J. E. Daniels, J. L. Jones, X. Tan, P. A. Thomas, D. Damjanovic, and J. Rödel, Journal of Applied Physics **109**, 014110 (2011).

[154] J. F. Li, K. Wang, F. Y. Zhu, L. Q. Cheng, and F. Z. Yao, Journal of the American Ceramic Society **96**, 3677 (2013).

[155] K. Wang and J. F. Li, Journal of Advanced Ceramics **1**, 24 (2012).

[156] A. A. Heitmann and G. A. Rossetti, Jr., Journal of the American Ceramic Society **97**, 1661 (2014).

[157] D. Damjanovic, IEEE Transactions on Ultrasonics, Ferroelectrics, and Frequency Control **56**, 1574 (2009).

[158] A. G. Khachaturyan, Philosophical Magazine **90**, 37 (2010).

[159] G. A. Rossetti, Jr., A. G. Khachaturyan, G. Akcay, and Y. Ni, Journal of Applied Physics **103**, 114113 (2008).

[160] Y. Ishibashi, Ferroelectrics **264**, 197 (2001).

[161] A. A. Heitmann and G. A. Rossetti, Jr., Philosophical Magazine **90**, 71 (2010).

[162] D. Damjanovic, M. Budimir, M. Davis, and N. Setter, Journal of Materials Science **41**, 65 (2006).

[163] Y. Ishibashi and M. Iwata, Japanese Journal of Applied Physics **38**, 1454 (1999).

[164] M. Iwata and Y. Ishibashi, Japanese Journal of Applied Physics **38**, 5670 (1999).

[165] M. Iwata, H. Orihara, and Y. Ishibashi, Japanese Journal of Applied Physics **40**, 703 (2001).

[166] M. Davis, M. Budimir, D. Damjanovic, and N. Setter, Journal of Applied Physics **101**, 054112 (2007).

[167] K. Carl and K. H. Härdtl, physica status solidi (a) **8**, 87 (1971).

[168] W. Cochran, Advances in Physics **9**, 387 (1960).

[169] D. Damjanovic, Applied Physics Letters **97**, 062906 (2010).

[170] B. Noheda, D. E. Cox, G. Shirane, J. A. Gonzalo, L. E. Cross, and S. E. Park, Applied Physics Letters **74**, 2059 (1999).

[171] R. Guo, L. E. Cross, S. E. Park, B. Noheda, D. E. Cox, and G. Shirane, Physical Review Letters **84**, 5423 (2000).

[172] B. Noheda, Current Opinion in Solid State and Materials Science **6**, 27 (2002).

[173] B. Noheda and D. E. Cox, Phase Transitions **79**, 5 (2006).

[174] W. F. Rao and Y. U. Wang, Applied Physics Letters **90**, 182906 (2007).

[175] D. Pandey, A. K. Singh, and S. Baik, Acta Crystallographica Section A **64**, 192 (2008).

[176] M. Davis, Journal of Electroceramics **19**, 25 (2007).

[177] *Crystallographic tables A1: Symmetry relations between space groups. Accesible online in* http://www.cryst.ehu.es/cryst/cellsub.html, (05/07/2015).

[178] Y. M. Jin, Y. U. Wang, A. G. Khachaturyan, J. F. Li, and D. Viehland, Journal of Applied Physics **94**, 3629 (2003).

[179] D. Viehland, Journal of Applied Physics **88**, 4794 (2000).

[180] Y. U. Wang, Physical Review B **76**, 024108 (2007).

[181] J. Frantti, Y. Fujioka, A. Puretzky, Y. Xie, Z. G. Ye, and A. M. Glazer, Journal of Applied Physics **113**, 174104 (2013).

[182] R. Kirchhofer, D. R. Diercks, B. P. Gorman, J. F. Ihlefeld, P. G. Kotula, C. T. Shelton, and G. L. Brennecka, Journal of the American Ceramic Society **97**, 2677 (2014).

[183] G. A. Rossetti, Jr. and A. G. Khachaturyan, Applied Physics Letters **91**, 072909 (2007).

[184] W. F. Rao and Y. U. Wang, Applied Physics Letters **91**, 052901 (2007).

[185] R. Theissmann, L. A. Schmitt, J. Kling, R. Schierholz, K. A. Schönau, H. Fuess, M. Knapp, H. Kungl, and M. J. Hoffmann, Journal of Applied Physics **102**, 024111 (2007).

[186] L. Jin, Z. He, and D. Damjanovic, Applied Physics Letters **95**, 012905 (2009).

[187] M. Budimir, D. Damjanovic, and N. Setter, Physical Review B **73**, 174106 (2006).

[188] Z. Kutnjak, J. Petzelt, and R. Blinc, Nature **441**, 956 (2006).

[189] Z. Kutnjak and R. Blinc, Physical Review B **76**, 104102 (2007).

[190] M. Porta, T. Lookman, and A. Saxena, Journal of Physics: Condensed Matter **22**, 345902 (2010).

[191] N. Novak, R. Pirc, and Z. Kutnjak, Physical Review B **87**, 104102 (2013).

[192] Z. K. Liu, X. Li, and Q. M. Zhang, Applied Physics Letters **101**, 082904 (2012).

[193] M. J. Haun, E. Furman, S. J. Jang, and L. E. Cross, Ferroelectrics **99**, 13 (1989).

[194] W. Liu and X. Ren, Physical Review Letters **103**, 257602 (2009).

[195] C. Zhou, W. Liu, D. Xue, X. Ren, H. Bao, J. Gao, and L. Zhang, Applied Physics Letters **100**, 222910 (2012).

[196] L. F. Zhu, B. P. Zhang, X. K. Zhao, L. Zhao, F. Z. Yao, X. Han, P. F. Zhou, and J. F. Li, Applied Physics Letters **103**, 072905 (2013).

[197] L. Jin, V. Porokhonskyy, and D. Damjanovic, Applied Physics Letters **96**, 242902 (2010).

[198] D. M. Smyth, *The Defect Chemistry of Metal Oxides* (Oxford University Press, 2000).

[199] C. A. Randall, N. Kim, J. P. Kucera, W. Cao, and T. R. Shrout, Journal of the American Ceramic Society **81**, 677 (1998).

[200] J. Hao, W. Bai, W. Li, and J. Zhai, Journal of the American Ceramic Society **95**, 1998 (2012).

[201] P. Zheng, J. L. Zhang, Y. Q. Tan, and C. L. Wang, Acta Materialia **60**, 5022 (2012).

[202] Y. Tan, J. Zhang, C. Wang, G. Viola, and H. Yan, physica status solidi (a) **212**, 433 (2015).

[203] Y. Tan, J. Zhang, Y. Wu, C. Wang, V. Koval, B. Shi, H. Ye, R. McKinnon, G. Viola, and H. Yan, Scientific reports **5**, Article number: 9953 (2015).

[204] D. Ghosh, A. Sakata, J. Carter, P. A. Thomas, H. Han, J. C. Nino, and J. L. Jones, Advanced Functional Materials **24**, 885 (2014).

[205] K. Uchino, E. Sadanaga, and T. Hirose, Journal of the American Ceramic Society **72**, 1555 (1989).

[206] S. Tsunekawa, S. Ito, T. Mori, K. Ishikawa, Z. Q. Li, and Y. Kawazoe, Physical Review B **62**, 3065 (2000).

[207] Z. Zhao, V. Buscaglia, M. Viviani, M. T. Buscaglia, L. Mitoseriu, A. Testino, M. Nygren, M. Johnsson, and P. Nanni, Physical Review B **70**, 024107 (2004).

[208] G. Arlt, Journal of Materials Science **25**, 2655 (1990).

[209] K. Ishikawa, K. Yoshikawa, and N. Okada, Physical Review B **37**, 5852 (1988).

[210] A. Roelofs, T. Schneller, K. Szot, and R. Waser, Applied Physics Letters **81**, 5231 (2002).

[211] W. D. Kingery, H. K. Bowen, and D. R. Uhlmann, *Introduction to Ceramics* (John Wiley & Sons, 1976).

[212] W. Cao and C. A. Randall, Journal of Physics and Chemistry of Solids **57**, 1499 (1996).

[213] G. Arlt, Ferroelectrics **104**, 217 (1990).

[214] H. Takahashi, Y. Numamoto, J. Tani, K. Matsuta, J. Qiu, and S. Tsurekawa, Japanese Journal of Applied Physics **45**, L30 (2006).

[215] H. Takahashi, Y. Numamoto, J. Tani, and S. Tsurekawa, Japanese Journal of Applied Physics **45**, 7405 (2006).

[216] T. Karaki, K. Yan, T. Miyamoto, and M. Adachi, Japanese Journal of Applied Physics **46**, L97 (2007).

[217] H. Takahashi, Y. Numamoto, J. Tani, and S. Tsurekawa, Japanese Journal of Applied Physics **46**, 7044 (2007).

[218] T. Karaki, K. Yan, and M. Adachi, Applied Physics Express **1**, 111402 (2008).

[219] S. Shao, J. Zhang, Z. Zhang, P. Zheng, M. Zhao, J. Li, and C. Wang, Journal of Physics D: Applied Physics **42**, 189801 (2009).

[220] Z. Y. Shen and J. F. Li, Journal of the Ceramic Society of Japan **118**, 940 (2010).

[221] N. Ma, B. P. Zhang, W. G. Yang, and D. Guo, Journal of the European Ceramic Society **32**, 1059 (2012).

[222] H. Takahashi, Electronics and Communications in Japan **95**, 20 (2012).

[223] T. Sluka, A. K. Tagantsev, D. Damjanovic, M. Gureev, and N. Setter, Nature Communications **3**, 748 (2012).

[224] T. Higuchi, K. Suzumori, and S. Tadokoro, *Next-Generation Actuators Leading Breakthroughs* (Springer-Verlag London Limited, 2010).

[225] S. Wada, K. Yako, H. Kakemoto, T. Tsurumi, and T. Kiguchi, Journal of Applied Physics **98**, 014109 (2005).

[226] S. Wada and T. Tsurumi, British Ceramic Transactions **103**, 1 (2004).

[227] D. Lin, S. Zhang, Z. Li, F. Li, Z. Xu, S. Wada, J. Luo, and T. R. Shrout, Journal of Applied Physics **110**, 084110 (2011).

[228] S. Wada and P. Pulpan, Key Engineering Materials **421-422**, 13 (2009).

[229] S. Wada, K. Takeda, T. Muraishi, H. Kakemoto, T. Tsurumi, and T. Kimura, Ferroelectrics **373**, 11 (2008).

[230] G. L. Messing, S. Trolier-McKinstry, E. M. Sabolsky, C. Duran, S. Kwon, B. Brahmaroutu, P. Park, H. Yilmaz, P. W. Rehrig, K. B. Eitel, E. Suvaci, M. Seabaugh, and K. S. Oh, Critical Reviews in Solid State and Materials Sciences **29**, 45 (2004).

[231] J. Zhao, F. Wang, W. Li, H. Li, D. Zhou, S. Gong, Y. Hu, and Q. Fu, Journal of Applied Physics **108**, 073535 (2010).

[232] R. E. Newnham, D. P. Skinner, and L. E. Cross, Materials Research Bulletin **13**, 525 (1978).

[233] D. S. Lee, D. H. Lim, M. S. Kim, K. H. Kim, and S. J. Jeong, Applied Physics Letters **99**, 062906 (2011).

[234] D. S. Lee, S. J. Jeong, M. S. Kim, and J. H. Koh, Journal of Applied Physics **112**, 124109 (2012).

[235] D. S. Lee, S. J. Jeong, M. S. Kim, and K. H. Kim, Japanese Journal of Applied Physics **52**, 021801 (2013).

[236] C. Groh, D. J. Franzbach, W. Jo, K. G. Webber, J. Kling, L. A. Schmitt, H. J. Kleebe, S. J. Jeong, J. S. Lee, and J. Rödel, Advanced Functional Materials **24**, 356 (2014).

[237] C. Groh, W. Jo, and J. Rödel, Journal of Applied Physics **115**, 234107 (2014).

[238] C. Groh, W. Jo, and J. Rödel, Journal of the American Ceramic Society **97**, 1465 (2014).

[239] S. J. Jeong, D. S. Lee, M. S. Kim, S. M. Jang, I. S. Kim, S. Mohsin, and J. S. Song, Journal of Electroceramics **33**, 230 (2014).

[240] N. H. Khansur, C. Groh, W. Jo, C. Reinhard, J. A. Kimpton, K. G. Webber, and J. E. Daniels, Journal of Applied Physics **115**, 124108 (2014).

[241] T. Shrout, W. A. Schulze, and J. V. Biggers, Ferroelectrics **29**, 129 (2011).

[242] J. E. Zhou, T. L. Cheng, and Y. U. Wang, Journal of Applied Physics **111**, 024105 (2012).

[243] H. Zhang, C. Groh, Q. Zhang, W. Jo, K. G. Webber, and J. Rödel, Advanced Electronic Materials **6**, DOI: 10.1002/aelm.201500018 (2015).

[244] G. Schileo, Progress in Solid State Chemistry **41**, 87 (2013).

[245] L. Mitoseriu and V. Buscaglia, Phase Transitions **79**, 1095 (2006).

[246] Z. Zhigang, Z. Weilong, W. Yugong, and Z. Ruitao, Ferroelectrics **101**, 55 (1990).

[247] C. A. Randall, S. F. Wang, D. Laubscher, J. P. Dougherty, and W. Huebner, Journal of Materials Research **8**, 871 (1993).

[248] Y. Park and Y. Kim, Journal of Materials Research **10**, 2770 (1995).

[249] Y. Park and H. G. Kim, Journal of the American Ceramic Society **80**, 106 (1997).

[250] Y. Sakabe, N. Wada, T. Hiramatsu, and T. Tonogaki, Japanese Journal of Applied Physics **41**, 6922 (2002).

[251] H. Tian, J. Qi, Y. Wang, H. L. W. Chan, and C. L. Choy, Progress in Solid State Chemistry **33**, 207 (2005).

[252] G. Yang, Z. Yue, Z. Gui, and L. Li, Journal of Applied Physics **104**, 074115 (2008).

[253] S. Y. Choi, S. J. Jeong, D. S. Lee, M. S. Kim, J. S. Lee, J. H. Cho, B. I. Kim, and Y. Ikuhara, Chemistry of Materials **24**, 3363 (2012).

[254] R. P. Mahajan, K. K. Patankar, M. B. Kothale, S. C. Chaudhari, V. L. Mathe, and S. A. Patil, Pramana **58**, 1115 (2002).

[255] R. G. Chaudhuri and S. Paria, Chemical reviews **112**, 2373 (2012).

[256] S. Y. Cheng, J. Shieh, N. J. Ho, and H. Y. Lu, Philosophical Magazine **91**, 4013 (2011).

[257] S. Y. Cheng, J. Shieh, H. Y. Lu, C. Y. Shen, Y. C. Tang, and N. J. Ho, Journal of the European Ceramic Society **33**, 2141 (2013).

[258] W. Krauss, D. Schütz, F. A. Mautner, A. Feteira, and K. Reichmann, Journal of the European Ceramic Society **30**, 1827 (2010).

[259] H. Jaffe, Industrial & Engineering Chemistry **42**, 264 (1950).

[260] A. von Hippel, R. G. Breckenridge, F. G. Chesley, and L. Tisza, Industrial & Engineering Chemistry **38**, 1097 (1946).

[261] B. Wul and J. M. Goldman, Academy of Sciences of the USSR **51**, 21 (1946).

[262] Y. Cui, X. Liu, M. Jiang, X. Zhao, X. Shan, W. Li, C. Yuan, and C. Zhou, Ceramics International **38**, 4761 (2012).

[263] L. Dong, D. S. Stone, and R. S. Lakes, Journal of Applied Physics **111**, 084107 (2012).

[264] D. Xue, Y. Zhou, H. Bao, J. Gao, C. Zhou, and X. Ren, Applied Physics Letters **99**, 122901 (2011).

[265] Y. Yao, C. Zhou, D. Lv, D. Wang, H. Wu, Y. Yang, and X. Ren, Europhysics Letters **98**, 27008 (2012).

[266] J. Nishikawa, T. Hagiwara, K. Kobayashi, Y. Mizuno, and H. Kishi, Japanese Journal of Applied Physics **46**, 6999 (2007).

[267] D. C. Sinclair and J. P. Attfield, Chemical Communications **16**, 1497 (1999).

[268] S. Suzuki, N. Iwaji, A. Honda, S. Higai, N. Wada, A. Ando, and H. Takagi, Japanese Journal of Applied Physics **51**, 09LC08 (2012).

[269] S. Suzuki, T. Takeda, A. Ando, T. Oyama, N. Wada, H. Niimi, and H. Takagi, Japanese Journal of Applied Physics **49**, 09MC04 (2010).

[270] T. Takenaka, K. I. Maruyama, and K. Sakata, Japanese Journal of Applied Physics **30**, 2236 (1991).

[271] T. Takenaka and K. Sakata, Ferroelectrics **95**, 153 (1989).

[272] J. König, M. Spreitzer, B. Jančar, D. Suvorov, Z. Samardžija, and A. Popovič, Journal of the European Ceramic Society **29**, 1695 (2009).

[273] J. Koruza and B. Malič, Journal of the European Ceramic Society **34**, 1971 (2014).

[274] A. Sasaki, T. Chiba, T. Mamiya, and E. Otsuki, Japanese Journal of Applied Physics **38**, 5564 (1999).

[275] Y. Hiruma, Y. Imai, Y. Watanabe, H. Nagata, and T. Takenaka, Applied Physics Letters **92**, 262904 (2008).

[276] J. Shi, H. Fan, X. Liu, and Q. Li, Journal of the European Ceramic Society **34**, 3675 (2014).

[277] F. Wang, C. L. Ming, Y. Tang, T. Wang, and W. Shi, Journal of Applied Physics **114**, 164105 (2013).

[278] F. Wang, M. Xu, Y. Tang, T. Wang, W. Shi, and C. M. Leung, Journal of the American Ceramic Society **95**, 1955 (2012).

[279] E. Ringgaard and T. Wurlitzer, Journal of the European Ceramic Society **25**, 2701 (2005).

[280] J. Fu, R. Zuo, X. Fang, and K. Liu, Materials Research Bulletin **44**, 1188 (2009).

[281] J. Fu, R. Zuo, X. Wang, and L. Li, Journal of Alloys and Compounds **486**, 790 (2009).

[282] K. Wang and J. F. Li, Advanced Functional Materials **20**, 1924 (2010).

[283] R. Zuo, J. Fu, and D. Lv, Journal of the American Ceramic Society **92**, 283 (2009).

[284] Y. Wang, D. Damjanovic, N. Klein, E. Hollenstein, and N. Setter, Journal of the American Ceramic Society **90**, 3485 (2007).

[285] F. Zhu, T. A. Skidmore, A. J. Bell, T. P. Comyn, C. W. James, M. Ward, and S. J. Milne, Materials Chemistry and Physics **129**, 411 (2011).

[286] N. M. Hagh, B. Jadidian, and A. Safari, Journal of Electroceramics **18**, 339 (2007).

[287] H. Birol, D. Damjanovic, and N. Setter, Journal of the American Ceramic Society **88**, 1754 (2005).

[288] J. Acker, H. Kungl, R. Schierholz, S. Wagner, R. A. Eichel, and M. J. Hoffmann, Journal of the European Ceramic Society **34**, 4213 (2014).

[289] P. Bomlai, P. Wichianrat, S. Muensit, and S. J. Milne, Journal of the American Ceramic Society **90**, 1650 (2007).

[290] M. Kosec and D. Kolar, Materials Research Bulletin **10**, 335 (1975).

[291] Y. Zhen and J. F. Li, Journal of the American Ceramic Society **89**, 3669 (2006).

[292] T. A. Skidmore, T. P. Comyn, A. J. Bell, F. Zhu, and S. J. Milne, IEEE Transactions on Ultrasonics, Ferroelectrics, and Frequency Control **58**, 1819 (2011).

[293] Y. Avrahami and H. L. Tuller, Journal of Electroceramics **13**, 463 (2004).

[294] A. Herabut and A. Safari, Journal of the American Ceramic Society **80**, 2954 (1997).

[295] W. Li, Z. Xu, R. Chu, P. Fu, and G. Zang, Journal of the American Ceramic Society **94**, 4131 (2011).

[296] T. R. Shrout and S. J. Zhang, Journal of Electroceramics **19**, 113 (2007).

[297] J. Wu, T. Wang, X. Cheng, X. Wang, B. Zhang, J. Zhu, and D. Xiao, Journal of Alloys and Compounds **576**, 299 (2013).

[298] S. Zhang, T. R. Shrout, H. Nagata, and Y. Hiruma, IEEE Transactions on Ultrasonics, Ferroelectrics, and Frequency Control **54**, 910 (2007).

[299] M. McQuarrie and F. W. Behnke, Journal of the American Ceramic Society **37**, 539 (1954).

[300] X. Yan, K. H. Lam, X. Li, R. Chen, W. Ren, X. Ren, Q. Zhou, and K. K. Shung, IEEE Transactions on Ultrasonics, Ferroelectrics, and Frequency Control **60**, 1272 (2013).

[301] S. H. Shin and J. H. Yoo, Transactions on Electrical and Electronic Materials **15**, 226 (2014).

[302] M. Hiroaki, S. Atsushi, and T. Hiroshi, *Dielectric ceramic composition and capacitor using the same. Patent application US 20030057405 A1* (2002).

[303] I. Kazushige and S. Akira, *Electronic device, dielectric ceramic composition and the production method. Patent application US 20060160692 A1* (2006).

[304] H. Jumpei, F. Tatsuo, S. Yasushi, M. Takanori, S. Hiroshi, and K. Makoto, *Piezoelectric material. Patent application WO2013005700 A1* (2012).

[305] Y. Zhang, J. Glaum, C. Groh, M. C. Ehmke, J. E. Blendell, K. J. Bowman, and M. J. Hoffman, Journal of the American Ceramic Society **97**, 2885 (2014).

[306] L. K. Templeton and J. A. Pask, Journal of the American Ceramic Society **42**, 212 (1959).

[307] P. Mishra, Sonia, and P. Kumar, Journal of Alloys and Compounds **545**, 210 (2012).

[308] S. Kokalj, *Master thesis "Synthesis and characterization of $Ba_{0.85}Ca_{0.15}Ti_{0.9}Zr_{0.1}O_3$", University of Ljubljana* (2011).

[309] D. Hennings and H. Schreinemacher, Materials Research Bulletin **12**, 1221 (1977).

[310] P. Wang, Y. Li, and Y. Lu, Journal of the European Ceramic Society **31**, 2005 (2011).

[311] W. Liu and S. Li, IEEE Transactions on Ultrasonics, Ferroelectrics, and Frequency Control **22**, 734 (2015).

[312] H. L. Sun, Q. J. Zheng, Y. Wan, Y. Chen, X. Wu, K. W. Kwok, H. L. W. Chan, and D. M. Lin, Journal of Materials Science: Materials in Electronics, 1 (2015).

[313] L. F. Zhu, B. P. Zhang, X. K. Zhao, L. Zhao, P. F. Zhou, and J. F. Li, Journal of the American Ceramic Society **96**, 241 (2013).

[314] J. Wu, D. Xiao, W. Wu, Q. Chen, J. Zhu, Z. Yang, and J. Wang, Journal of the European Ceramic Society **32**, 891 (2012).

[315] W. Wang, W. L. Li, D. Xu, W. P. Cao, Y. F. Hou, and W. D. Fei, Ceramics International **40**, 3933 (2014).

[316] W. F. Bai, W. Li, B. Shen, and J. W. Zhai, Key Engineering Materials **512-515**, 1385 (2012).

[317] H. Bao, C. Zhou, D. Xue, J. Gao, and X. Ren, Journal of Physics D: Applied Physics **43**, 465401 (2010).

[318] F. Cordero, F. Craciun, M. Dinescu, N. Scarisoreanu, C. Galassi, W. Schranz, and V. Soprunyuk, Applied Physics Letters **105**, 232904 (2014).

[319] J. Gao, D. Xue, Y. Wang, D. Wang, L. Zhang, H. Wu, S. Guo, H. Bao, C. Zhou, W. Liu, S. Hou, G. Xiao, and X. Ren, Applied Physics Letters **99**, 092901 (2011).

[320] D. Xue, Y. Zhou, H. Bao, C. Zhou, J. Gao, and X. Ren, Journal of Applied Physics **109**, 054110 (2011).

[321] H. Guo, B. K. Voas, S. Zhang, C. Zhou, X. Ren, S. P. Beckman, and X. Tan, Physical Review B **90**, 014103 (2014).

[322] L. Zhang, M. Zhang, L. Wang, C. Zhou, Z. Zhang, Y. Yao, L. Zhang, D. Xue, X. Lou, and X. Ren, Applied Physics Letters **105**, 162908 (2014).

[323] J. Gao, X. Hu, L. Zhang, F. Li, L. Zhang, Y. Wang, Y. Hao, L. Zhong, and X. Ren, Applied Physics Letters **104**, 252909 (2014).

[324] B. Li, M. C. Ehmke, J. E. Blendell, and K. J. Bowman, Journal of the European Ceramic Society **33**, 3037 (2013).

[325] M. C. Ehmke, S. N. Ehrlich, J. E. Blendell, and K. J. Bowman, Journal of Applied Physics **111**, 124110 (2012).

[326] M. C. Ehmke, J. E. Daniels, J. Glaum, M. Hoffman, J. E. Blendell, and K. J. Bowman, Journal of Applied Physics **112**, 114108 (2012).

[327] M. C. Ehmke, J. Glaum, M. Hoffman, J. E. Blendell, and K. J. Bowman, Journal of the American Ceramic Society **96**, 2913 (2013).

[328] M. C. Ehmke, J. Glaum, M. Hoffman, J. E. Blendell, and K. J. Bowman, Journal of the American Ceramic Society **96**, 3805 (2013).

[329] M. C. Ehmke, N. H. Khansur, J. E. Daniels, J. E. Blendell, and K. J. Bowman, Acta Materialia **66**, 340 (2014).

[330] M. C. Ehmke, F. H. Schader, K. G. Webber, J. Rödel, J. E. Blendell, and K. J. Bowman, Acta Materialia **78**, 37 (2014).

[331] A. Bjørnetun Haugen, J. S. Forrester, D. Damjanovic, B. Li, K. J. Bowman, and J. L. Jones, Journal of Applied Physics **113**, 014103 (2013).

[332] F. Benabdallah, A. Simon, H. Khemakhem, C. Elissalde, and M. Maglione, Journal of Applied Physics **109**, 124116 (2011).

[333] D. S. Keeble, F. Benabdallah, P. A. Thomas, M. Maglione, and J. Kreisel, Applied Physics Letters **102**, 092903 (2013).

[334] P. Sciau, G. Calvarin, and J. Ravez, Solid State Communications **113**, 77 (2000).

[335] Z. Yu, C. Ang, R. Guo, and A. S. Bhalla, Journal of Applied Physics **92**, 1489 (2002).

[336] X. Wang, H. Yamada, and C. N. Xu, Applied Physics Letters **86**, 022905 (2005).

[337] T. Shi, L. Xie, L. Gu, and J. Zhu, Scientific reports **5**, Article number: 8606 (2015).

[338] I. Coondoo, N. Panwar, H. Amorín, M. Alguero, and A. L. Kholkin, Journal of Applied Physics **113**, 214107 (2013).

[339] H. Guo, C. Zhou, X. Ren, and X. Tan, Physical Review B **89**, 100104(R) (2014).

[340] I. K. Jeong and J. S. Ahn, Applied Physics Letters **101**, 242901 (2012).

[341] D. Xue, J. Gao, Y. Zhou, X. Ding, J. Sun, T. Lookman, and X. Ren, Journal of Applied Physics **117**, 124107 (2015).

[342] D. Wang, Z. Jiang, B. Yang, S. Zhang, M. Zhang, F. Guo, and W. Cao, Journal of the American Ceramic Society **97**, 3244 (2014).

[343] Y. Tian, X. Chao, L. Jin, L. Wei, P. Liang, and Z. Yang, Applied Physics Letters **104**, 112901 (2014).

[344] J. Gao, L. Zhang, D. Xue, T. Kimoto, M. Song, L. Zhong, and X. Ren, Journal of Applied Physics **115**, 054108 (2014).

[345] G. Singh, V. Sathe, and V. S. Tiwari, Journal of Applied Physics **115**, 044103 (2014).

[346] T. Hoshina, K. Takizawa, J. Li, T. Kasama, H. Kakemoto, and T. Tsurumi, Japanese Journal of Applied Physics **47**, 7607 (2008).

[347] S. Lu, Z. Xu, S. Su, and R. Zuo, Applied Physics Letters **105**, 032903 (2014).

[348] G. Tutuncu, B. Li, K. Bowman, and J. L. Jones, Journal of Applied Physics **115**, 144104 (2014).

[349] D. Damjanovic, A. Biancoli, L. Batooli, A. Vahabzadeh, and J. Trodahl, Applied Physics Letters **100**, 192907 (2012).

[350] F. Li, L. Jin, and R. Guo, Applied Physics Letters **105**, 232903 (2014).

[351] B. Li, J. E. Blendell, and K. J. Bowman, Journal of the American Ceramic Society **94**, 3192 (2011).

[352] S. Su, R. Zuo, S. Lu, Z. Xu, X. Wang, and L. Li, Current Applied Physics **11**, S120 (2011).

[353] K. Sakata and Y. Masuda, Ferroelectrics **7**, 347 (1974).

[354] C. Tian, F. Wang, X. Ye, Y. Xie, T. Wang, Y. Tang, D. Sun, and W. Shi, Scripta Materialia **83**, 25 (2014).

[355] H. E. Mgbemere, R. P. Fernandes, and G. A. Schneider, Journal of the European Ceramic Society **33**, 3015 (2013).

[356] W. Bai, L. Li, W. Li, B. Shen, J. Zhai, and H. Chen, Journal of the American Ceramic Society **97**, 3510 (2014).

[357] L. Liu, D. Shi, M. Knapp, H. Ehrenberg, L. Fang, and J. Chen, Journal of Applied Physics **116**, 184104 (2014).

[358] C. Ang and Z. Yu, Advanced Materials **18**, 103 (2006).

[359] F. Wang, C. Jin, Q. Yao, and W. Shi, Journal of Applied Physics **114**, 027004 (2013).

[360] H. Tagawa and K. Igarashi, Journal of the American Ceramic Society **69**, 310 (1986).

[361] H. Tagawa, K. Kimura, T. Fujino, and K. Ouchi, Denki Kagaku **52**, 154 (1984).

[362] J. Gomah-Pettry, S. Said, M. Pascal, and J. P. Mercurio, Journal of the European Ceramic Society **24**, 1165 (2004).

[363] D. Rout, K. S. Moon, S. J. L. Kang, and I. W. Kim, Journal of Applied Physics **108**, 084102 (2010).

[364] Y. Watanabe, Y. Hiruma, H. Nagata, and T. Takenaka, Ceramics International **34**, 761 (2008).

[365] J. K. Lee, K. S. Hong, C. K. Kim, and S. E. Park, Journal of Applied Physics **91**, 4538 (2002).

[366] S. E. Park and K. S. Hong, Journal of Materials Research **12**, 2152 (1997).

[367] G. O. Jones and P. A. Thomas, Acta Crystallographica Section B **58**, 168 (2002).

[368] A. M. Glazer, Acta Crystallographica Section B **B28**, 3384 (1972).

[369] R. A. Cowley, Physical Review **134**, A981 (1964).

[370] S. A. Hayward and E. K. H. Salje, Phase Transitions **68**, 501 (1999).

[371] Y. P. Cai, D. Z. Han, and R. Y. Ning, Chinese Journal of Chemical Physics **23**, 237 (2010).

[372] J. M. Kiat and R. Thierry, Journal of Physics: Condensed Matter **8**, 3471 (1996).

[373] A. Buckley, J. P. Rivera, and E. K. H. Salje, Journal of Applied Physics **86**, 1653 (1999).

[374] J. G. Bednorz and K. A. Müller, Physical Review Letters **52**, 2289 (1984).

[375] M. Choi, F. Oba, Y. Kumagai, and I. Tanaka, Advance Materials **25**, 86 (2013).

[376] J. R. Gomah-Pettry, P. Marchet, A. Salak, V. M. Ferreira, and J. P. Mercurio, Integrated Ferroelectrics **61**, 159 (2004).

[377] R. Garg, B. N. Rao, A. Senyshyn, P. S. R. Krishna, and R. Ranjan, Physical Review B **88**, 014103 (2013).

[378] *National Institute of Standards and Technology: Guide for the Use of the International System of Units*, *Special Publication 811* (2008).

[379] B. D. Cullity, *Elements of X-ray Diffraction* (Addison-Wesley, 1956).

[380] A. J. Studer, M. E. Hagen, and T. J. Noakes, Physica B: Condensed Matter **385-386**, 1013 (2006).

[381] M. Hinterstein, M. Hoelzel, J. Rouquette, J. Haines, J. Glaum, H. Kungl, and M. Hoffman, Acta Materialia **94**, 319 (2015).

[382] M. I. Mendelson, Journal of the American Ceramic Society **52**, 443 (1969).

[383] P. A. Tipler, *College Physics*, Vol. 1 (Worth Pub, 1987).

[384] T. Leist, J. Chen, W. Jo, E. Aulbach, J. Suffner, and J. Rödel, Journal of the American Ceramic Society **95**, 711 (2012).

[385] *Institute of Electrical and Electronics Engineers: IEEE Standard on Piezoelectricity*, *176* (1987).

[386] T. A. Jain, K. Z. Fung, and J. Chan, Journal of Alloys and Compounds **468**, 370 (2009).

[387] K. W. Kirby and B. A. Wechsler, Journal of the American Ceramic Society **74**, 1841 (1991).

[388] D. E. Rase and R. Rutsum, Journal of the American Ceramic Society **38**, 102 (1955).

[389] S. Lee, C. A. Randall, and Z. K. Liu, Journal of the American Ceramic Society **90**, 2589 (2007).

[390] M. N. Rahaman, *Ceramic Processing and Sintering* (Marcel Dekker, 2003).

[391] J. Rödel and A. M. Glaeser, Nippon Seramikkusu Kyokai Gakujutsu Ronbunshi-Journal of the Ceramic Society of Japan **99**, 251 (1991).

[392] P. Chu, D. P. Chen, Y. L. Wang, Y. L. Xie, Z. B. Yan, J. G. Wan, J. M. Liu, and J. Y. Li, Scientific reports **4**, Article number: 5007 (2014).

[393] L. Shaoping, W. Cao, R. E. Newnham, and L. E. Cross, Ferroelectrics **139**, 25 (1993).

[394] J. L. Jones, M. Hoffman, and S. C. Vogel, Mechanics of Materials **39**, 283 (2007).

[395] J. Wu, A. Habibul, X. Cheng, X. Wang, and B. Zhang, Materials Research Bulletin **48**, 4411 (2013).

[396] Y. Tian, L. Wei, X. Chao, Z. Liu, and Z. Yang, Journal of the American Ceramic Society **96**, 496 (2012).

[397] C. Fujioka, R. Aoyagi, H. Takeda, S. Okamura, and T. Shiosaki, Journal of the European Ceramic Society **25**, 2723 (2005).

[398] H. Y. Park, I. T. Seo, M. K. Choi, S. Nahm, H. G. Lee, H. W. Kang, and B. H. Choi, Journal of Applied Physics **104**, 034103 (2008).

[399] Q. Chen, Z. Peng, H. Liu, D. Xiao, J. Zhu, and J. Zhu, Journal of the American Ceramic Society **93**, 2788 (2010).

[400] J. W. Northrip, Journal of Applied Physics **31**, 2293 (1960).

[401] R. G. Sabat, B. K. Mukherjee, W. Ren, and G. Yang, Journal of Applied Physics **101**, 064111 (2007).

[402] D. Tanaka, J. Yamazaki, M. Furukawa, and T. Tsukada, Japanese Journal of Applied Physics **49**, 09MD03 (2010).

[403] Y. Doshida, H. Shimizu, Y. Mizuno, and H. Tamura, Japanese Journal of Applied Physics **52**, 07HE01 (2013).

[404] K. Hiroki, N. Yuichi, T. Tadashi, and S. Koichiro, Japanese Journal of Applied Physics **28**, 114 (1989).

[405] D. Bolten, U. Böttger, and R. Waser, Journal of Applied Physics **93**, 1735 (2003).

[406] D. Bolten, U. Böttger, and R. Waser, Journal of the European Ceramic Society **24**, 725 (2004).

[407] G. Picht, K. G. Webber, Y. Zhang, H. Kungl, D. Damjanovic, and M. J. Hoffmann, Journal of Applied Physics **112**, 124101 (2012).

[408] J. E. Daniels, G. Picht, S. Kimber, and K. G. Webber, Applied Physics Letters **103**, 122902 (2013).

[409] Z. Wang, K. G. Webber, J. M. Hudspeth, M. Hinterstein, and J. E. Daniels, Applied Physics Letters **105**, 161903 (2014).

[410] H. G. Baerwald and D. A. Berlincourt, The Journal of the Acoustical Society of America **24**, 457 (1952).

[411] T. Leist, T. Granzow, W. Jo, and J. Rödel, Journal of Applied Physics **108**, 014103 (2010).

[412] S. Tashiro, K. Ishii, and K. Nagata, Japanese Journal of Applied Physics **42**, 6068 (2003).

[413] F. X. Li and R. K. N. D. Rajapakse, Acta Materialia **55**, 6472 (2007).

[414] F. X. Li and R. K. N. D. Rajapakse, Acta Materialia **55**, 6481 (2007).

[415] A. F. Devonshire, Philosophical Magazine **42**, 1065 (1951).

[416] M. Budimir, D. Damjanovic, and N. Setter, Journal of Applied Physics **94**, 6753 (2003).

[417] A. K. Singh, S. K. Mishra, Ragini, D. Pandey, S. Yoon, S. Baik, and N. Shin, Applied Physics Letters **92**, 022910 (2008).

[418] T. Kainz, M. Naderer, D. Schütz, O. Fruhwirth, F. A. Mautner, and K. Reichmann, Journal of the European Ceramic Society **34**, 3685 (2014).

[419] D. A. H. Hanaor and C. C. Sorrell, Journal of Materials Science **46**, 855 (2010).

[420] M. Meven, *Lecture Notes of the 43rd IFF Spring School 2012. Chapter D3 - Powder and Single Crystal Diffractometry: Chemical and Magnetic Structures* (ISBN 978-3-89336-759-7, 2012).

[421] S. Šturm, A. Benčan, M. A. Gulgun, B. Malič, and M. Kosec, Journal of the American Ceramic Society **94**, 2633 (2011).

[422] S. C. Jeon, B. K. Yoon, K. H. Kim, and S. J. L. Kang, Journal of Advanced Ceramics **3**, 76 (2014).

[423] H. Chazono and H. Kishi, Journal of the American Ceramic Society **83**, 101 (2000).

[424] D. Hennings and G. Rosenstein, Journal of the American Ceramic Society **67**, 249 (1984).

[425] Y. Zhen and J. F. Li, Journal of the American Ceramic Society **90**, 3496 (2007).

[426] S. C. Jeon and S. J. L. Kang, Applied Physics Letters **102**, 112915 (2013).

[427] K. Kobayashi, T. Suzuki, and Y. Mizuno, Key Engineering Materials **388**, 273 (2009).

[428] L. A. Schmitt, D. Schrade, H. Kungl, B. X. Xu, R. Mueller, M. J. Hoffmann, H. J. Kleebe, and H. Fuess, Computational Materials Science **81**, 123 (2014).

[429] M. Iwamoto, *Maxwell-Wagner Effect* in *Encyclopedia of Nanotechnology* (Springer Netherlands, 2012).

[430] L. A. Schmitt, J. Kling, M. Hinterstein, M. Hoelzel, W. Jo, H. J. Kleebe, and H. Fuess, Journal of Materials Science **46**, 4368 (2011).

[431] L. A. Schmitt and H. J. Kleebe, Functional Materials Letters **3**, 55 (2010).

[432] K. Kishida, K. Goto, and H. Inui, Acta Crystallographica Section B **65**, 405 (2009).

[433] A. M. Glazer, Acta Crystallographica Section A **31**, 756 (1975).

[434] L. A. Schmitt, M. Hinterstein, H. J. Kleebe, and H. Fuess, Journal of Applied Crystallography **43**, 805 (2010).

[435] X. Dai, Z. Xu, and D. Viehland, Philosophical Magazine Part B **70**, 33 (1994).

[436] J. Kling, W. Jo, R. Dittmer, S. Schaab, and H. J. Kleebe, Journal of the American Ceramic Society **96**, 3312 (2013).

[437] W. Jo, S. Schaab, E. Sapper, L. A. Schmitt, H. J. Kleebe, A. J. Bell, and J. Rödel, Journal of Applied Physics **110**, 074106 (2011).

[438] N. BarChaim, M. Brunstein, J. Grunberg, and A. Seidmantm, Ferroelectrics **6**, 299 (1973).

[439] N. Novak and Z. Kutnjak, Ferroelectrics **447**, 40 (2013).

[440] W. Jo and J. Rödel, Applied Physics Letters **99**, 042901 (2011).

[441] Y. Ishibashi and H. Orihara, Integrated Ferroelectrics **9**, 57 (1995).

[442] Y. A. Genenko, S. Zhukov, S. V. Yampolskii, J. Schütrumpf, R. Dittmer, W. Jo, H. Kungl, M. J. Hoffmann, and H. von Seggern, Advanced Functional Materials **22**, 2058 (2012).

[443] H. Orihara, S. Hashimoto, and Y. Ishibashi, Journal of the Physical Society of Japan **63**, 1031 (1994).

[444] S. Fahy and R. Merlin, Physical Review Letters **73**, 1122 (1994).

[445] Z. Sun, D. Xue, H. Wu, Y. Ji, X. Ding, D. Wang, Y. Yang, and X. Ren, Applied Physics Letters **102**, 222907 (2013).

[446] X. Dai, Z. Xu, and D. Viehland, Journal of the American Ceramic Society **79**, 1957 (1996).

[447] B. Dkhil and J. M. Kiat, Journal of Applied Physics **90**, 4676 (2001).

[448] H. Amorín, R. Jiménez, T. Hungría, A. Castro, and M. Algueró, Applied Physics Letters **94**, 152902 (2009).

[449] S. V. Kalinin, B. J. Rodriguez, S. Jesse, A. N. Morozovska, A. A. Bokov, and Z. G. Ye, Applied Physics Letters **95**, 142902 (2009).

[450] D. Berlincourt, IEEE Transactions on Sonics and Ultrasonics **13**, 116 (1966).

[451] A. E. Glazounov, A. K. Tagantsev, and A. J. Bell, Physical Review B **53**, 11281 (1996).

[452] J. Y. Li, R. C. Rogan, E. Ustundag, and K. Bhattacharya, Nature materials **4**, 776 (2005).

[453] D. A. Hall, A. Steuwer, B. Cherdhirunkorn, T. Mori, and P. J. Withers, Journal of Applied Physics **96**, 4245 (2004).

[454] C. M. Fancher, T. Iamsasri, J. E. Blendell, and K. J. Bowman, Materials Research Letters **1**, 156 (2013).

[455] C. Luo, W. Ge, Q. Zhang, J. Li, H. Luo, and D. Viehland, Applied Physics Letters **101**, 141912 (2012).

[456] E. J. Nichols, S. M. Pilgrim, and S. T. Misture, IEEE Transactions on Ultrasonics, Ferroelectrics, and Frequency Control **60**, 265 (2013).

[457] C. N. W. Darlington, Philosophical Magazine **31**, 1159 (1975).

[458] T. R. Halemane, M. J. Haun, L. E. Cross, and R. E. Newnham, Ferroelectrics **62**, 149 (2011).

[459] M. J. Haun, E. Furman, T. R. Halemane, and L. E. Cross, Ferroelectrics **99**, 55 (1989).

[460] N. Cereceda, B. Noheda, T. Iglesias, J. R. Fernandez-del-Castillo, and J. A. Gonzalo, Physical Review B **55**, 6174 (1997).

[461] M. Fornari and D. J. Singh, Physical Review B **63**, 092101 (2001).

[462] G. Fraysse, A. Al-Zein, J. Haines, J. Rouquette, V. Bornand, P. Papet, C. Bogicevic, and S. Hull, Physical Review B **84**, 144110 (2011).

[463] B. Noheda, N. Duan, N. Cereceda, and J. A. Gonzalo, Journal of the Korean Physical Society **32**, S162 (1998).

[464] X. Zhu, M. Fu, M. C. Stennett, P. M. Vilarinho, I. Levin, C. A. Randall, J. Gardner, F. D. Morrison, and I. M. Reaney, Chemistry of Materials **27**, 3250 (2015).

[465] M. A. Mabe and M. Amin, Aslib Proceedings **54**, 149 (2002).

[466] X. Ren, Nature materials **3**, 91 (2004).

[467] C. A. Randall, A. Kelnberger, G. Y. Yang, R. E. Eitel, and T. R. Shrout, Journal of Electroceramics **14**, 177 (2005).

[468] J. S. Kim and S. J. L. Kang, Journal of the American Ceramic Society **82**, 1085 (1999).

[469] R. Naccache, F. Vetrone, V. Mahalingam, L. A. Cuccia, and J. A. Capobianco, Chemistry of Materials **21**, 717 (2009).

[470] A. Umar, M. S. Akhtar, G. N. Dar, and S. Baskoutas, Talanta **116**, 1060 (2013).

[471] J. Wang, T. Tsuzuki, L. Sun, and X. Wang, ACS Applied Materials & Interfaces **2**, 957 (2010).

[472] L. Lartigue, P. Hugounenq, D. Alloyeau, S. P. Clarke, M. Lévy, J. C. Bacri, R. Bazzi, D. F. Brougham, C. Wilhelm, and F. Gazeau, ACS Nano **6**, 10935 (2012).

[473] C. Radloff and N. J. Halas, Nano Letters **4**, 1323 (2004).

[474] Z. Abdullaeva, E. Omurzak, C. Iwamoto, H. S. Ganapathy, S. Sulaimankulova, C. Liliang, and T. Mashimo, Carbon **50**, 1776 (2012).

[475] K. Kamata, Y. Lu, and Y. Xia, Journal of the American Chemical Society **125**, 2384 (2003).

[476] M. Ji, B. Liu, X. Yang, and J. Wang, Polymer **50**, 5970 (2009).

[477] M. Li, T. S. Mayer, J. A. Sioss, C. D. Keating, and R. B. Bhiladvala, Nano Letters **7**, 3281 (2007).

[478] G. Cao and D. Liu, Advances in Colloid and Interface Science **136**, 45 (2008).

[479] M. Yuan, L. Cheng, Q. Xu, W. Wu, S. Bai, L. Gu, Z. Wang, J. Lu, H. Li, Y. Qin, T. Jing, and Z. L. Wang, Advanced Materials **26**, 7432 (2014).

[480] *British Standard: Piezoelectric properties of ceramic materials and components. Part 2: Methods of measurement-low power*, *BS EN 50324-2:2002* (2002).

[481] J. Glaum and M. Hoffman, Journal of the American Ceramic Society **97**, 665 (2014).

[482] Y. A. Genenko, J. Glaum, M. J. Hoffmann, and K. Albe, Materials Science and Engineering: B **192**, 52 (2015).

[483] J. Pritchard, C. R. Bowen, and F. Lowrie, British Ceramic Transactions **100**, 265 (2001).

[484] D. S. Eddy and D. R. Sparks, *Application of MEMS Techonlogy in Automotive Sensors and Actuators. IEEE Proceedings of the International Symposium on Micromechatronics and Human Science*, Nagoya, Japan (1998).

[485] S. T. Zhang, A. B. Kounga, W. Jo, C. Jamin, K. Seifert, T. Granzow, J. Rödel, and D. Damjanovic, Advanced Materials **21**, 4716 (2009).

[486] K. Furutani, M. Urushibata, and N. Mohri, *Improvement of Control Method for Piezoelectric Actuator by Combining Induced Charge Feedback with Inverse Transfer Function Compensation. IEEE International Conference on Robotics and Automation*, Leuven, Belgium (1998).

[487] G. M. Clayton, S. Tien, A. J. Fleming, S. O. R. Moheimani, and S. Devasia, *Hysteresis and Vibration Compensation in Piezoelectric Actuators by Integrating Charge Control and Inverse Feedforward. 4th IFAC Symposium Mechatronic Systems*, Heidelberg, Germany (2006).

Curriculum Vitae

Personal Information

- Name: Matias
- Surname: Acosta
- Nationality: Argentinian - Italian
- Date of birth: 10/17/1987
- Place of birth: Mar del Plata, Buenos Aires, Argentina

Education and Training

- **2010-2011**: Representative student in the Superior Advisory Council of the Professor Jorge A. Sabato Institute-National University of General San Martín-National Atomic Commission, Buenos Aires, Argentina.
- **2005-2011**: 6-years undergraduate degree in materials engineering from Professor Jorge A. Sabato Institute and National University of Mar del Plata.
- **2005**: School leaving certificate in natural sciences, San Alberto Institute, Mar del Plata, Buenos Aires, Argentina.

Teaching and Supervisions

- **September-December, 2014**: Supervisor of bachelor thesis titled: "Elektromechanische Eigenschaften des Groß- und Kleinsignals von bleifreien Piezokeramiken".
- **May-September, 2013**: Supervisor of an advanced research work (analogous to a bachelor thesis) titled: "Crack propagation and electromechanical characterization of the (1-x)$Ba(Zr_{0.2}Ti_{0.8})O_3$-x$(Ba_{0.7}Ca_{0.3})TiO_3$ system".
- **May-September, 2013**: Supervisor of a bachelor thesis titled: "Electromechanical characterization of the (1-x)$Ba(Zr_{0.2}Ti_{0.8})O_3$-x$(Ba_{0.7}Ca_{0.3})TiO_3$ system".
- **March-August, 2013**: Supervisor of an advanced research work (analogous to a bachelor thesis) titled: "Synthesis and electromechanical characterization of lead-free $Bi_{1/2}Na_{1/2}TiO_3$-$SrTiO_3$ based piezoelectric composites".
- **March-September, 2013**: Supervisor of a master thesis titled: "Influence of donor and acceptor doping on the electromechanical properties of (1-x)$Ba(Zr_{0.2}Ti_{0.8})O_3$-x$(Ba_{0.7}Ca_{0.3})TiO_3$ system".
- **April-July, 2012**: Supervisor of a bachelor thesis titled: "Effect of A-site lanthanum doping of $Bi_{1/2}Na_{1/2}TiO_3$-$Bi_{1/2}K_{1/2}TiO_3$ ceramics on its electrical and electromechanical properties".

- **April-July, 2012/2013/2014/2015**: Supervisor of the laboratory course "ceramic processing" in the materials science department of the Technical University of Darmstadt, Darmstadt, Germany.
- **July-December, 2007**: Mathematics assistant teacher, National University of Mar del Plata, Buenos Aires, Argentina.

Refereed Publications

- **M. Acosta**, N. Novak, G. A. Rossetti, Jr., and J. Rödel, "Mechanisms of electromechanical response in $(1-x)Ba(Zr_{0.2}Ti_{0.8})O_3-x(Ba_{0.7}Ca_{0.3})TiO_3$ ceramics", Applied Physics Letters **107**, 142906 (2015).
- S. Zhukov, **M. Acosta**, Y. A. Genenko, and H. von Seggern, "Polarization dynamics variation across the temperature- and composition-driven phase transitions in the lead-free $(1-x)Ba(Zr_{0.2}Ti_{0.8})O_3-x(Ba_{0.7}Ca_{0.3})TiO_3$ ferroelectrics", Journal of Applied Physics **118**, 134104 (2015).
- M. Vögler, **M. Acosta**, D. R. J. Brandt, L. Molina-Luna, and K. G. Webber, "Temperature-dependent R-curve behavior of the lead-free ferroelectric $0.615Ba(Zr_{0.2}Ti_{0.8})O_3$-$0.385(Ba_{0.7}Ca_{0.3})TiO_3$ ceramic", Engineering Fracture Mechanics **144**, 68 (2015).
- M. Zakhozheva, L. A. Schmitt, **M. Acosta**, H. Guo, W. Jo, R. Schierholz, H. J. Kleebe, and X. Tan, "Wide compositional range *in situ* electric field investigations on lead-free $(1-x)Ba(Zr_{0.2}Ti_{0.8})O_3$-$x(Ba_{0.7}Ca_{0.3})TiO_3$ piezoceramic", Physical Review Applied **3**, 064018 (2015).
- **M. Acosta**, N. Liu, M. Deluca, S. Heidt, I. Ringl, C. Dietz, R. W. Stark, and W. Jo, "Tailoring ergodicity through selective A-site doping in the $Bi_{1/2}Na_{1/2}TiO_3$-$Bi_{1/2}K_{1/2}TiO_3$ system", Journal of Applied Physics **117**, 134106 (2015).
- **M. Acosta**, N. Khakpash, T. Someya, N. Novak, W. Jo, H. Nagata, G. A. Rossetti, Jr., and J. Rödel, "Origin of the large piezoelectric activity in $(1-x)Ba(Zr_{0.2}Ti_{0.8})O_3$-$x(Ba_{0.7}Ca_{0.3})TiO_3$ ceramics", Physical Review B **91**, 104108 (2015).
- M. Sanlialp, V.V. Shvartsman, **M. Acosta**, B. Dkhil, and D. Lupascu, "Strong electrocaloric effect in lead-free $0.65Ba(Zr_{0.2}Ti_{0.8})O_3$-$0.35(Ba_{0.7}Ca_{0.3})TiO_3$ ceramics obtained by direct measurements", Applied Physics Letters **106**, 062901 (2015).
- H. Humburg, **M. Acosta**, W. Jo, K. G. Webber, and J. Rödel, "Stress-dependent electromechanical properties of doped $(Ba_{1-x}Ca_x)(Zr_yTi_{1-y})O_3$", Journal of the European Ceramic Society **35**, 1209 (2015).
- M. Zakhozheva, L. A. Schmitt, **M. Acosta**, W. Jo, J. Rödel, and H. J. Kleebe, "*In situ* electric field induced domain evolution in $0.7Ba(Zr_{0.2}Ti_{0.8})O_3$-$0.3(Ba_{0.7}Ca_{0.3})TiO_3$ ferroelectrics", Applied Physics Letters **105**, 112904 (2014).

- **M. Acosta**, N. Novak, W. Jo, and J. Rödel, "Relationship between electromechanical properties and phase diagram in the (1-x)Ba($Zr_{0.2}Ti_{0.8}$)O_3-x($Ba_{0.7}Ca_{0.3}$)TiO_3 lead-free piezoceramic", Acta Materialia **80**, 48 (2014).
- **M. Acosta**, W. Jo, and J. Rödel, "Temperature- and Frequency-Dependent Properties of the 0.75$Bi_{1/2}Na_{1/2}TiO_3$-0.25$SrTiO_3$ Lead-Free Incipient Piezoceramic", Journal of the American Ceramic Society **97**, 1937 (2014).
- D. R. J. Brandt, **M. Acosta**, K. Jurij, and K. G. Webber, "Mechanical constitutive behavior and exceptional blocking force of lead-free (1-x)BZT-xBCT piezoceramics", Journal of Applied Physics **115**, 204107 (2014).
- S. Zhukov, Y. A. Genenko, **M. Acosta**, H. Humburg, W. Jo, J. Rödel, and H. von Seggern, "Polarization dynamics across the morphotropic phase boundary in (1-x)Ba($Zr_{0.2}Ti_{0.8}$)O_3-x($Ba_{0.7}Ca_{0.3}$)TiO_3 ferroelectrics", Applied Physics Letters **103**, 152904 (2013).
- J. Glaum, H. Simons, **M. Acosta**, and M. Hoffman "Tailoring the Piezoelectric and Relaxor Properties of ($Bi_{1/2}Na_{1/2}$)TiO_3-$BaTiO_3$ via Zirconium Doping", Journal of the American Ceramic Society **96**, 2881 (2013).
- **M. Acosta**, J. Zang, W. Jo, and J. Rödel, "High temperature dielectrics in $CaZrO_3$-modified $Bi_{1/2}Na_{1/2}TiO_3$-based lead-free ceramics", Journal of the European Ceramic Society **32**, 4327 (2012).

Invited Refereed Publications

- **Feature article: M. Acosta**, L. A. Schmitt, L. Molina-Luna, M. C. Scherrer, M. Brilz, K. G. Webber, M. Deluca, H. J. Kleebe, J. Rödel, and W. Donner, "Core-shell lead-free piezoelectric ceramics: current status and advanced characterization of the $Bi_{1/2}Na_{1/2}TiO_3$-$SrTiO_3$ system", Journal of the American Ceramic Society **98**, 3405 (2015).
- **Special issue:** A. Ayrikyan, V. Rojas, L. Molina-Luna, **M. Acosta**, J. Koruza, and K. G. Webber, "Enhancing Electromechanical Properties of Lead-Free Ferroelectrics With Bilayer Ceramic/Ceramic Composites", IEEE Transactions on Ultrasonics, Ferroelectrics, and Frequency Control **62**, 997 (2015).
- **Feature article:** W. Jo, R. Dittmer, **M. Acosta**, J. Zang, C. Groh, E. Sapper, K. Wang, and J. Rödel, "Giant electric-field-induced strains in lead-free ceramics for actuator applications-status and perspective", Journal of Electroceramics **29**, 71 (2012).

Patents and Book Chapter

- **Patent: M. Acosta**, R. Salloum, and J. Rödel, “Multifunktionale Ultraschallschneidvorrichtung zur Befestigung an einer Vorrichtung für einen minimalinvasiven Eingriff”, Patent application number DE 10 2015 106 749.8 (2015).
- **Patent:** J. Rödel, W. Jo, M. E. Anton, R. Dittmer, J. Zang, and **M. Acosta**, “Dielektrischer keramischer Werkstoff sowie Verwendung einer dielektrischen Komponente aus dem Werkstoff”, Patent application number DE 10 2012 106 743 (2013).
- **Book chapter:** C. Groh, M. Gröting, L. A. Schmitt, G. Mera, **M. Acosta**, A. Gurlo, E. M. Anton, W. Jo, T. Granzow, K. Albe, H. J. Kleebe, R. Riedel, and J. Rödel, “Lead-Free Piezoceramics”, to be published within Adaptronics book from AdRIA state center of Adaptronics (2012).

Conferences

Oral Contributions

- **M. Acosta**, T. Someya, S. Zhukov, Y. Genenko, N. Novak, W. Jo, H. Nagata, H. von Seggern, and J. Rödel, “Relationship between electromechanical properties and phase diagram in the (1-x)$Ba(Zr_{0.2}Ti_{0.8})O_3$-x$(Ba_{0.7}Ca_{0.3})TiO_3$ lead-free piezoceramic”, International Conference Electronic Materials and Applications, Orlando, United States (2015).
- J. Glaum, H. Simons, **M. Acosta**, S. Hu, J. Seidel, J. Daniels, and M. Hoffman, “Relaxor-ferroelectric transition in BNT-based piezoceramics”, International Conference Electronic Materials and Applications, Orlando, United States (2015).
- A. Ayrikyan, J. Koruza, **M. Acosta**, V. Rojas, L. Molina-Luna, T. Frömling, H. Hutter, and K. Webber, “Tailoring Lead-Free Ferroelectric Composites”, International Conference Electronic Materials and Applications, Orlando, United States (2015).
- M. Vögler, **M. Acosta**, D. R. J. Brandt, J. Rödel, and K. G. Webber, “Temperature-dependent R-curve behavior of the lead-free (1-x)$Ba(Zr_{0.2}Ti_{0.8})O_3$-x$(Ba_{0.7}Ca_{0.3})TiO_3$”, International Conference of Materials and Science Engineering MSE, Darmstadt, Germany (2014).
- M. Zakhozheva, L. A. Schmitt, **M. Acosta**, J. Rödel, W. Jo, and H. J. Kleebe, “*In situ* electric field transmission electron microscopy studies of 0.7$Ba(Zr_{0.2}Ti_{0.8})O_3$-0.3$(Ba_{0.7}Ca_{0.3})TiO_3$ ferroelectrics", 18th International Microscopy Conference, Prague, Check Republic (2014).
- J. Glaum, H. Simons, **M. Acosta**, and M. Hoffman, “Relaxor-ferroelectric transition in BNT-based piezoceramics”, 3rd Biennial Conference of the Combined Australian Materials Societies, Sydney, Australia (2014).
- S. Zhukov, Y. Genenko, **M. Acosta**, H. Humburg, W. Jo, J. Rödel, and H. von Seggern, “Polarization dynamics across the morphotropic phase boundary in Lead-free BZT-xBCT Ferroelectrics”, International Conference on Electroceramics, Bucharest, Romania (2014).

- M. Zakhozheva, L. A. Schmitt, J. Glaum, **M. Acosta**, W. Jo, J. Rödel, and H. J. Kleebe, "Transmission electron microscopy of $0.94Bi_{1/2}Na_{1/2}TiO_3$-$0.06BaZr_xTi_{1-x}O_3$ piezoceramics", 25th Russian Conference on Electron Microscopy, Chernogolovka, Russia (2014).
- **M. Acosta**, W. Jo, M. Scherrer, L. A. Schmitt, M. Deluca, W. Donner, H. J. Kleebe, and J. Rödel, "Microstructure, dielectric, and electromechanical properties of the $75Bi_{1/2}Na_{1/2}TiO_3$-$25SrTiO_3$ lead-free incipient piezoceramic", Joint IEEE International Symposium on the Applications of Ferroelectric, International Workshop on Acoustic Transduction Materials and Devices & Workshop on Piezoresponse Force Microscopy, Pennsylvania, United States (2014).
- **M. Acosta**, D. Brandt, M. Völger, H. Humburg, W. Jo, J. Koruza, K. Webber, and J. Rödel, "Characterization of (1-x)$Ba(Zr_{0.2}Ti_{0.8})O_3$-x$(Ba_{0.7}Ca_{0.3})TiO_3$ for large signal actuator applications", Joint IEEE International Symposium on the Applications of Ferroelectric, International Workshop on Acoustic Transduction Materials and Devices & Workshop on Piezoresponse Force Microscopy, Pennsylvania, United States (2014).
- **M. Acosta**, D. Brandt, M. Völger, H. Humburg, W. Jo, J. Koruza, K. Webber, and J. Rödel, "Characterization of (1-x)$Ba(Zr_{0.2}Ti_{0.8})O_3$-x$(Ba_{0.7}Ca_{0.3})TiO_3$ for large signal actuator applications", Japanese Ceramic Society Meeting, Tokyo, Japan (2014).
- J. Glaum, H. Simons, **M. Acosta**, and M. Hoffman, "Relaxor-ferroelectric transition in BNT-based piezoceramics", International Conference on Small Science, Las Vegas, United States (2013).
- **M. Acosta**, H. Humburg, W. Jo, M. Scherrer, L. A. Schmitt, H. J. Kleebe, and J. Rödel, "Electromechanical, piezoelectric and microstructure study of the (1-x)$Ba(Zr_{0.2}Ti_{0.8})O_3$-x$(Ba_{0.7}Ca_{0.3})TiO_3$ system", 2nd International Conference on Advanced Electroceramics, ICC Jeju, Korea (2013).
- **M. Acosta**, C. Groh, W. Jo, D. Franzbach, K. Webber, M. Scherrer, L. A. Schmitt, H. J. Kleebe, and J. Rödel, "Lead-free relaxor/ferroelectrics composites for actuator applications", International Symposium on Piezocomposite Applications, Dresden, Germany (2013).
- S. Zhukov, Y. Genenko, **M. Acosta**, H. Humburg, W. Jo, and H. von Seggern, "Exploration of Microscopic Mechanisms of the Polarization Switching in Lead-free (1-x)BZT-xBCT Ferroelectrics", IEEE International Ultrasonics Symposium, Prague, Czech Republic (2013).
- J. Glaum, **M. Acosta**, H. Simons, and M. Hoffman, "Temperature-dependency of the relaxor-ferroelectric transition in BNT-BZT ceramics", IEEE International Ultrasonics Symposium, Prague, Czech Republic (2013).
- G. H. Ryu, **M. Acosta**, W. Jo, J. Rödel, C. Cheon, and M. H. Kim, "Leakage Current Behavior of Lead-free $(Na_{0.53}K_{0.47})NbO_3$ Piezoelectric Ceramics", Korean Society Conference, Geongnam, Korea (2013).
- J. Glaum, H. Simons, **M. Acosta**, and M. Hoffman, "Manipulation of the relaxor behavior of BNT-BT ceramics due to Zr addition", International Conference Electronic Materials and Applications 2013, Orlando, United States (2013).

- **M. Acosta**, J. Zang, W. Jo, and J. Rödel, "High temperature dielectrics in $CaZrO_3$-modified $Bi_{1/2}Na_{1/2}TiO_3$-based lead-free ceramics", International Conference Frontiers of Condensed Matter, Buenos Aires, Argentina (2012).
- **M. Acosta**, J. Zang, W. Jo, and J. Rödel, "High temperature dielectrics with an extremely large temperature stability in $Bi_{1/2}Na_{1/2}TiO_3$-based lead-free ceramics", International Conference of Materials and Science Engineering MSE, Darmstadt, Germany (2012).
- J. Glaum, H. Simons, **M. Acosta**, and M. Hoffman, "Influence of Bipolar Electric Cycling on the Macroscopic and Structural Properties of BNT-Based Lead-free Piezoceramics", International Conference Material and Science Engineering MSE, Darmstadt, Germany (2012).
- J. Glaum, H. Simons, **M. Acosta**, and M. Hoffman, "Influence of electric field cycling on the macroscopic and structural properties of BNT-BZT ceramics", International Symposium on Applications of Ferroelectrics, Aveiro, Portugal (2012).

Poster Contributions

- J. Rödel, **M. Acosta**, N. Khakpash, T. Someya, N. Novak, W. Jo, H. Nagata, and G. A. Rossetti, Jr., "Computed Phase Diagram and Temperature-Dependent Properties of the (1-x)$Ba(Zr_{0.2}Ti_{0.8})O_3$-x$(Ba_{0.7}Ca_{0.3})TiO_3$ Lead-Free Piezoceramic", Joint IEEE International Symposium on the Applications of Ferroelectric, International Workshop on Acoustic Transduction Materials and Devices & Workshop on Piezoresponse Force Microscopy, Singapore (2015).
- **M. Acosta**, M. C. Scherrer, M. Brilz, W. Jo, L. A. Schmitt, H. J. Kleebe, W. Donner, and J. Rödel, "Characterization of the $75Bi_{1/2}Na_{1/2}TiO_3$-$25SrTiO_3$ lead-free incipient core-shell piezoceramic", International Conference Electronic Materials and Applications, Orlando, United States (2015).
- **M. Acosta**, M. Scherrer, M. Brilz, W. Jo, L. Molina-Luna, L. A. Schmitt, W. Donner, H. J. Kleebe, and J. Rödel, "$Bi_{1/2}Na_{1/2}TiO_3$-$SrTiO_3$: A core-shell piezoceramic for actuator applications", International Symposium on Electrical Fatigue in Functional Materials, Sellin, Germany (2014).
- **M. Acosta**, D. Brandt, M. Völger, H. Humburg, W. Jo, J. Koruza, K. Webber, and J. Rödel, "Characterization of (1-x)$Ba(Zr_{0.2}Ti_{0.8})O_3$-x$(Ba_{0.7}Ca_{0.3})TiO_3$ for large signal actuator applications", Joint IEEE International Symposium on the Applications of Ferroelectric, International Workshop on Acoustic Transduction Materials and Devices & Workshop on Piezoresponse Force Microscopy, Pennsylvania, United States (2014).
- **M. Acosta**, W. Jo, M. Scherrer, L. A. Schmitt, H. J. Kleebe, and J. Rödel, "Temperature- and frequency-dependent properties of the $75Bi_{1/2}Na_{1/2}TiO_3$-$25SrTiO_3$ lead-free incipient piezoceramic", 2nd International Conference on Advanced Electroceramics, ICC Jeju, Korea (2013).
- E. A. Patterson, **M. Acosta**, W. Jo, J. Rödel, and D. P. Cann, "Incipient Piezoelectric Transitions in $(Bi_{1/2}Na_{1/2})TiO_3$-based Lead-free Ceramics", 16th US-Japan Seminar on Dielectric and Piezoelectric Materials, Raleigh, United States (2013).

- N. H. Khansur, **M. Acosta**, C. Groh, W. Jo, J. Rödel, and J. Daniels, "*In situ* diffraction studies of electric field induced strain response in polycrystalline composite materials", 2nd International Conference on Advanced Electroceramics, ICC Jeju, Korea (2013).
- G. H. Ryu, M. H. Kim, J. S. Kim, M. H. Lee, **M. Acosta**, W. Jo, J. Rödel, and C. Cheon, "Study on Conduction Behavior of $(Na_{0.53}K_{0.47})NbO_3$ Piezoelectric Ceramics", 2nd International Conference on Advanced Electroceramics, ICC Jeju, Korea (2013).
- M. C. Scherrer, L. A. Schmitt, **M. Acosta**, W. Jo, J. Rödel, and H. J. Kleebe, "*In situ* TEM investigation on lead-free $(1\text{-}x)Bi_{1/2}Na_{1/2}TiO_3\text{-}xSrTiO_3$", International Microscopy Conference, Regensburg, Germany (2013).
- **M. Acosta**, H. J. Kleebe, W. Donner, H. Seggern, A. Klein, H. Breitzke, G. Buntkowsky, K. Albe, Y. Genenko, and J. Rödel, "Research on Ferroelectrics in SFB 595 as project of 2011", International Conference Frontiers of Condensed Matter, Buenos Aires, Argentina (2012).
- C. Groh, **M. Acosta**, W. Jo, and J. Rödel, "Composite ferroelectrics for high strain actuator applications", International Conference of Materials and Science Engineering MSE, Darmstadt, Germany (2012).
- J. Glaum, H. Simons, **M. Acosta**, and M. Hoffman, "Influence of Bipolar Electric Cycling on the Macroscopic and Structural Properties of BNT-Based Lead-free Piezoceramics", International workshop of relaxor materials, Edesheim, Germany (2012).
- **M. Acosta**, B. L. Da Silva, D. G. Serrano, and A. Serquis, "Theoretical analysis of MgB_2. Experimental characterization and optimization of its superconducting properties", International Conference of Metallurgic and Materials Science and Technology, Buenos Aires, Argentina (2009).

Recognitions

- **January, 2015**: "PiezoRobotics: Multifunctional Piezoelectric Robot" project (initiator, manager, and coordinator) was **awarded with the price to the second best idea of Technical University of Darmstadt of 2014**.
- **May, 2014**: Presentation as an author of a work titled "Characterization of $(1\text{-}x)Ba(Zr_{0.2}Ti_{0.8})O_3\text{-}x(Ba_{0.7}Ca_{0.3})TiO_3$ for large signal actuator applications", Joint IEEE International Symposium on the Applications of Ferroelectrics, International Workshop on Acoustic Transduction Materials and Devices & Workshop on Piezoresponse Force Microscopy, Pennsylvania, United States 2014. **Award to the best poster** of the joint Conference.
- **November, 2013**: Presentation as an author of a work titled "Temperature- and frequency-dependent properties of the $75Bi_{1/2}Na_{1/2}TiO_3\text{-}25SrTiO_3$ lead-free incipient piezoceramic" at the 2nd International Conference on Advanced Electroceramics, ICC Jeju, Korea 2013. **Award to the best poster** of the symposium Ferroelectrics, Piezoelectrics, and Dielectrics: Processing and Applications.

- **May-September, 2013**: **Supervisor of the best bachelor thesis in the materials science department of the Technical University of Darmsadt in 2014.** Bachelor thesis titled: "Electromechanical characterization of the (1-x)$Ba(Zr_{0.2}Ti_{0.8})O_3$-x$(Ba_{0.7}Ca_{0.3})TiO_3$ system".
- **March-September, 2013**: **Supervisor of the best master thesis in the materials science department of the Technical University of Darmstadt in 2013.** Master thesis titled: "Influence of donor and acceptor doping on the electromechanical properties of (1-x)$Ba(Zr_{0.2}Ti_{0.8})O_3$-x$(Ba_{0.7}Ca_{0.3})TiO_3$ system".
- **December, 2012**: **Invited talk** "High temperature dielectrics in $CaZrO_3$-modified $Bi_{1/2}Na_{1/2}TiO_3$-based lead-free ceramics" at the International Conference Frontiers of Condensed Matter, Buenos Aires, Argentina.
- **September, 2012**: Presentation as an author of a work titled "High temperature dielectrics with an extremely large temperature stability in $Bi_{1/2}Na_{1/2}TiO_3$-based lead-free ceramics" at the international Conference Material and Science Engineering MSE. **Awarded with one of the two "highlighted" works** in the oral presentations of the High temperature functional materials symposium.
- **September, 2012**: Presentation as co-author of a work titled "Influence of Bipolar Electric Cycling on the Macroscopic and Structural Properties of BNT-Based Lead-free Piezoceramics" in the international Conference Material and Science Engineering MSE. **Awarded with one of the two "highlighted" works** in the oral presentations of the electrical fatigue of functional materials.
- **October, 2009**: Presentation as an author of a work titled "Theoretical analysis of MgB_2. Experimental characterization and optimization of its superconducting properties" at the International Conference of Metallurgic and Materials Science and Technology, Buenos Aires, Argentina. **Award to the best poster** at the "undergraduate students" competition.
- **2007-2011**: **Full time scholarship** at the Professor Jorge A. Sabato Institute, Buenos Aires, Argentina.

Erklärung zur Dissertation

Ich erkläre hiermit ehrenwörtlich, dass ich die vorliegende Arbeit selbstständig angefertigt habe. Sämtliche aus fremden Quellen direkt oder indirekt übernommenen Gedanken sind als solche kenntlich gemacht.

Die Arbeit wurde bisher keiner anderen Prüfungsbehörde vorgelegt und noch nicht veröffentlicht.

Darmstadt, den

(Ing. Matias Acosta)